The Use of Flexible Biomimetic Fins in Propulsion

Riggs, Paul

Award date:
2010

Awarding institution:
University of Bath

The Use of Flexible Biomimetic Fins in Propulsion

Paul Richard Riggs

A thesis submitted for the degree of Doctor of Philosophy

University of Bath

Department of Mechanical Engineering

June 2010

Paul Richard Riggs

p.riggs@alumni.bath.ac.uk

Abstract

This thesis documents a series of investigations exploring the role of stiffness profile in propulsion using pitching flexible fins. Stiffness profile is defined as the variation in local bending stiffness along the chord of a fin, from leading to trailing edge.

An unmanned robotic submarine was created, using simple pitching flexible fins for propulsion. Its design and performance prompted a review of literature covering many aspects of oscillating fin propulsion, paying special attention to the studies of pitching flexible fins, of the type used in the submarine. In the body of previous work, fin stiffness profile was a consequence of the external shape profile of a fin; fins had not thus far been designed with stiffness profile specifically in mind. A hypothesis was proposed: *"Use of a biomimetic fin stiffness profile can improve the effectiveness of a flexible oscillating fin, over that of a standard NACA designated fin shape."*

Rectangular planform flexible fins of standard NACA 0012 design and 1:1 aspect ratio were tested alongside similar fins with a stiffness profile mimicking that of a pumpkinseed sunfish (*Lepomis gibbosus*). The fins were oscillated with a pitching-only sinusoidal motion over a range of frequencies and amplitudes, while torque, lateral force and static thrust were measured. Over the range of oscillation parameters tested, it was shown that the fin with a biomimetic stiffness profile offered a significant improvement in static thrust over a fin of similar dimensions with a standard NACA 0012 aerofoil shape, and produced thrust more consistently over each oscillation cycle.

A comparison of different moulding materials showed that the improvement was due to the stiffness profile itself, and was not simply an effect of altering the overall stiffness of the fin, or changing its natural frequency. Within the range of stiffnesses and oscillation conditions tested, fins of the same stiffness profile were found to follow similar thrust-power curves, independently of their moulding material. Biomimetic fins were shown to produce between 10% and 25% more thrust per watt of mechanical input power.

Acknowledgements

A very special thank you goes to my supervisors Adrian Bowyer and Julian Vincent, for their advice, their academic wisdom, and their understanding and patience in putting up with me these last few years. I hope I've produced a work you'll be proud to have your names on.

This research was been funded by a grant from the Engineering and Physical Sciences Research Council of the United Kingdom. I thank them for allowing this project to happen. I also thank the Royal Academy of Engineering for providing travel grants on two occasions.

I would also like to thank:

William Megill, for his advice and encouragement, and for giving me the opportunity to work on the Bathymysis submarine, and to experience the fascinating world of marine biology.

The Bathymysis submarine team undergraduates: Georg Brindlinger, Aidan Coxon, Grant Klimaytys, Chris Pattinson, Chris Wallis, and Glen Waterhouse.

Technicians Steve Dolan, Jeff Brewster for their generous provision of time and skills, frequently beyond the call of duty.

I gratefully acknowledge the help of Nicole Augustin, for the statistical advice she kindly provided, and Dr. Philippe Blondel for allowing me access to his facilities.

Many thanks go to my officemates past and present: Keith Paskins, Rhodri Armour, Thomas Hesselberg, Francisco Rojo-Perez, Jen Wladichuk, Sabine Graf, Keri Collins, Ed Sells, and everyone else who passed through our department. I thank them for their friendship, encouragement, company, and for making the office fun, both in the tough times and the easy ones.

Lastly I would like to thank all of my friends, my mother and father, my sister, and other family members for their support, encouragement, kind words and timely advice. I hope I'll get to explain my gratitude to each of you in person very soon. And with my thesis submitted, for the first time in years you'll have my undivided attention!

Table of Contents

Chapter One

Introduction

1.1 Biomimetics

Biomimetics is the application of biologically inspired methods and principles to engineering and technology. The term is often used interchangeably with 'bioinspiration', 'biomimicry', and 'bionics', all of which have similar meanings. Engineers and scientists have looked to nature for inspiration since long before the term was coined, but in recent years, cross-disciplinary research has become more prevalent in many areas, and the search for naturally inspired solutions to specific problems has grown more deliberate.

There are many well-known examples of biomimetic solutions to engineering problems. Cats' eyes; road markers designed to reflect the headlights of approaching cars are based on the design of their biological counterparts. Velcro, the reusable fastening material, was inspired by the mechanism by which burrs from plants disperse themselves by sticking to passing animals. Lotus plants have a water-repellent surface microstructure which helps them to keep clean; as water droplets roll over their leaves, dirt particles are carried away. The 'Lotus effect' has been exploited by chemical engineers to create paints that exhibit the same water and dirt repellent properties. These applications highlight the relevance and value of the biomimetic approach to all areas of engineering and design.

1.2 Flexible Fin Propulsion

Nature displays many diverse and excellent means of underwater propulsion. Different species display a multitude of propulsion and manoeuvring methods appropriate for their environments. The combinations of agility, efficiency and simplicity they achieve are far beyond the best attempts of humans to emulate them, so they are a valuable source of information and inspiration for engineers seeking to design the propulsion systems of the future.

While conventional rotary propellers are widely used and very effective in many applications, there are areas in which flexible fin propulsion can prove superior.

Propellers rotating at high speed can cause cavitation, and in doing so, generate noise, and accumulate damage. When a propeller blade passes through water at high speed, the pressure behind it can be low enough to form small vacuum pockets in the water. When normal pressure is restored, these pockets implode, and the energy that went into creating them is

released in a very small space, creating a shockwave. When cavitation occurs near a propeller surface, it can cause corrosion and wear, shortening the useful life of the propeller. The gentler motion of an oscillating fin means it does not create any areas of extreme low pressure in which cavitation is likely to occur.

Propellers leave a large amount of turbulent fluid in their wake as they move, as they impart kinetic energy to the water not only in the direction of travel, but also in a helical column behind the propeller blades. Ultimately, energy spent creating this spinning helix is wasted, as the movement dissipates into the surrounding water. Highly efficient fins, such as those of a tuna, leave a wake in which almost all the momentum is in the opposite direction to the motion of the fish (Lauder, 2000, Triantafyllou and Triantafyllou, 1995). This means that the energy transferred to the water to create the vortices behind the fish has been spent very efficiently for the generation of thrust.

Another advantage of finned propulsion is that fins do not suffer from many of the risks that conventional propellers do. Propellers are prone to damage from objects with which they collide, they can become tangled in weeds, and are dangerous to nearby people, animals and objects unless properly guarded. The gentler motion of flexible fins means they suffer no such drawbacks.

1.2.1 Non-Propulsive Applications

The ability of flexible fins to move liquids can be exploited in applications other than water vehicle propulsion. Pumping and liquid handling machinery is another situation where their properties can be put to good use. Their simplicity and minimization of moving parts will be advantageous in industrial applications. Their ability to operate within heterogeneous substances and neither to damage nor be damaged by them is another positive quality.

1.3 Outline of Chapters

This thesis grew out of a general study of finned propulsion on the platform of a robotic submarine. By way of a series of investigations, it became focussed on a specific aspect of fin propulsion: the use of biomimetic stiffness profiles in improving the thrust and efficiency of finned propulsion. In its structure, this thesis follows the path of research, experiments and discoveries that lead from the initial submarine project to the conclusions of the biomimetic fin experiments. The order in which events are presented is loosely chronological, although some events are grouped together to aid clarity. The chapters are as follows:

Chapter One: Introduction

This chapter provides context to the following chapters, briefly discussing the field of biomimetics, and the reasons for interest in fin-based propulsion. It introduces some of the terminology and conventions used throughout the rest of the thesis.

Chapter Two: Background and Literature Survey

Chapter Two reviews a selection of literature from the fields of fish locomotion, hydrodynamics, and more specifically, oscillating fin research, in order to lay the foundations of the work in the following chapters. It establishes that the stiffness profile of fins is a compelling area for further study, and introduces a hypothesis to be put to the test in subsequent chapters: that use of a biomimetic fin stiffness profile can improve the effectiveness of a flexible oscillating fin, over a standard NACA (National Advisory Committee for Aeronautics) designated fin shape.

Chapter Three: Preliminary Investigations

Chapter Three describes several brief investigations that were carried out before the commencement of the work described in the main experimental chapters. Investigations included the dissection of a dogfish fin, and experiments on the materials used to mould flexible fins in the subsequent chapters.

Chapter Four: Development of Experimental Methods

Chapter Four covers the materials and methods used for the experiments described in subsequent chapters, development of the fin moulding technique, fin actuation method, and force measurement instrumentation are discussed in some detail, together with the decisions made about how to carry out experiments, and the methods of data analysis used.

Chapter Five: NACA vs. Biomimetic Fin Experiments

Chapter Five is the first chapter of experimental data, which describes tests on biomimetic and NACA-derived fins, at a range of frequencies and amplitudes. The results appeared to show a considerable advantage to the biomimetic design, but the data gathered was not enough to attribute it to the fin stiffness profile alone, necessitating a second round of experiments.

Chapter Six: Fin Material Experiments

Chapter Six discusses improvements made to the experimental equipment and methods after the first round of experiments, and describes the next set of experiments to be carried out. These experiments show similar findings to the previous ones, but the extra data gathered was used to confirm that the improvement in thrust-to-power ratio seen in the biomimetic fin

design was attributable to its stiffness profile, and is not being caused by another, unforeseen property of the fin design.

Chapter Seven: Summary of Conclusions and Future Work

Chapter Seven discusses the potential avenues for further study that have resulted from the work presented in this thesis.

References

A comprehensive list of all journals, books, reports and other literature referred to in all sections of this thesis.

Appendices

The Appendices contain supplementary details, included as an aid to understanding of the main body of the thesis.

1.4 Terminology and Conventions

Throughout the thesis, care is taken to explain engineering terms and concepts to readers with a background in biology, who may be less familiar with them than those from a mechanical engineering background. Similarly, ideas from the biological sciences are also introduced with a diverse readership in mind.

This section addresses some of the ambiguities that can arise in discussion of flexible fins, aerodynamics, hydrodynamics, and propulsion, and lays down some conventions that are adhered to throughout the thesis.

1.4.1 Nomenclature

To avoid confusion it is necessary to define the terms commonly used to describe properties of aerofoils, hydrofoils, and experiments involving them. The term 'aerofoil' in this report refers not only to fins designed to operate in air, but also to the geometric shape of a foil, such as in the NACA standard (Jacobs*, et al.*, 1933). 'Foil' is used in this report to describe an aerofoil shape of rectangular planform and constant section, and unless otherwise specified, refers to one that is rigid, not flexible. 'Fin' is used of other types of foil, whether flexible, or more elaborate in shape and design.

Chord and span are the basic size parameters of a foil, as shown in Figure 1. However, since this thesis deal with fins of both engineering and biomimetic origin, in a vertical orientation, the term 'length' is sometimes used in place of 'chord', and 'height' instead of 'span', as would be the case when describing a fish.

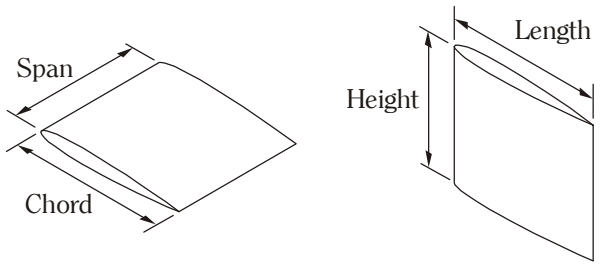

Figure 1: Foil dimensions.

Previously published works dealing with oscillating fins in the fields of aerodynamics and hydrodynamics usually test fins with their span in a horizontal orientation. The experiments in this thesis have been performed on vertically orientated fins, for reasons discussed in Section 4.3.2 (page 72). According to conventions of marine dynamics, the correct terms for the movements of an oscillating foil in this orientation are yaw (rotation) and sway (translation). However for clarity, the terminology used in this thesis is in common with the previous literature. Linear movement perpendicular to the chord and span of the fin is often referred to as 'plunge' or 'heave'; the latter term is used in this thesis. Angular rotation about an axis parallel to the span is referred to as 'pitch'. These motions are shown diagrammatically in Figure 2.

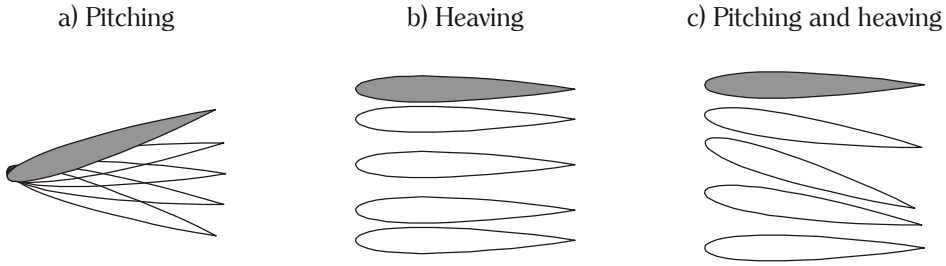

Figure 2: Types of fin oscillation.

1.4.2 Stiffness Terminology

Bending stiffness is defined as *EI*, from engineering beam theory, where *E* is Young's modulus and *I* is the beam's second moment of area (Roark, 1943). Biological studies often refer to *EI* as flexural stiffness, a term used in this thesis when describing biological data.

Another term used frequently in this thesis is 'stiffness profile'. This refers to the way a fin's bending stiffness varies from leading to trailing edge. In a fin made from a homogenous material, stiffness profile and shape are directly related. However, internal stiffening members can be used to modify the stiffness profile independently from its external shape profile.

While the term 'hardness' can have several well-defined meanings within the fields of engineering and biology, in this thesis the terms 'soft' and 'hard' are used to describe the resins

from which flexible fins are made. The terms refer to the stiffness of a material, ultimately defined by its Young's modulus.

1.4.3 Fish Anatomy

Figure 3 shows the terms used to describe anatomical locations in fish:

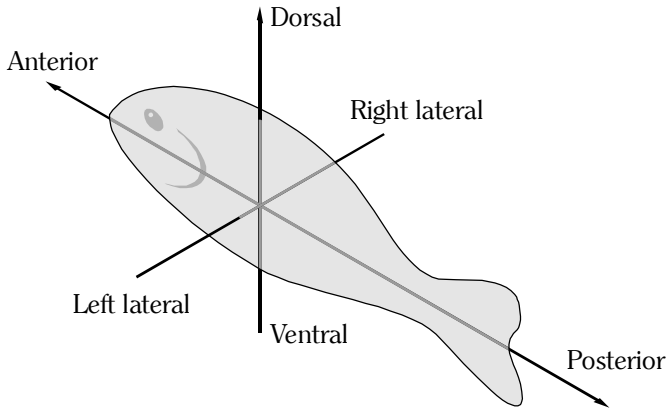

Figure 3: Anatomical terms of location in fish.

1.4.4 Fin Axes and Loads

The convention shown in Figure 4 is used to describe the axes in which fins operate. If the fin is operating in flowing water, the flow is in the positive *x* direction. Heaving motion occurs in the *y* direction, and pitching about the *z* axis.

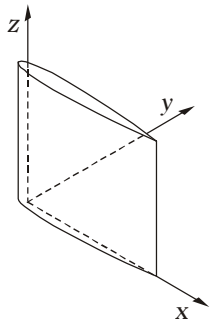

Figure 4: Axes relating to a foil.

Because the fin has a plane of symmetry parallel to the *x*-*y* plane, forces generated by any part of the fin that are not parallel to the plane of symmetry will be counteracted by forces from the opposite side of the plane. Therefore the overall forces generated by the fin can be simplified to a force vector and a torque, acting at a point halfway along the span of the fin, on the *z* axis. In this thesis, the term 'thrust', when used of a fin, refers the component of the overall force vector acting in the negative *x* direction, and can be given an average or instantaneous

value. 'Lateral force' refers to the *y* component, and refers to a mean absolute value, unless declared otherwise in the text. 'Torque' is measured about the *z* axis unless otherwise stated.

Chapter Two

Background and Literature Survey

2.1 Introduction

The motivation for much of the work documented in this thesis began with the creation of a fin-propelled robotic submarine. Details of the submarine's conception, design and testing can be found in Appendix A. Constraints of time and budget meant the original submarine's fins were designed with little reference to existing designs and literature. For this reason, it was decided that an appropriate next step would be to undertake a thorough literature survey, in an effort to identify areas with scope for further research, within the field of flexible fin design. This research would then feed back into the design process to create a more effective fin propulsion system for use in future submarine projects.

The purpose of this chapter is to give an overview of the current state of research in areas related to oscillating fin propulsion. It also introduces many concepts and methods from areas of both biological and engineering sciences, in terms familiar to both disciplines. Attention is paid to methods of describing and evaluating fin performance, in order to lay the foundations to the experiments documented in later chapters.

There is a particular focus on flexible oscillating fins, and the chapter concludes by establishing a hypothesis about the role of stiffness profile in flexible fin propulsion, to be tested experimentally.

2.2 Hydrodynamic Theory

A great deal of work has been carried out on foils and wings operating in both air and water. Theories have been established about many aspects of foil dynamics, and it is important to take these into account when researching more novel areas within the field. The following sections summarise areas of hydrodynamic and aerodynamic theory from previous work, that are relevant to this thesis. Occasionally, more than one definition exists for a particular term. These cases can cause confusion, as the most appropriate definition depends on the context in which the term is being used. The terms are still helpful, provided that conventions are applied correctly and consistently.

2.2.1 Thrust

2.2.1.1 Definition

In most papers pertaining to fin propulsion, thrust refers to the useful forward force generated by a propulsor. It is usually measured as the mean force generated over an entire fin cycle, in the direction of its centre of oscillation. This is distinct from instantaneous thrust, which varies over each fin cycle. In this thesis, where the term 'thrust' is used on its own, it refers to mean thrust per fin cycle, as in the following definition (Hover, *et al.*, 2004):

$$\overline{F}_x = \frac{1}{T}\int_0^T F_x(t)dt \qquad (1)$$

Where F_x is the instantaneous force in the x (forward) direction. The instantaneous thrust is integrated with respect to time (t), and divided by the time taken for a full oscillation cycle (T).

Thrust generated under conditions of zero flow can be termed 'static' thrust. In the field of aerodynamics, static thrust is not regarded as a useful metric of propulsion performance, since aircraft propellers are designed to work in high stream velocities. In hydrodynamic propulsion, however, propulsion units are often required to generate thrust in zero or even negative flow conditions, so static thrust is a helpful term. Static thrust is also known as 'bollard thrust' in marine engineering.

In the case of moving propulsion devices, thrust power is a useful way of measuring a fin's output. It is simply the thrust generated multiplied by its forward velocity (U).

$$P = \overline{F}_x U \qquad (2)$$

2.2.1.2 Lift and drag-based thrust

'Drag-based' and 'lift-based' are terms used to describe the generation of thrust by different means. Drag-based thrust generation results from a body or appendage pushing against a fluid such that the drag acting on it propels the parent body in the intended direction; for example, as an oar propels a rowing boat. It is suited to low-speed manoeuvring, because thrust can only be generated if the speed of the object generating the drag is less than the speed of the fluid flowing past the body. Lift-based propulsion uses the forward component of the lift force that is generated when fin moves through the fluid. It does not suffer the same drawbacks at high speeds as drag-based propulsion.

Studies of the propulsive efficiency (see Section 2.2.3.1) of mammals employing different modes of swimming have found many lift-based swimmers operate in the region of 80%

propulsive efficiency, while drag-based, 'paddlers', much less well adapted to swimming, have efficiencies below 30% (Fish, 1996).

2.2.2 Nondimensional Parameters

Many of the previous studies of fin propulsion use nondimensional parameters to describe the motion of a fin (Triantafyllou, *et al.*, 2004). The following are particularly relevant to the research discussed in this thesis:

2.2.2.1 Reynolds number

The Reynolds number can be used to determine whether different experiments are dynamically similar, and its magnitude is a guide as to whether flow around a body will be laminar or turbulent. It is defined as:

$$\mathrm{Re} = \frac{\rho v_s L}{\mu} = \frac{v_s L}{\nu} \tag{3}$$

Where ρ is the fluid density, v_s is the flow velocity, L is a characteristic length of the body under observation (usually the chord when dealing with aerofoil shapes), and μ is the dynamic fluid viscosity. ρ and μ can be combined into ν, the kinematic fluid viscosity.

2.2.2.2 Aspect ratio

Aspect Ratio (*AR*) is the span of a foil (*s*) divided by its chord (*c*). For non-rectangular shapes, average values are used, or the square of the span is divided by the wing area (*A*), to the same effect.

$$AR = \frac{s}{c} = \frac{s^2}{A} \tag{4}$$

Aspect ratio is useful for making generalised comparisons between fins using a single number, but of course overlooks many of the geometric subtleties of a fin's shape.

2.2.2.3 Thrust coefficient

A thrust coefficient is a dimensionless number describing how effectively thrust is produced by a propulsion device. For a propeller, it can be expressed in a number of ways, the simplest of which is the following (Carlton, 1994):

$$C_{TPS} = \frac{\overline{F_x}}{\rho n^2 D^4} \tag{5}$$

Where C_{TPS} is the propeller's static thrust coefficient, F_x is the thrust generated by the propeller, ρ is the fluid density, n is the number of revolutions the propeller makes per second, and D the propeller diameter. Other definitions equate to the same value with a different multiplication factor.

Other definitions take the flow speed (U) into account, such as:

$$C_{TP} = \frac{\overline{F_x}}{\rho U^2 A} \tag{6}$$

The definition above can be adapted to describe the thrust coefficient of an oscillating fin. The following equation takes the properties of a fin into account to produce a dimensionless number describing the ability of a fin to generate thrust at a given stream velocity (Hover, *et al.*, 2004).

$$C_T = \frac{2\overline{F_x}}{\rho U^2 cs} \tag{7}$$

Where C_T is the thrust coefficient, F_x is the forward thrust of the fin, the average of which is taken over an integer number of cycles, U is the forward velocity of the fin, and c and s the chord and span respectively. The equation applies to fins of rectangular profile, but different characteristic dimensions could be chosen to apply it to other shapes.

2.2.2.4 Internal Froude number

The Froude number (Fr), in its simplest form, is the ratio of a characteristic velocity (V) of an object to the wave propagation velocity (c_{wave}) in the liquid it inhabits:

$$Fr = \frac{V}{c_{wave}} \tag{8}$$

The propagation velocity of a wave of length L is can be calculated as:

$$c_{wave} = \sqrt{gL} \tag{9}$$

The time period (T) for a pendulum swinging at its natural frequency under gravity (g) is defined as:

$$T = 2\pi\sqrt{L/g} \tag{10}$$

Equations (8) - (10) can be combined to cancel the gravity term. The resulting non-dimensional number is known as the internal Froude number.

$$Fr = \frac{V}{\sqrt{gL}} = \left(\sqrt{\frac{L}{g}}\right)\frac{V}{L} = \frac{T}{2\pi} \times \frac{V}{L} = \frac{1}{2\pi}\frac{T}{L/V} \tag{11}$$

Comparison of the internal Froude numbers of many animals and man-made craft reveals a tendency towards Fr = 1 in both nature and engineering. A review of biorobotic undersea vehicles (Bandyopadhyay, 2005), observes that most animals swim within the range of one body length per oscillation cycle. However the wide spread of data around Fr = 1 condition in the same paper suggests that the correlation is only an approximate one.

2.2.2.5 Strouhal number

The Strouhal number, or non-dimensional frequency, is another very important parameter describing the motion of a foil, and is defined:

$$St = \frac{Af}{U} \tag{12}$$

Where A is the width of the foil's wake, f is the oscillation frequency, and U is the average forward velocity. In practice, the Figure 5 shows the difference between low and high Strouhal number wake patterns.

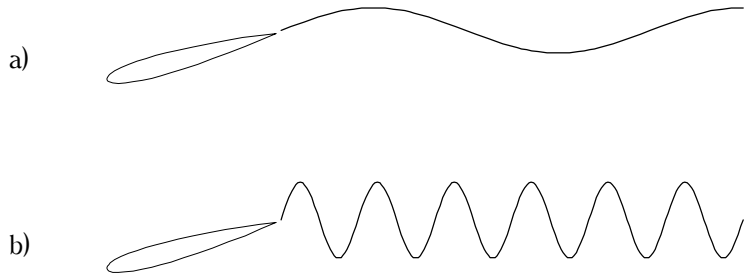

Figure 5: a) Low and b) high Strouhal number wakes.

For simplicity, the wake width is often approximated as double the heave amplitude of a pitching and heaving foil, illustrated in Figure 6.

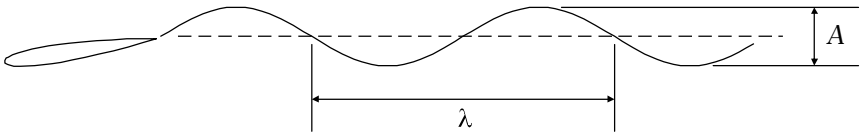

Figure 6: Strouhal number is equal to the ratio of these two dimensions.

The Strouhal number can be perhaps more usefully described as the ratio of the wake width (A) to the oscillation wavelength (λ).

$$St = \frac{A}{\lambda} \tag{13}$$

A fin oscillating in a stationary fluid can be described as having an infinite Strouhal number.

2.2.2.6 Heave to chord ratio

Another important characteristic of oscillating foils (Anderson, *et al.*, 1998) is the ratio of the amplitude of the heaving motion (h) to the chord length (c) of the foil, defined here as R_{hc}.

$$R_{hc} = \frac{h}{c} \tag{14}$$

2.2.2.7 Reduced frequency

The reduced frequency of an oscillating foil is another important variable governing fin performance (Koochesfahani, 1989) It could also be called the 'wavenumber' of an oscillating fin system, since it describes the number of fin oscillations in a given length. It is calculated as follows:

$$k = \frac{\omega c}{2U} = \frac{2\pi f c}{2U} = \frac{\pi f c}{U} \tag{15}$$

Where f is the frequency of oscillation in Hz, ω the angular frequency, c is the chord length, and U is the average forward velocity. It can be helpful to consider reduced frequency in terms of the chord length (c) and oscillation wavelength (λ):

$$k = \frac{\pi c}{\lambda} \tag{16}$$

It is proportional to the ratio of chord length to wavelength, or alternatively to the number of oscillations that occur while the fin travels a chord length (Figure 7).

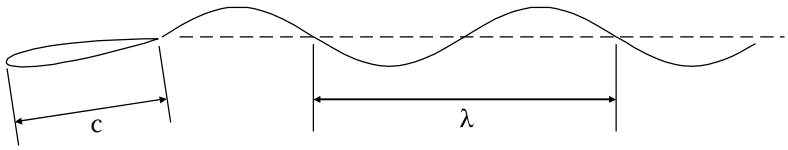

Figure 7: Two dimensions that that define reduced frequency.

2.2.2.8 Maximum unsteady angle of attack

The unsteady angle of attack (often referred to simply as the angle of attack or instantaneous angle of attack) is the angle between a foil's instantaneous direction of travel and its chord. It

takes into account both pitching and the heaving motion of a foil as it moves through the water, as in Figure 8.

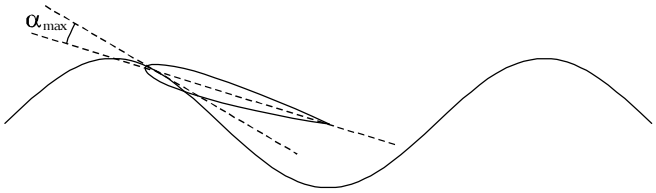

Figure 8: Maximum unsteady angle of attack.

The maximum angle attack of a flapping foil can greatly exceed that of a fixed foil in a steady flow. Fixed wings usually begin to stall at attack angles of around 15°, but oscillating foils can achieve much higher angles (Triantafyllou and Triantafyllou, 1995).

At low Strouhal numbers, the unsteady angle of attack is approximately equal to the pitching angle. The difference between the two becomes more pronounced as Strouhal number increases, because the effect of the heaving motion as the foil moves through the fluid becomes more significant.

2.2.3 Measuring Efficiency

There are several ways of quantifying the efficiency of fins and propellers. Efficiency terms often have more than one definition, depending on the context of their use, and the type of propulsion device to which they are being applied. The following terms have all been used in previous literature in the forms shown below, and are used where relevant in this thesis.

2.2.3.1 Propulsive efficiency

The propulsive efficiency of a fin or propeller (η) can be described as the ratio between input power (P_I) and useful thrust power, which is equal to the product of the mean thrust (F_x) and free stream velocity (U), as follows:

$$\eta = \frac{\overline{F_x} U}{P_I} \tag{17}$$

2.2.3.2 Bollard efficiency

'Bollard pull' is a naval term describing the maximum static thrust that can be generated by a ship at full power. It is measured by securing the ship to an immovable object (such as a bollard). This empirical method of determining a ship's power has descended into hydrodynamic theory in the form of 'bollard efficiency' - a term that describes the ability of a propulsion device to produce thrust at zero velocity.

Actuator disk theory reduces the complex fluid-structure interactions of a rotating propeller to a simplified model, in which a two-dimensional disk induces a given velocity to the fluid passing through it. Calculations can then be carried out concerning the conservation of mass flow, momentum, and energy, through the system, and equations derived to represent the theoretical ideal performance of a propeller (Horlock, 1978). One such equation represents the ideal static thrust (T_I) that can be achieved by a propeller of a given area:

$$T_I = \sqrt[3]{2\rho A P_{in}^{\ 2}} \tag{18}$$

Where ρ is the fluid density, A is the propeller's cross-sectional area, and P_{in} is the power consumed.

'Bollard efficiency' is another term of naval origin, used of propellers generating static thrust. It is not strictly a measure of efficiency, since efficiency is only a meaningful term where work is being done, and the generation of thrust without movement implies no useful work. It is, however, a practical measure of the *efficacy* of the propeller. It is defined as the ratio of thrust generated by the propeller, to the ideal thrust generated by a theoretical actuator disk of the same area, with the same power:

$$\eta_B = \frac{F_x}{T_I} = \frac{F_x}{\sqrt[3]{2\rho A P_{in}^{\ 2}}} \tag{19}$$

Where η_B is the bollard efficiency, F_x is the forward thrust, and T_I the ideal static thrust, as above. In this thesis, unless otherwise stated, values for power describe mechanical power supplied, excluding motor and drivetrain losses.

An equivalent method for calculating static efficiency of fins has been proposed, which assumes A to be the area swept by the trailing edge of the fin in the y-z plane (Kemp and Hobson, 2001). In situations where A cannot easily be measured, it can be approximated by the area that would be swept by the fin if it were rigid:

$$A = 2H(1 - x_p)C\sin\alpha \tag{20}$$

Where H is the height of the fin, C is its chord length, x_p is the location of the fin's pivot point as a fraction of its chord (0.1 in all the fins tested in this thesis), and α is the centre-to-peak amplitude of oscillation.

2.2.3.3 Thrust-to-power ratio

The ratio of thrust output to power supplied cannot be described as a measure of efficiency, for the same reasons as those stated above. It is, however, a useful term for evaluating static

thrust performance (Kemp, *et al.*, 2003). It is defined as the ratio of mean static thrust generated by a fin, to the power supplied to it, and is measured in NW^{-1}.

$$R_{TP} = \frac{\overline{F_x}}{P} \tag{21}$$

2.2.4 The Reverse Kármán Street

Under certain flow conditions of flow speed and viscosity, a bluff body placed in a moving flow of fluid will leave a pattern in its wake known as a Kármán vortex street (Kármán and Burgess, 1935). The incongruity between the stationary fluid behind the bluff body and that flowing past it causes eddies to form between the two. As the eddies are carried further from the body, they increase in size, but diminish in vorticity, until the kinetic energy they contain is dissipated by the viscosity of the fluid (Figure 9).

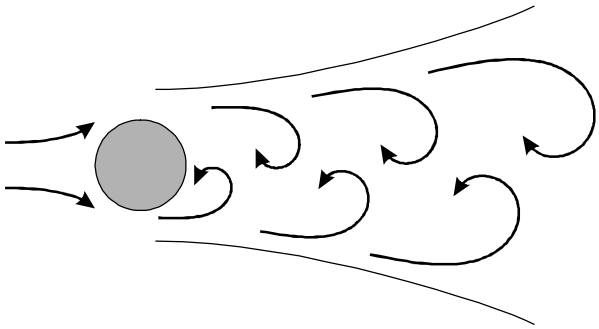

Figure 9: Kármán vortex street.

Fins produce thrust by inducing a jet flow in the opposite direction to the resultant thrust. This jet takes the form of a reverse Kármán street: a moving column of water flowing away from the fin, with a staggered row of vortices down either side (Figure 10).

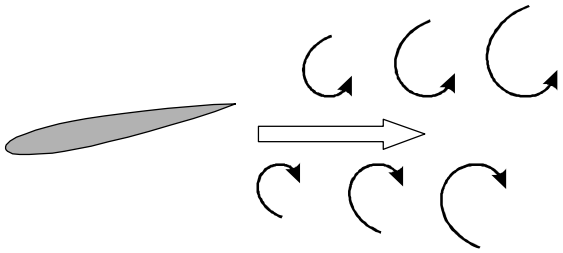

Figure 10: Reverse Kármán vortex street.

Fishes demonstrate more complex control over the shedding of vortices than the examples above describe. A study of mullet (*Chelon labrosus*) looked at the flow patterns past the fish, and at the relative contributions of the body and the tail to thrust production (Ahlborn, *et al.*, 1991). It revealed that vortices were being created by the frontal region of the body, and when they reached the tail, the tail's movement passed through each vortex, reducing its size and

extracting some of the energy embodied within it. This behaviour both reduced the wake of the fish, and increased its efficiency, since less energy was left behind in the vortices.

2.2.5 Types of Instability

The flow of water past an oscillating fin can be classified as unstable steady flow. Disturbances in such a flow can be divided into two distinct categories:

Absolute instability: Where a perturbation develops close to a body that causes it, and stays close to the body, not being carried away in the wake.

Convective instability: Where the body causes a perturbation that is then carried downstream in the wake, away from the body.

The vortices that compose a reverse Kármán street, and therefore govern the effectiveness of a fin in propulsion, are convective, because they leave the trailing edge of the fin, and disperse into its wake.

2.2.6 Optimal Strouhal Number

Experiments carried out at the Massachusetts Institute of Technology (Triantafyllou, *et al.*, 1993, Triantafyllou, *et al.*, 1991), led to the discovery that the Strouhal number is of particular relevance to the efficiency of a fin being used for oscillatory propulsion. Theories governing convective instabilities were used to show that peak efficiency of a fin occurs in a narrow band of conditions of 'maximum amplification', where a reverse Kármán street can form. They were found to suggest that fins operate at peak efficiency at a Strouhal number of 0.25 to 0.35. Experiments were devised to test this theory, using a pitching and heaving foil, and the results of a number of previous studies of swimming animals are re-assessed. The fin experiments fell within the range predicted by the theory, with efficiency reaching a peak at St = 0.25. The animals studied ranged in size from goldfish to dolphins, but despite the wide range of Reynolds numbers at which they operate (from 10^4 to 10^6), most yielded Strouhal numbers within the 0.25 to 0.35 range, as predicted.

Studies of birds in flight find a similar convergence of Strouhal numbers, indicating their adaptation for high aerodynamic efficiency (Nudds, *et al.*, 2004).

2.3 Fish Locomotion Theory

2.3.1 Swimming Modes

Methods of fish propulsion vary widely between species, and also sometimes between different gaits of a single species. The most common modes of locomotion can be categorised accord-

ing to how much of the body moves during swimming (Figure 11). They progress from anguilliform, where undulation of the entire body provides thrust, through carangiform, where only the rear portion of the fish undulates, to thunniform, where thrust comes from the caudal fin (tail) being oscillated to provide lift-based propulsion (Breder, 1926, Lindsey, 1978, Sfakiotakis, *et al.*, 1999).

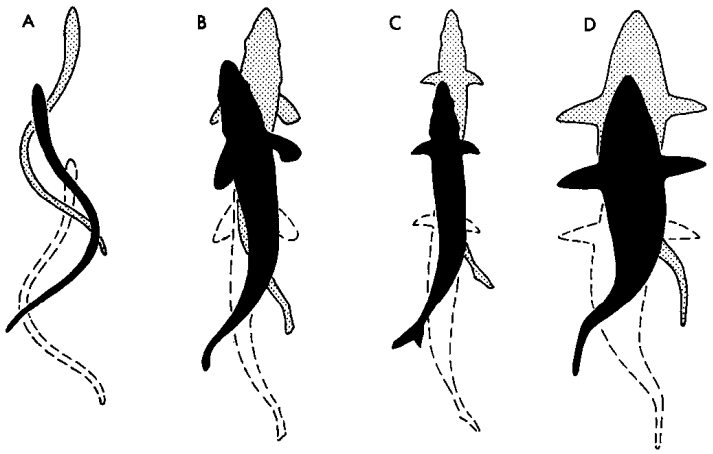

Figure 11: Anguilliform, Subcarangiform, Carangiform, and Thunniform modes (Lindsey, 1978).

The modes are described more fully below:

Anguilliform: An undulatory form of movement, whereby a wave travels down the length of the fish body, including the head, so that the entire body is used as a propulsion surface. Eels are examples of fish that employ an anguilliform swimming method.

Subcarangiform: Similar to anguilliform motion, but with less movement of the head. Many freshwater fish such as trout and salmon use this method of swimming, which is usually associated with manoeuvrability. The flexibility of the body allows for sharp cornering and acceleration, making them well adapted to swimming in turbulent, flowing water.

Carangiform: Involves only the rear portion of the body, with the head remaining almost stationary while a short wave propagates down the rear of the fish to the tail. The reduced flexibility compromises acceleration and manoeuvrability, but increases efficiency with respect to subcarangiform swimmers. Herring swim primarily in the carangiform mode.

Thunniform: Almost all thrust is produced by oscillation of the tail, with little lateral movement in the rest of the body. The tuna is an example of a fish that employs thunniform motion. It is particularly well adapted to efficient, long distance cruising, but is less adept than other species at rapid changes of speed and direction (Webb, 1984).

Other modes of propulsion involve the fins of a fish being used independently from the body, as appendages, while the body provides little thrust of its own. Amiiform, gymnotiform and rajiform modes employ the dorsal, anal, and pectoral fins respectively. The fins, which are

elongated and enlarged compared to fish of other swimming modes, are oscillated with an undulating waveform to generate thrust. In ostraciiform motion, the caudal fin is flapped independently from the body. It is one of the more inefficient and less common swimming, modes, found in fish with unusually rigid bodies, such as the boxfish. Figure 12 shows the full range of swimming modes. Fish are arranged along the horizontal axis from those employing undulatory motion, where more than one wavelength is present, to oscillation, where a rigid, flapping, fan-like motion is used. They are categorised in the vertical axis by the location from which the thrust is produced (Lindsey, 1978).

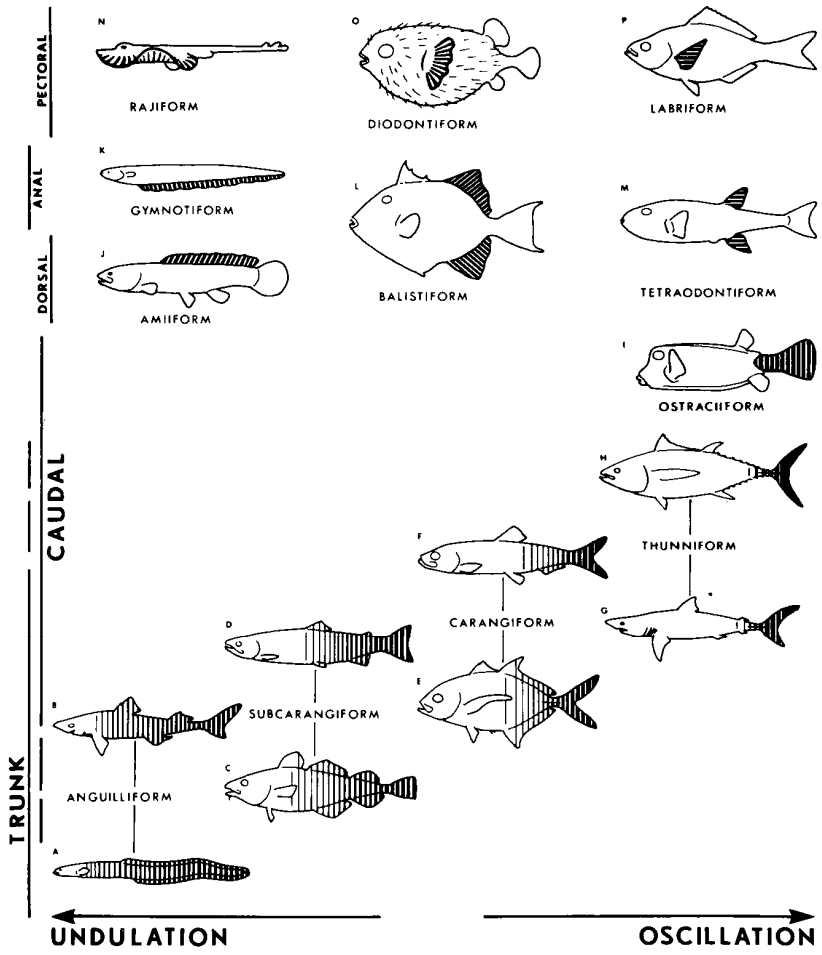

Figure 12: Modes of forward swimming in fish (Lindsey, 1978).

2.3.2 Wake Analysis

Many studies have been carried out with the aim of understanding the hydrodynamic mechanisms by which fish propel themselves. In recent years, the rapid development and increasing availability of Particle Image Velocimetry (PIV) techniques has enabled researchers to investigate the wake patterns fish leave behind in more detail than ever before. One of the basic structures that has been observed is that of opposing toroidal vortex loops.

2.3.2.1 Toroidal vortices

Bluegill sunfish (*Lepomis macrochirus*) use a combination of subcarangiform and labriform swimming, similar to many other species of their approximate shape. They have two distinct swimming gaits; they use their pectoral fins for low-speed locomotion, and at higher speeds they make a transition to their more powerful caudal fin. A study of the sunfish, (Lauder and Drucker, 2002) revealed toroidal vortices were shed from both the caudal fin and pectoral fins (Figure 13). A horizontal plane through the centre of this wake formation resembles a clean reverse Kármán street.

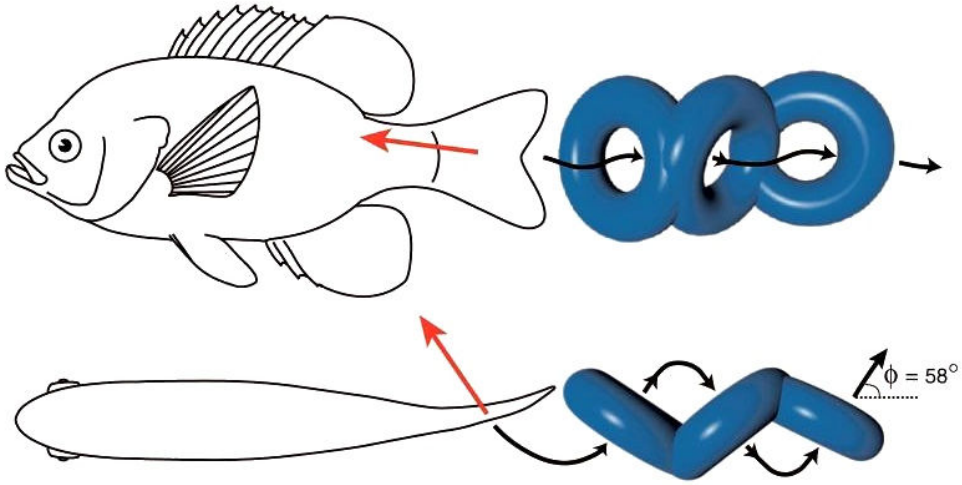

Figure 13: Vortex wake of a sunfish (Lauder and Drucker, 2002).

A later, more detailed study gave further insights into pectoral fin motion, and indicated how finely tuned the fins and their patterns of movement are. Their structure and actuation allows them to produce continuous thrust over an entire cycle; that is, the instantaneous thrust fluctuates, but never dips below zero (Lauder and Madden, 2007). This is possible through intricate control, allowing this fin's area, stiffness and position to be varied such that in an instroke, outstroke, or transition period, part of the fin is always producing thrust from at least part of its surface.

2.3.2.2 Vortex variants

A similar study on dogfish shark (*Squalus acanthias*) (Wilga and Lauder, 2004), revealed more complex vortex chains in their wake. Most sharks display an asymmetrical caudal fin, with an upper lobe larger than the lower one (see Figure 14, top). PIV analysis of the wake behind a freely swimming dogfish revealed a ring-within-a-ring formation. The two rings produced jets in approximately the same direction (labelled A and B below) which combined downstream to form a single jet at an average angle of -35° to the free stream direction.

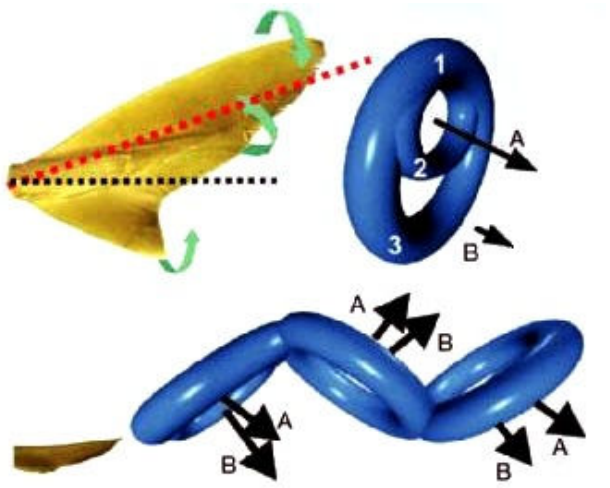

Figure 14: Side (top) and dorsal (bottom) views of a dogfish vortex chain (Wilga and Lauder, 2004).

2.4 Biological Studies

2.4.1 Insect Wing Stiffness

Several studies have concentrated on the role of stiffness in insect wings. Insects allow their wings to deform considerably during flight, to produce lift and thrust. The movements of the wings are caused by aerodynamic forces, but controlled by the intricate structure of veins that support the wing membrane. A study of sixteen different flying insects produced data on the chordwise and spanwise flexural stiffness of the wings, at regular intervals (Combes and Daniel, 2003a). Although the data was gathered from a diverse range of flying insects, spanning six biological orders and encompassing dragonflies, flies and moths, the data was surprisingly consistent. The measurements showed that "spanwise flexural stiffness scales strongly with the cube of wing span, whereas chordwise flexural stiffness scales with the square of chord length." (Combes and Daniel, 2003a). Furthermore, spanwise flexural stiffness of the insect wings was found to be 1-2 orders of magnitude greater than chordwise stiffness, mostly due to the leading edge vein. Although the study concentrates on insect flight rather than hydrodynamic propulsion, it is of interest because of its focus on the role of local stiffness variation in determining aerodynamic performance. Further work by the same researchers used more complex measurement methods, and finite element models to analyse the responses of the wings to aerodynamic loading (Combes and Daniel, 2003b). They concluded that the local flexibility of the wing structures had an important role in controlling aerodynamic force production. Specifically, the structure helped to confine most of the bending movement to the tip and trailing edge of the wings, the geometry of which is of particular importance in the generation of thrust and lift.

2.4.2 Relevant Fish Physiology

The studies referenced below show how some fish vary the stiffness of both their bodies and appendages to achieve efficient propulsion.

2.4.2.1 Fin structure

The internal structure of fish fins is difficult to mimic, being complex and heterogeneous. An important study on the mechanical properties of bluegill sunfish fins proposed a theoretical model of their structure (Alben, *et al.*, 2007). The model was suggested to hold true for other ray-finned fishes, and was tested and verified against stiffness data from a real fin. The fins of ray-finned fishes consist of a membrane supported across multiple rays. Each ray is split along its axis, in the same plane as the membrane. The two halves of the ray are known as 'hemitrichs'; they can move in relation to each other, but their movement limited by the flexible layer of collagen linking them together. A cross-section of a fin is shown in Figure 15, in which the components are labelled.

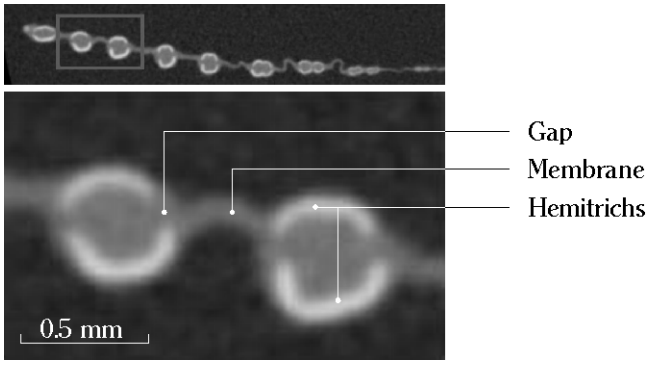

Figure 15: Fin ray cross-section (Alben, et al., 2007).

At the base of the fin, the opposing hemitrichs are attached to muscles via tendons, while the centre of the fin is supported by a structure of cartilage and ligament (Figure 16). By actuating the muscles controlling the two surfaces of the fin, the fish can achieve a variety of movements to achieve propulsion and manoeuvring, and can adjust the stiffness of the fin rays by more than an order of magnitude.

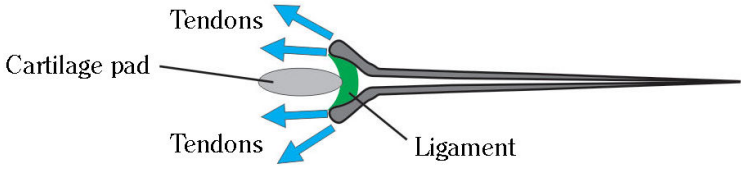

Figure 16: Fin ray actuation (Alben, et al., 2007).

The theoretical model simplified the hemitrichs as being two parallel rows of jointed elements, each pair linked by a third element, simulating the layer of collagen between the two hemitrichs. Analysis of both the real and simulated fin rays showed that actuation by pulling on the tendons of one hemitrich in relation to the cartilage pad caused curvature of the ray, particularly at the base.

Pectoral fins, with an internal structure similar to that described above, have been the subject of computational studies, in which simulations show that their anisotropic distribution of stiffness is critical to their ability to generate thrust (Zhu and Shoele, 2008).

2.4.2.2 Body stiffness

Studies by Long *et al.* showed that fish use their muscles not only to generate movement, and consequently thrust, but also to vary the stiffness of their bodies, allowing them to undulate efficiently at a range of frequencies, and by doing so, to aid efficient propulsion (Long, *et al.*, 1994, Long and Nipper, 1996). The results were gained by taking measurements of the body stiffness of a dead fish while electrically stimulating its muscles.

2.5 Materials Science

The fins tested in this thesis were made from flexible materials. The following section covers the basic terms that can be used in describing their properties, and briefly introduces some materials science theory useful in understanding their behaviour.

2.5.1 Stress and Strain

2.5.1.1 Engineering strain

Engineering strain is the change in length of a sample, divided by its original length:

$$\varepsilon = \frac{\Delta l}{l_0} \tag{22}$$

Where ε is the strain, Δl is the change in length, and l_0 is the original length of the sample. It can also be written:

$$\varepsilon = \frac{l_i - l_0}{l_0} \tag{23}$$

Where l_i is the instantaneous sample length.

2.5.1.2 Engineering stress

Engineering stress is defined as:

$$\sigma = \frac{F}{A_o} \tag{24}$$

Where σ is stress, F is the force applied, and A_o is the initial cross-sectional area of the sample.

2.5.1.3 Young's modulus

Young's modulus (E) is the ratio of the stress and strain, given by the following formula:

$$E = \frac{\sigma}{\varepsilon} \tag{25}$$

2.5.1.4 Poisson's ratio

Poisson's ratio describes the tendency of a material to change in cross-sectional area under strain, and is defined as the ratio between transverse and axial strain, as shown in the following equation:

$$v = \frac{\varepsilon_T}{\varepsilon_A} \tag{26}$$

Where v is Poisson's ratio, ε_T is the transverse strain, and ε_A is the axial strain.

2.5.2 True Stress and True Strain

Engineering stress and strain are measures of force and extension, with respect to a sample's original dimensions. However, these dimensions change from their original values as more strain is applied. This change is insignificant at low values of strain, so the simplified formula for engineering stress and strain can be used without problems, but for more accurate calculations involving large deformations, alternative methods are necessary, which take into account the instantaneous dimensions of the sample, rather than the initial size only.

2.5.2.1 True stress

True stress (σ_T) is defined as:

$$\sigma_T = \frac{F}{A_i} \tag{27}$$

Where F is the force applied, and A_i is the instantaneous cross-sectional area of the sample. A_i can be determined in a number of ways. If constant volume can be assumed, cross-sectional area will change in the inverse proportion to the sample length, so the following is true:

$$A_i = A_0 \frac{l_0}{l_i} \tag{28}$$

Where and A_o is the initial cross-sectional area, l_i is the instantaneous length of the sample (an easier measurement to take), and l_0 is its original length. (Askeland and Phulé, 1989)

2.5.2.2 True strain

True strain (ε_{TRUE}) is an alternative measure of strain, defined as:

$$\varepsilon_{TRUE} = \ln\left(\frac{l_i}{l_0}\right) \tag{29}$$

Where l_i is the instantaneous length of the sample under test, and l_o is its original length. In terms of engineering strain (ε), it can also be expressed as:

$$\varepsilon_{TRUE} = \ln(1+\varepsilon) \tag{30}$$

Another advantage of using true strain is that strain measurements of consecutive deformations can be added together, without loss of accuracy, to give a figure for total strain. The same is not true of engineering strain, since the two deformations will have different initial lengths.

In this thesis, the words 'stress' and 'strain' on their own refer to engineering stress and strain. True stress and strain are always referred to by their full names.

2.6 Relevant Work on Rigid Pitching and Heaving Foils

The investigations referenced in this section were carried out with rigid foils, mostly of the NACA 0012 profile, shown in Figure 17. The National Advisory Committee for Aeronautics (NACA) of the USA devised the four digit airfoil series to simplify and standardise airfoil design (Jacobs, *et al.*, 1933). The first two digits relate to the camber of the foil (00 denotes a symmetrical foil), and the last two are a two-digit number representing the foil's thickness as a percentage of its chord length.

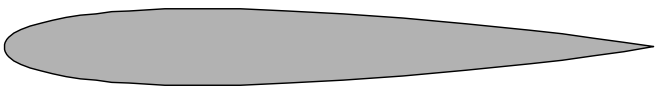

Figure 17: NACA 0012 aerofoil profile.

2.6.1 Pitching Only

Experiments have been carried out on rigid fins with variable frequency and amplitude, using different waveforms, sinusoidal and non-sinusoidal (Koochesfahani, 1989). One of the chief findings of this work is that there is an axial flow of fluid through the cores of the vortices produced by pitching fins, with a flow magnitude roughly proportional to the oscillation frequency and amplitude. Developments in flow visualisation technologies mean more recent studies are able to examine the wake patterns produced by fins in some detail, as well as forces. In a study of a flat, rigid foil of low (0.54) aspect ratio (Buchholz and Smits, 2005), a wake pattern was produced which, in the horizontal plane resembled a reverse Kármán vortex street. Viewed in three dimensions, the vortices curled into a horseshoe shape, joining the fin at its trailing edge, and alternating in rotational polarity with each half cycle of the fin. A diagram of the wake structure is shown in Figure 18. The arrow indicates the direction of water flowing past the fin.

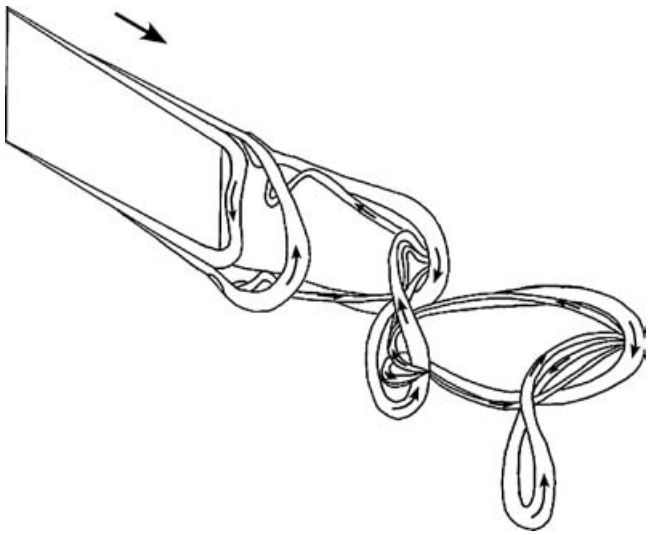

Figure 18: 3-dimensional wake structure behind a rigid pitching foil (Buchholz and Smits, 2005).

The structure in Buchholz's work appeared over a range Reynolds numbers, aspect ratios, and oscillation amplitudes. Numerical studies have also been carried out and are consistent with his findings (Dong, *et al.*, 2005, Guglielmini, 2004). It also bears some resemblance to the wake structures observed behind swimming fish in PIV-based studies (Lauder and Drucker, 2002, Wilga and Lauder, 2004), although the rotating vortices in these studies are toroidal rather than horseshoe-shaped. The recurrence of similar findings in many works and different types of study show that counter-rotating vortices such as those shown above are fundamental structures in oscillatory propulsion.

2.6.2 Heaving Only

Water tunnel experiments with a rigid heaving NACA 0012 foil have shown the foil begins to produce a visible jet of fluid in its wake, moving faster than the free stream velocity, at a Strouhal number of approximately 0.08 (Lai and Platzer, 1999). At $St \approx 0.13$ and above, a thrust-producing jet flow with accompanying vortices becomes apparent in the wake. (An explanation of how these figures were derived can be found in Appendix A) The jet velocity in Lai and Platzer's experiments was found to be to be proportional to the Strouhal number.

An elegant demonstration by Vandenberghe *et al.* showed how simple heaving motion of a wing can generate thrust, perpendicular to the driving oscillation (Vandenberghe, *et al.*, 2004). A flat horizontal wing was suspended in a circular tank, free to rotate, and oscillated with a heaving motion (Figure 19). At certain Reynolds numbers, ($20 < Re < 55$), a sharp bifurcation was observed between the wing heaving in a steady state with no rotational movement, and the onset of asymmetric vortices from the upper and lower faces of the wing, with the consequent generation of thrust, and rotation of the wing.

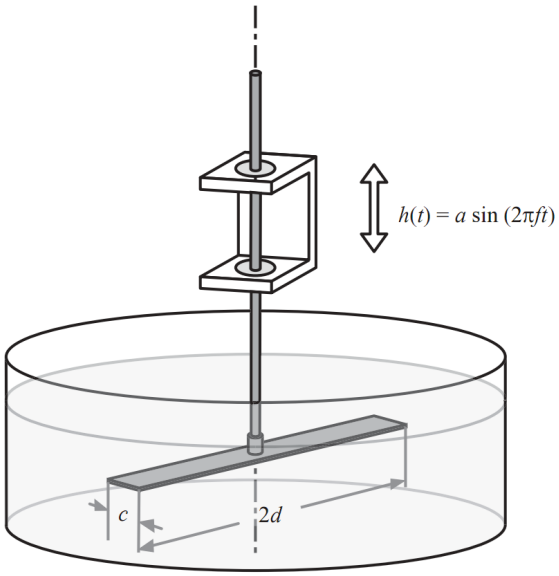

Figure 19: Apparatus for Vandenberghe's heaving wing experiment (Vandenberghe, et al., 2004).

Further analysis of the phenomenon was offered in later numerical studies (Alben and Shelley, 2005). The effect demonstrates how even simple oscillation of a rigid body can produce locomotion when combined with the complex dynamic response of its fluid environment.

2.6.3 Simultaneous Pitching and Heaving

2.6.3.1 Phase offset

The phase offset between pitching and heaving oscillation has been found to be a critical factor in the interaction between leading edge and trailing edge vortices (Anderson, *et al.*, 1998). When the angle of attack is great enough, flow separates from the leading edge of a foil and forms a leading edge vortex. This moves down the fin and interacts with the vortex that forms on the trailing edge. If the two vortices combine constructively, an increase in performance can result. Soap-film experiments on oscillating foils have shown that the interactions between leading and trailing edge vortices are somewhat chaotic; a small change in fin oscillation parameters can cause a large change in the combined wake formation (Lentink, *et al.*, 2008, Schnipper, *et al.*, 2009).

A phase angle of 90° between pitch and heave has been found to produce the best thrust performance in pitching and heaving foil experiments (Read, *et al.*, 2003). The 90° phase angle allowed efficient, high-thrust fin performance over a wider range of Strouhal numbers than other phase offsets.

2.6.3.2 Angle of attack profile

It has been established that changing from a sinusoidal heave waveform to a more complicated oscillation mode can increase the thrust coefficient of a fin (Read, *et al.*, 2003). If the fin is pitching and heaving with a sinusoidal motion, the combination of pitch and heave means the attack profile is not sinusoidal, especially at high Strouhal numbers. If higher harmonics are introduced into the heave motion to turn the foil's angle of attack profile back into a sine wave, the thrust coefficient increases.

More thorough tests have been performed on foils to determine the effect of angle of attack profiles on performance of a pitching and heaving foil (Hover, *et al.*, 2004). Experiments were carried out with the pitching angle and heave position in simple harmonic motion, out of phase by 90°, and also with complex waveforms calculated to provide predefined angle of attack profiles when combined with the heaving motion. Various profiles were tried, including square, saw-tooth, and cosine functions. The cosine profile yielded the best performance when thrust and efficiency were taken into account, although the sawtooth profile provided the highest thrust. The cosine function was found to produce a clean reverse Kármán street in the foil's wake, consisting of two large opposing vortices per cycle, which has been shown to be a highly efficient wake pattern for the production of thrust (Anderson, *et al.*, 1998). Introducing other harmonics into the profile added extra, smaller vortices into the wake pattern, decreasing efficiency.

2.6.3.3 Active vorticity control

Another pitching and heaving foil study examined the effect of a fin oscillating in a Kármán street wake (Gopalkrishnan, *et al.*, 1994). A D-section prism was placed in flowing water, upstream of the test area, to introduce a convective instability into the flow. The Kármán street shed from the prism consisted of alternate counter-rotating vortices, much like those shown in Figure 9. The pitching and heaving foil was set up to oscillate with the same frequency as the oncoming vortices of the prism wake. It was found to interact with the wake in a variety of modes; it served either to amplify, diminish, or add an extra set of vortices to those already present in the stream. When the foil interfered destructively with the existing vortices, it was found to be generating thrust with enhanced efficiency. It is by this method that some fishes are able to extract energy from their own leading-edge vortices (Ahlborn, *et al.*, 1991) as discussed previously in Section 2.2.4 (page 27). Fish are also able to gain hydrodynamically from swimming in schools (Breder, 1965, Liao, *et al.*, 2003, Weihs, 1973).

2.6.3.4 Numerical studies

Numerical studies allow many tests to be performed, and parameters optimised, entirely in software, and without the need for physical models. One such study was carried out to examine the behaviour of pitching and heaving rigid NACA 0012 foils, with the specific aim of applying the results to micro-air vehicle (MAV) flight (Tuncer and Kaya, 2005). A two-dimensional model was created, and the parameters of pitch and heave amplitude and the phase angle between pitch and heave were optimised using the steepest descent method. It was found that high thrust production and high efficiency were mutually exclusive optimisation goals; one can be obtained only at the expense of the other.

2.7 Relevant Work on Flexible Fin Propulsion

2.7.1 Pitching Flexible Fins

2.7.1.1 Homogenous flexible fins

Nekton Research[1] carried out many experiments in the field of flexible fin propulsion. Many of their findings are applied commercially, and so remain unreleased. However, some of their published work reveals interesting findings.

[1] Nekton Research was a private research company founded by Charles Pell, formerly of Duke University, MA.. Nekton was acquired by iRobot Corporation in 2008. (www.irobot.com)

Earlier studies had established the importance of flexibility in pitching fin propulsion, using fins in short bursts of oscillation to emulate fast-start swimming (Ahlborn, *et al.*, 1997). Nekton's experiments used flexible NACA 0014 fins oscillating sinusoidally and continuously about a single axis, and achieved static thrust-to-power ratios that compared favourably with conventional propeller-driven thrusters (Kemp, *et al.*, 2003). Kemp proposed that the efficiency of flexible fin thrusters is due to their ability to store energy, and release it to the water out of phase with the driving torque. Results have shown that when flexible fins are operating at peak efficiency, the torque required to oscillate them is out of phase with their angular velocity, as shown in Figure 20.

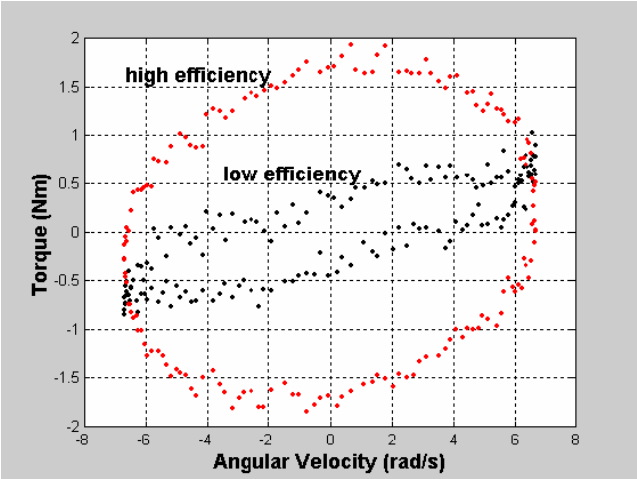

Figure 20: Torque-velocity plot (Kemp, et al., 2003).

However, the effect could be caused by the fin imparting momentum to the water around it, then being 'pushed' by the moving water as it decelerates, or simply by the inertia of the fin necessitating a negative torque to decelerate it and change its direction. Furthermore, the difference in between the high and low efficiency profiles in the plot above seems chiefly to be of torque amplitude rather than phase angle. There is room for further experimentation in this area, to find out what role the flexibility of the fins plays in their efficiency.

Figure 21 shows the range of fins used in Nekton's trials. Most use a standard NACA 0012 profile.

Figure 21: Foils used by Nekton Research.

Another of Nekton's findings was that fin flexibility had little effect on efficiency. More rigid fins produced more thrust but required more torque to drive them (Hobson, *et al.*, 2003). Aspect ratio was found to have more influence on efficiency, with an optimum ratio of 1:1. Little data on these findings is available, and more precise information on the roles of fin flexibility and aspect ratio would be valuable.

A numerical study looked at thin fins of uniform flexibility, in pitching oscillation about their leading edges (Alben, 2008). These were intended as simplified models of the flapping appendages of flying and swimming animals, such as caudal fins of fish. One of the chief findings of the study was that the thrust power developed by such a fin went through a number of resonant peaks, depending on the driving frequency. The highest thrust power attained was at the resonant peak with the lowest frequency; an oscillation mode in which the fin described a quarter wave shape at the extreme of its deformation.

Rigid fins produced the greatest thrust at low frequencies, but were considerably less efficient than the flexible fins. A degree of flexibility was shown to be beneficial to thrust production at higher frequencies, as well as increasing efficiency.

2.7.1.2 Active stiffness control

The optimal stiffness of a fin for maximum efficiency or thrust generation changes depending on the frequency and amplitude of oscillation, and other parameters. A research team tested a novel method for adapting the stiffness of a pitching fin while in operation (Kobayashi, *et al.*, 2006). The fin comprised two rigid sections, connected by a variable length leaf spring, as shown in Figure 22.

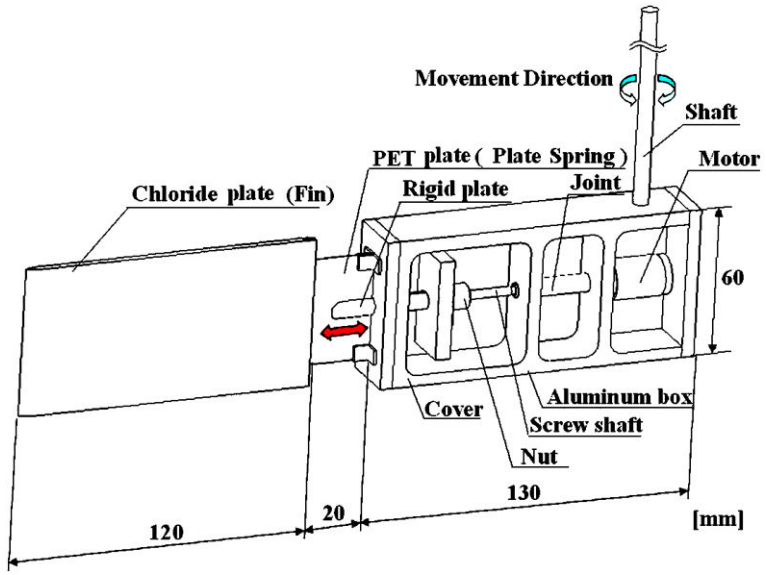

Figure 22: Mechanical design of a variable stiffness fin (Kobayashi, et al., 2006)

The effective spring length, and therefore its stiffness, was adjusted through a range of values, while the fin was oscillated with different parameters. The results revealed optimal stiffness values for each combination of frequencies and amplitudes. The study was a preliminary one, leaving many questions open for further research. Later studies with the same apparatus investigated the effectiveness of dynamically varying fin stiffness during each fin cycle, concluding, amongst other findings, that free-swimming velocity could be increased with dynamic stiffness control, as could thrust efficiency under certain conditions (Nakabayashi, *et al.*, 2009). The method for adapting the stiffness of the fin was simple, but it proved the concept that active stiffness control can be beneficial to a fin's performance. As suitable actuator technologies such as electroactive polymer muscles (see Section 2.8.4) improve, the scope for practical use of active stiffness control increases.

2.7.2 Heaving Flexible Foils

Studies of heaving-only oscillation in flexible foils have shown that adding flexibility increases fin performance in experiments at zero velocity, and under flow conditions at low Reynolds numbers. Heathcote and Gursul conducted several studies in which foils of different stiffness were actuated in heave only. The foils were of high aspect ratio, and flat, with uniform stiffness, apart from a rigid leading edge. Under static thrust conditions, introducing flexibility to the fin caused the thrust-to-power ratio to increase, compared to that of a rigid fin (Heathcote, *et al.*, 2004). However, too much flexibility was found to be detrimental. A similar finding resulted from experiments in flowing water, where efficiency was found to benefit from a degree of flexibility in the foil (Heathcote and Gursul, 2007). The results suggested the existence of an optimal stiffness value for a given frequency and amplitude of oscillation. Flexibility was found

to facilitate passive pitching of the foil behind the rigid leading edge. The phase angle between the induced pitch and the heave oscillation was found to be an important factor in the efficient generation of thrust.

2.7.3 Pitching and Heaving Flexible Foils

Experiments show that using flexible, rather than rigid foils under pitching and heaving conditions can improve efficiency (Prempraneerach, *et al.*, 2003). The work of Prempraneerach *et al.* showed that a flexible foil of Shore hardness A60 (see Appendix C) operated with a 36% higher efficiency than a similar rigid fin, under pitching and heaving conditions previously found favourable to the rigid fin. The improvement in efficiency was accompanied by a slight decrease in thrust. The experiments concerned used a NACA 0014 aerofoil shape, being moved through a towing tank whilst pitching and heaving. One of the kinematic methods employed used sinusoidal oscillation of both pitching and heaving motions. The other method used a more complex pitching waveform to produce a sinusoidal variation in instantaneous angle of attack. Both methods saw an improvement in efficiency when a flexible foil was used.

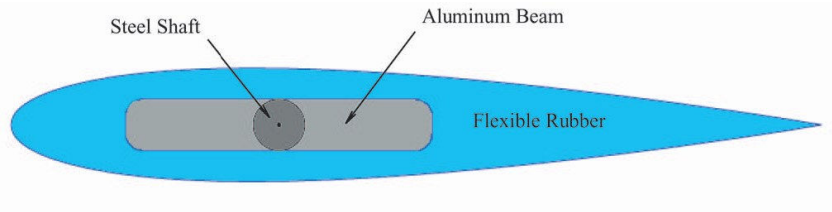

Figure 23: Cross-section of the foil design (Prempraneerach, et al., 2003).

The experiment used a foil with a pivot point around the 0.3 chord point (see Figure 23). Torque was transferred to the fin through a solid core extending forwards, and also backwards inside the fin approximately to the 0.5 chord point, as can be seen in Figure 23. This meant that the effects of using a flexible material were limited to the rear 40% of the foil, so its movement was most closely approximated by Lindsey's carangiform and thunniform modes (Figure 12, page 30).

The fin's construction relies on lateral movement of the axle to reproduce natural and efficient propulsion. The distance from the axle to the leading edge means that using angular oscillation alone would cause the leading edge to oscillate with an amplitude almost as great as the trailing edge, a characteristic of anguilliform swimmers, but without the associated propagation of a wave down the fin body, due to the fin's rigid core.

2.7.4 Numerical Analysis of Flexible Foils

As well as studies of rigid fins, numerical studies have been performed in which non-rigid bodies and their movements in fluids have been analysed. One such study modelled a free-

swimming body, undulating with a travelling sine wave (Lu and Yin, 2005). The simulation was used to investigate the effects of various parameters on the flow over the body, and its thrust generation. Optimal values obtained from the simulation were found to be closely matched to those observed in nature. A similar, more advanced study modelled a swimming body as a chain of linked elements, each of which had its own stiffness, damping, and driving parameters (Farnell, *et al.*, 2005).

Both of the studies mentioned above simulated a self-propelled free-swimming body. More recently, work has been carried out on flexible foils in propulsive applications. Shin *et al.* have modelled a flexible NACA 0012 foil and its fluid-structure interactions in various flow situations, including heaving oscillation (Shin, *et al.*, 2009, Shin and Kim, 2008). The movements of the fin were entirely passive; the model used a combination of computational fluid dynamics (CFD) techniques to simulate the surrounding fluid and the consequent forces exerted on the fin, and dynamic thin-plate mechanics to simulate the movement of the fin itself. Interestingly, the bending model did not account for the fin's stiffness profile, simplifying it instead to a flat plate of uniform stiffness.

2.7.5 Spanwise Flexibility

Most literature on flexible foils discusses flexibility in the chordwise direction. However, spanwise flexibility has also been studied and found to be beneficial in some circumstances (Heathcote, *et al.*, 2008). For the tests carried out in the Heathcote's study, introducing a degree of spanwise flexibility to a heaving high aspect ratio fin was found to increase its efficiency, particularly at Strouhal numbers between 0.2 and 0.3, the range most commonly observed in the natural world. Increasing the flexibility still further had a detrimental effect, suggesting the existence of an optimal stiffness for peak efficiency.

2.7.6 Summary

In each of the studies described above, it has been found that some degree of flexibility is beneficial to the efficient generation of thrust by oscillating fins. Many of the studies postulated a peak stiffness value dependent on the other attributes of the fin and its oscillation. In each of the studies, the stiffness profile was defined by the shape of the fin, or by its internal structure, which in turn was chosen for practical or reasons, or in accordance with conventions laid down in previous works, to aid comparison between studies.

2.8 Fin Actuation Methods

The following sections describe the methods in which other investigators have actuated fins in previous studies.

2.8.1 Industrial Motion Control Systems

Commercially available servomotor systems have been used in many previous studies of this nature (Hover, *et al.*, 2004, Read, *et al.*, 2003). Brushless DC motors are often used, since their design means they have a lower mass rotor than other configurations, and the lower inertia allows faster acceleration and deceleration. They can be specified to be as fast and powerful as necessary, but are very costly.

2.8.2 Servomotors

Model servomotors are inexpensive, easy to control, and highly versatile, making them ideal for robotic projects. Many experimental robots, fish-like and otherwise, use them for actuation. Their drawbacks are that they are not as accurate as industrial servo systems, and tend to use small motors with limited output power. Servos with different gear ratios provide a compromise between output speed and torque.

2.8.3 Shape Memory Alloys

Shape memory alloys (SMAs) are usually used in the form of thin wires that change length when heated by an electric current. They are useful for actuating robots and other devices where space is in short supply. Mechanically they are very simple and effective, but they are also fragile, and break if subjected to too much tension. They are inefficient, and slow to respond, especially where the heat they generate is not easily conducted away. Like real muscles, they can only pull, not push, but using them in opposing pairs requires careful control, so that the contraction of one side does not over-stress and break the other.

They have been used to actuate a biomimetic hydrofoil (Rediniotis, *et al.*, 2002), which consisted of a six-segment skeleton with SMA actuators articulating each segment (Figure 24). It achieved oscillations of 1 Hz, but needed active cooling of the SMA wires to achieve that response time. Opposing pairs of SMA actuators were found to have a short life due to the high stress levels, and were replaced with SMA-spring combinations.

Figure 24: Shape Memory Alloy actuated hydrofoil.

2.8.4 Electroactive Polymers

Electroactive polymers are a relatively new form of actuator. They produce very small forces in comparison to more conventional actuators. However they are extremely compact, and provide movement with no need for gearboxes and other mechanisms. Although power-hungry, their unique properties give them advantages over conventional motors that have been exploited in biomimetic projects (Lauder, 2007, Punning, *et al.*, 2004).

2.8.5 Mechanisms

Mechanical linkages are a simple, reliable way of producing cyclic motion. Through ingenious design, many different output motions can be created, but a disadvantage is that the range of output waveforms is not infinitely variable, as it is for electronically-controlled methods. The Scotch yoke is a common mechanism for turning rotational movement into sinusoidal linear oscillation. It consists of a linear slider, constrained in all but one direction, coupled to a rotating arm via a pin, allowed to slide freely in a slot in the yoke, as shown in Figure 25.

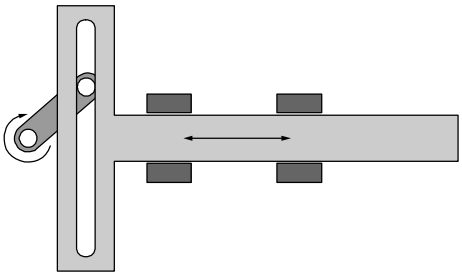

Figure 25: Scotch Yoke mechanism.

When this linear motion is converted back into rotation by a rack and pinion, sinusoidal rotational oscillation results. A combination of mechanisms was used by Gopalkrishnan *et al.* in their work studying the effects of a flapping foil on an oncoming Kármán vortex street (Gopalkrishnan, *et al.*, 1994).

2.9 Applications of Fin Propulsion

Many robots have been created with biomimetic propulsion systems, for a variety of purposes. Some studies concentrate on the control systems necessary to achieve optimal performance from a specific mechanical system. Others develop biomimetic swimming machines as an aid to understanding how real animals propel themselves. Biorobotic models mimic the movements of their natural counterparts in a realistic and repeatable way, and are far more tolerant of instrumentation and flow analysis techniques used to observe their motion than real fish.

This section discusses several examples of complete vehicles using biomimetic propulsion that have been created to date.

2.9.1 Robotuna and Successors

Robotuna was a project carried out at the Massachusetts Institute of Technology (MIT) in which the motion of a swimming tuna was mimicked with a 6-jointed structure surrounded by a metal skeleton, encased in a flexible skin.

Figure 26: Robotuna II.

Extensive experiments were performed with Robotuna with the aim of gaining a better understanding of how real tuna swim. The flow patterns around a tuna's caudal fin were mathematically modelled, and a later project, Robotuna II (shown in Figure 26), produced an untethered free-swimming submarine mimicking a tuna's swimming gait, based on the findings of the original Robotuna project. The data gathered from MIT's Robotuna projects was used by the Draper Laboratory[2] to develop the Vorticity Control Unmanned Undersea Vehicle (VCUUV), a more advanced, untethered robot, capable of swimming at up to 1.2 ms^{-1} (Anderson and Kerrebrock, 1999). The craft has a body length (BL) of 2.4 m, so this equates to a normalised speed of 0.5 $BL\ s^{-1}$. Bluefin tuna (*Thunnus thynnus*) comfortably cruise at

[2] www.draper.com

more than double this normalised speed over long periods, and in short bursts can attain speeds of over 22 ms^{-1} (80 kph) (Wardle, *et al.*, 1989).

More recent work has built on the success of earlier biorobotic studies, with new robot designs providing deeper insights into fish swimming dynamics. In a departure from the rigid mechanisms with multiple joints seen in Robotuna and its siblings, robotic fish with semi-compliant bodies have been developed, using much simpler actuation, but nonetheless producing a realistic gait (Alvarado and Youcef-Toumi, 2006). These robots have been used successfully to study the characteristics of specific composite wake formations, using PIV equipment (Epps, et al., 2009).

2.9.2 Proteus

Proteus, the 'Penguin Boat' (Figure 27) was created by engineers at the Massachusetts Institute of Technology. Its fins were rigid, and its configuration similar to that of most ordinary ships: a long, narrow body with a propulsion unit at the rear.

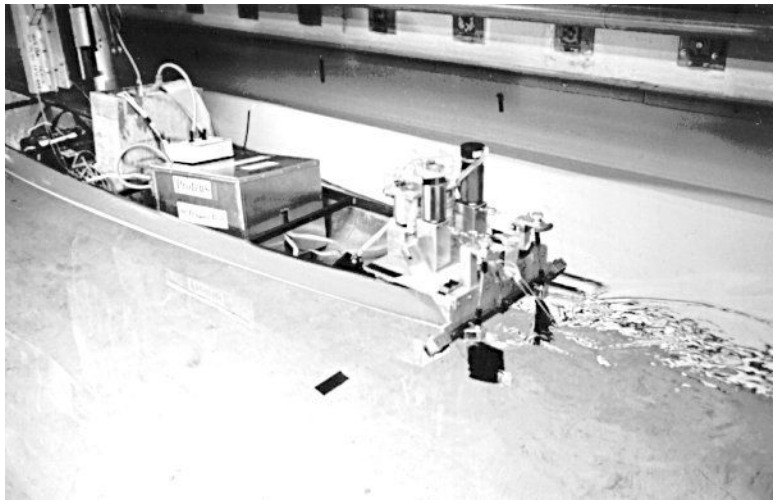

Figure 27: Proteus, the 'Penguin boat'.

In scale trials the propulsion system achieved propulsive efficiencies of up to 87%, compared to efficiencies of around 70% for propeller-driven craft (Thomson, 1997), However, issues of cost, actuation and technical complexity have so far prevented the penguin boat's propulsors moving beyond the prototype stage.

2.9.3 Morpheus

Nekton Research and Florida Atlantic University constructed a highly successful example of a biomimetically propelled submersible robot (Hobson and Kemp, 2002, Hobson, *et al.*, 2003). Morpheus (Figure 28) was an existing Unmanned Undersea Vehicle (UUV) to which researchers at Nekton were able to add oscillating fin thrusters.

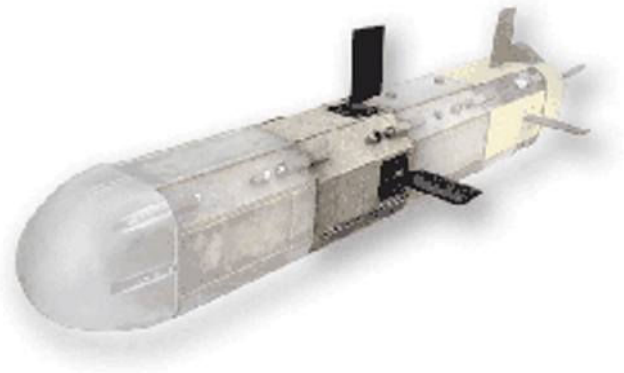

Figure 28: Morpheus UUV with Nekton flexible fin thrusters.

They found the fins' ability to provide large amounts of thrust very rapidly allowed very responsive manoeuvring of the submarine. It was able to hold its position in moving waters better than had previously been possible using conventional propeller-driven thrusters. The ability to start and stop abruptly was also welcome, as they increased the submarine's ability to manoeuvre and avoid obstacles.

2.9.4 Madeleine

Nekton's most recent fin-powered robot used four flexible fin thrusters operating on parallel axes in each corner of a flat, rectangular body (Figure 29). While the design is not biomimetic in the sense that there are no animals using a similar configuration of fins, it has been useful for studying the control of multi-finned robots.

Figure 29: Nekton Research's 4-finned swimming robot, Madeleine.

Madeleine is extremely manoeuvrable, and good at starting and stopping quickly. One of the project's findings so far is that four fins are good for manoeuvrability, but two suffice for efficient propulsion. The robot has the added advantage of being amphibious; it can 'walk' by pushing its body forward with its fins, with a gait similar to that of a seal on land.

One of the studies carried out with Madeleine looked at the benefits and drawbacks of using four fins instead of two, finding that four fins were good at producing high instantaneous thrust, while two were optimal for efficient swimming (Long, *et al.*, 2006).

More recently, six-finned robots have been produced, such as AQUA, from McGill University, Canada (Dudek, *et al.*, 2008). Its extra fins make it more capable on land than four-fined predecessors, and its fins are interchangeable with compliant legs, allowing it to function on a variety of terrain types. Both types of appendage work to some extent, both on land and underwater (Figure 30), so a compromise between the properties of legs and fins could be reached to give the robot optimal amphibious characteristics for a given application.

Figure 30: AQUA 6-finned robot in legged and finned configurations.

2.9.5 Further Examples

Several examples exist of relatively simple robotic fish being created, in order to experiment with their control systems and mimic different swimming modes and behaviours. A common design is to build a chain of independently controlled servomotors, housed inside a streamlined body, and weighted to float in an upright orientation. One such a craft (Liu, *et al.*, 2004) used a control system that moved the segments of the robot in a way that best approximated a travelling wave, moving down the fish's body. This system was built upon, to mimic cruise turns and sharp turns of the kind observed in carangiform fishes.

The robotic fish shown in Figure 31 is of a very similar mechanical design, but employs a radically different control system. It is the result of a combination of different research projects, in fuzzy logic control, vision systems, and mathematical systems modelling (Yu, *et al.*, 2004, Yu, *et al.*, 2005, Yu, *et al.*, 2003).

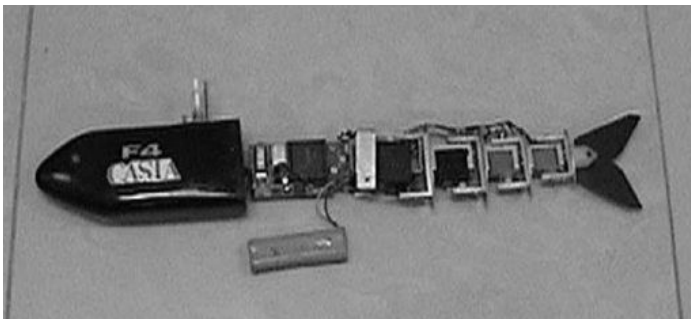

Figure 31: Yu's 4-link robotic fish (Yu, et al., 2003).

The AUV shown in Figure 32 was designed to show that flapping foils are a viable propulsion source for an underwater vehicle (Licht, *et al.*, 2004). It uses four pitching and rotating foils and achieves good manoeuvrability through complex control systems.

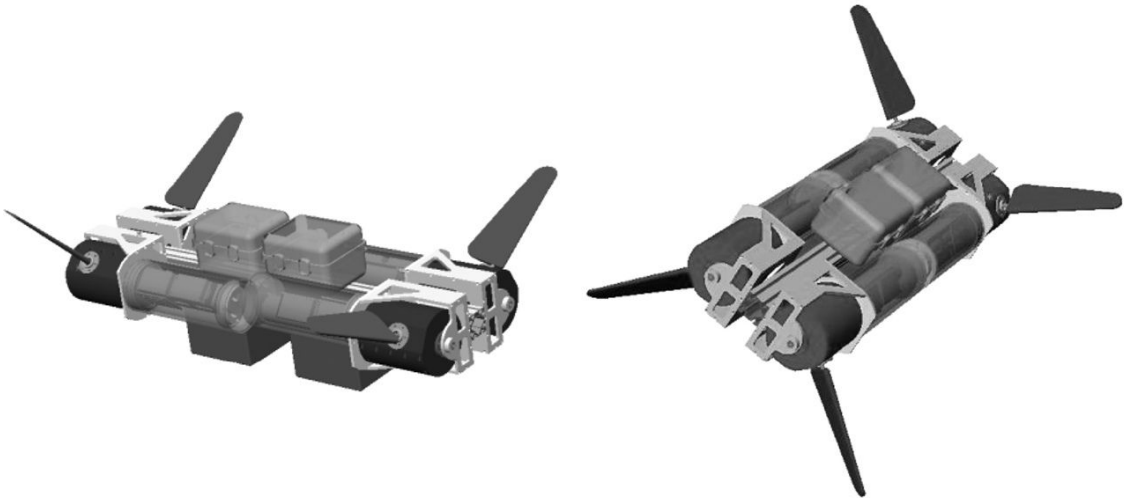

Figure 32: Flapping Foil AUV (Licht, et al., 2004).

Fish are not the only animals to employ finned propulsion. Researchers created a robot with a pair of rigid fins at the rear, which could be flapped in opposite phase, with a 'clapping' motion derived from seals, or in phase, for a more fish-like gait (Bandyopadhyay, *et al.*, 2000). Essentially the work agreed with several others in the field, that the large unsteady forces generated by the fins made them well suited to manoeuvring applications.

Several more abstract applications of biomimetic propulsion exist, which take their inspiration from biological examples. The Amoebot (Chen, *et al.*, 2003), is a 'Metamorphic Underwater Vehicle' that propels itself by changing its body shape, similar to an amoeba (see Figure 33). Flagellar propulsion, that is, using a spinning helix to generate thrust, has also been tested as a means of propelling swimming robots (Behkam and Sitti, 2005).

While interesting, at their current scales these methods are extremely slow and inefficient, so their applications are limited at present. However, as actuators and manufacturing methods

become available at ever-decreasing scales, they may start to find applications in the field of nanorobotics, which has particularly interesting implications in biomedical research.

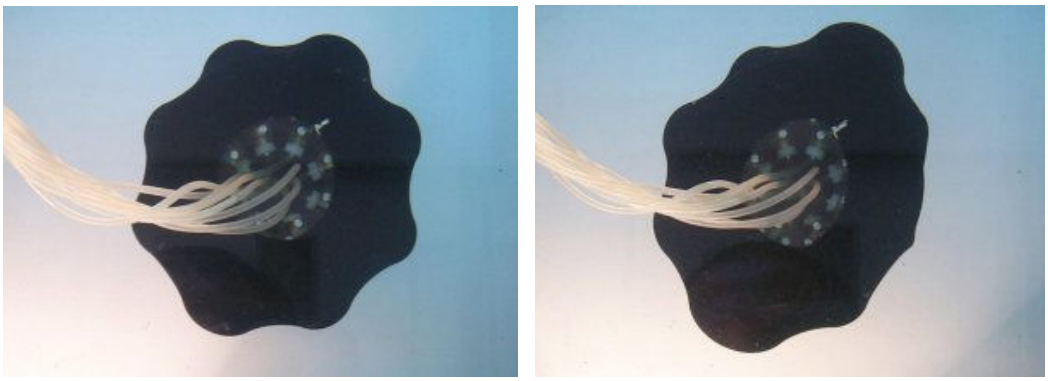

Figure 33: Amoebot, shown in two positions.

A more frivolous application of biomimetic robotic swimming is the creation of animatronic fish designed to form a 'virtual aquarium' (Figure 34).

Figure 34: A trial virtual aquarium in Japan created by Mitsubishi (Terada and Yamamoto, 2004).

2.9.6 Summary

Propellers and conventional thrusters have already reached a high level of maturity, and perform very well in conditions of high-speed steady-state thrust. However, there exists a considerable gap in manoeuvring performance between fish and engineered underwater vehicles (Bandyopadhyay, 2001). Consequently the practical applications for fin propulsion that are under the most serious consideration are those in low-speed manoeuvring. The bio-inspired robots that exist for purposes other than this are generally motivated by academic interest, rather than with specific applications in mind.

2.10 Conclusion

2.10.1 Findings

This literature review has revealed a large body of work of relevance to flexible oscillating fin propulsion. There was a loose division between work that sought to further understanding of biological swimming mechanisms through animal experimentation, and physical and numerical models of living creatures; and work inspired by particular physical phenomena, observed and replicated, again with the aid of mechanical test equipment and numerical models.

Observation of the methods used in previous studies yielded some helpful discoveries. Paying attention to precedents set in previous work has been beneficial, allowing this thesis to cover new ground whilst heeding the examples and lessons learned from previous studies.

The purpose of the literature review was, however, to identify areas with scope for further research, within the field of flexible fin design. One specific area was identified as having particular potential: the role of stiffness profile in oscillating fin performance. Very few studies were found to pay special attention to localised stiffness properties, the closest example being that of Combes and Daniel's study of insect wing dynamics, and the work of Alben *et al.* on pectoral fin rays. Bearing in mind the significance of local stiffness and its contribution to the overall dynamics of insect flight, in-depth discussion of the role of stiffness profile was notably absent from many studies of oscillating flexible fins.

Several studies found flexibility to be beneficial to fin performance, especially when the oscillation properties were tuned accordingly, but where flexibility in fins was explored, it was generally applied in one of two ways: To use a flat plate of uniform stiffness, or to use a fin of arbitrary shape, made from a flexible material, such that its stiffness varied from leading to trailing edge dependent on its thickness. NACA designated fin designs have been used widely in oscillating fin research, but their popularity is due to precedents set in previous rigid-foil studies, rather than to their stiffness properties. The stiffness profile of a NACA fin is inherent to its shape, and its shape was originally conceived as a rigid structure, optimised primarily for its aerodynamic properties.

2.10.2 Hypothesis

Therefore, the role of stiffness profile in thrust generation seemed an exciting area for further study. The following hypothesis was proposed, to be tested experimentally:

> *"Use of a biomimetic fin stiffness profile can improve the effectiveness of a flexible oscillating fin, over that of a standard NACA designated fin shape."*

'Effectiveness' is chosen as general term to encompass any metrics that make one fin design preferable to another in real-world applications. Thrust production and efficiency are the most important measurable variables, but other factors such as lateral force should also be taken into account.

The remaining chapters in this thesis concentrate largely, although not exclusively, on gathering evidence to support or disprove this hypothesis.

2.10.3 Aims and Objectives

With a hypothesis in place, the next step was to identify the necessary steps towards its validation or disproof. The following aims and objectives were defined, to guide the subsequent investigations and set milestones for each stage of the research.

2.10.3.1 Fin fabrication technique

- Design a fabrication method for manufacturing fins:
    - Accurately and consistently
    - With a definable stiffness profile
    - In a range of material stiffnesses
- Investigate potential moulding materials, and select one that is:
    - Readily available
    - Suitable for creating flexible fins with the chosen manufacturing method
    - Available in a range of stiffnesses

2.10.3.2 Develop experimental methods

- Choose appropriate fin profiles for testing, which:
    - Are suitable for manufacturing with the chosen materials and methods
    - Satisfy the requirements of the hypothesis
- Design and build apparatus for testing the fins:
    - Capable of oscillating fins of the selected designs at a range of frequencies and amplitudes
    - Capable of measuring thrust production and other parameters that have a bearing on the effectiveness of a fin

  - Automated, to carry out sequences of tests without time-consuming adjustment

- Develop methods for analysing the collected data, which:
  - Reveal key indicators of real-world performance, so that fins can be assessed comparatively
  - Are able to process data from numerous experiments without excessive manual input
  - Visualise the data in a descriptive and helpful way

2.10.3.3 Conduct experiments

- Conduct experiments to characterise the performance of the selected fins, within the experimental range of the test equipment
- Continue experimental phase until enough data has been collected to validate or disprove the hypothesis

2.10.3.4 Draw conclusions

- Analyse the implications of the experiments on the hypothesis
- Identify potential avenues for further investigation based on experimental findings

Chapter Three

Preliminary Investigations

3.1 Introduction

Before the work described in the main experimental chapters of this thesis took place, several brief speculative investigations were carried out in a variety of areas. These included image analysis methods, simple physical and numerical fin models, and investigations into actuation and manufacturing techniques. Further information about them can be found in the transfer report that precedes this thesis (Riggs, 2006), which is included on the accompanying supplementary data CD.

Of these preliminary investigations, several were not ultimately of relevance to the work presented in this thesis, and have been omitted. Others were of more significance, and their findings are presented in this chapter. The testing of the fin moulding material yielded useful results of interest both here and in future experiments with flexible fins. The dissection of a dogfish gave insights into the complexity and structure of an elegant natural fin design.

3.2 Fin Material Testing

3.2.1 Introduction

A selection of materials was explored to find one suitable for making flexible fins. Polyurethane and silicone rubbers were quickly identified as good candidates. After searching datasheets of several resins, a silicone rubber moulding compound sold under the name 'Moldsil'[3] was identified as having good properties for the task.

Moldsil consisted of a resin and a catalyst component, which were mixed together with a ratio of 10:1. The resin mixture was a viscous liquid, able to flow around objects and reproduce complex shapes. Different catalysts resulted in different hardening times, and slightly different material properties. The standard catalyst gave a working time of about an hour before the mixture showed signs of solidifying. It then became solid within 10 hours, and reached its final properties within 24 hours of mixing. Its density was 1150 kgm^{-3}. It was available in different hardness grades, all of which used the same catalyst. Its softest grade had a much lower

[3] Supplied by W.P. Notcutt Ltd. (www.notcutt.co.uk)

stiffness than other liquid resins, allowing fins to be produced with greater flexibility; this was one of the key factors in its selection.

Its intended application was producing negative moulds of solid objects, so another of its strengths was that it did not adhere to most materials after setting. This meant a variety of mould materials could be used, usually without the use of release agents to prevent sticking. These materials included flexible polypropylene sheet, useful for creating hand-built, smoothly contoured moulds; acrylic, which is well suited to computer numerical controlled (CNC) machining; and Acrylonitrile Butadiene Styrene (ABS), the material used by the rapid prototyping machine described in Appendix D.3 (page 200).

Because Moldsil was intended as a moulding compound for model-makers rather than an engineering material, the literature supplied with it gave only basic details about its material properties. Also, no data was available on mixing different grades of resin to create rubbers with varying properties, so it was necessary to carry out some materials tests on samples of the rubber. The goal of the experiments documented below was to ascertain the stiffness properties of the material when mixed with different ratios of hard and soft resin, and to make sure the resin was suitable for future fin experiments.

Since the silicone under test was capable of elongation of up to 600% before breaking, and was designed to return to its original shape after such stretching, a silicone fin oscillating underwater was likely to be flexing well within its elastic limit. Therefore the most important property affecting its behaviour was elastic modulus. Its tensile elasticity (Young's modulus) could be determined with a simple tensile test, along with the Poisson's ratio for the material. Silicone rubber is isotropic, so from these two figures, the material's shear modulus could be calculated if necessary.

An experiment was performed to determine how the resin mixing ratio influences these properties. The following sections refer to this proportion as a percentage by mass of soft resin in the mixture, not including the catalyst. For example, a 20% mixture would consist of 2 parts soft resin, 8 parts hard resin, and 1 part catalyst.

3.2.2 Testing Methods

3.2.2.1 Sample shape

The usual method for tensile testing is to create a sample in a 'dog bone' shape as illustrated in Figure 35.

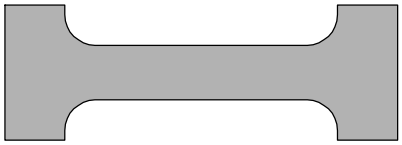

Figure 35: Dog-bone sample shape.

The shape is necessary to ensure there are no stress concentrations around the clamping areas at either end, or where the wider section necks down to the test section. However, stress concentrations are irrelevant when a material is not being tested close to its yield stress. In fact, with a highly elastic material, deformation occurring in the wider section of the sample as well as the narrow section may have caused ambiguity in the results. So for the following tests, a sample shape was chosen that was easier to make than the dog-bone profile, wasted a minimum amount of resin, and gave more accurate results.

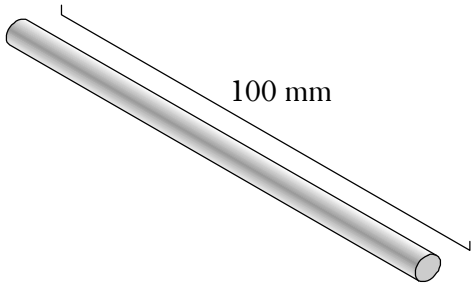

Figure 36: Chosen silicone rubber test sample shape.

The shape was a long, slender cylinder, with a length to diameter ratio of around 20:1, shown in Figure 36. It was created using a drinking straw as a mould - one end of the straw was sealed with candle wax, and the other end was placed in a cup containing a small amount of resin; approximately double the volume of the straw, to include a reasonable safety margin. The cup was suspended at an angle such that the unsealed end of the straw was submerged in resin, and then placed in a vacuum chamber. The vacuum drew the trapped air out of the drinking straw, through the resin. When the air was returned to the vacuum chamber, the ambient air pressure pushed the resin up the straw, which set to form a flawless, bubble-free cylinder. Clamping the sample at both ends resulted in slight deformation of the material near the clamps, but the large aspect ratio of the sample meant this deformation had a negligible effect on the results.

Figure 37: Apparatus for creating resin test samples.

The samples were created by adding small portions of resin to a mixture, and accurately weighing how much had been added (Figure 37). This meant the resin proportions were a measured variable rather than a controlled one, but resulted in better accuracy than the alternative, which was to try to measure and add a known quantity of each resin many times over. A spreadsheet was used to keep track of the precise proportions of soft and hard resins.

3.2.2.2 Test equipment

Tests were carried out on an Instron[4] 1195 tensile testing machine, equipped with a 20 N load cell. Before testing, the sample diameters were measured with a micrometer. All the samples were identical within the measurement resolution of ±0.05 mm, having been moulded by the same process. The jaws of the Instron were moved to a distance of approximately 60 mm from each other, and the rubber test sample was clamped firmly between them. The jaws were then moved a few millimetres closer together, to ensure the stress on the sample was negative, before beginning the test, stretching the sample at a rate of 50 mm min^{-1}. The distance at which the stress became positive was recorded as the true sample length, from which the strain was calculated. The samples where stretched to double their original length (100% strain), then their diameters were measured, before they were relaxed to zero stress at the same rate of 50 mm min^{-1}.

[4] www.instron.co.uk

3.2.3 Results

3.2.3.1 Stress-strain behaviour

The results over a full test cycle from 0 to 100% strain are shown in Figure 38, and demonstrate that the resin is subject to hysteresis, like all natural and artificial rubber compounds. This appears to be more pronounced in the hard resin than the soft. The drop in stress on the right hand side of the graph occurred during a pause of approximately one minute, while the stretched sample diameter was being measured. Further testing would be necessary to determine the precise nature of the hysteresis, but it is not relevant to the tests carried out in this thesis, for which the strain placed on the rubber will be momentary, and small (of the order of 10%).

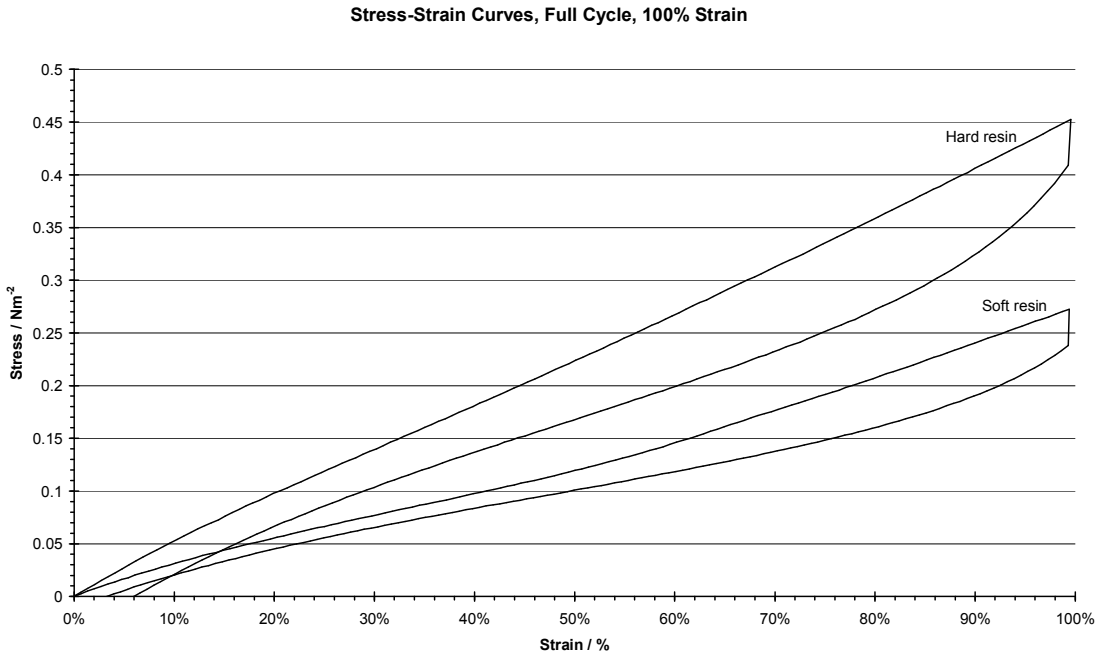

Figure 38: Stress – Strain curves over a full test cycle of the silicone rubber moulding compound.

Figure 39 shows the results of all of the resin tests, up to a strain of 30%. The ratio of hard to soft resin is shown as a percentage at the end of each curve. Slight non-linearity is apparent, with the gradients reducing slightly as strain increases. A correlation can be seen between each resin mixture and its properties, a relationship shown more clearly in Figure 40.

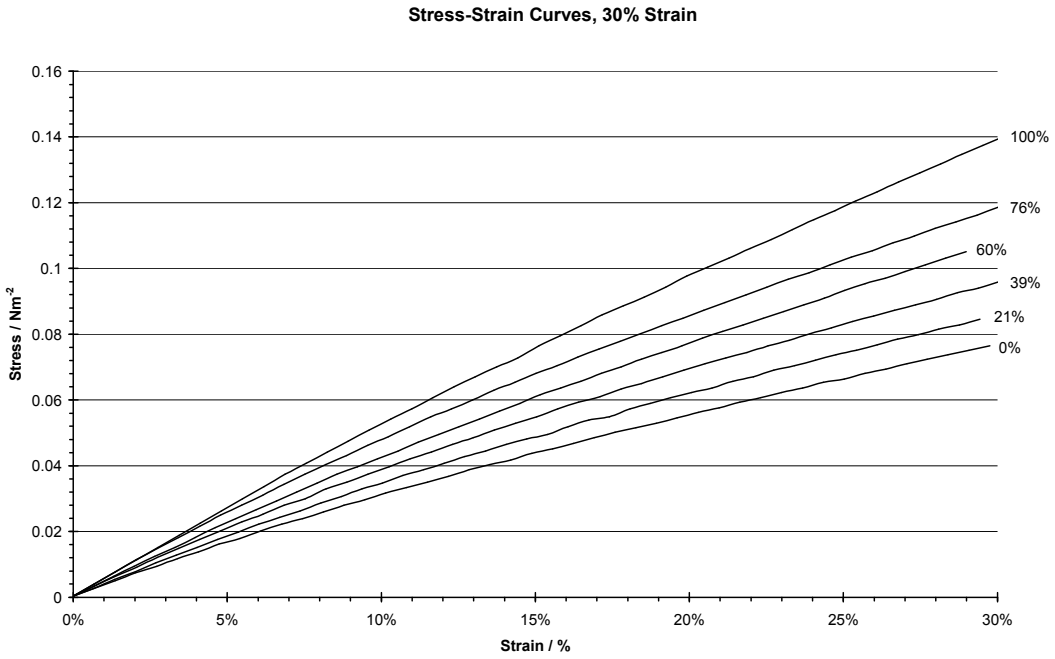

Figure 39: Stress – Strain curves to 30% strain.

3.2.3.2 Young's modulus

To gain a representative Young's modulus for the samples, the gradient of the stress-strain curves up to 10% strain was measured. Plotting these values against the proportion of hard to soft resin in each sample yielded the graph in Figure 40, which shows the relationship to be linear within the bounds of the experiment.

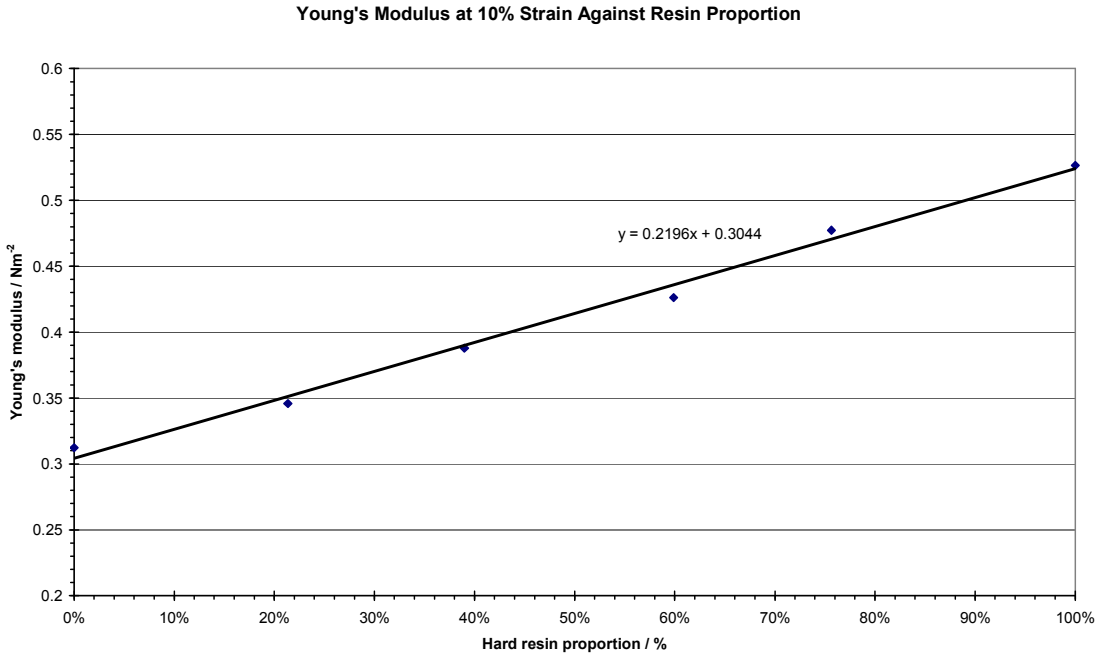

Figure 40: Relationship between Young's Modulus and hard / soft resin mixture.

The Young's modulus of the resin mixtures varies between 0.31 Nm^{-2} for the soft resin and 0.53 Nm^{-2} for the hard. The relationship between resin proportion (P_{hard}) and Young's modulus (E) can be expressed as:

$$E = 0.22P_{resin} + 0.304 \quad (31)$$

Where P_{resin} is a value between 0 (100% soft resin) and 1 (100% hard resin).

3.2.3.3 Poisson's ratio

Table 1 shows the values of Poisson's ratio calculated for the rubber samples. The diameter of the samples was measured under 0% and 100% strain, and the Poisson's ratio calculated using equation (26). The materials conform to expectations for rubber, having Poisson's ratios of around 0.5, indicating that the material is incompressible. The scatter in the results is most likely caused by the samples not being perfectly circular in cross-section, leading to discrepancies in the diameter measurements depending on the orientation of the sample.

Ratio of hard resin	Diameter before (mm)	Diameter after (mm)	Poisson's ratio
0%	5.8	4.20	0.47
21%	5.8	4.15	0.48
39%	5.8	4.30	0.43
60%	5.8	4.20	0.47
76%	5.8	4.15	0.48
100%	5.8	4.30	0.43

Table 1: Poisson's ratio calculations.

3.2.4 Conclusions

The experiments revealed the properties of the resins with greater detail than had been provided in their datasheets, and confirmed that the properties were consistent and predictable when different grades of resin were mixed together. The relationship between resin proportion and Young's modulus was defined with a linear equation. Overall, the experiments confirmed the suitability of the Moldsil resin for making fins, and confirmed that the hard and soft grades could be mixed together in different proportions to achieve a range of stiffnesses.

3.3 Dogfish Dissection

3.3.1 Introduction

As an aid to understanding the structure of a biological fin, a dissection was carried out on a fin from *Scyliorhinus caniculus*, commonly known as a dogfish, or cat shark. The way in which dogfish use a largely passive caudal fin actuated by muscles further up the body was of interest, because an understanding of the mechanisms involved can provide clues about how to design an effective biomimetic copy. The dogfish before the dissection is shown in Figure 41.

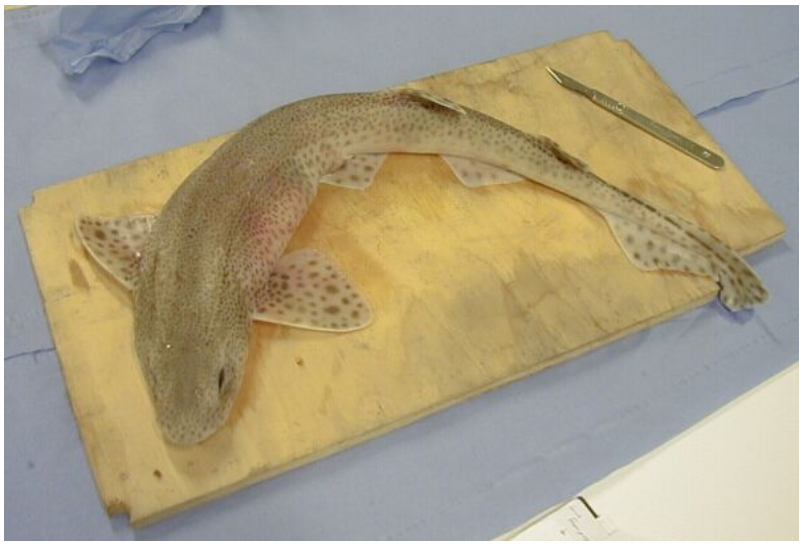

Figure 41: Lesser Spotted Dogfish (Scyliorhinus caniculus).

The dogfish has several fins along the length of its body, labelled in Figure 42:

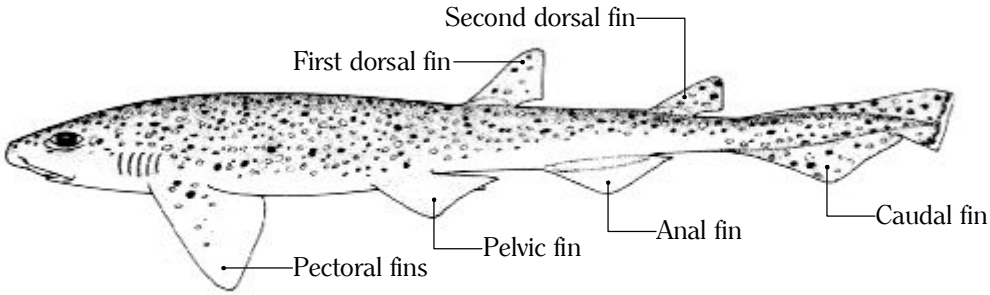

Figure 42: Dogfish fins.

3.3.2 Fin Behaviour and Microstructure

An interesting property of the fins became apparent when they were detached from the body of the dogfish (Figure 43). Holding a small sample of the fin at the base and subjecting it to a shear force applied to its upper and lower surface caused the whole fin to curl, all the way to

the tip, suggesting the forces were being transmitted by a complex, anisotropic internal structure.

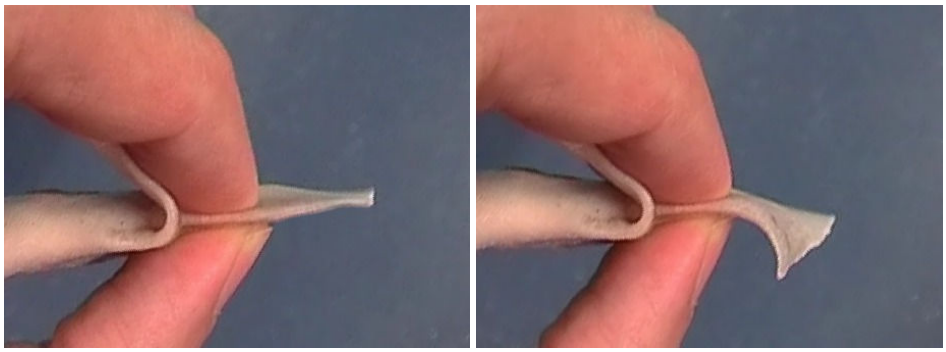

Figure 43: Dogfish fin behaviour.

When observed in the correct light, lines can be seen from the base to the tip of the fins, suggesting the orientation of the internal structure. The lines are hard to distinguish in the photograph in Figure 44, so extra lines have been added for emphasis.

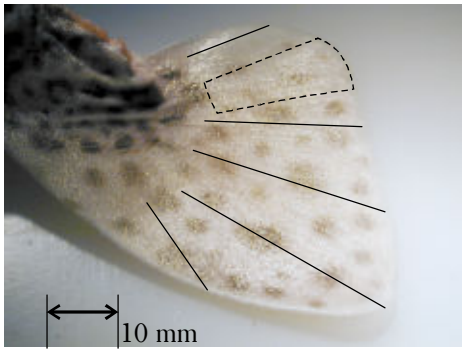

Figure 44: Lines indicating internal structure of dogfish pectoral fin.

A sample was taken from the fin, as shown by the dotted line in Figure 44. After staining the fin with the biological stain toluidine blue, its constituent materials could be easily distinguished. Figure 45 shows a magnified view of the fin's cross-section, perpendicular to the fibres that run through the fin. The images showed a composite microstructure, consisting of a thick layer of remarkably tough skin, with underlying elastoidin fibres running through a weaker fleshy matrix of collagen-based connective tissue.

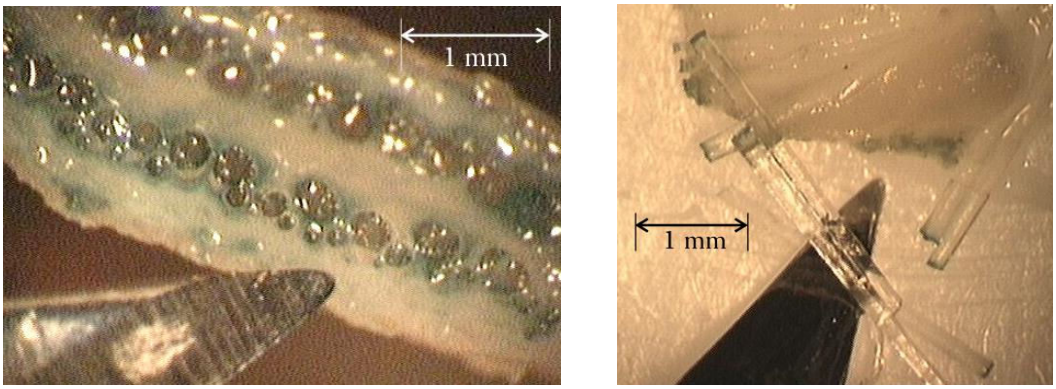

Figure 45: Microscope photographs showing internal microstructure of dogfish fin (left) and elastoidin fibres (right).

The fibres are strong and stiff in tension and appear to be the component that transmits forces along the length of the fin. The connective material had interesting properties - time did not permit detailed analysis of its behaviour, but simple manual manipulation under the microscope of the material joining the two sides of the fin suggested it had a shear stress / shear strain curve similar to that depicted in Figure 46. Applying a shear force to the material caused it to deform, but the greater the deformation, the more resistance it provided to further deformation.

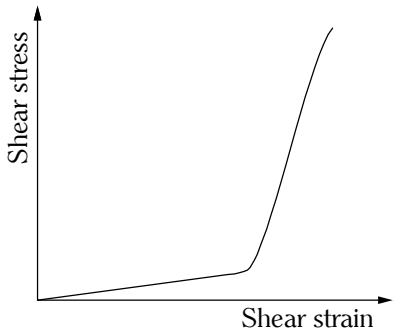

Figure 46: Predicted shear stress / shear strain curve for dogfish fin matrix material.

3.3.3 Skin

The skin of the dogfish was covered in tiny spines (see Figure 47). It is likely that the surface of the fin assists the dogfish in passing through the water with the minimum of boundary layer drag, thus saving energy (Lang, *et al.*, 2008).

The most efficient way for shapes to pass through fluid is under laminar flow conditions. However, imperfections over the surface of a body can reduce drag over objects where Reynolds numbers are too high to allow completely laminar flow. By inducing small vortices in a controlled way, larger ones can be prevented, and the overall drag cost of the turbulence is reduced.

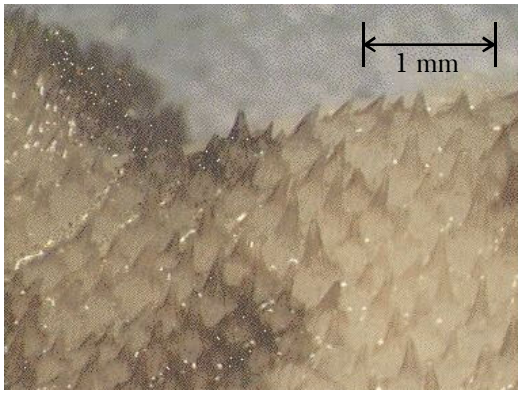

Figure 47: Microscope photograph showing dogfish skin.

3.3.4 Conclusions

Actuators are a serious bottleneck in the development of many biomimetic systems, as the current state of the art in actuator technology lags far behind the speed, efficiency and strength of biological muscles. While the intricate structure of the dogfish fin would be extremely hard to mimic, the principle of achieving complex motion with structure rather than actuators is an interesting one. It is possible that innovative biomimetic propulsion designs may be able to utilise very simple actuators, and rely on internal structure to produce the desired motion.

Chapter Four

Development of Experimental Methods

4.1 Introduction

This chapter follows the development of experimental equipment and methods to test the hypothesis given at the end of Chapter Two. The chapter is divided into sections, each of which covers a major aspect of the methods and equipment used in this thesis. It describes in detail the alternatives considered, and the design process that lead up to each accepted solution. Sometimes, several iterations of thought or design were necessary, and each step toward the final, successful design is documented. Several software packages are referred to; descriptions of these can be found in Appendix F.

4.2 Fin Fabrication Methods

In order to test different shapes and sizes of fin, it was necessary to build an apparatus to fabricate the fins in an accurate and repeatable way. Several methods were considered for this task, and their design, construction and testing is documented in Appendix D in some detail. Ultimately, one method proved most suitable, and was used to create all the fins tested in this thesis. The method is described in the sections below.

4.2.1 Hybrid CNC Method

Machining a two-piece plastic mould with a computer numerical controlled (CNC) milling machine was considered as a method for creating fins, but needed some improvement to overcome the limits of the available CNC equipment (see Appendix D.4, page 206). A modified version of the CNC machining method was developed, and resulted in a good combination of cost, accuracy and repeatability. Acrylic was chosen as an appropriate material for the mould, as it is stiff, inexpensive and easy to machine.

A four-part mould was designed, in which the curved surfaces of the fin were formed by two identical CNC machined acrylic blocks. The top and bottom surfaces used thinner acrylic plates, with holes to hold the fin axle in position, and allow filling. Accurately positioned ridges in the plates held the acrylic blocks together while the resin cured.

Because the flat surfaces of the fin were formed by the additional flat plates rather than the CNC machined blocks, the blocks themselves could be simple, prismatic shapes, as shown in

Figure 48, with no sharp corners, and needing only a ball-nose cutter to reproduce. The smooth contours of the fin mould in the Z (vertical) axis required many passes of the machine tool to produce a smooth surface, but the finished mould was of very high quality, with no visible surface rutting.

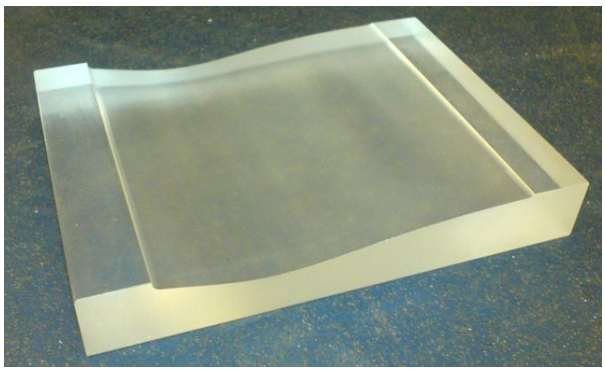

Figure 48: CNC machined fin profile mould.

When all the mould components were assembled and in position, with the axle in place, the interfaces were sealed with latex adhesive. Resin was poured in via a receptacle fixed to the top plate of the mould, and connected to the mould cavity via a small hole. The mould was filled in a vacuum to ensure there were no bubbles in the completed fin. Figure 49 shows the mould assembled and ready to be filled with resin. The rod protruding vertically from the mould is the fin axle.

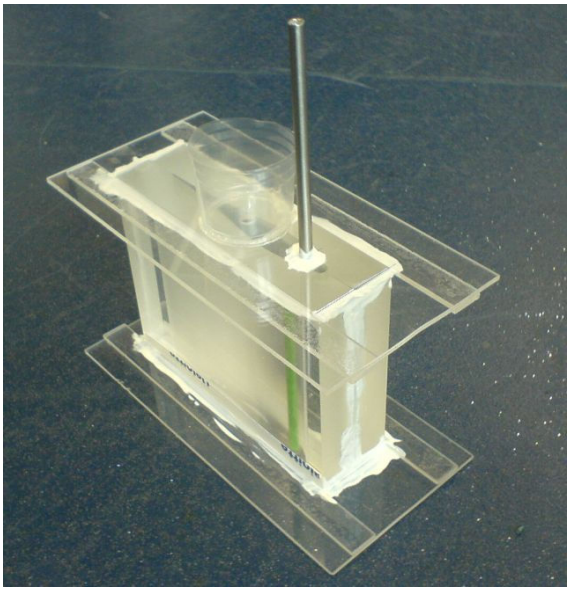

Figure 49: Hybrid CNC fin mould.

4.2.2 Adhesion to Fin Axle

4.2.2.1 Absorbent fabric

Regardless of the fin mould design, special attention must be paid to the interface between the silicone rubber fin material, and the stainless steel axle. The silicone naturally peels away from the steel very easily, so a combination of materials is required to allow the axle to transmit force to the fin without this happening. One solution is to insert a rigid core into the fin, and mould the rubber around it (Prempraneerach, *et al.*, 2003), but this affects the stiffness of the fin considerably, meaning it is no longer entirely flexible. The first solution chosen for this investigation uses a combination of cyanoacrylate glue (superglue), which bonds very effectively to the steel fin axle, and thin cotton-polyester fabric, the porosity of which allows both the superglue and the silicone resin to seep in and set, creating a strong interface between all components, resistant to peeling and shear (Figure 50).

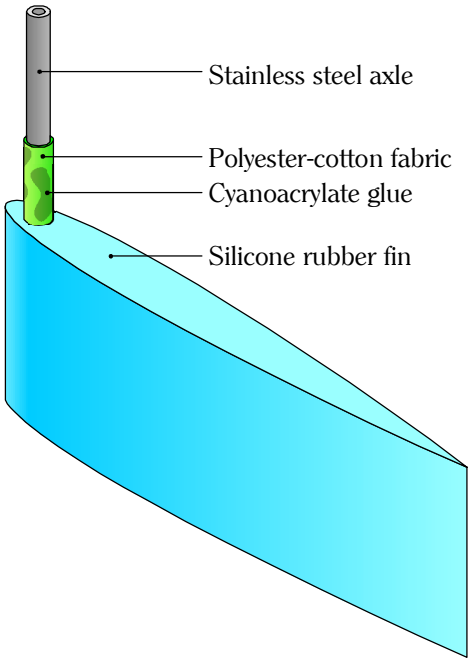

Figure 50: Cutaway diagram of the fin-axle interface.

4.3 Fin Actuator

4.3.1 Introduction

A number of fin actuation methods were used over the course of this investigation.

- Scotch yoke mechanism - a simple and entirely mechanical system providing sinusoidal motion at a range of frequencies and amplitudes.

- DC motor and control system – A DC servomotor and encoder, linked to a computer, providing closed-loop position control.
- Model servomotor – A system using computer control of a high-performance model servomotor to replicate arbitrary waveforms.

Each of these methods is discussed in detail in subsequent sections.

4.3.2 Fin Orientation

Although much of the previous work in the field of oscillating fin propulsion has used fins with their leading edge in a horizontal orientation, the decision was taken to oscillate fins in a vertical orientation for the experiments in this thesis.

For a rigid or near-rigid fin, the direction of gravity can be assumed to have negligible effect on behaviour, because the hydrodynamic forces at work will have a far greater effect on the fin's deformation than the influence of gravity. Assuming the surrounding fluid is incompressible and of uniform density, it will also be unaffected by gravity.

Compared to those used in previous work (Prempraneerach, *et al.*, 2003), the fins used in the experiments described in this thesis were of low stiffness, and their density was slightly greater than that of water (1150 kgm^{-3}), making them droop slightly if held in a horizontal orientation. Oscillating the fins under these conditions could result in the generation of asymmetrical forces. Therefore, vertical orientation was selected as the most appropriate. A beneficial side-effect of this decision was that it allowed the fin to be actuated via a rigid shaft from above, with no need for any mechanisms beneath the surface of the water.

4.3.3 Scotch Yoke Mechanism

The first mechanism constructed for testing fins was a mechanical device capable of producing sinusoidal oscillation about the fin axis. It used a scotch yoke mechanism to produce a sinusoidal linear oscillating motion, which was converted to axial oscillation by a rack and pinion (Figure 51). A small pitch was selected for the rack and pinion to minimise backlash and allow smooth transmission of force to torque.

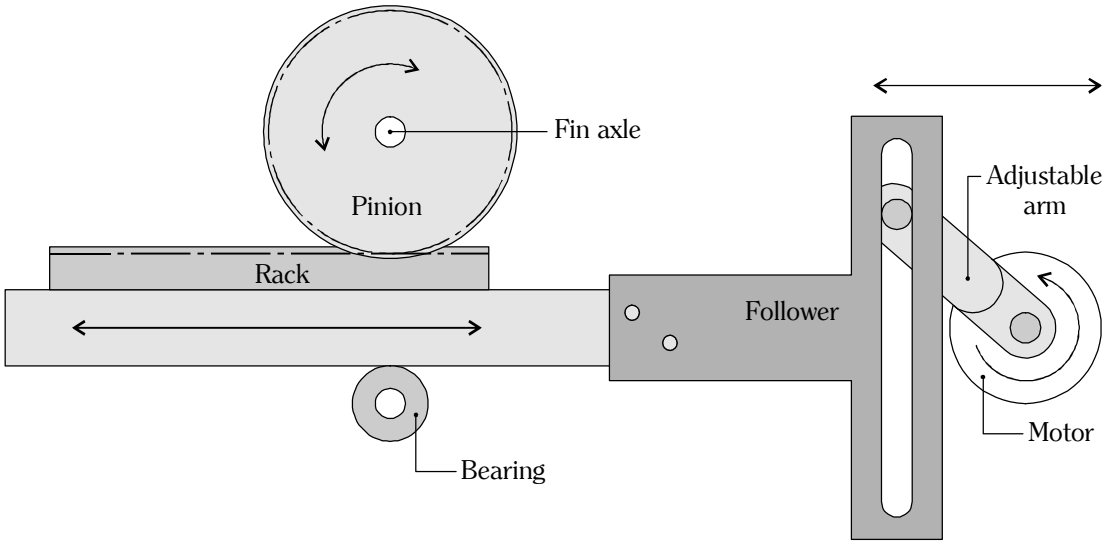

Figure 51: Scotch yoke mechanism.

The amplitude was adjustable by changing the length of the yoke arm, if necessary down to zero amplitude operation, where the pin engaged by the yoke is concentric with the motor axle. The arm was constructed from two parts, fixed securely together with two hex bolts. Loosening the bolts allowed the two sections of the arm to slide past each other. It was found that the manual method of adjusting the arm's length made it difficult to produce accurate, repeatable results, so an adjustment mechanism was devised and constructed from RP components, which fitted around the arm, allowing the total length to be varied by a screw thread, and the diameter read from a scale. Far more accurate adjustments were possible after this modification. The frequency of oscillation was controlled by adjusting the power supplied to the motor. This was achieved using a PWM variable motor speed controller adjustable via a potentiometer. The fin axle passed down through the rig to the fin, and was constrained by two bearings, one above and one below the rack and pinion (Figure 52). At the top end of the fin axle, a potentiometer was connected via a zero-backlash flexible coupling, to measure the angular displacement of the fin. The coupling was necessary so that the potentiometer and fin axle could both be constrained securely, without generating excessive forces in the event of imperfect alignment between the two axles.

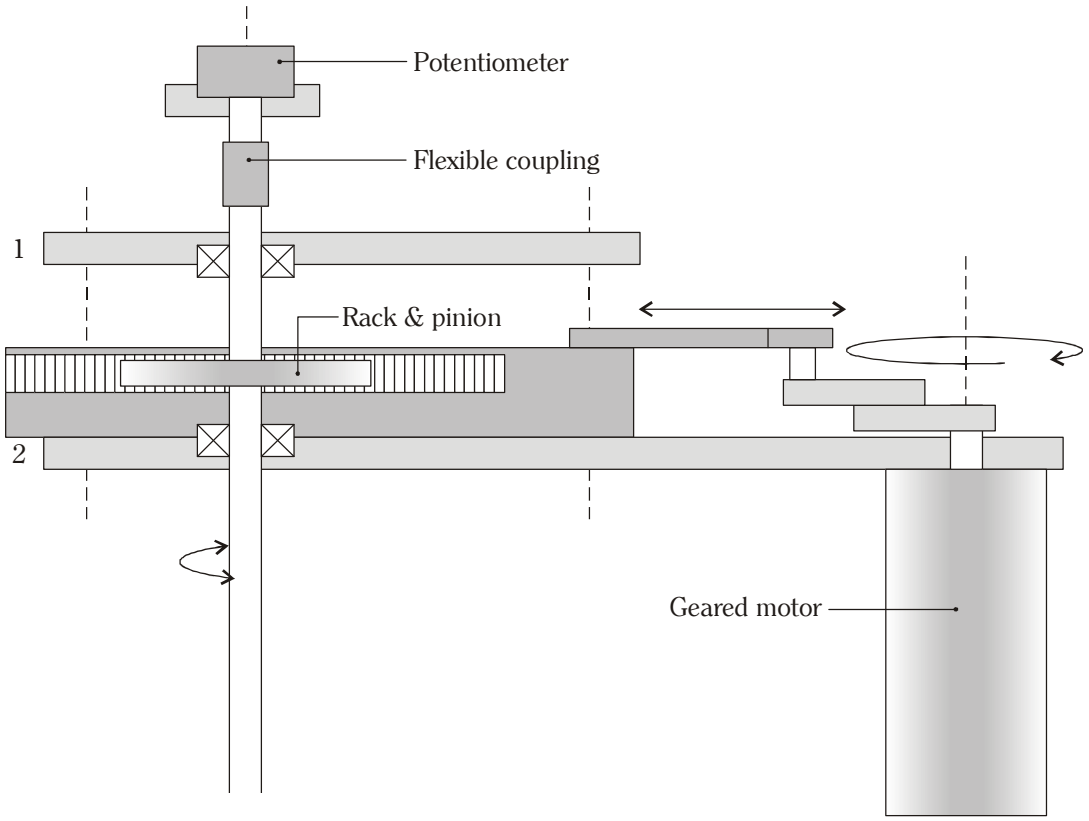

Figure 52: First generation fin oscillation device.

The mechanism on the top layer of the rig is shown in Figure 53.

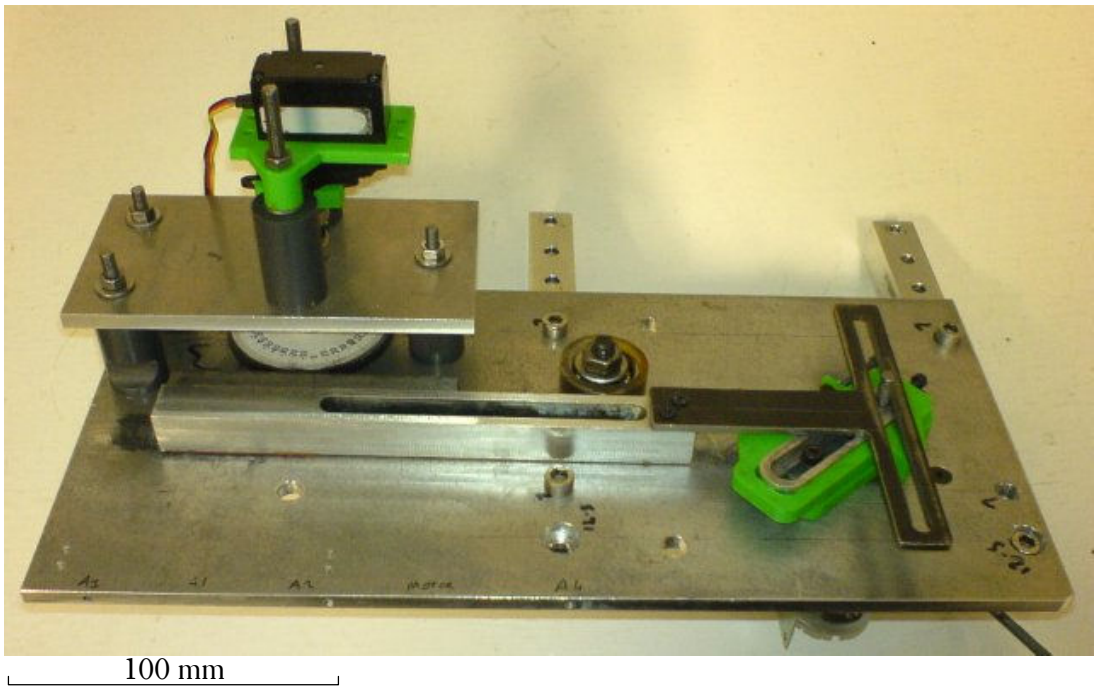

Figure 53: Scotch yoke mechanism on the test rig.

The design has the advantage of being simple and reliable by design, and so less susceptible to errors in software and electronics. However, play in the scotch yoke mechanism could cause clipping of the sine wave output, and jarring of the rig, which would in turn cause unwanted noise in the force sensors. Another drawback to this design is the lack of feedback in the motor speed control, which means the oscillation frequency is a measured, rather than independent variable, and can drift over time for a number of electrical and mechanical reasons. Furthermore, the large mass of moving parts that accelerate and decelerate in every cycle could cause erroneous readings in the force sensors measuring the rig.

4.3.4 Industrial DC Servomotor

The next mechanism to be used for oscillating the fins was the fin actuator from the Bathymysis submersible. It consisted of a low-inertia geared DC motor driving an axle through a further reduction gear. The motor shaft was connected to an encoder, which allowed closed-loop control of the fin position via custom-built control electronics and a PureBASIC[5] program running on a PC. The design of the fin actuator design is covered in Appendix A.7 (page 186).

The submarine fin actuator was used for some initial sets of experiments, but the PC-dependent control system meant that it was very susceptible to communications glitches, which would occasionally cause the fin to stray temporarily from its intended path. The software was able to recover quickly from such problems, which were barely noticeable in the submarine application, but for experimental purposes, a more reliable actuation method was deemed necessary.

4.3.5 Model Servomotor

The final and most successful fin actuator, used for the all the experiments described in the following chapters, was based on a high-spec model servomotor. Despite the disadvantages of model servomotors discussed in Section 2.8.2 (page 46), a motor was sourced with sufficiently high performance to overcome the problems discussed. The fins were actuated by a Hitec HS-5945MG high speed servomotor, driven by a Pololu USC01A servo controller. The servo was capable of a maximum slew rate of 5.8 $rads^{-1}$, and an output torque of 1.2 Nm. Complete specifications of both of these items can be found in 0. The controller was operated by custom-written software which allowed it to be calibrated, and to reproduce user-defined waveforms accurately. The range of waveforms was limited by the maximum speed and torque output of the servomotor. More discussion of its accuracy can be found in Section 6.3.1 (page 131).

[5] www.purebasic.com. See Appendix F.

4.4 Fin Force Measurement Rig

4.4.1 Introduction

It was necessary to design a method for measuring the resultant forces from the fins as they were tested. The following measurements were considered vital to understanding how the fins were performing (illustrated in Figure 54):

- Thrust - drag (x): The useful forward force produced by the fin
- Lateral force (y): Force in the direction perpendicular to the flow, in the horizontal plane, resulting from the fin's oscillation
- Torque (T): the torque supplied by the drive system to oscillate the fin

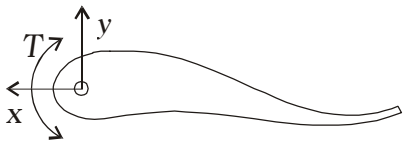

Figure 54: Force and torque produced by the fin in motion.

Torques about the other axes, and force in the z direction, have been neglected, as their magnitude was likely to be very small, tending towards zero in a symmetrical, well-adjusted fin.

The system devised for measuring these loads consisted of an instrumented force platform, data acquisition equipment to take the readings, and software to link the elements of the system together. These components of the force measurement rig are described in the sections below.

4.4.2 Force Platform Design

A rig was designed to allow accurate measurement of the forces generated by oscillating fins. It was required to be versatile, allowing for a range of actuation methods. It needed to measure the primary forces applied to the fin actuator shaft, and the torque being exerted on it, over a wide range, and with a good degree of accuracy.

The resulting design fulfilled these requirements. Its modular construction allowed the measurement range to be adjusted by making simple modifications to the rig's geometry. Numerous mounting points made it simple to attach different types of fin actuator mechanism. The design was reconfigurable, allowing components to be mounted in different locations, and counterweights could be added and moved around to ensure the force sensors were correctly preloaded, and never overloaded. A diagram of the rig, produced from its CAD assembly is shown in Figure 55.

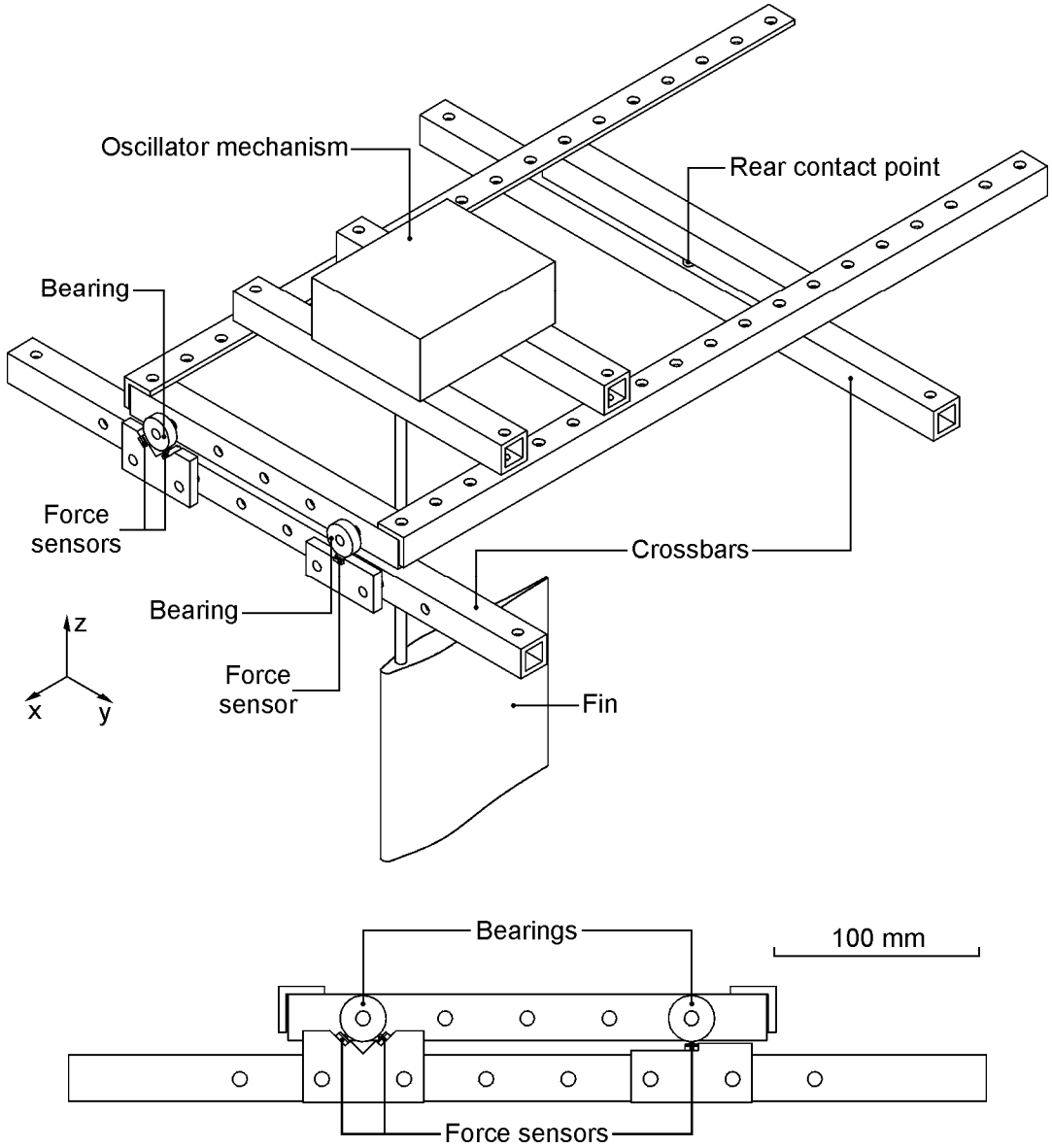

Figure 55: Force sensor assembly of fin test rig.

4.4.2.1 Mechanical design

The rig's structure was built from 19 mm (3/4 inch) L-section and box-section aluminium. Two supporting beams spanned the test tank, and supported a rectangular test bed. The test bed rested on a single spike at its rear, which supported most of the weight of the test bed. The spike prevented translation of the bed in any direction, but allowed rotation, reducing the movement of the rig to the three rotational degrees of freedom. There were two bearings at the front of the test bed, on which the remainder of the test bed's weight rested. One of these bearings rested on a single force sensor, pointing directly upward, the other rested on two more force sensors, pointing diagonally upward and toward each other at an angle of 45° (Figure 56). These three sensors constrained all three remaining degrees of freedom, such that any torque acting on the test bed about the *x*, *y*, or *z* axis caused a change in the readings of

the sensors. The torques were calculated using simple moment equations, and used to derive the forces acting on the fin suspended below the rig.

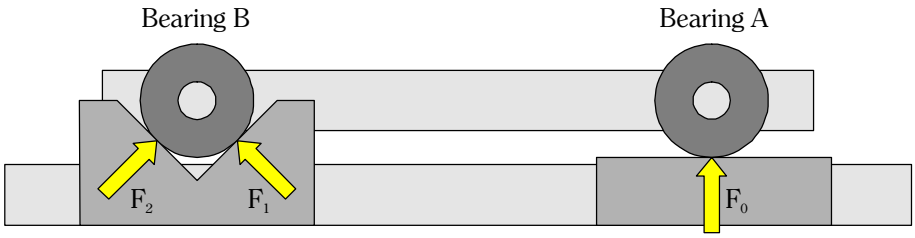

Figure 56: Force sensor locations on force platform test rig.

The rig was designed to be stiff enough to ensure any natural vibrations are of a far higher frequency than the forces being measured, allowing them to be filtered out. It was adjustable in several ways; the distance between the bearings could be changed, to vary sensitivity to torque about the *x* axis. The length of the rig in the *x* direction was also adjustable, changing the rig's sensitivity to torque about the *y* and *z* axes. Furthermore, the position of the fin actuator could be varied, changing the mechanical advantage of forces being transferred between the fin and the sensors.

4.4.2.2 Sensors

Honeywell FSS1500-NSB force sensors were selected for force measurement in the test rig. They were small and low in cost, but accurate when amplified sufficiently. They consisted of a silicon-etched strain gauge in a rigid package, with a small ball bearing resting on the silicon surface, transmitting force to it. Internally, they were analogous to an ordinary Wheatstone bridge strain gauge circuit (Figure 57), which, when an excitation voltage was applied, produced an output voltage proportional to the force being applied to it. The FSS1500 sensors had a measurement range of 1500 g (14.7 N). They were stable, robust, tolerant to overloading, and exhibited extremely low deflection (30 µm at full loading). Combined with the stiffness of the rig's structure, this ensured any movement of the rig was kept to a minimum, avoiding the risk of resonance induced by repetitive forces acting on it. Further specifications of the sensors are included in 0.

Figure 57: Honeywell FSS1500-NSB force sensor used in the fin test rig.

4.4.2.3 Sensor calibration

To calibrate the force sensors, it was necessary to load the force sensors to approximately their maximum capacity. This required two calibration weights to be hung from specific locations on the rig. Taking the spike at the rear of the rig to be the origin, the forces acting vertically on the test bed were as follows (Figure 58):

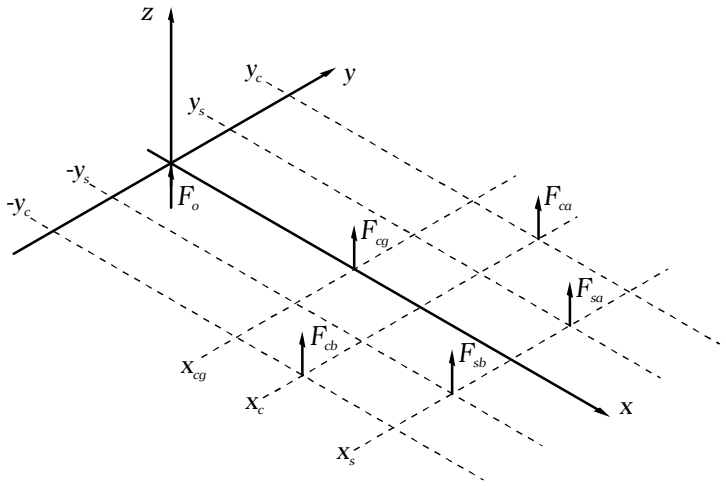

Figure 58: Diagram of vertically-acting forces on the test rig, used for moment calculations.

Table 2 defines of the terms used:

F_o	Force the supporting spike exerts at the test bed pivot, located at the origin
F_{cg}	Weight of test bed, acting from its centre of gravity (negative)
F_{ca}, F_{cb}	Calibration weights, acting at two predefined points on the test bed
F_{sa}, F_{sb}	Force of the sensors, acting from the two sensor locations at the end of the test bed
x_c, y_c	Calibration point coordinates
x_s, y_s	Force sensor coordinates
x_{cg}	x coordinate of centre of gravity (y coordinate = 0)

Table 2: Forces acting on test bed

To simplify the resulting equations, all forces were defined as acting in the z direction. The rig was stationary, so the sum of all forces must equal zero:

$$\sum F = F_{ca} + F_{cb} + F_{sa} + F_{cb} + F_o + F_{cg} = 0 \quad (32)$$

Likewise, the sum of moments about *x* must also equal zero:

$$(F_{ca} - F_{cb})y_c + (F_{sa} - F_{sb})y_s = 0 \tag{33}$$

And also the sum of moments about *y*:

$$(F_{sa} + F_{sb})x_s + (F_{ca} + F_{cb})x_c + F_{cg}x_{cg} = 0 \tag{34}$$

These equations were used to calculate the forces present at the force sensors for given calibration weights. These in turn were used to determine the scaling factors needed to convert the raw sensor outputs into meaningful force measurements. Solving the equations for F_{sa} and F_{sb} gives:

$$F_{sa} = \frac{c_1 + c_2}{2} \quad \text{and} \quad F_{sb} = \frac{c_1 - c_2}{2} \tag{35}$$

Where the intermediate variables c_1 and c_2, represent the force on each sensor, due to the moments about the *x* and *y* axis respectively. They are defined as:

$$c_1 = \frac{(F_{ca} + F_{cb})x_c + F_{cg}x_{cg}}{-x_s} \quad \text{and} \quad c_2 = \frac{(F_{ca} - F_{cb})y_c}{-y_s} \tag{36}$$

The masses required for calibration were determined by solving equations (33) and (34) to give F_{ca} and F_{cb} in terms of the other variables:

$$F_{ca} = \frac{c_3 + c_4}{2} \quad \text{and} \quad F_{cb} = \frac{c_3 - c_4}{2} \tag{37}$$

Where the corresponding intermediate variables c_3 and c_4 are:

$$c_3 = \frac{(F_{sa} + F_{sb})x_s + F_{cg}x_{cg}}{-x_c} \quad \text{and} \quad c_4 = \frac{(F_{sa} - F_{sb})y_s}{-y_c} \tag{38}$$

The force sensors were linear, so two readings needed to be taken to calibrate them; one at each end of the sensors' range. To avoid the added complication and error of including the weight and centre of gravity of the test bed in the measurements, the bed was counterweighted until most of its weight was resting on the pivot point, with only a small force being exerted on the sensors. Then the lower calibration reading was taken. The upper reading was taken when known calibration weights were loading the force sensors close to the upper limit of their range (14.7 N). The small force exerted by the rig's mass on the sensors was equal in both calibration measurements, so its exact magnitude and location could remain unknown without affecting the calculations. The geometry of the rig sensors and their loading forces is shown in Figure 59:

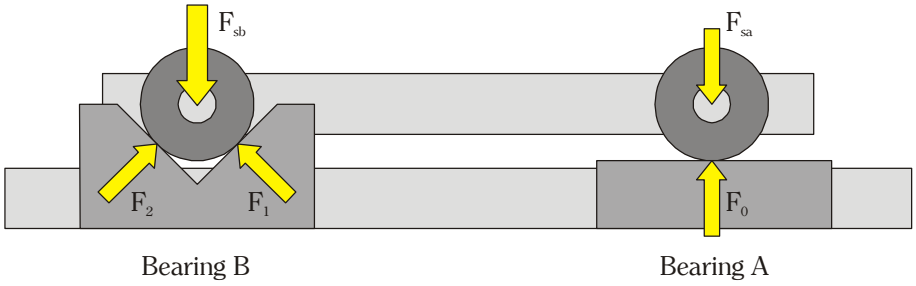

Figure 59: Test rig sensor loadings.

The 45° angle of F_1 and F_2 to the vertical axis meant the desired calibration force at F_{sa} and F_{sb} was as follows:

$$F_{sa} = F_0 \quad \text{and} \quad F_{sb} = \sqrt{F_1^{\,2} + F_2^{\,2}} \tag{39}$$

Where ideally, $F_0 = F_1 = F_2 = 13.98$ N, which was 95% of the maximum range of the FSS1500-NSB force sensors used in the rig.

Therefore, from equation (39), $F_{sa} \approx 14.0$ N and $F_{sb} \approx 19.8$ N. These approximate values were used, along with the rig dimensions, in equations (37) and (38), to find the target masses for the calibration weights. Approximate values sufficed because when the actual calibration weights were selected, they were accurately measured, and their masses fed back into the calibration equations (35) and (36), to give true values for the forces exerted at the sensors. These values were then used to calculate calibration factors for each of the three force sensors, and ensure they provided accurate readings across their range.

The following model was used to describe the behaviour of the force sensors and A-D equipment. F_s is the force exerted on the sensor, f_{cal} is the sensor's calibration factor, R is the raw reading given by the A-D equipment monitoring the sensor, and R_0 is the offset; the reading given by the sensor when the rig was at rest.

$$R = \frac{F_s}{f_{cal}} + R_0 \quad \Rightarrow \quad F_s = f_{cal}(R - R_0) \tag{40}$$

The offset value was applied to the raw reading before the calibration factor to simplify recalibration of the rig. The zero offset was likely to vary due to the effects of sensor drift, or changes to the weight distribution on the test bed caused by, for example, changing to a new fin. To negate these effects, new sensor offsets were calculated for each channel by taking an average of several raw readings while the rig was at rest, and this average was applied as the new offset, without affecting the calibration factor.

4.4.2.4 Fin force calculation

The three force sensor outputs from the measurement rig are defined as F_0, F_1, and F_2, as shown in Figure 56. In Figure 60, F_{saz} represents the upward force acting on bearing A, and is the same as F_0. F_{sby} and F_{sbz} are the horizontal and vertical components of F_1, and F_2, the forces acting on bearing B. These definitions of forces acting on bearing B are related by equations (42) and (43):

$$F_{saz} = F_0 \tag{41}$$

$$F_{sby} = \frac{F_1 + F_2}{\sqrt{2}} \tag{42}$$

$$F_{sby} = \frac{F_1 - F_2}{\sqrt{2}} \tag{43}$$

The weight of the rig and fin can be neglected, since its effect is constant, and can be cancelled out by subtracting the readings from the rig at rest from all subsequent readings.

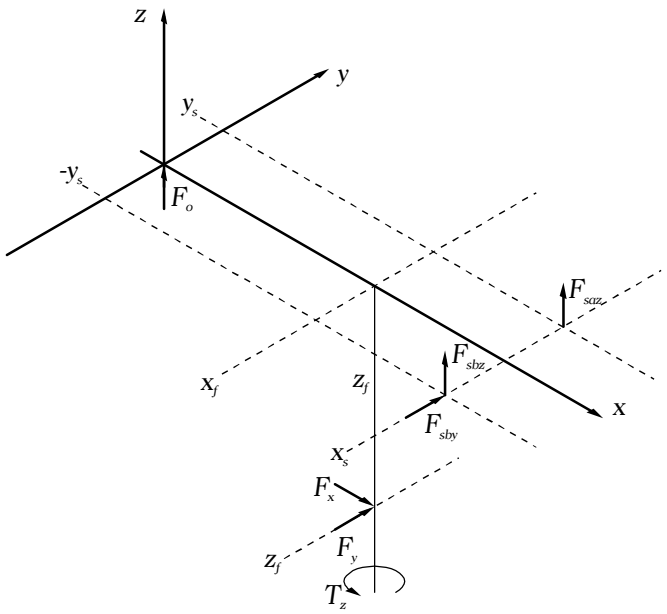

Figure 60: Diagram of forces acting on the test rig, used for calculating fin forces.

The terms are described in Table 3.

F_y	Lateral force exerted by the water on the fin and vice versa
F_x	Thrust / drag force, acting in the direction of the water flow
T_z	Torque being supplied to the fin by the actuator mechanism

Table 3: Forces acting on test bed

When the rig is in equilibrium, the moments about *x*, *y*, and *z* must all be zero.

Moment about *x* axis:

$$(F_{saz} - F_{sbz})y_s + F_y z_f = 0 \tag{44}$$

Moment about *y* axis:

$$(F_{saz} + F_{sbz})x_s - F_x z_f = 0 \tag{45}$$

Moment about *z* axis:

$$F_{sby}x_s + F_y x_f + T_z = 0 \tag{46}$$

Thus equations can be derived for obtaining the three measured fin loads F_x, F_y and T_z from the rig forces F_0, F_1 and F_2:

$$F_x = \frac{(F_{saz} + F_{sbz})y_s}{z_f} = \frac{(F_0 + \frac{F_1 + F_2}{\sqrt{2}})y_s}{z_f} \tag{47}$$

$$F_y = \frac{(F_{sbz} - F_{saz})y_s}{z_f} = \frac{(\frac{F_1 + F_2}{\sqrt{2}} - F_0)y_s}{z_f} \tag{48}$$

$$T_z = -F_{sby}x_s - F_y x_f = \frac{F_2 - F_1}{\sqrt{2}}x_s - F_y x_f \tag{49}$$

The implementation of these equations in the PureBasic test rig control program is shown in Appendix G.

4.4.3 Data Acquisition Equipment

The FSS1500 force sensors were connected to a set of instrumentation amplifiers, which provided them with an appropriate excitation voltage, and conditioned the output signals. The amplified analogue signals were then sent to Measurement Computing[6] PMD-1208FS Personal Measurement Device, which was in turn connected via a UBS cable to a computer. The PMD's functions could be called from LabVIEW, PureBasic, and most other modern programming languages. As well as eight channels of analogue to digital input, it has two analogue and 16 digital outputs. It is capable of sampling a single channel at up to 50,000 samples per second, up to a maximum throughput of 150,000 samples per second.

[6] www.measurementcomputing.com

4.4.4 Rig Calibration Experiments

The force sensors on the rig were calibrated by measuring their amplified outputs with the A-D equipment under no load, then loading them to their design maximum and taking another set of readings. This provided a zero offset value and a scaling value for each of the sensors, which was recorded and used in subsequent tests to convert the raw data from the equipment to meaningful force measurements. Calibration points were marked on the rig, from which known weights could be hung, to enable testing of the rig's accuracy, and to facilitate recalibration if necessary, using the method described in Section 4.4.2.3 (page 87).

4.4.4.1 Noise experiments

After the individual sensors had been calibrated to provide accurate readings, it was necessary to test the rig's ability to measure the forces and torques produced at the fin. The sensitivity of the rig was not in question, as its geometry was carefully calculated, and the selection of the force sensors made with this purpose in mind. However, the rig's ability to measure accurately the conditions at the fin whilst rejecting noise from the fin actuator mechanism needed to be tested.

At this stage in the rig's development, the fin actuator was a scotch yoke mechanism, as described in Section 4.3.3 (page 73). Experiments were performed in which data was recorded from the rig as it ran at a range of frequencies, with no fin attached. As expected, noise was measured on the force readings, a sample of which is shown below. The following graph is for an oscillation frequency of 2.5 Hz, at an amplitude of 40° (80° peak-to-peak). The high amplitude was deliberately chosen to generate high levels of noise with which to test the noise reduction technique.

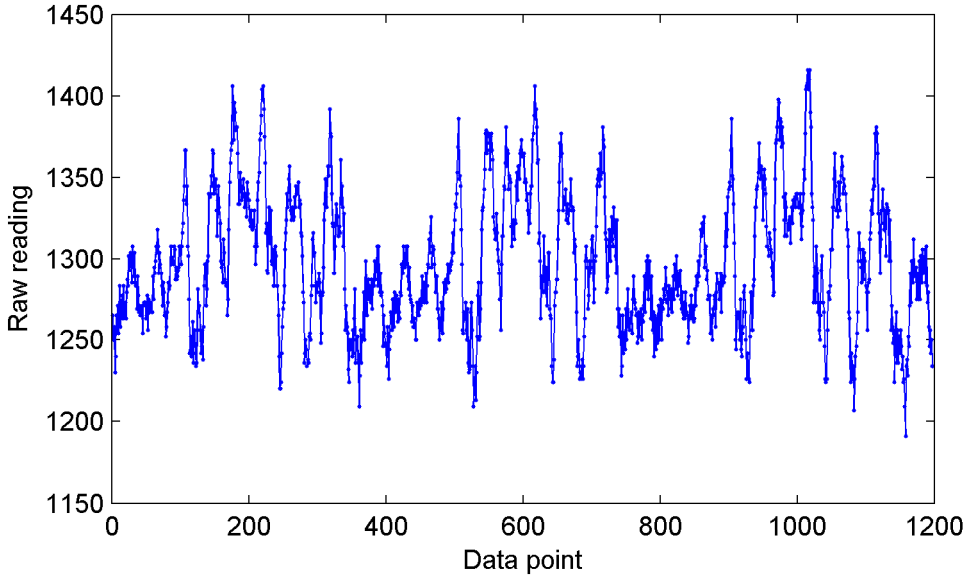

Figure 61: Noise reading from three oscillation cycles of the test rig.

Figure 61 shows the noise output from sensor F_0 for three cycles of the fin oscillation mechanism. It is possible to distinguish three similar cycles in the noise output, suggesting the noise was not entirely random, but in part caused by the movement of the fin mechanism itself. By superimposing noise readings from a number of consecutive cycles over each other, it is possible to see both a random and a repeating element to the noise (Figure 62):

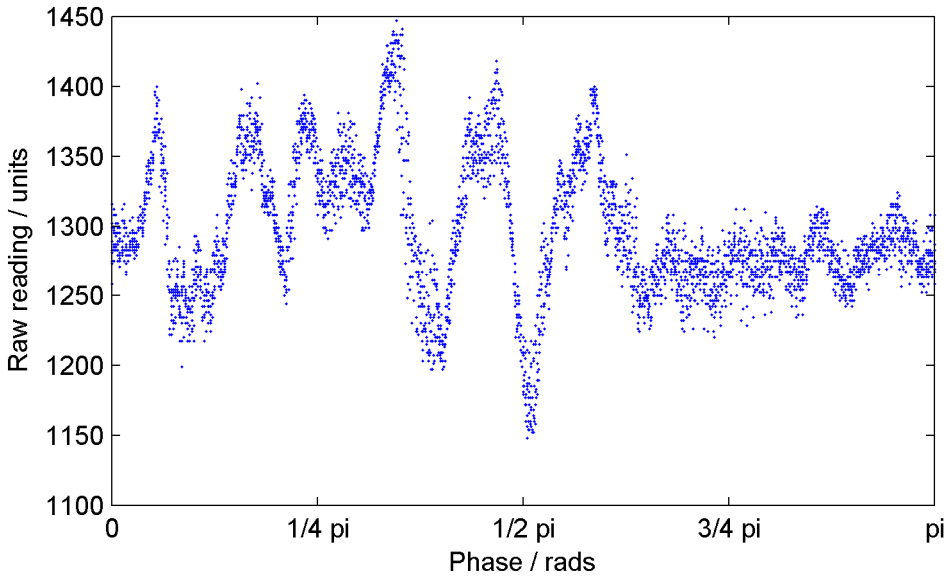

Figure 62: Superimposed noise readings from several cycles of the test rig.

Noise that repeats predictably on every cycle of the fin oscillator could be cancelled by subtracting the repeating noise pattern from all subsequent readings. Random noise produces a steady average over a large enough number of cycles, and so could also be cancelled. Figure

63 shows the result of this noise cancelling process. A sample of 100 cycles of the fin mechanism was recorded, and the raw data divided into cycles and plotted as a point cloud on the graph. The readings were combined using a moving average method; the resulting noise profile consisted of 200 points, each of which was an average of the data points closest to it. This is shown as a solid line shown on the graph. Next, a separate dataset of 20 cycles of the mechanism was recorded to simulate a fin test. The averaged readings from this data set are shown as a dashed line on the graph. The result of subtracting the 20 cycle from the 100 cycle dataset is shown on the lower of the two graphs. Ideally, this would be a flat line at zero, because no loading was applied to the fin axle for either of the reading sets.

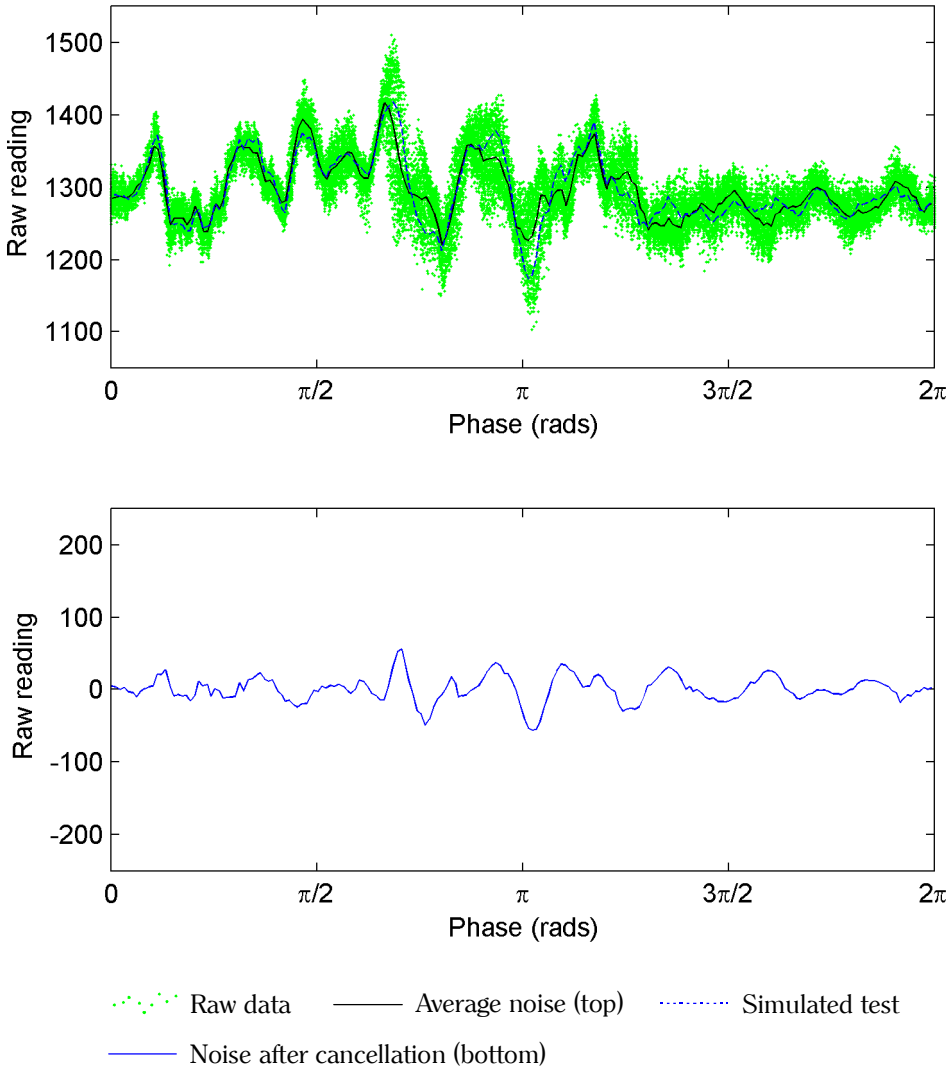

Figure 63: Noise cancelling results, showing noise calibration data (top) and simulated test result (bottom).

The method achieved a reduction of around 60% in peak-to-peak noise. This was less effective than had been hoped, as it still left a noise level comparable to the expected signal, making it

difficult to form conclusions about fin behaviour from the recorded outputs. The disappointing performance of the noise reduction method was due to the nature of the noise coming from the rig. Both cyclic noise and purely random noise would have been cancelled by the process described above, but the noise in question was neither entirely cyclic nor entirely random. It appeared to subtly change in amplitude and phase over a number of fin cycles, meaning the cyclic noise peaks did not line up accurately from one fin cycle to the next. Therefore subtracting one set of cycles from another left new peaks wherever the original peaks were out of alignment.

4.4.4.2 Noise experiments after redesign

It was apparent that using computational noise reduction alone could not produce clean data from the test rig design; further mechanical improvements would be necessary. First, the scotch yoke mechanism was lowered to bring it closer to the height of the force sensors. This reduced the amplification of the forces it generated by reducing the effective lever arm distance between the mechanism and the rig's pivot point. Loose components were fixed securely to the rig, play in the mechanism was reduced as much as possible, and all the moving parts were greased to reduce friction. These improvements reduced the noise by approximately 50%, but, even in conjunction with post-experiment noise reduction, this was not enough to make the rig sensitive to the subtle changes in force produced by an oscillating fin.

As part of a major design overhaul, the scotch yoke mechanism was removed from the rig and replaced with a servomotor system as described in Section 4.3.5 (page 75). A test was performed near the maximum frequency and amplitude that the rig could reproduce. The graph in Figure 64 shows the improvement in noise level in comparison to Figure 63. Note that the scale is increased approximately tenfold in the *y*-axis to make the readings visible.

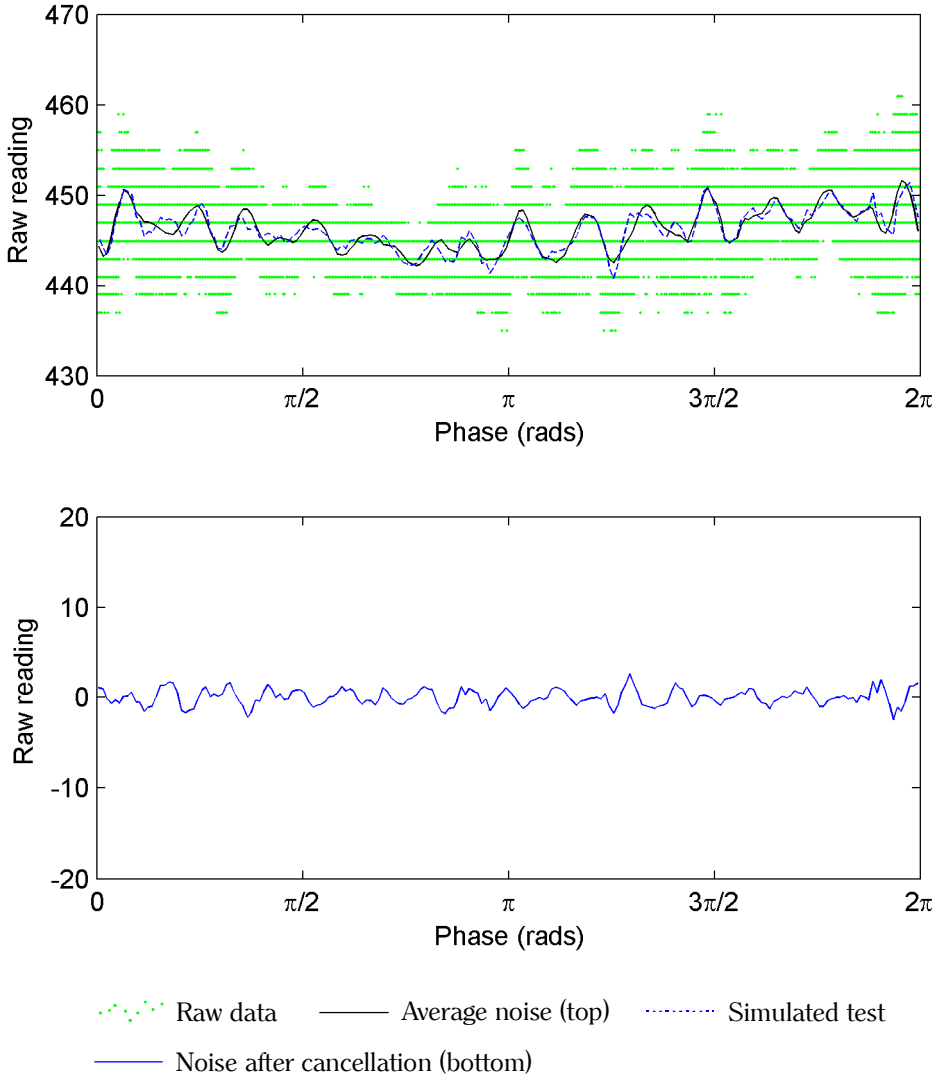

Figure 64: Noise cancelling results after rig redesign, showing noise calibration data (top) and simulated test result (bottom).

The spread of raw readings in the upper graph shows the servomotor mechanism produces significantly less noise than the scotch yoke mechanism; around 8% of the level measured before. The raw data appears in horizontal stripes because the noise is sufficiently low in magnitude that the resolution of the A-D converter is visible. After noise reduction has been performed, peak-to-peak noise of around 4 units is visible, in the lower graph. Upgrading to the servo fin drive caused a dramatic improvement in signal noise over the scotch yoke

mechanism, ensuring that any noise remaining in the signal could be cancelled by averaging several fin cycles together.

4.4.4.3 Experimental accuracy

In experiments, noise at the level shown above equates to an error of up to 0.04 N at the force sensors, which, using the rig geometry used for the experiments in the following chapters, implies a worst-case error in instantaneous force measurement of 0.06 N at the fin. It is important to note, however, that the noise over several cycle averages to zero, so the mean thrust readings will be unaffected by this type of signal noise.

4.4.4.4 Servo signal latency

Servo signal latency was another aspect of the rig that required calibration. Sending signals from the control software to the servo controller via a serial connection incurred a time delay. Since the delay was consistent between experiments, it could be accounted for in software. The easiest way to calculate the latency was to make the rig follow a square wave and to monitor the output angle and measure the delay. Figure 65 shows the latency to be 65 ms.

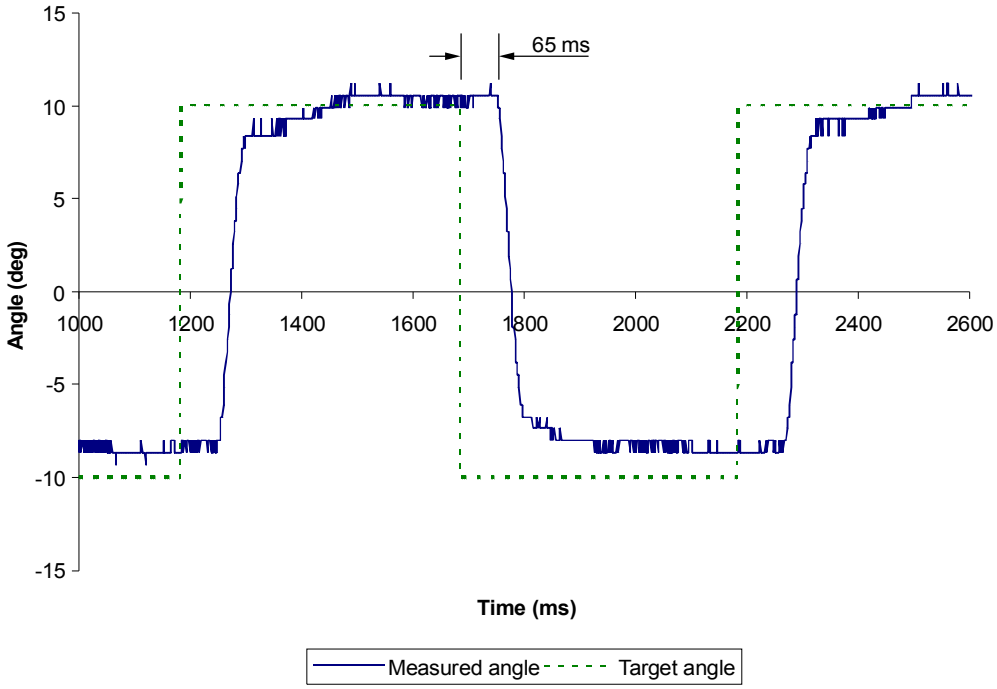

Figure 65: Servo signal latency.

The servo control loop ran independently within the rig control software as a high-priority thread, and used timing data from the PMD-1208FS to ensure the motion control and data acquisition parts of the software operated in synchrony.

4.4.4.5 Fin orientation

The geometry of the rig was adjustable several ways, to allow changes to be made to its sensitivity, as described in Section 4.4.2.1. Its design allowed greater extension in the *x* direction than the *y* direction. In the first round of fin tests; those described in Chapter Five; the fin under test was orientated with its chord parallel to the *x* axis. The experiments were successful, and all forces generated were within the measurement range of the sensors. The following round of experiments, documented in Chapter Six, generated higher forces. Early trials of these tests caused the rig to overload, and fail to collect a complete dataset for some of the fins. An example of a failed experiment set is shown in Figure 66, where many of the high thrust-producing tests have been aborted automatically due to excessive force generation.

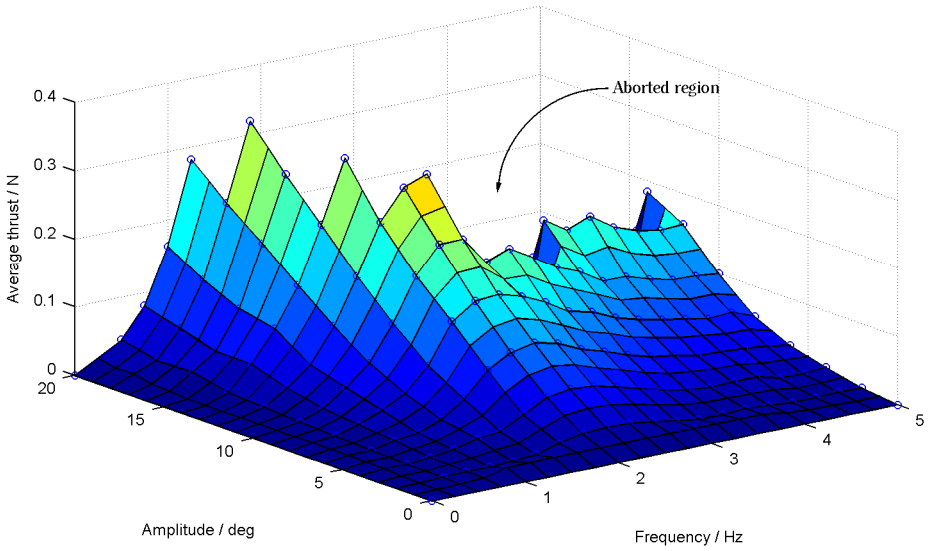

Figure 66: Example of an incomplete dataset due to rig overloading.

Modifying the rig geometry so that the distance between the bearings was at its maximum was not enough to keep the forces within the allowable limits. However, since the lateral forces generated by fins are generally larger than the thrust, turning the fin through 90°, parallel to the *y* axis, meant the largest forces were creating a torque about the *y* axis instead of the *x* axis, such that increasing the length of the rig in the *x* direction reduced the forces at the sensors to an acceptable level.

To test the effect of rotating the fin on the results, two experiment sets were carried out, identical in every respect except the orientation of the fin. The fin was parallel to the *y* axis in both experiments, facing in the *y* direction for one, and the -*y* direction for the other Figure 67.

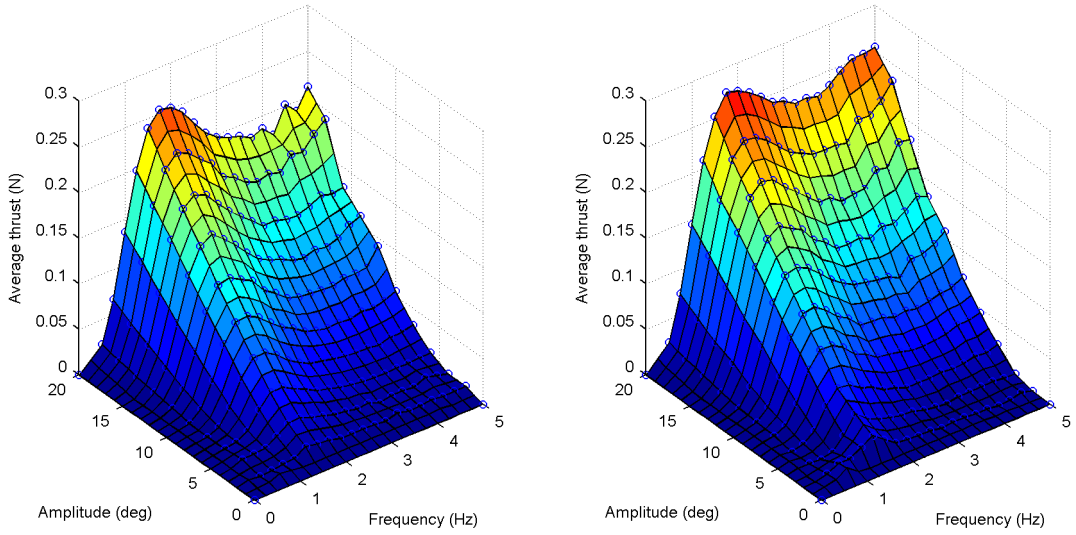

Figure 67: Difference caused by change in fin orientation, parallel to y axis (left), and -y (right).

Disappointingly, the experiments revealed a difference between the two fin orientations. Figure 68 shows the difference between readings in the two experiments as a percentage of the range being measured. Most of the tests in each experiment exhibit a difference of less than 12%. The tests with the largest discrepancies (12-26%) are those in the high amplitude, high frequency region. In these tests, repeatability is impaired by the servo operating close to its performance limits, and being less able to follow a waveform to the same accuracy as in the lower frequency and amplitude experiments.

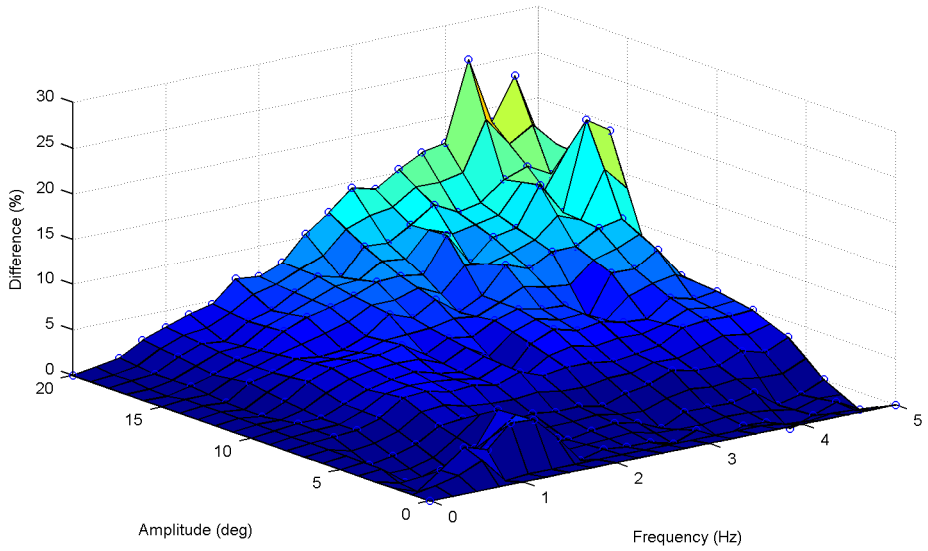

Figure 68: Difference between orientation experiments as a percentage of maximum reading.

A possible reason for the discrepancy was the indirect way in which the forces were measured. Since it was not possible to directly measure the forces being generated by the fins, forces had to be derived from other variables (see Section 4.4.2.4, page 82). Thrust, for example, depended on measurements from all three force sensors, the dimensions of the rig, and the positions of the fin and force sensors all being accurately known. Orientating the fin in the opposite direction meant these variables were combined in a different way, such that deviation in any of the variables could introduce an error. Another source of asymmetry in the readings could have been the alignment of the two opposing force sensors (Figure 56, page 78); if they were not located correctly, at 45° to the horizontal, the vertical force applied to them would not have been divided equally between them, and an asymmetrical response to loading would result.

The difference in sensitivity brought about by changing the orientation of the fin was inherent to the rig's design, and would have been difficult to fix without a major revision. Since the rig was capable of gathering consistent readings for any one fin orientation, the best response to the problems described here was to ensure the rig was correctly calibrated, and use it in one orientation only. To maintain a high level of consistence and accuracy, all of the results included in this thesis for comparison with each other were obtained in this way.

4.4.4.6 Calibration between experiments

The test rig's force sensors were affected by gradual zero drift. Over the course of a single experiment its effect was negligible, but when running a set of many experiments over several hours, the effects became significant and had to be mitigated. The solution was to add a routine to the rig control software which took 10 seconds' worth of samples before each experiment, while the rig was at rest. The average of these readings was then taken as a zero point for the experiment. Figure 69 shows the zero drift over a set of experiments lasting approximately 6 hours. Individual experiments in this set took between 3 and 30 seconds, depending on the frequency of oscillation.

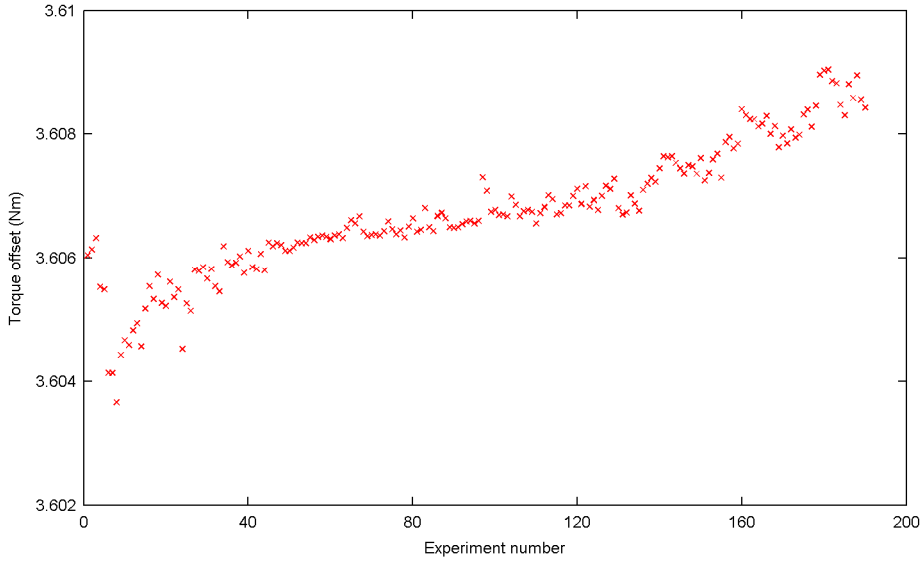

Figure 69: Zero drift over a large number of experiments.

As a proportion of the total range of the readings, the error was small, no more than 0.2 %. However, it was important to account for, because some of the average thrust readings were also very small, and so their accuracy would be affected by the error to an unacceptable extent.

4.5 Test Rig Software

The software used to gather data and control the rig was written in PureBasic. It performed several functions, which are described below.

4.5.1 Motion Control

4.5.1.1 Asymmetry

The rig software communicated with the servo controller via a serial connection, and reproduced waveforms at different frequencies and amplitudes. Square, triangle, and sine wave functions were programmed, but any waveforms that could be defined mathematically as a function of the phase angle were reproducible. An asymmetry factor was built into the program; it was a floating-point value between 0 and 1, which adjusted the portion of time spent in the first and second halves of the waveform. An asymmetry value of 0.5 resulted in a symmetrical wave. Figure 70 shows a sine wave adjusted with an asymmetry factor of 0.25. It therefore spends 25% of the cycle time travelling in one direction, and 75% in the other.

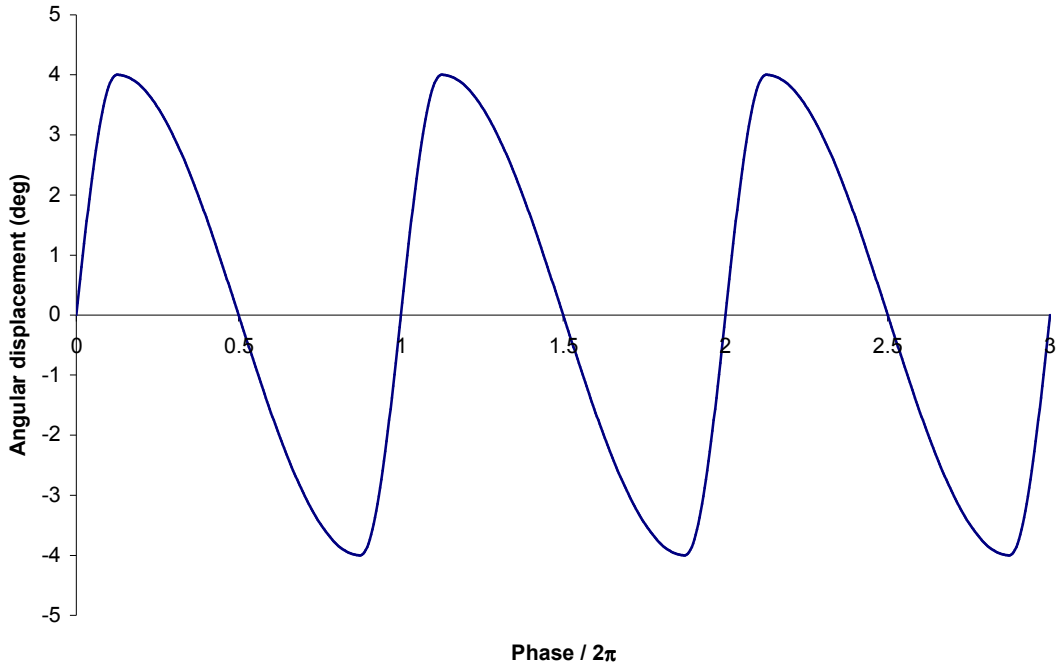

Figure 70: Asymmetrical sine wave.

4.5.1.2 Ramp time

When a pitching fin starts to oscillate, it accelerates in a short time, pushing hard against the stationary water surrounding it. The resulting peak of thrust or lateral force is often much higher than the steady-state value after a number of cycles have taken place, and a more consistent flow pattern is established. For this reason, a 'ramp' facility was added to the control software, allowing the wave to start with an amplitude of zero, and increase to a target amplitude over a number of cycles. This allowed higher final amplitudes to be reached without overloading the force sensors during start-up. Figure 71 shows a sine wave actuation profile with a ramp of three cycles.

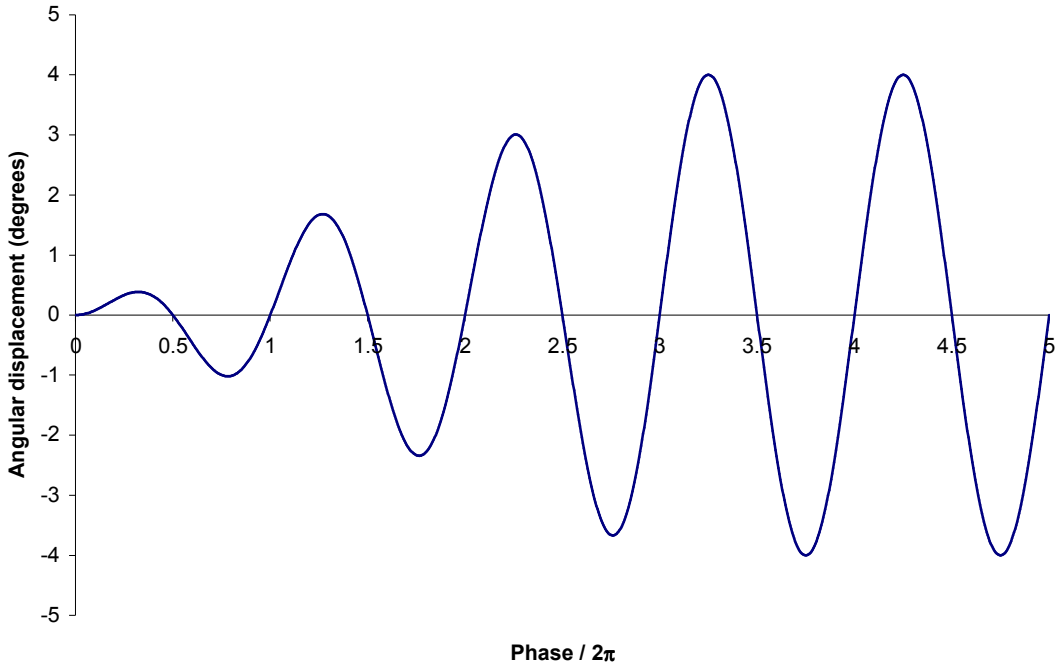

Figure 71: Ramped start-up example.

4.5.2 Data Acquisition

Another important function of the test rig control software was to receive the readings from the rig's sensors, interpret them, and record them to files. The data acquisition device (Measurement Computing PMD-1208FS, described in Section 4.4.3, page 83) was set to read 1000 samples per second from each of the data channels into a memory buffer large enough to store two seconds' worth of samples. This buffer was read by the program approximately every 100 ms, ensuring a continuous stream of data, and the raw data was then processed by the software. Firstly the forces on each sensor were calculated using the calibration factors derived from earlier experiments. These sensor forces were then converted to forces in the x and z directions at the force sensor locations. Then the torque on the rig about the three axes was calculated, and the forces and torque at the fin derived from them.

Each set of samples was recorded with a time stamp from the data acquisition device's internal clock, and a phase angle, which represented a position in time along the target waveform. In later experiments the rig was upgraded to accommodate a potentiometer connected to the axle (Section 6.2.2.1, page 124). This detected the fin's position, and the acquisition software applied a scaling factor to convert the raw reading converted to a position in degrees.

For every new fin test, a CSV (comma separated variable) file was created, with a header containing all the details of the test. The information shown in Table 4 was recorded in the header of each file.

Variable	Description
`Date`	Time and date that the experiment was carried out
`FileVersion`	File version number, allows analysis software to read the file in the correct way
`Tx, Ty, Tz`	Torque readings while the rig is at rest, for *x*, *y*, and z axes (Nm)
`Angle`	Zero angle reading (degrees)
`XSensor, YSensor`	*x* and y positions of force sensors, allowing for variable rig geometry (m)
`XFin, ZFin`	*x* and *z* positions of fin, allowing for changes to rig geometry and axle length (m)
`FinDirection`	Direction of the fin at rest (rads)
`Waveform`	Number representing sine, triangle or square wave
`WaveCenter`	Wave centre location from 0 - 1, allowing asymmetrical waves
`RampCycles`	Number of ramp cycles before full amplitude is reached
`Experiment`	Y/N value, identifying dataset as part of an experiment series, or a one-off test.
`FinCycles`	Number of fin cycles in experiment
`Frequency`	Oscillation frequency (Hz)
`Amplitude`	Oscillation amplitude (degrees)

Table 4: File header variables.

Table 5 shows the data columns contained within the main body of the CSV file.

Variable	Description
`Time`	Time from start of test (ms)
`Channel0 - Channel3`	Raw integer readings from A-D channels
`F0, F1, F2`	Force readings from sensors (N)
`Angle`	Angle reading from potentiometer (degrees)
`Tx, Ty, Tz`	Torque readings about rig axes (Nm)
`Phase`	Oscillation phase angle / 2π
`TargetAngle`	Target fin angle (degrees)
`Thrust, Lateral`	Force readings at fin (N)
`Torque`	Torque readings at fin (Nm)

Table 5: CSV data file columns.

Part of an example CSV data file can be found in Appendix H.

As well as the data file, the software produces a log file, in which each line summarises a single oscillation of the fin, with each of the variables shown in Table 6:

Variable	Description
`FileNumber`	Number of corresponding CSV data file
`Frequency`	Oscillation frequency (Hz)
`Amplitude`	Oscillation amplitude (degrees)
`Cycle`	Number of fin cycle
`TxAvg, TyAvg, TzAvg`	Average torque readings about rig axes (Nm)
`TxRMS, TyRMS, TzRMS`	RMS torque readings about rig axes (Nm)
`OK`	Records if error condition has been triggered by force over/under-load during test

Table 6: Log file columns.

4.5.3 Automation

Large numbers of individual fin tests are required to build up a profile of a fin's performance. The test rig control software allowed the user to specify any number of tests to be carried out sequentially, with programmable delays between each one. Each test can be defined by the parameters shown in Table 7.

Variable	Description
`Command`	Command type: Zero sensors, wait, or perform a test
`SaveFileName`	Filename to identify experiment set
`Frequency`	Oscillation frequency (Hz)
`Amplitude`	Oscillation amplitude (degrees)
`Oscillations`	Number of oscillations in this test
`Waveform`	Number representing sine, triangle or square wave
`WaveCenter`	Wave centre location from 0 - 1, allowing asymmetrical waves
`RampCycles`	Number of ramp cycles before full amplitude is reached
`Wait`	Length of pause to be used between experiments (s)

Table 7: Command list parameters.

4.5.4 Rig Protection

It was important to keep loading on the force sensors within their specified measurement range of 0 - 14.7 N. The sensors' accuracy could only be relied upon when they were being used within their design parameters, and damage to the force sensors could result from

extreme overloading. The sensors were able to withstand to ten times their upper limit, but if the rig were to rise off the force sensors and drop back onto them from a height of more than a few millimetres, the spike in force resulting from its rapid deceleration could easily have exceeded this limit. Therefore protecting the sensors from under-loading was equally important.

The control software continually monitored the forces being applied to the sensors, even between fin tests. If any sensor detected a potentially dangerous over or under-load, for example while making adjustments to the rig, an audible alarm was sounded to warn the user to take extra care. If the alarm occurred during the course of an experiment, for example by using a high amplitude setting with a stiff fin, the experiment was automatically aborted. The fin was gently returned to its centre location by the control software, and an 'error' tag was appended to the CSV data file and the experiment log, so that the problematic test would not be processed by the analysis software. The test rig software then continued with the remaining experiments in the set.

4.6 Test Environment

4.6.1 Water Tank

Investigating the performance of flexible fins required a method of operating fins in water, under known conditions. The tank used for the experiments in Chapter Five and Chapter Six of this thesis measured 2 x 1.5 m in area, and 1.5 m in depth. The test equipment was suspended above the water from two U section aluminium bars, below which a frame was constructed from Dexion[7] bars to support the force measurement rig, shown in Figure 72. The Dexion frame was triangulated in order to provide a very stiff platform from which to measure the forces generated by the fin.

[7] www.dexion.com

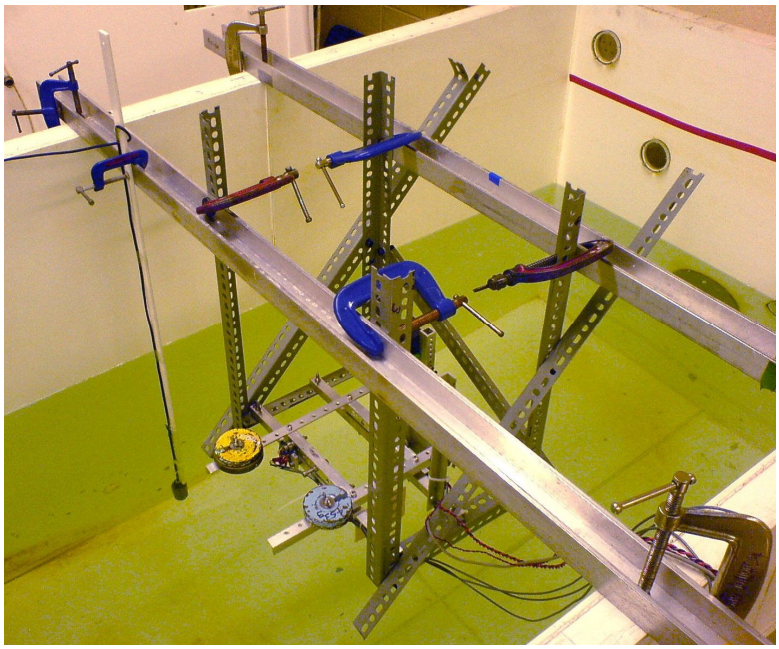

Figure 72: Structure supporting test equipment over tank.

A large tank was selected so that edge effects would have a negligible influence on the performance of the fin, and that fin large-scale currents would not become established over the course of a fin test. Currents would have the effect of reducing the thrust generated by the fin, since it would no longer be operating in a bollard state, but in flowing water. The tank's natural period of oscillation was slow, at around 1.7 seconds, and the volume of water sufficiently large that the disturbance caused by each individual fin test was barely visible after a period of 30 seconds. The energy imparted by single fin tests caused only localised disturbance to the water, but in order to avoid the possibility of multiple experiments constructively adding to a standing wave, a delay was observed between consecutive fin tests, and is discussed further in Section 4.7.2 (page 104).

4.6.2 Static vs. Flow Testing

Most of the investigations summarised in Chapter Two were performed under flow conditions. In order to fully examine the performance of a fin, it is important to perform tests at a range of flow velocities. A fin's thrust and efficiency are highly dependent on the interactions between vortices that are shed from its leading and trailing edges, and in turn these are affected by the speed at which water flows past the fin.

Many previous studies have focussed on the role of Strouhal number in determining performance and efficiency, and this is a term that is only applicable to fins with non-zero forward velocity. Some studies aim to test fins or other oscillating devices under conditions analogous to self-propelled free swimming. In these cases, the flow velocity is adjusted to create a steady state in which no net thrust is being generated, because the thrust and drag are balanced.

Measurements are then carried out at this velocity. While this method offers a close approximation to free swimming, it is not entirely equivalent, since the imposed velocity is constant, whilst the velocity of the body under natural conditions may not be.

Efficiency is another term that loses some of its meaning when forward velocity is zero, because useful energy out requires a force and a distance moved. There are other methods of quantifying effectiveness at converting energy to thrust; for example, bollard efficiency and thrust-to-power ratio (see Section 2.2.3, page 25).

Useful information can, however, be gained from tests under static, or 'hover' conditions, and there are several reasons why static water has been used in the experiments in this thesis. The starting point for this investigation was a finned robot submarine, in which oscillating fin thrusters were used for propulsion and manoeuvring. In the case of a fin being used to propel a larger object through water, the object's drag and inertia works against the thrust generated by the fin, so that it will never reach, or even come close to a 'free swimming' state. Instead, it will spend most of its time operating closer to a 'bollard' state; providing thrust to manoeuvre the submarine by pushing against stationary or slow-moving water. The generation of thrust for low-speed manoeuvring was the type of performance of most value on the Bathymysis project, and receives less coverage in existing literature than the performance of flexible fins under flow conditions.

For this reason, optimising fin design to achieve the greatest static thrust from a given fin size for the least energy seemed an appropriate course of action for this thesis. This decision reduced the number of variables affecting the fins' performance, whilst keeping the study relevant to its original inspiration; the development of oscillating fin propulsors for a small undersea vehicle.

Neglecting flowing water tests is of course, at the expense of being able to fully characterise a fin's behaviour over a full range of flow conditions, but while such investigations are beyond the scope of this thesis, they are discussed in Chapter Seven, 'Summary of Conclusions and Future Work'.

4.7 Experimental Procedures

4.7.1 Number of Cycles

There is always some variation in the production of forces between consecutive fin cycles in a single test. To gain an understanding of the performance of a fin under a given set of conditions, it is necessary to take an average reading from a number of fin cycles. The more cycles are recorded, the more the effect of anomalous readings can be reduced. There are, however,

drawbacks to conducting fin tests over a large number of cycles in static water, so the number of cycles to include in the data analysis is a compromise accounting for several factors.

4.7.1.1 Ramp time

Ramp time is described in Section 4.5.1.2, (page 94). A ramp time of three cycles was found experimentally to be long enough for all of the fins to reach their maximum amplitude at maximum frequency without overloading the force sensors. A further buffer of two cycles was added after maximum amplitude had been reached, to account for any residual effects of the ramp cycles on the movement of the fin, for example in the propagation of waves down the fin body, which never exceeded more than two wavelengths under any of the experimental conditions. For these reasons, the force data from the first five cycles of each fin test were ignored.

4.7.1.2 Repeatability of results

Figure 73 illustrates the effects of changing the number of fin cycles included in each test. The graphs show data from a full set of tests on a NACA 0012 fin in stationary water. They are analysed with slightly different criteria; graph a) only shows thrust data from a single oscillation in each test. While the underlying trend of the data is visible, there is significant scatter in the results. Graph b) shows the same set of tests analysed over 5 cycles of the fin, reducing the scatter significantly. The final graph c) shows the data averaged over 10 cycles of each test, reducing the scatter still further.

a)

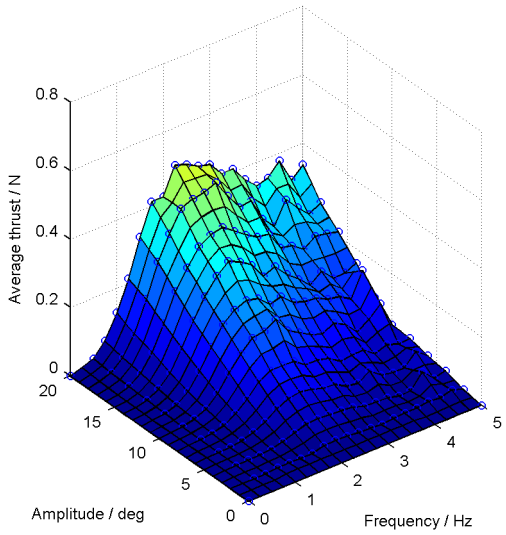

b)

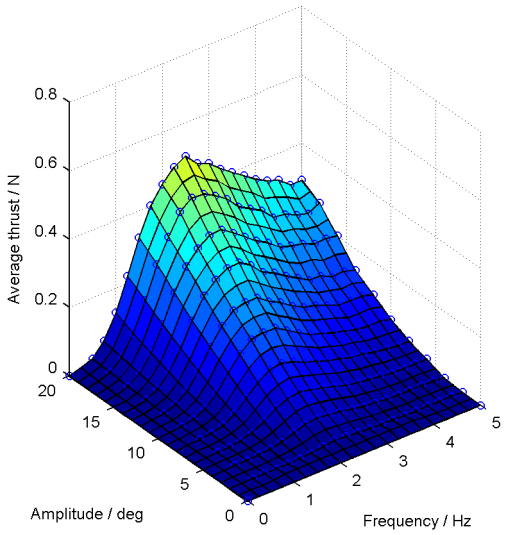

c)

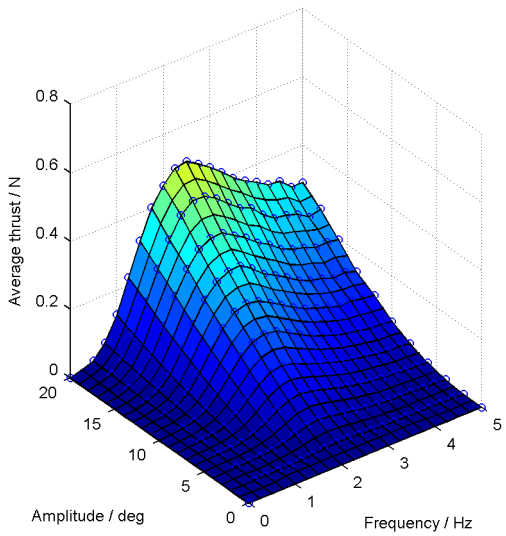

Figure 73: Comparing results gathered from a) a single oscillation, b) 5 fin cycles c) 10 cycles.

Further analysis of groups of test data was carried out, to ascertain the optimal number of fin cycles to measure. The mean thrust readings from a single fin cycle differed from those taken over 10 cycles with an average deviation of 31%. The largest deviations occurred in the fin tests producing the lowest thrust. The average error in thrust for all tests was 0.009 N. A similar calculation on thrust readings averaged over 5 cycles showed a deviation of 3% when compared to the 10 cycle results; a difference in thrust of 0.002 N. The difference in mean deviation between tests of 10 cycles and more was found to be negligible.

4.7.1.3 Large-scale currents

Since an oscillating fin imparts momentum to the surrounding fluid, large-scale currents can build up over time. Water flows past the fin, around the edges of the tank, and back to the front of the fin. The movement of water means the test is no longer being carried out in a bollard condition, but in a state of unknown flow velocity. In a finite tank, it is impossible to eliminate large scale currents from tests altogether, but if allowed to develop to a significant level, the induced flow can influence results to an unacceptable extent. The effects of large-scale currents on the measurements taken in the following chapters were mitigated in the following ways:

- The tank in which the experiments were performed was at least an order of magnitude greater than the size of the fin in every dimension. The large volume of water minimised the effect of the moving fin.
- Individual fin tests were kept as short as possible; enough cycles were recorded to provide reliable and repeatable data, but no more.
- Residual currents, which were of the order of millimetres per second, were given time to dissipate before the next fin test began, so that the influence of consecutive tests would not be combined, and allow flow to build up over a sequence of tests.

4.7.1.4 Framing the fin tests

Figure 74 shows the constraints on choosing a safe timeframe for fin tests. The first five fin cycles are ignored because of the effects of ramping the fin's amplitude, and the number of cycles in the test is selected bearing in mind the consequences of both too many, and too few fin cycles being used.

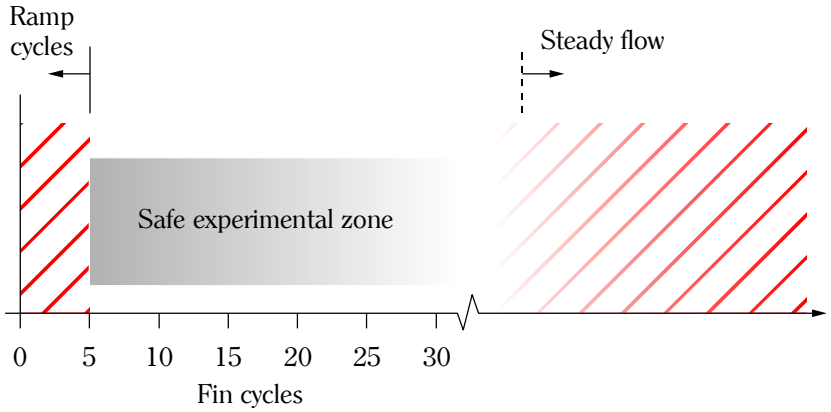

Figure 74: Safe experimental zone

The experiments in Chapter Five used a sample size of 15 cycles, but this was reduced to 10 cycles in the second round of experiments, after it was shown that the change could be made with a no discernible effect on the clarity of the data.

4.7.2 Delay Between Experiments

Each automated test sequence included delays of 90 seconds between consecutive fin tests, to allow vortices introduced to the tank to dissipate to a level where their effect was not felt during the next fin test. It also prevented the energy imparted from multiple tests building up and causing large-scale currents or standing waves in the tank. The figure of 90 seconds was chosen as a compromise, to include a large enough safety factor to ensure no disturbance remained in the water, yet not so long as to make long successions of fin tests impractical.

4.8 Data Analysis

After a set of data had been gathered from the test rig, further processing was still required. The next stage of the analysis used a set of MATLAB programs to interpret the data files. Their roles are discussed in this section.

4.8.1 Summarising Data

The test rig produced a data file containing thousands of samples for each individual fin test, so a very large quantity of data was produced in each experiment set. To speed up the process of analysing the data, each new dataset was processed in a MATLAB program after it was obtained from the rig. The program summarised the data and saved key values and averages to a smaller file, which could then be used to plot graphs and conduct further analysis, without having to refer to the unwieldy original dataset.

The program's first task was to recalculate all of the measured variables from the raw data stored in the file. Although the data-gathering software performed these calculations while experiments were taking place, the ability to regenerate the same results post-experiment allowed different analysis methods to be tried without having to run sets of experiments again. Access to the raw data proved very useful when a bug was discovered in the data-gathering software, which caused small errors in the force calculations. It allowed old data to be recalculated correctly after the experiments had taken place.

After recalculating the variables, the MATLAB program analysed a number of complete fin cycles from each experiment. The 'ramp' cycles, where the fin amplitude was being gradually increased, could be eliminated at this stage, so that the cropped datasets represented the fins' performance in a steady state.

Average readings were then taken for a number of variables in the dataset. The list of data recorded in each summary file is shown in Table 8.

Variable	Description
Frequency	Oscillation frequency.
Target amplitude	Nominal oscillation amplitude.
Actual amplitude	Actual oscillation amplitude, based on measured angular displacement.
Mean thrust	Mean force in the direction of the fin's centre of oscillation.
Mean absolute lateral force	Mean absolute force perpendicular to the thrust axis. Absolute values are used because a mean value of approximately zero would be expected for all symmetrical fins.
Power	Mean power applied to the fin, calculated from the change in measured angle and the instantaneous torque.
Virtual power	Power calculated using the target angle rather than the measured angle, for comparison with the other power variable.
Thrust / power ratio	Mean thrust per unit power.
Mean direction of thrust	Mean angle at which thrust is generated; usually similar direction of the centre of oscillation, but tends to deviate from this at low frequencies and amplitudes.
Total mean force	Mean force in the direction of mean thrust.
Mean angle deviation	Mean deviation of the measured angle from the target angle.
Torque offsets	Offsets applied to the torque readings when rig is zeroed at the start of each individual test. Interesting for measuring sensor drift over a series of experiments.

Table 8: Data recorded in results summary files.

Another function of the program was to eliminate bad data. When individual fin tests in a series were aborted due to excessive force, the fin was brought to rest, but data was still recorded for the intended duration of the test. When this happened, the data file was tagged with an error message, so that when the data set was analysed, the flawed file could be skipped. This resulted in a gap in the summary data, but since very few fin tests were aborted due to overloading, and the data are closely spaced, this did not cause any problems.

4.8.2 Plotting Graphs

Another set of programs were created to present the data in graphical form. MATLAB includes a range of tools to visualise data in two and three dimensions.

4.8.2.1 3D surface and contour plots

3D surface plots were used extensively to provide a graphical representation of test data from an entire set of experiments, most commonly for showing the response of different variables to frequency and amplitude. Programs were written to display most of the variables in Table 8 in this way, and are used throughout this thesis. The source data used to create the 3D surface are shown as circular points, in blue where colour is used.

3D graphs provide a striking display of the trends in data, but can lack clarity in situations where individual values need to be discerned. In these cases, contour plots have been included, to show the three-dimensional data in an unambiguous, 2D form.

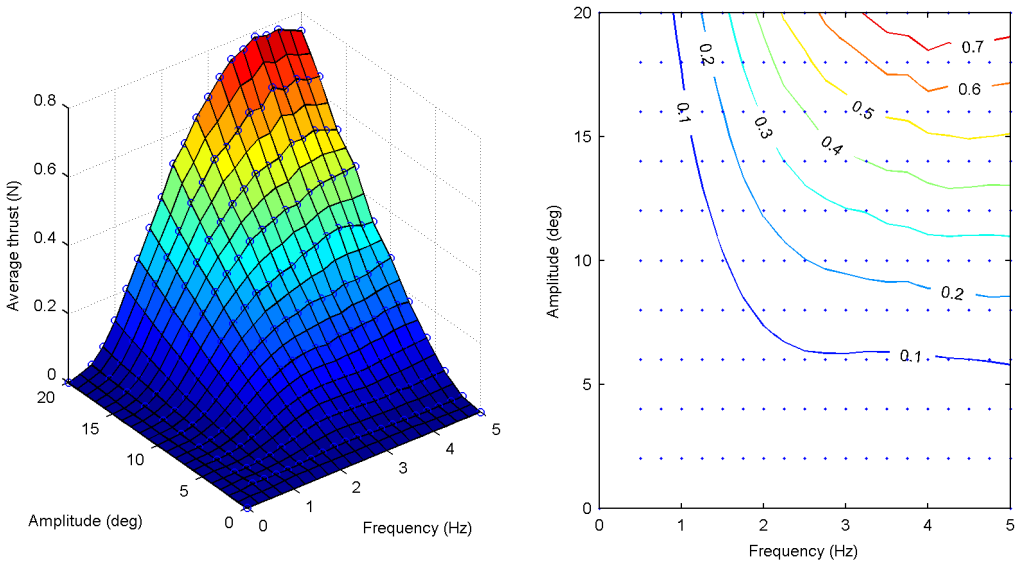

Figure 75: Examples of a surface plot (left) and contour plot (right).

Both of these plotting methods can cope with unevenly spaced data, and when individual data points are missing, for the reasons described in Section 4.8.1 (page 104), a continuous surface or contour space can still be produced, using linear interpolation. Actual data points are displayed as small circles on 3D plots, and as dots on contour plots. This allows the viewer to see where data has been interpolated. Figure 75 shows the same data displayed as a 3D surface and contour plot.

4.8.2.2 Force traces

A different kind of visualisation was necessary to show the force data for individual fin tests at a given frequency and amplitude. The 'force trace' graphs used in this thesis were developed using MATLAB to represent how the forces produced by a fin varied throughout an average cycle. A typical force trace, with its features labelled, is shown in Figure 76. The thin, faint line shows how the instantaneous force generated by the fin varied over a number of cycles. The thick line shows an average force trace over a number of cycles. Black dots along the average force trace occur at regular intervals in time, and give an indication of whether the force is changing rapidly or slowly. Other symbols mark points along the average cycle trace, and are described in the figure. In the cycle start marker, the largest circle denotes the start point, and the diminishing circles indicate the direction of travel.

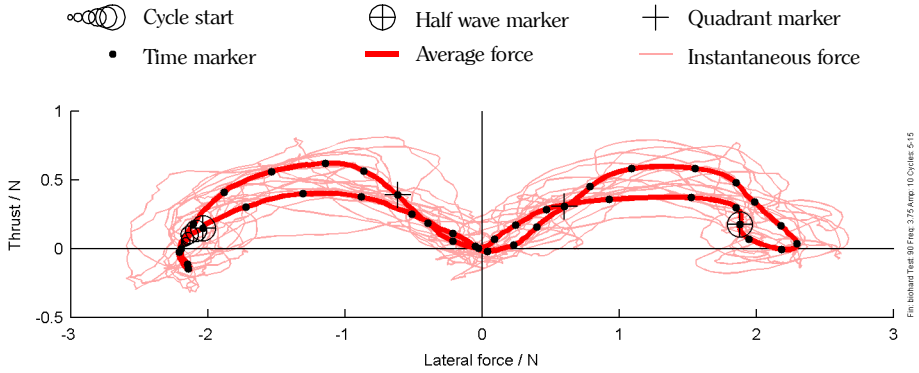

Figure 76: Example of a force trace for a hard compound biomimetic fin, 3.75 Hz, 10° amplitude.

Chapter Five

NACA vs. Biomimetic Fin Experiments

5.1 Introduction

The hypothesis guiding the experiments within this thesis was introduced at the end of Chapter Two. It was arrived at following a review of literature in the field, and identifies an area of research not covered by previous published investigations. The experiments described in this chapter were designed as a first step towards answering the questions posed by the hypothesis.

This was the first complete set of experiments performed with the equipment described in Chapter Four. A standard, aerofoil-shaped fin was tested at a range of frequencies and amplitudes against an alternative biomimetic design.

5.1.1 Selection of Fin Profiles

5.1.1.1 NACA 0012 fin

The NACA 0012 aerofoil was chosen as a benchmark fin profile for the following reasons. Fins of the NACA four-digit family are ubiquitous in studies of aero- and hydrodynamics, and have been for many decades. Several more complex methods of defining aerofoil shapes exist, but are mostly intended for specific applications within the field of aeronautical engineering. Four-digit NACA designations are the simplest, most widely understood framework for aerofoil design. NACA 0012 and NACA 0014 fins were used for all the studies reviewed in Chapter Two, in which an aeronautically-derived fin profile was tested.

As described in Section 2.6 (page 36), foils within the NACA 00xx subset are symmetrical, with the last two digits referring only to the thickness of the foil as a percentage of its chord length. A consequence of this method of definition is that all NACA 00xx fins share a common stiffness profile, multiplied by a scale factor.

The difference in thickness between the NACA 0012 and NACA 0014 foils is 16.7%, which equates to a much larger difference of 58.8% in flexural stiffness. Preliminary tests with the moulding resins to be used in the experiments had revealed the stiffness of the most flexible readily available silicone resin, and therefore the lower limit of fin stiffness that was practical to produce. So as not to limit the stiffness of the resulting fins at too high a value, the

NACA 0012 fin was selected, because it was the thinner, and therefore more flexible of the two foil designs.

5.1.1.2 Biomimetic fin

In order to test the hypothesis proposed at the end of Chapter Two, a biomimetic fin design was required. The aim was not to produce an optimal design for the intended application, but to make a rational selection from the available data, and use it to produce a fin of biomimetic origin, for comparative testing against the NACA fin.

The decision was made to mimic the entire body of a fish rather than a single fin. Although an oscillating propulsor would most likely be deployed as an appendage to a waterborne craft in the same way that fish employ their fins, fish are not analogous to submarines. Many, like the pumpkinseed sunfish, use their pectoral and other ancillary fins for low-speed manoeuvring, but when extra exertion is required, use their caudal fins and entire bodies to generate thrust. The goal of generating thrust with a simple, homogenous flexible fin did not lend itself to mimicry of single fish appendages, which are very intricate in structure, as was seen in the dogfish dissection discussed in Section 3.3 (page 65). Since the fin was to be actuated in a pitching-only mode, a carangiform swimmer seemed a good choice of fish to mimic.

The fin was to be actuated from a rigid axle, the same as the NACA fin, allowing no lateral movement of the leading edge. Therefore it was to move in approximation to a carangiform swimmer, whose head travels almost in a straight line, with undulatory waves propagating down the body, increasing in amplitude toward the tail.

Of the carangiform swimmers, one specific species came to light, which had an accurately measured and complete stiffness profile presented in existing literature (McHenry, *et al.*, 1995). Pumpkinseed sunfish (*Lepomis gibbosus*, shown in Figure 77), are carangiform swimmers, but also employ labriform swimming; that is, swimming using only their pectoral fins. They employ this propulsion method when manoeuvring at low speeds, and do so with considerable efficiency (Jones, *et al.*, 2007).

Figure 77: An adult pumpkinseed sunfish.[8]

The dataset was selected for use in the biomimetic fin design, and used in the experiments described below.

5.2 Methods

5.2.1 Fin Designs

The two fin shapes used in this set of experiments were a standard NACA 0012 aerofoil and a biomimetic fin designed to mimic the flexural stiffness profile of a pumpkinseed sunfish (*Lepomis gibbosus*). The two fins were of similar volume, identical in material, and were made using the CNC mould technique described in Appendix D.4 (page 206). Both had a length and height of 120 mm, since previous work has identified an aspect ratio of 1:1 as being optimal for efficiency (Hobson, *et al.*, 2003). The dataset used for calculating the biomimetic stiffness profile came from a study in which the flexural stiffness (EI) of a pumpkinseed sunfish was measured at points along its chord (McHenry, *et al.*, 1995). Figure 78 shows the dataset from the study in its original form.

[8] Image provided with permission from NYSDEC.

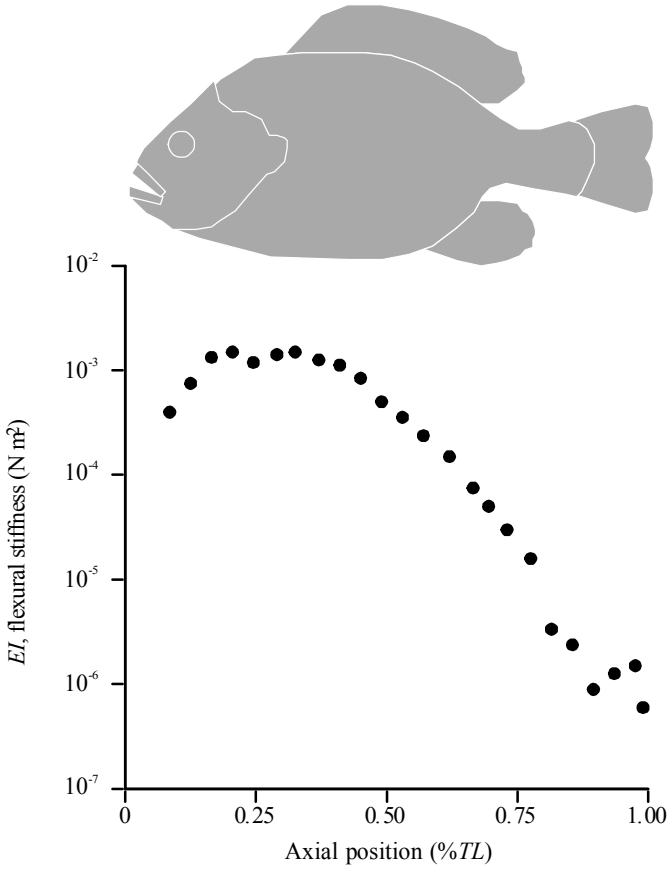

Figure 78: Sunfish stiffness data (McHenry, et al., 1995).

A cubic function was fitted to the logarithm of these stiffness measurements, and used to calculate the thickness profile of the biomimetic fin. The cubic function was as follows:

$$\log(EI) = 9.6598x^3 - 22.006x^2 + 10.192x - 4.1127 \tag{50}$$

Where x is the axial position along the fin, from 0 to 1 (front and rear respectively). E is Young's modulus, a basic property of the moulding resin, measured in Section 3.1 (page 57), and I is the second moment of area, defined for a rectangular cross-section as:

$$I = \frac{bd^3}{12} \tag{51}$$

Where b is breadth, in this case the height of the fin, and d is the fin's depth, or thickness. The fin's thickness was varied along its chord such that its flexural stiffness EI was proportional to that of the sunfish. A factor of 14 was applied to the stiffness data, to make the biomimetic fin's width comparable to that of the NACA fin (i.e. the biomimetic fin was 14 times stiffer than the sunfish).

It is reasonable to assume the front 10% of the sunfish is not optimised for locomotion to the same degree as the rest of its body, as there are many other structural and functional demands on the fish's head that must take precedence. The priority in mimicking the stiffness of

the sunfish was to create a good approximation in the biomimetic fin in the region behind the axle, which actuates the fin from the 0.1 chord point.

Stiffness data was absent from McHenry's paper for the anterior (front) portion of the fish, up to the 0.1 chord point, so the profile in this section was extrapolated from the existing data using the cubic function described above. However, the extrapolated data left sharp corners at the fin's leading edge, forming an unnatural shape, likely to introduce unnatural turbulence into the flow over the rest of the fin (see Figure 79). Since sunfish do not have a 'leading edge' to mimic, at this point the sunfish analogy could be carried no further. For the purposes of the fin mould, it seemed appropriate to depart from the extrapolated data between the 0 and 0.025 chord points, and to round the corners to create a more natural profile. This also facilitated the CNC machining and moulding processes. A radius of 3 mm was chosen as a compromise between leaving unnaturally sharp corners at the leading edge, and straying too far from the extrapolated data being used to construct the fin.

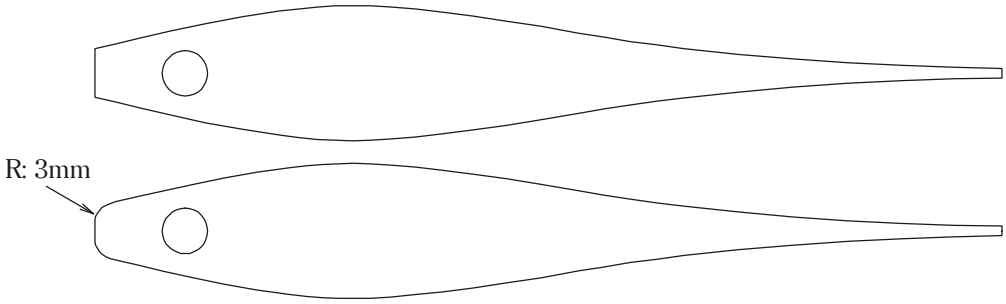

Figure 79: Biomimetic fin profile before (top) and after (bottom) smoothing.

Although the aim of the exercise was to mimic the body stiffness profile, and not the shape of the sunfish, the sunfish data produced a more fish-like shape, thicker around the midsection and thinner towards the trailing edge than the aerofoil-shaped fin. Figure 80 shows the two fin profiles side by side, and the difference between them.

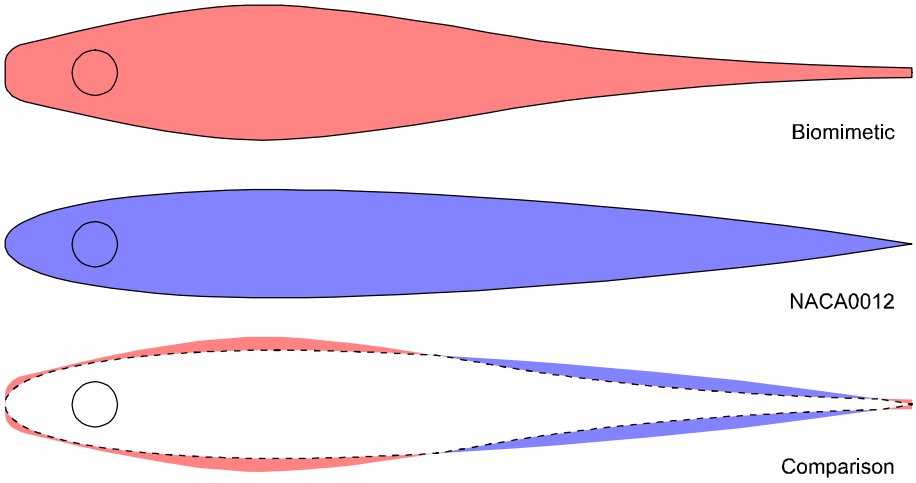

Figure 80: Biomimetic and NACA 0012 fin profiles.

Figure 81 shows how the second moment of area (*I*) varies along the chord length for both of the fins.

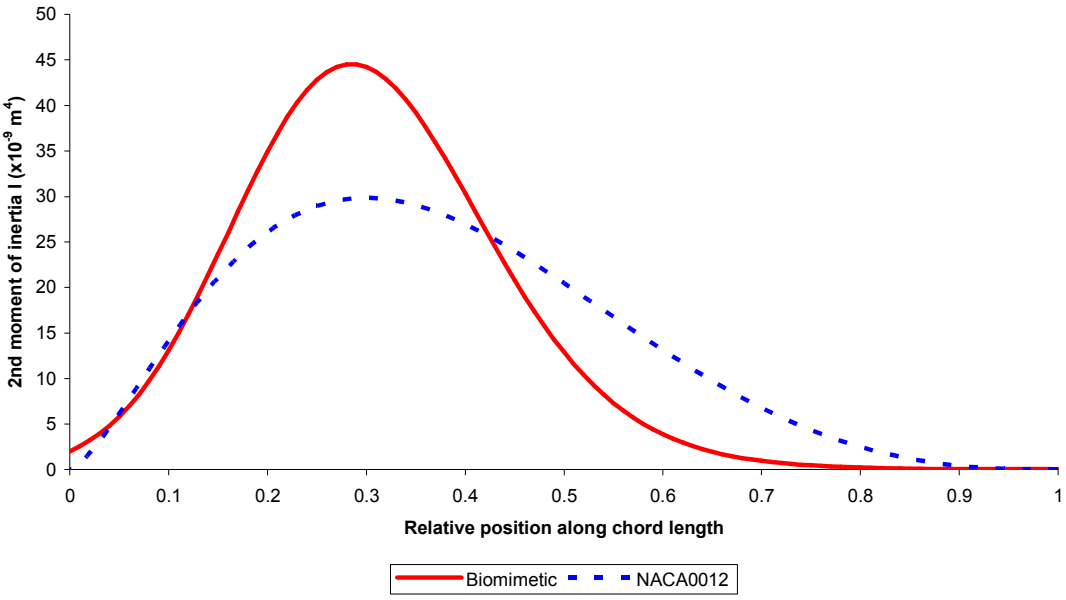

Figure 81: Calculated 2nd moment of area of fin profiles.

Figure 82 shows the flexural stiffness (*EI*) of the two fin designs, and includes the original sunfish stiffness data for reference.

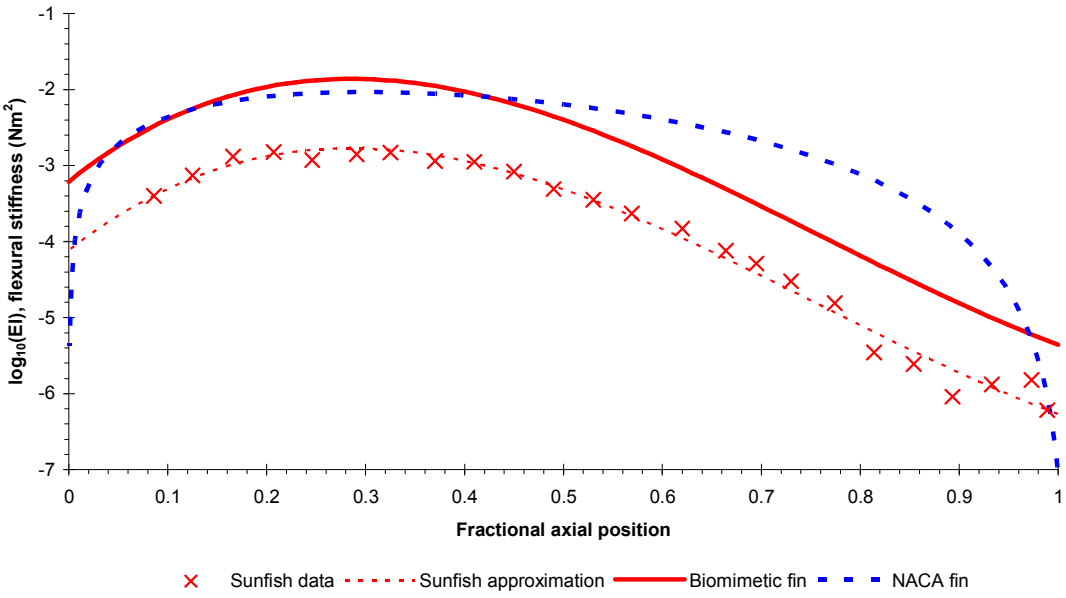

Figure 82: Flexural stiffness of fin profiles, and source data.

5.2.2 Experimental Methods

Each fin was submerged in the static water tank described in Section 4.6.1 (page 98), with the centreline of the fin at a depth of 0.2 m, and the axle protruding above the surface. The fin was oscillated about its axle with a sinusoidal angular displacement, at a range of frequencies and amplitudes. The fins were actuated by a Hitec HS-5945MG high speed servomotor, driven by a Pololu USC01A servo controller, as described in Section 4.3.5 (page 75). The motion was purely a pitching oscillation; no lateral motion was imparted, and the axle was constrained such that no passive lateral motion could take place. This was so that the effect of the fin's compliance on its lateral motion, and consequently its performance, could be observed.

The experiments consisted of a series of tests at centre-to-peak amplitudes ranging from 3-18° in steps of 3° and frequencies from 0.5-5 Hz in steps of 0.5 Hz. Tests were carried out automatically, with a pause of 60 seconds between each one, to allow disturbances in the water to dissipate before more measurements were taken. Each test lasted for 20 cycles of the fin, and the thrust, lateral force and torque were recorded at a sample rate of 1000 Hz for the test's duration, using the equipment described in Section 4.4.3 (page 83). One of the aims of the setup was to avoid wall effects, and produce results as close as possible to those that would result from experiments in an infinite body of water. From the analysis of individual fin tests, 20 cycles was determined to be long enough for the thrust produced by consecutive fin cycles to stabilise, but not so long that significant large-scale currents could develop in the tank, giving the effect of flowing water. The first 5 cycles of each fin test were neglected, as the amplitude was gradually ramped up from zero during this period, to avoid the large transient force spikes associated with suddenly beginning oscillation at high amplitudes. Further information on the experimental procedures observed can be found in Section 4.7 (page 100).

Each test started with the fin in a central position, pointing along the axis in which thrust was to be measured. A complete fin cycle was taken to be the time between consecutive zero crossings of the fin axle in the same direction. After the full set of tests had been completed, the data were analysed in MATLAB, using the methods described in Section 4.8 (page 104).

5.3 Results

5.3.1 Mean Thrust

There was a considerable difference in average steady-state thrust between the NACA and biomimetic fins (Figure 83). Both fins produced maximum thrust at maximum frequency and amplitude, but the biomimetic fin's thrust was approximately double that of the NACA fin. The NACA fin's thrust performance was highly sensitive to oscillation frequency, with an apparent optimal frequency of 2 Hz. Above this frequency there was a reduction in thrust, followed by a

further rise towards maximum frequency. This suggests a second thrust peak may occur beyond the frequency range of this experiment; however the postulated second peak does not occur at 4 Hz, so was unlikely simply to be a harmonic of the 2 Hz peak.

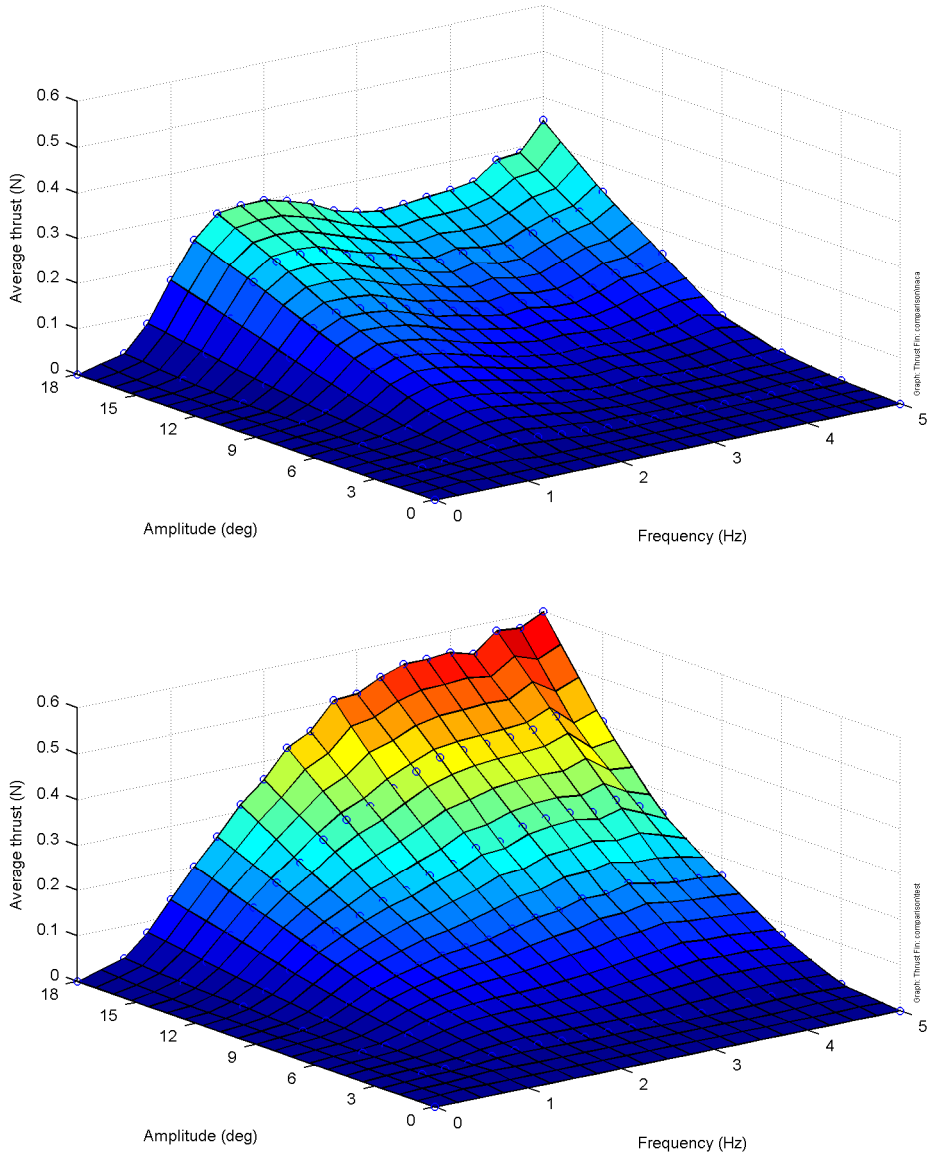

Figure 83: Comparison between NACA (top) and biomimetic (bottom) fin performance.

The biomimetic fin showed no such sensitivity to frequency. Its thrust increased steadily with both amplitude and frequency, although it showed signs of reaching a plateau towards the highest frequencies.

For easier comparison, the same data is expressed in contour form in Figure 84, below.

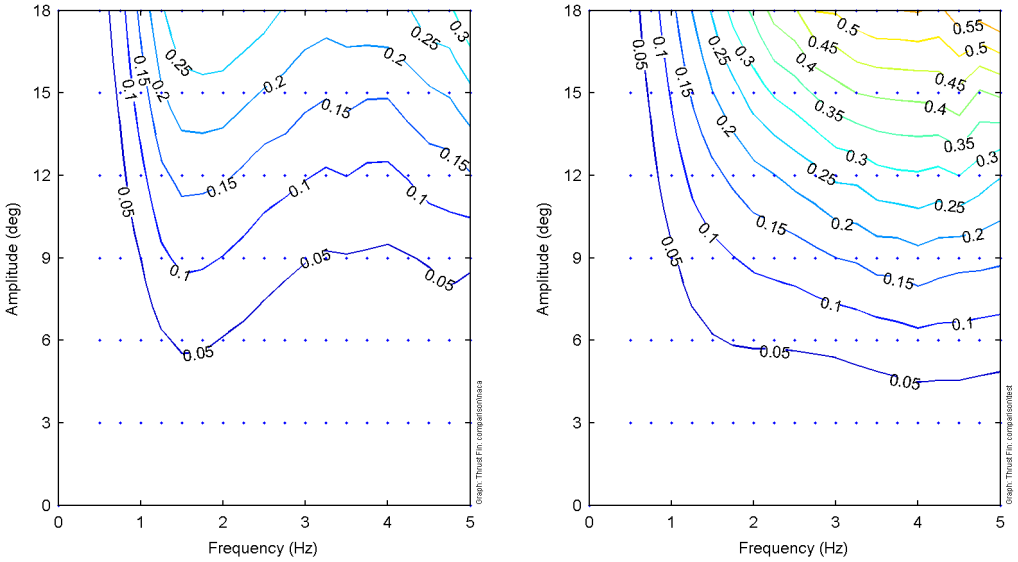

Figure 84: Comparison between NACA (left) and biomimetic (right) fin performance.

The difference between the two fins was most pronounced at around 3.5 Hz, at which frequency the biomimetic fin produced approximately double the thrust of the NACA fin at all amplitudes.

5.3.2 Force Direction

Figure 85 shows the instantaneous force direction for the two fins. The NACA 0012 fin (top) and biomimetic (bottom) fin profiles are operating at 3.5 Hz and 15° amplitude. Bold lines represent average readings, and the pale lines show the raw force data. Circles on the lines indicate phase angles of 0 and π, where the fin displacement is zero and angular velocity is at a maximum. Crosses indicate quarter-cycle intervals. The crosses without circles occur at phase angles of π/2 and 3π/2, where displacement is at a maximum and angular velocity is zero. The cycle start marker indicates the direction of the graph with respect to time.

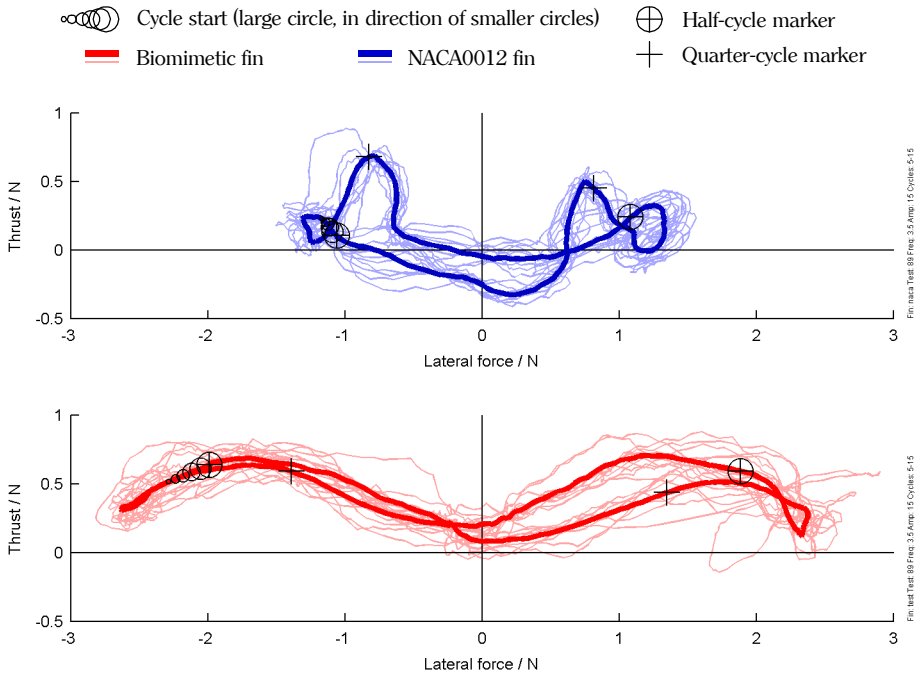

Figure 85: Instantaneous force direction analysis for NACA (top) and biomimetic (bottom) fins.

Figure 86 shows the two force profiles on the same axes. Maximum instantaneous thrust is comparable in the two fins, but in the NACA fin, the thrust peak is counteracted by negative thrust for a significant portion of the oscillation cycle. The biomimetic fin produces consistently positive thrust, in two long surges per cycle, but the lateral force is also much higher, peaking at approximately double that of the NACA fin. Some asymmetry in the force profiles is apparent, due possibly to imperfections in the manufacture of the fins.

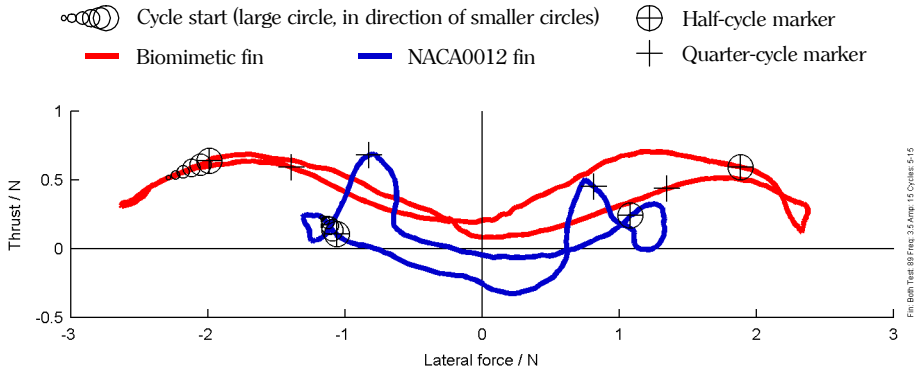

Figure 86: Comparison of force direction profiles at 3.5 Hz, 15°.

Figure 87 shows the same force data for an experiment at 1.5 Hz and 15°, during which the mean thrust generated by the different fins was very similar. The NACA fin produced significant peaks of forward thrust, but again they were counteracted by periods of negative thrust. This time the NACA fin produced greater instantaneous forces in all directions, with peak lateral force slightly exceeding that of the biomimetic fin.

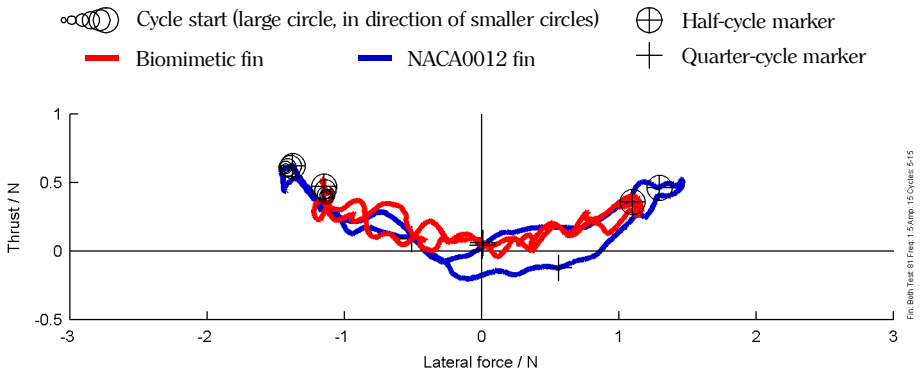

Figure 87: Comparison of force direction profiles at 1.5 Hz, 15°.

5.3.3 Power Consumption

Figure 88 shows thrust production vs. input power. Power indicates mechanical power delivered to the fin, excluding motor and drivetrain losses. It should be noted that since the actual position of the fin was not recorded for the experiments in this chapter, the power readings used to construct this graph are estimations based on the instantaneous torque and angular velocity based on the *target* position of the fin. They represent the best estimation of input power attainable from the available data. They were used to give an indication of the trends in power consumption, and were used to make decisions about subsequent experiments, and the future development of the rig, described in Section 6.2.2 (page 124).

Up to an input power of around 0.2 W, both fins follow approximately the same thrust-power curve. Beyond this point the NACA fin hits a ceiling at around 0.3 N thrust, while the biomimetic fin is able to produce greater thrust as input power is increased, up to its own maximum of around 0.6 N. These maximum values occur at the limits of the fin oscillating apparatus, so do not represent the greatest thrust that can be produced by the fins. If higher frequencies and amplitudes were attainable, the trends indicate that greater thrust would result.

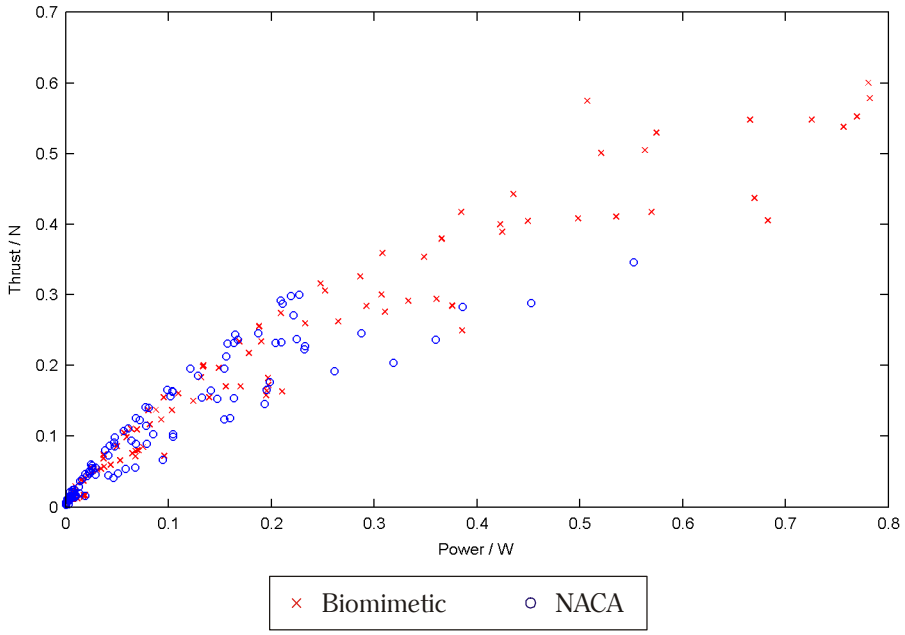

Figure 88: Thrust production against input power.

5.4 Discussion

The results provide some interesting insights into the importance of stiffness profile in the performance of pitching flexible fins.

5.4.1 Mean Thrust

The two fins responded very differently to the range of oscillation conditions. While the fins' thrust production was similar at lower frequencies, the biomimetic fin became considerably more effective as frequency was increased, in some cases producing more than double the thrust of the NACA fin.

Most of the variation in thrust production was due to oscillation frequency. The two fins responded to changes in amplitude in a very similar way; with a steady increase from low to high thrust as amplitude increased, following a similar path regardless of frequency. However, it cannot be assumed that this trend continues indefinitely: As the peak-to-peak amplitude tends towards 180° and more, an increasing portion of its cycle will be generating force in the wrong direction, counteracting the useful thrust. This effect was not observed in the experiments described above because the maximum amplitude of 36° peak-to-peak was too low for it to be noticeable.

The way in which thrust increased steadily with oscillation amplitude is also partly a consequence of the tests being performed at zero forward velocity; the correlation between amplitude and thrust would be curtailed at a lower amplitude if the velocity had been greater than

zero, since drag on the fin at the extremes of its movement would begin to counteract the thrust.

The NACA fin generated up to 25% more thrust than the biomimetic fin within a narrow band of oscillation frequencies from 0.25 to 1.5 Hz. Observation of the fin oscillating at these frequencies showed the trailing edge was moving with a large amplitude, in phase with the oscillation of the axle; no wave was being carried down the fin, it was simply moving in a side-to-side motion, at its lowest resonant frequency. These were the frequencies of peak thrust for the NACA fin, and the only frequencies at which it produced greater thrust than the biomimetic fin. The difference in thrust between the two fins was still small in comparison to that observed at higher frequencies. The NACA fin's mode of oscillation in this frequency range was of a quarter-wavelength at maximum deflection (see Figure 89).

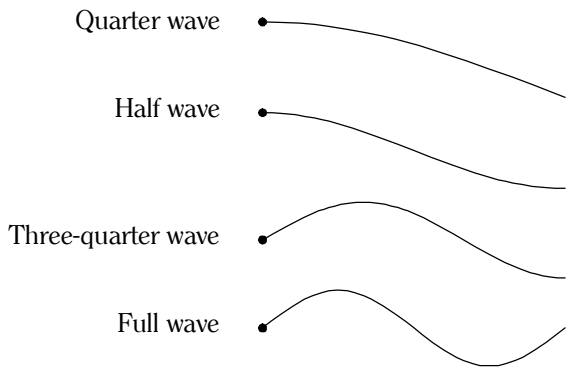

Figure 89: Example of modes of oscillation in an oscillating flexible fin.

This is a similar finding to that described in a previous numerical investigation reviewed in Section 2.7.1.1 (page 40), in which a simulated pitching flexible fin of uniform stiffness profile exhibited peak thrust capability at the same quarter-wave oscillation mode (Alben, 2008). Both the simulated fin in Alben's study, and the real fin with the NACA 0012-derived stiffness profile in this study, exhibited an initial peak of thrust as frequency increased from zero, which then reduced as the frequency was increased further. Alben's work showed that after this initial peak, no higher thrust peaks resulted at higher oscillation modes. This finding could not be replicated in the NACA fin, because its second thrust peak occurred beyond the maximum frequency of the oscillation equipment. It can be said, however, that both NACA fins exhibited a dip in thrust beyond the quarter-wave peak.

The biomimetic fin, did not display the same behaviour. Despite achieving almost the same thrust as the NACA fin in low-frequency quarter-wave oscillation, it went on to produce double the thrust at higher frequencies, with no dip in thrust performance between oscillation modes. Observation of the biomimetic fin producing its peak thrust showed it to be operating in at least a full-wave oscillation mode, meaning the transition from lower modes occurred with no

discernible dip in thrust, and that higher oscillation modes within the experimental parameters produced more thrust than the lower ones.

5.4.2 Force Direction

At higher frequencies, at which the biomimetic fin produced around double the thrust of the NACA fin, its force profile showed smooth and consistent thrust production, with correspondingly large lateral forces (Figure 86). Under the same conditions the NACA fin produced sudden spikes of thrust which quickly subsided into long periods of low or even negative thrust. Both fins flexed during the tests, storing energy elastically, but while the biomimetic profile appeared to encourage the propagation of a wave down the fin, all the way to the tail, the NACA fin, being thicker at its trailing edge, prevented such waves from forming. Instead, the stored energy was dissipated in a rapid flick of the tail, creating local turbulence, but little thrust.

The biomimetic fin was more consistent than the NACA fin in its production of thrust. Its instantaneous thrust rarely dropped below zero, a characteristic it shared with the pectoral fins of bluegill sunfish (Lauder and Madden, 2007), discussed in Section 2.3.2.1 (page 31). To compare these types of fin is not necessarily to compare like with like, because the structures and actuation modes of the fins are very different. However, they do share some common characteristics. The sunfish's pectoral fin uses an intricate structure combined with complex actuation to actively control its stiffness and shape. In doing so it is able to sustain constant positive thrust in circumstances where this is difficult to achieve. The artificial biomimetic fin was given a stiffness profile copied from the body of a real sunfish, in an effort to achieve more natural interaction with the surrounding fluid. It too demonstrated an ability to sustain constant thrust, under conditions in which the standard aerofoil-shaped fin could not. The biomimetic fin showed consistency, never dipping into negative thrust when operating under optimal conditions, and even when oscillation conditions were not favourable, its instantaneous thrust was almost always positive, and less erratic than the NACA fin.

The biomimetic fin generated greater lateral forces than the NACA fin. In some applications, this could be seen as a disadvantage, but if the fin is supported in such a way as to allow lateral movement, it is possible that the heaving motion induced by the forces could be beneficial to thrust production. Alternatively, the high lateral forces on the fin may be necessary to form the fin into the correct shape for efficient thrust generation, in which case allowing lateral movement may hinder generation of thrust. Discerning which of these two hypotheses is closer to the truth will require further experimentation.

If high lateral forces are necessary, this need not be a hindrance to real-world application of finned propulsion. A simple solution would be to use two parallel fins oscillating in opposite

phase, so that the lateral forces cancelled each other. This approach is favoured by many swimming mammals that use paired appendages as their means of propulsion, and inspired the designers of the Proteus 'penguin boat' (Thomson, 1997).

5.5 Conclusions

Overall, the biomimetic fin showed a better response to the range of oscillation conditions, slightly below the thrust of the NACA fin at low oscillation frequencies, but far exceeding it as the frequency was increased. The consistency of its thrust generation was also an improvement on the NACA fin, with the instantaneous thrust rarely dropping below zero, even under sub-optimal oscillation conditions.

One very promising finding was the consistent increase in thrust production beyond the first resonant mode in the biomimetic fin, which could translate to more predictable performance in real-world applications. Dips in thrust after the first resonant peak were observed in the NACA fin and, in previous work, simulated in fins of uniform stiffness profile. The biomimetic fin suffered no such reduction, showing smooth transitions through oscillation modes.

Fin performance is affected by many variables, and although this experiment only covered a small selection of them, the higher thrust generated by the biomimetic fin over such a range of conditions was an interesting result, and warranted further study. In relation to the hypothesis, no claims could be made at this stage about the specific effectiveness of using a biomimetic stiffness profile; the success of the biomimetic fin could have been caused by other factors. In particular, it was vital to assess whether the greater thrust of the biomimetic fin was a consequence of its shape, or simply due to it having a greater average stiffness than its NACA counterpart.

The power readings suggest the two types of fin followed similar thrust-power curves, but the power readings in these experiments were only nominal, so it was unwise to draw conclusions from them without further data. Therefore another aim of future work was to improve the test rig to provide accurate and reliable position measurements, from which accurate power readings can be calculated.

And so the goals of the next round of experiments were set: To discern whether the superior performance of the biomimetic fin was due to its shape, or simply due to it having a higher average stiffness than the NACA fin. Secondly, to introduce a more accurate method of angle measurement, and gather accurate information on the power consumption of the two fin designs.

Chapter Six

Fin Material Experiments

6.1 Introduction

The previous chapter described a set of experiments that were carried out on two silicone rubber fins, both 120 x 120 mm in size, and of constant spanwise cross-section. One had a standard NACA 0012 aerofoil shape, and the other used a biomimetic stiffness profile derived from a pumpkinseed sunfish. The biomimetic fin produced considerably greater average static thrust than the NACA fin over a wide range of frequencies and amplitudes, but further experiments were required to discern whether the advantage in thrust came from its biomimetic profile, or simply from the fact that it had a greater overall rigidity than the NACA fin, owing to its thicker profile near the fin axle.

This chapter describes improvements that were made to the test equipment to increase the accuracy of its measurements. It also documents the second round of experiments, in which the role of material stiffness is examined in the performance of both the biomimetic and NACA fins, and the power consumption of the fins is calculated with greater accuracy than had previously been achieved.

6.2 Changes to Methods and Equipment

Several changes were made to the experimental setup described in Section 5.2 (page 110). Technical improvements to the rig, described below, meant that amplitudes could be measured more accurately than in the previous round of experiments, and that power readings were also more reliable. The experimental methods were also refined to make use of the rig's enhanced abilities.

6.2.1 Changes to Experimental Methods

Because of greater confidence in the equipment's ability to perform large numbers of tests automatically, accurately, and without errors, the number of tests that were performed in each experiment set was increased from 114 to 190. Amplitude was varied between 2 and 20° centre-to-peak in steps of 2°, and frequency from 0.5 to 5 Hz in steps of 0.25 Hz. The slight increase in maximum amplitude meant that the servo was being used very close to its angular velocity limits, but a newly installed angle measurement sensor meant that any shortcomings in its performance would not affect the results adversely.

The total number of fin cycles per test was reduced from 20 to 15, with the last 10 being analysed. Discarding the first 5 cycles allowed time for the fin to reach a steady state before measurements commenced. The reduction from 15 to 10 measured cycles reduced the time necessary for an experimental set, and reduced build-up of turbulence in the water, whilst having a negligible effect on the quality of the data. Further information on the number of cycles necessary per test has been given in Section 4.7.1 (page 100).

6.2.2 Improvements to the Test Rig

6.2.2.1 Angle measurement sensor

A good quality servomotor, even one designed for use in radio-controlled models, can reproduce angles to an accuracy of around one degree, provided excessive loading does not prevent it from moving to its intended position. Because the desired motion of the fin and the expected forces were within the servo's capabilities, the servo-actuated test rig used for the experiments in Chapter Five was designed with no direct feedback of the servo's position. The position data used in calculations of angular speed and power consumption was the target position of the fin, rather than its actual position.

The drawback of this method was that the servo's dynamic response was not perfect, so there was a small time lag between the intended output wave and the actual fin position. This resulted in the position readings being out of sync with the force readings, reducing the accuracy of the power calculations. The time lag varied depending on the frequency and amplitude of the target wave, and so could not be cancelled as easily as the servo signal latency had been (Section 4.4.4.4, page 89). Figure 90 shows an example of a test affected by time lag, where the torque reading should have been approximately in opposite phase with the target angular velocity, but is clearly not.

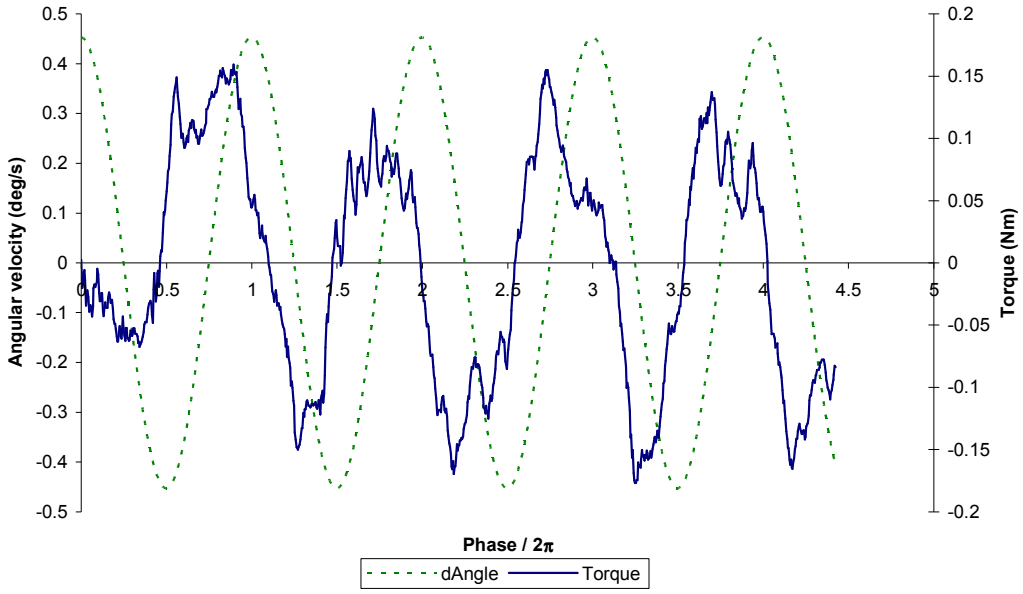

Figure 90: A sample of force and angle data showing problematic time lag.

This problem did not affect the accuracy of the force readings, because they were not influenced by the angular position of the fin. It did, however, mean the power and amplitude readings for the fin were nominal rather than exact, being based on the target position of the fin rather than a direct measurement. The solution to this problem was to add a potentiometer to the rig, to provide feedback of the servo's true position. This allowed the power consumption to be calculated from real values, unaffected by any lag between intended and real location.

The modification consisted of two arms of equal length, made from ABS, created using a rapid prototyping machine. One of the arms was attached to the fin axle, near the servomotor, and the other was connected to a potentiometer. A high-precision potentiometer was selected, with a linear response, so that the voltage produced would be proportional to the fin's angular displacement. It was of a conductive plastic type, rather than wire-wound, to cut down noise, and give the readings the highest resolution possible. The potentiometer was mounted securely on the rig, and the two arms coupled together using a length of steel rod (Figure 91). Tolerances were carefully controlled to ensure there was negligible play, which could have caused hysteresis in the angle readings, and also to ensure friction was kept to a minimum, so that the motion of the motor was not impeded.

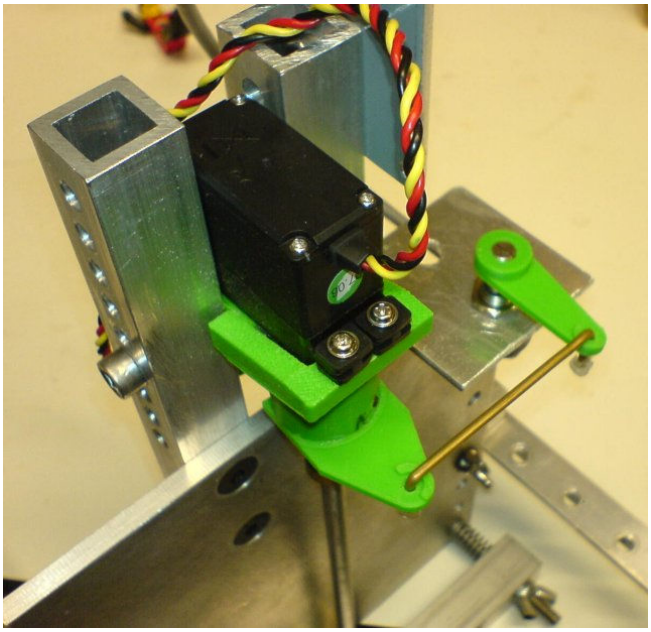

Figure 91: Fin angle sensor modification.

6.2.2.2 Angle deviation

A drawback of using a model servo as an actuator was that model servos use proportional control to follow the demand position, rather than more accurate proportional-integral-derivative (PID) control. Proportionally controlled servos are well suited to applications where they have to move quickly and accurately to a particular position, but are less adept at following a defined path at variable speed. It meant that at any given time, the speed of the servo was proportional to its distance from the intended target, so it only moved at its maximum speed when there was an error of several degrees in its position. The faster the servo was required to move, the further it lagged behind its desired position, even when operating within its maximum slew speed. A consequence of this time lag was that the waveform was slightly compressed in the amplitude axis, because as the servo was still travelling towards its maximum displacement, the desired location had already reached its maximum and was beginning to return.

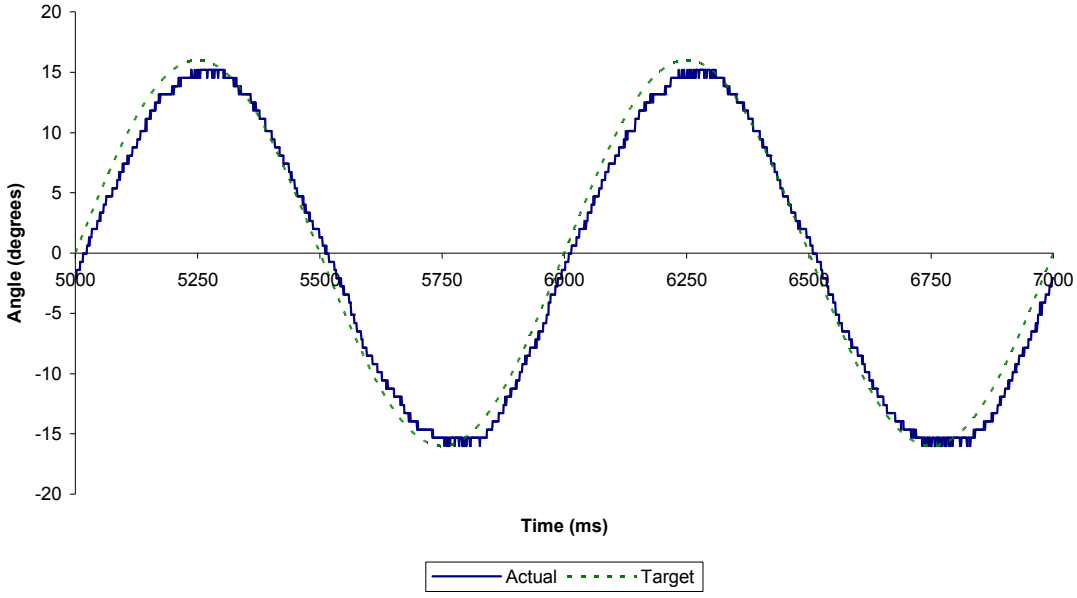

Figure 92: Servo accuracy at amplitude 16°, frequency 1 Hz.

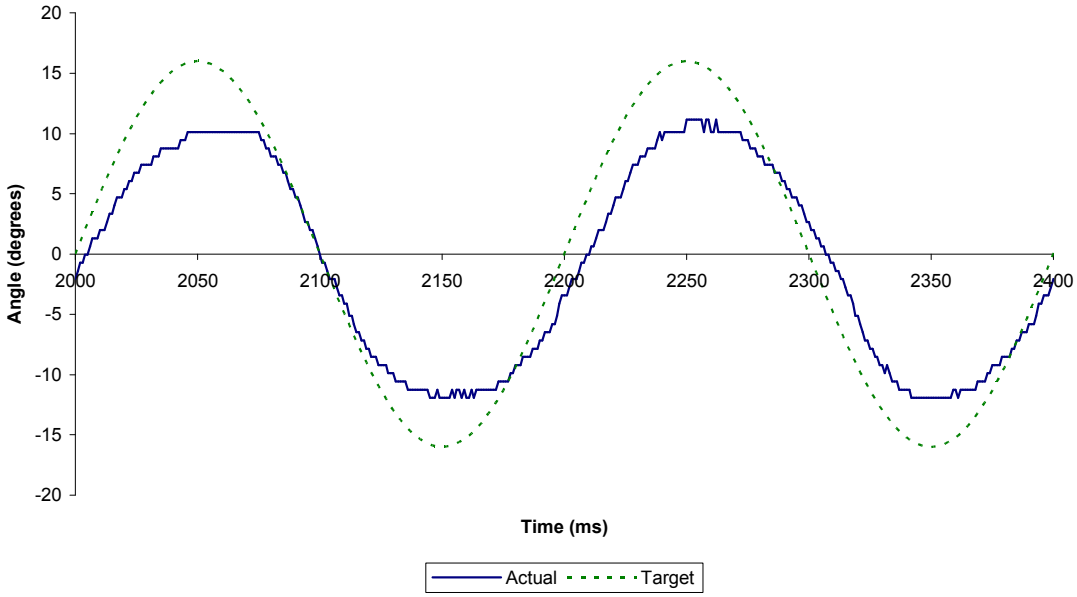

Figure 93: Servo accuracy at amplitude 16°, frequency 5 Hz.

Figure 92 and Figure 93 show the effect of frequency on the accuracy of the servo. Both graphs show short samples of two cycles from relatively high-amplitude tests on a hard compound biomimetic fin. Figure 92 shows a low-frequency test, at 1 Hz, where the angle reproduction was very accurate. Figure 93 shows the servo struggling to follow the demand curve when the frequency was increased to 5 Hz. It is important to note that the frequency reproduction is unaffected by the servo's shortcomings, and the waveform is still close to sinusoidal. The most significant effect of the servo's shortcomings was to reduce the amplitude

of the waveform, and introduce a small time lag in comparison to the target waveform. Neither of these effects compromised the accuracy of the results, since the measured angle was used in calculations, not the target angle. Therefore, the rig could be safely operated at higher target amplitudes than the motor could reproduce, and the results would take the discrepancy into account, and not be affected by it. This was a significant improvement over the experimental setup used in Chapter Five, because it meant real power measurements could be gathered for all fin tests, eliminating the need for estimates based on target fin positions.

6.2.3 Fins

6.2.3.1 Fin materials

In the previous chapter, two different fins were created, from the same resin, with different stiffness profiles. This time, a total of four fins were used: two biomimetic and two of NACA 0012 profile. Each of the two profiles was created in two different silicone resin compounds; the two ends of the stiffness scale discussed in Section 3.1 (page 57). The softer resin had a Young's Modulus of 0.32 Nm^{-2}, and the harder resin one of 0.52 Nm^{-2}.

Although the soft-compound biomimetic and NACA 0012 fins were the same in shape and material as those in Chapter Five, a slightly different technique was used in their manufacture, as explained in Section 4.2.1 (page 69). The soft fins had a stiffness 14 times greater than the sunfish that supplied the source data, as in the earlier experiments. The harder resin compound used for the other fins gave them a stiffness factor of around 23 in comparison to the sunfish. Figure 94 shows the stiffness profiles of all four fins, together with source data from the pumpkinseed sunfish. A logarithmic scale is used, since the stiffness of the fins varied from leading to trailing edge over more than 3 orders of magnitude.

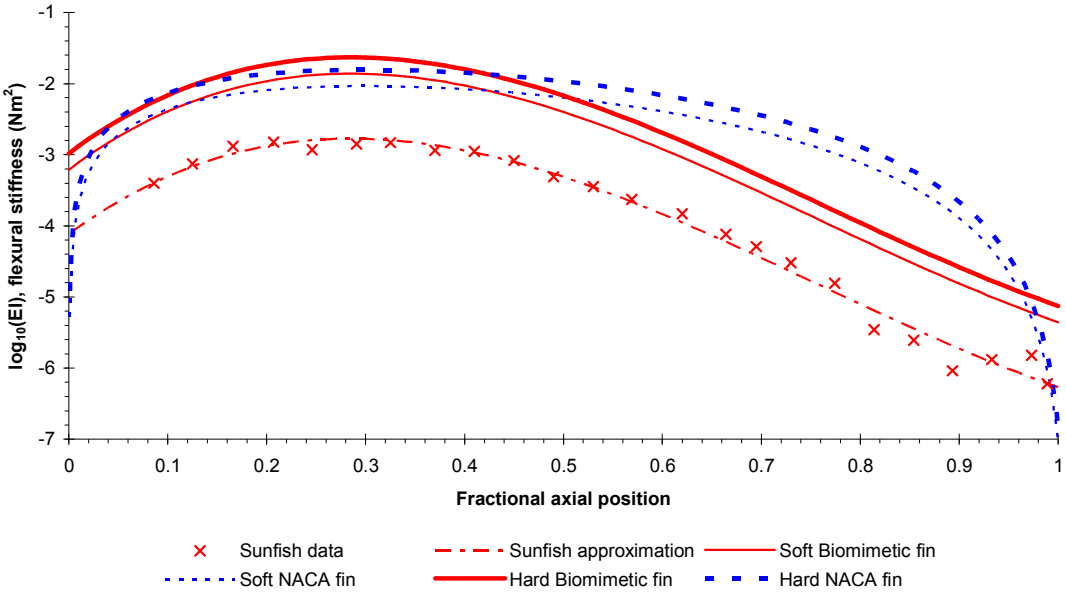

Figure 94: Flexural stiffness of all four fins, and source data.

6.2.3.2 Test rig setup

The test rig setup was also changed for this set of experiments. The hard-compound fins were found to produce larger forces than the softer ones used in Chapter Five, so the rig geometry and fin direction were changed so as not to overload the sensors, as explained in Section 4.4.4.5 (page 90).

It was important that the data from all four fins was gathered in an identical experimental setup. For this reason, and because the variable ranges had been increased, a new set of data was gathered for all the fins, using the same rig setup for all experiment sets,

6.2.3.3 Axle adhesion method

The adhesion method described in Section 4.2.2 (page 71) worked adequately for the experiments in the previous chapter, but for the second set of fins, an alternative method was devised which gave even better adhesion to the fin axle.

The weakest link in the former method was observed to be the adhesion between the porous fabric and the silicone rubber. The weave of the fabric was too tight to allow the resin to seep through and wet it thoroughly, resulting in a bond that could, with some force, be peeled apart.

The new method used a similar process, but instead of thin fabric, cotton string was wrapped tightly around the axle (Figure 95). The cyanoacrylate glue adhered very well to both the string

and the axle, and the coarser texture of the string allowed the silicone to grip it very effectively. The new method was used in the all of the experiments described in this chapter.

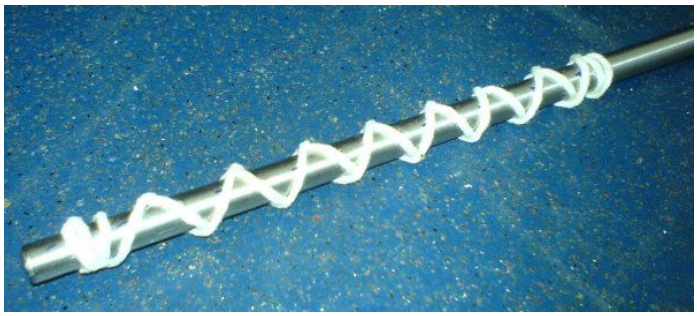

Figure 95: String-wrap adhesion method.

6.3 Results

6.3.1 Experimental Accuracy

Improvements to the rig since the experiments described in Chapter Five meant that the accuracy of the motion control system could be measured. The mean deviation from the intended angle was calculated for every individual fin test, and the results are shown in Figure 96.

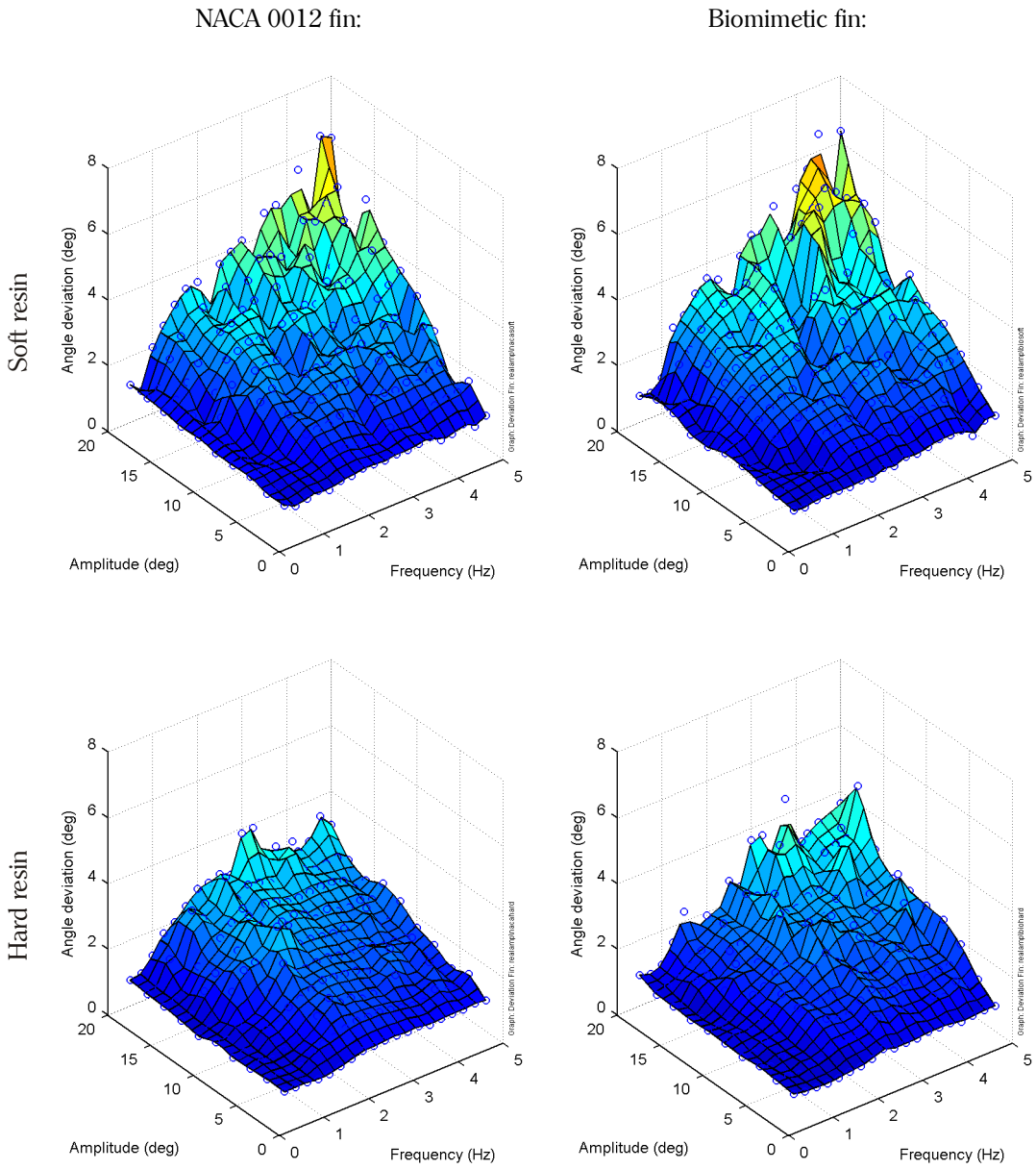

Figure 96: Average deviation from target angle for all four fins; nominal amplitudes are displayed.

All experiment sets show a minimum mean deviation of around 1° in the lowest frequency and amplitude tests. Figure 97 shows a small sample of raw angle data from one of these

tests, revealing that most of this deviation was caused by signal noise in the angle sensor channel, which had a resolution of around two thirds of a degree.

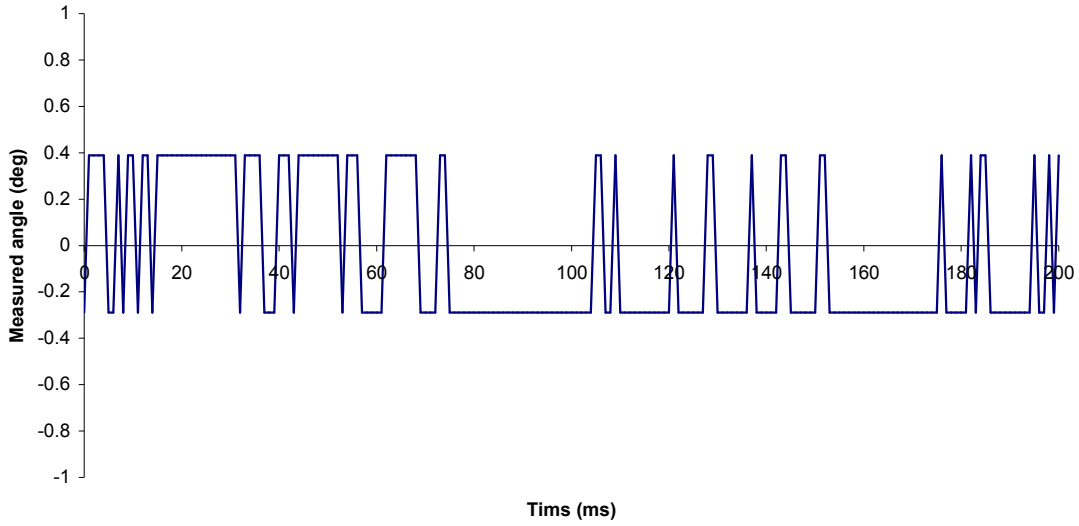

Figure 97: Noise from the angle sensor.

At higher frequencies and amplitudes the deviation was significantly greater, reaching a maximum of nearly 7° in the some cases. Interestingly, the deviation in the soft resin fin was greater than in the hard fin. The hard fin generated higher forces than the soft fin, so the result suggests that magnitude of deviation was not simply related to the mean forces generated by the fins as they moved. A possible explanation for the greater deviation in the soft fins is the difference in dynamic response of the two fin materials. All the fins stored elastic energy and released it to the water as they oscillated, but subtle differences in the phase of this cycle in relation to the target path of the motor, could either help or hinder the servo from following its target path.

Despite the drawbacks mentioned in Section 4.3.5 (page 75), using the Hitec HS-5945MG servomotor to actuate the fin yielded good results. Its performance was more than adequate for the majority of the tests performed, and where it fell short, the effect on the fin's path could be measured, and included in subsequent calculations. The deviation in fin angle therefore did not compromise the accuracy of any of the following results.

6.3.2 Mean Thrust

Figure 98 shows the mean thrust production of all four fins across the range of frequencies (0-5 Hz) and amplitudes (0-20°).

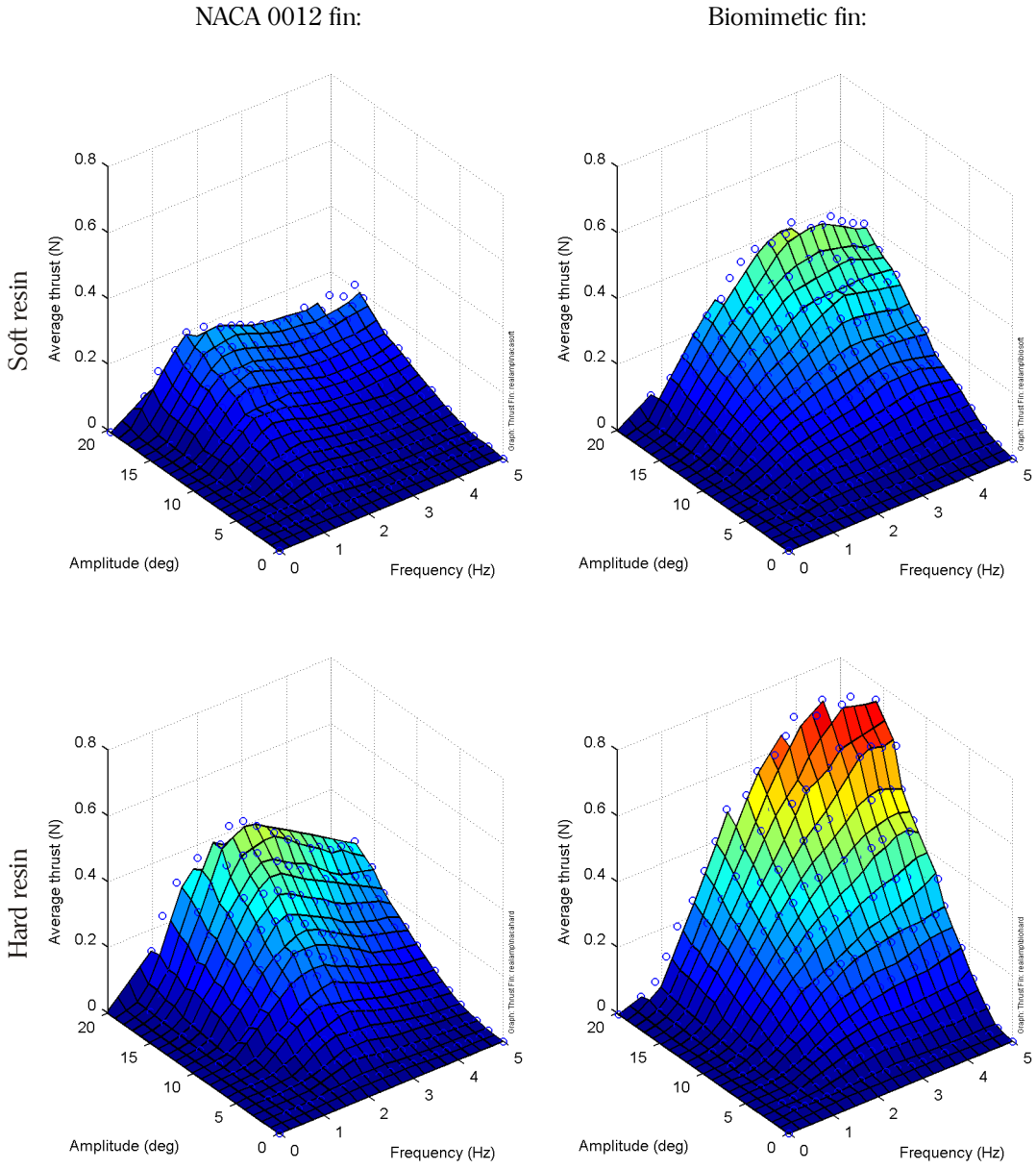

Figure 98: Mean thrust surface plots for all four fins.

Table 9 shows the maximum thrust generated by each of the fins.

	NACA 0012	Biomimetic
Soft	0.25 N	0.47 N
Hard	0.49 N	0.79 N

Table 9: Maximum mean thrust generated by fins.

The dramatic difference in thrust production between the biomimetic and NACA 0012 fin profile appears to be just as pronounced for the hard resin compound as for the soft one. The biomimetic fin produced around double the peak thrust of the NACA fin, and at specific frequencies and amplitudes exceeded it by almost three times. Again, the biomimetic fin responded well across the range of frequencies and amplitudes. The hard NACA fin showed a peak of thrust at around 2.5 Hz, above which the thrust decreased more than it had for the identical soft-compound fin, falling by 30-50% towards the maximum frequency of 5 Hz.

The soft-compound biomimetic fin tests showed an apparent resonant frequency of around 3.75 Hz, which had not been distinguishable in former experiments. This suggests that the hard-compound biomimetic fin also has a resonant frequency, at around 5 Hz, but its exact location is hard to discern, being on the edge of the rig's frequency capability.

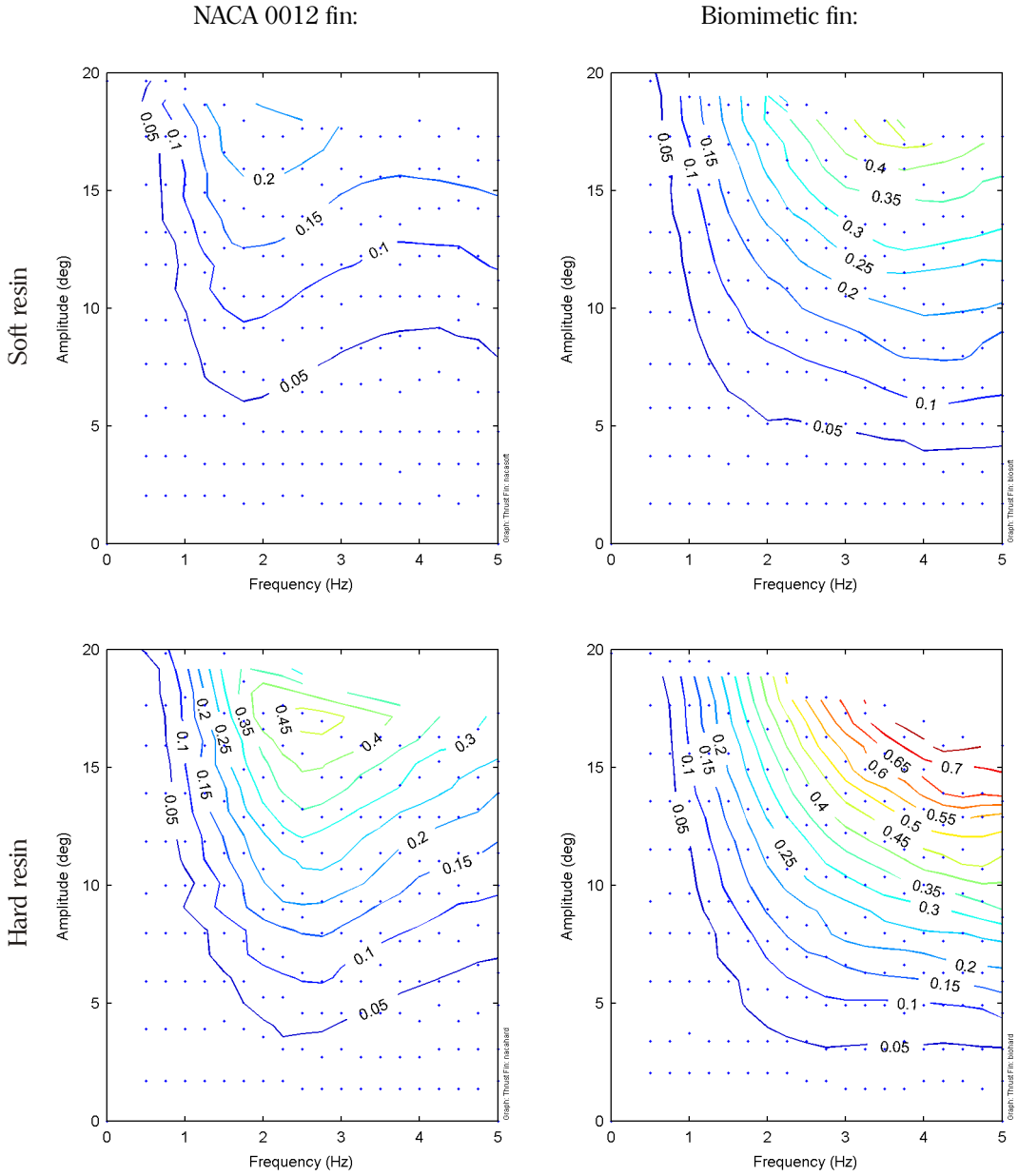

Figure 99: Thrust (N) contour plots for all four fins.

Figure 99 shows the same data in the form of a contour plot. Some care must be taken to note the locations of data points when interpreting the contour lines. Where the hard-compound NACA fin displays a peak thrust of just over 0.45 N, the contour lines suggest a downward trend as amplitude increases from this point. However, it should be noted that there are no data points in this region; the downward slope is an artefact of the interpolation method, based on more distant points. This phenomenon is apparent in some of the other plots in this thesis, usually to a lesser extent, but demonstrates the drawbacks of data interpolation, and why the locations of data points are included.

Interestingly, the thrust profile of the NACA 0012 hard-compound fin was similar to that of the biomimetic soft-compound fin, but the NACA fin achieved peak thrust at a lower frequency, and was less responsive to higher frequencies.

6.3.3 Force Direction

Figure 100 shows the instantaneous force direction plot for all four fins, at a frequency of 2.5 Hz and amplitude of 16° centre-to-peak. 2.5 Hz was the frequency at which the hard NACA fin generated its maximum thrust, yet was still matched in performance by the biomimetic fin.

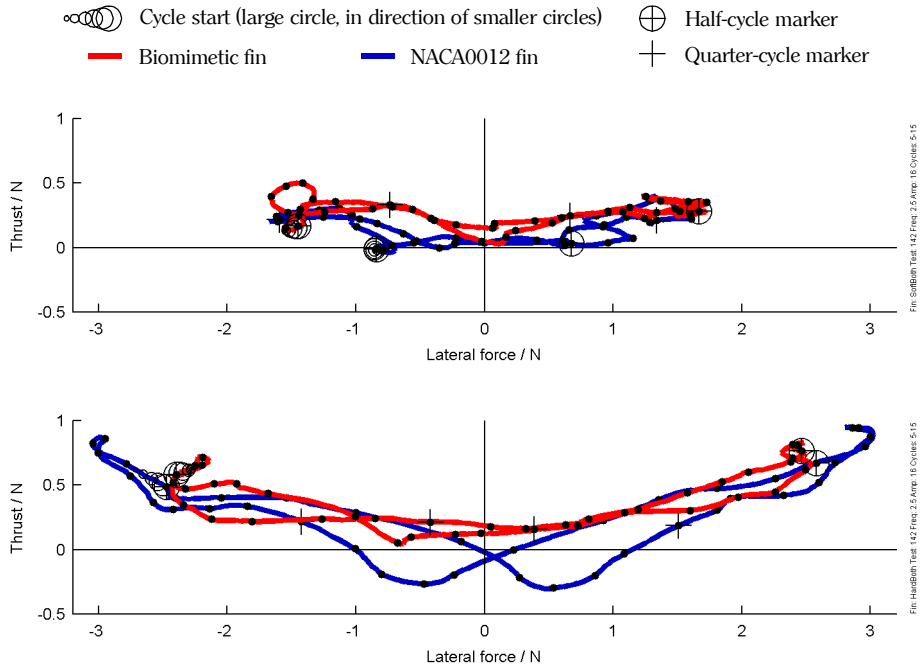

Figure 100: Instantaneous force trace under oscillation at 2.5 Hz, 16° amplitude; soft fins (top) and hard fins (bottom)

Consistent with the observations made in Chapter Five, the hard biomimetic fin produced consistently positive thrust, while the hard NACA fin produced greater instantaneous forces in all directions, including being in a negative thrust condition for 20% of the fin cycle. The biomimetic fin produced positive thrust throughout its entire cycle. The same oscillation conditions did not correspond with peak thrust production for either of the soft fins (Figure 100, top), but the graph shows the biomimetic fin producing greater thrust than the NACA fin, with comparable levels of lateral force.

Figure 101 shows force traces for both pairs of fins at the slightly higher frequency of 3.5 Hz. This is higher than the optimal frequency of the NACA fins, and under these conditions the biomimetic continued to produce consistent forward thrust throughout the entire fin cycle, with a mean thrust up to double that of the NACA fins.

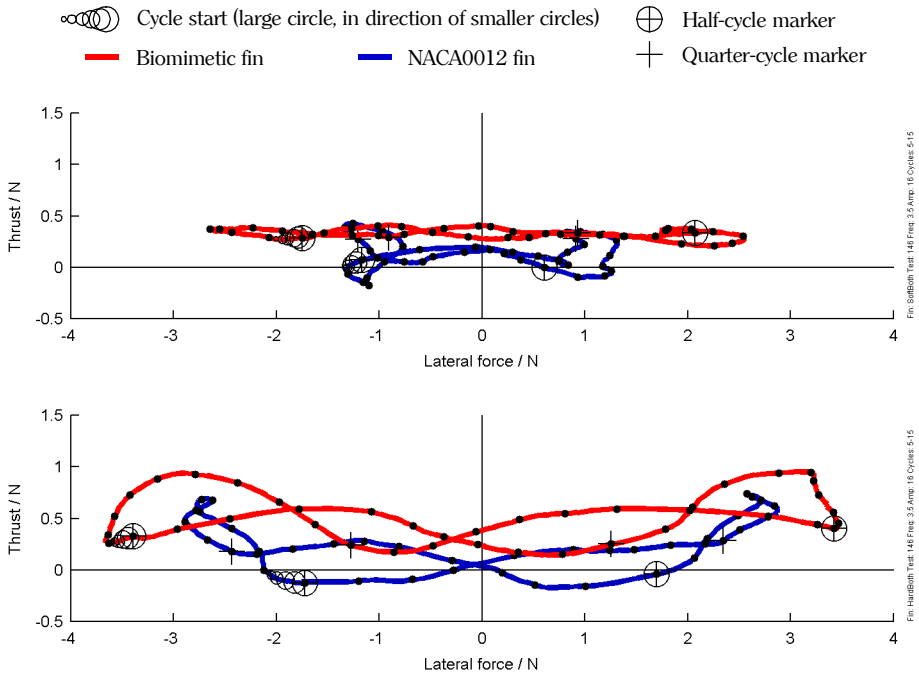

Figure 101: Instantaneous force trace under oscillation at 3.5 Hz, 16° amplitude; soft fins (top) and hard fins (bottom)

6.3.4 Lateral Force Generation

The results for lateral force generation in all of the fin experiments are shown below, as surface (Figure 102) and contour plots (Figure 103). Lateral force generation correlates approximately with the production of thrust. However, the peaks in lateral force production in the NACA fins are less pronounced than those on the thrust plots, and occur at higher frequencies. The biomimetic fins do not show peaks at all, with lateral force production rising continuously as oscillation frequency increases.

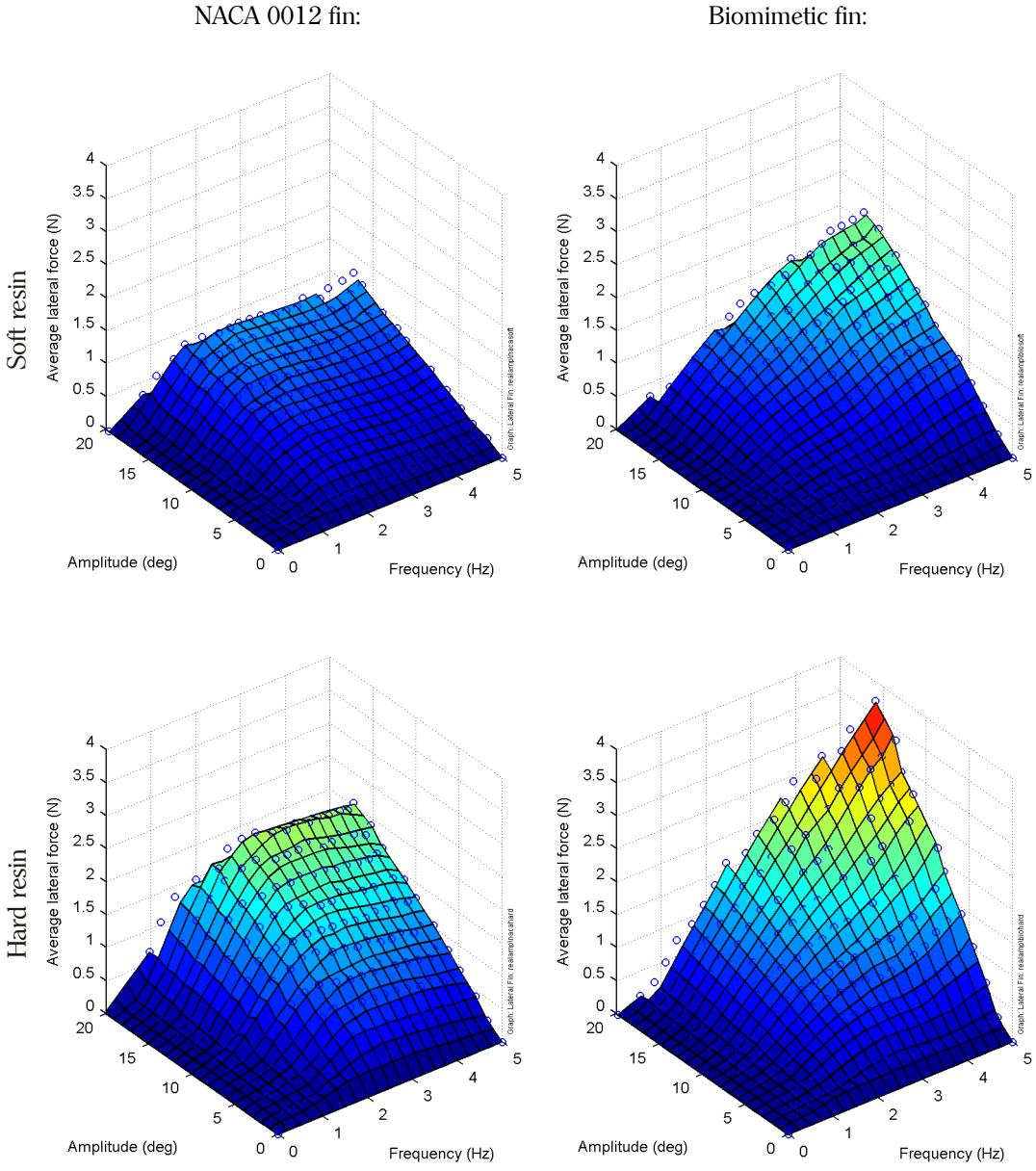

Figure 102: Average absolute lateral force (N) surface plots for all four fins.

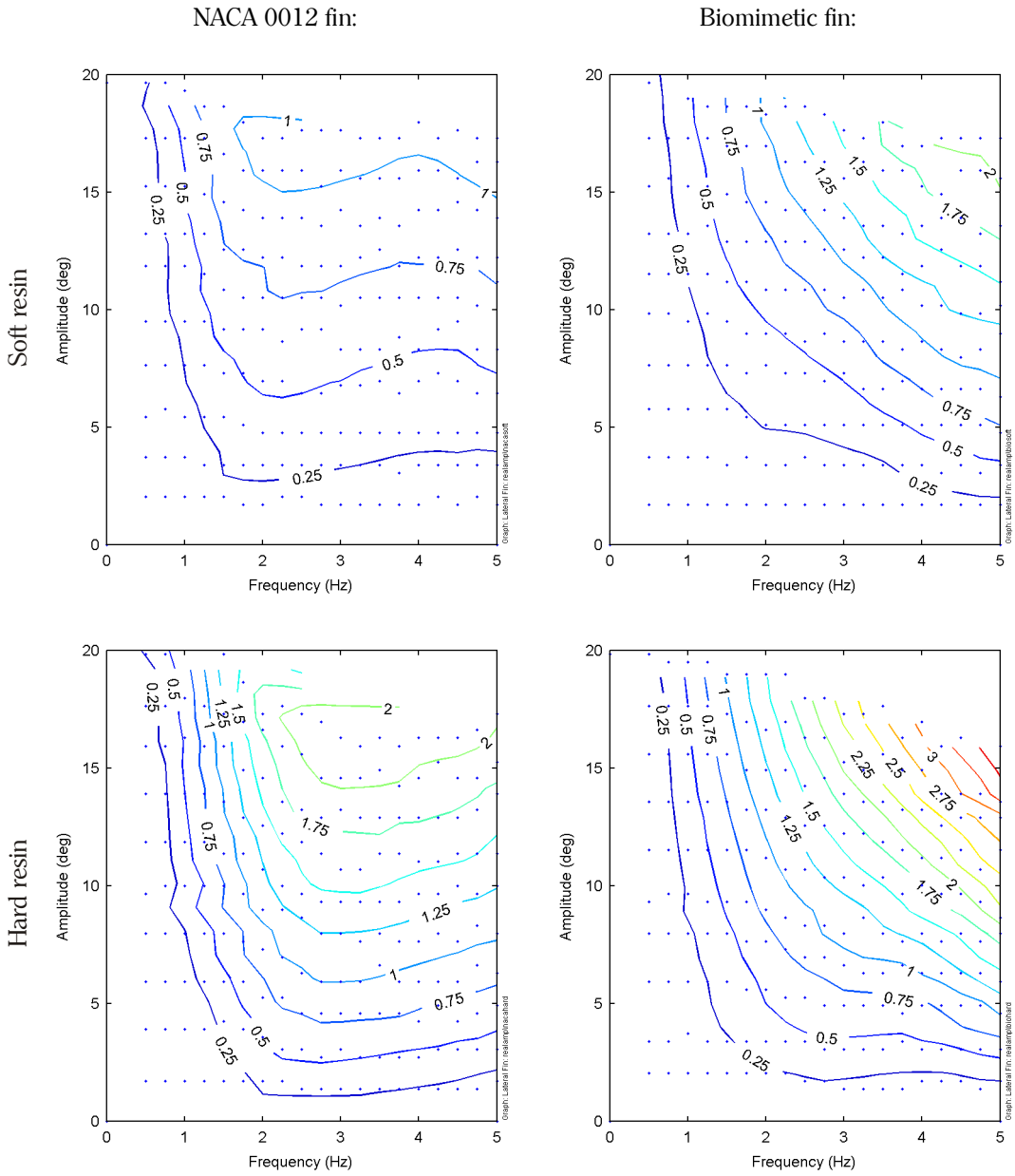

Figure 103: Average absolute lateral force (N) contour plots for all four fins.

6.3.5 Power Consumption

6.3.5.1 With respect to frequency and amplitude

The power readings for this round of experiments were derived from the actual angular displacement of the fin axle, rather than from an estimation based on the target angle. This method increases accuracy, particularly at high amplitudes and frequencies. The mechanical power consumption of the fin, excluding motor losses, is shown below both as surface (Figure 104) and contour plots (Figure 105).

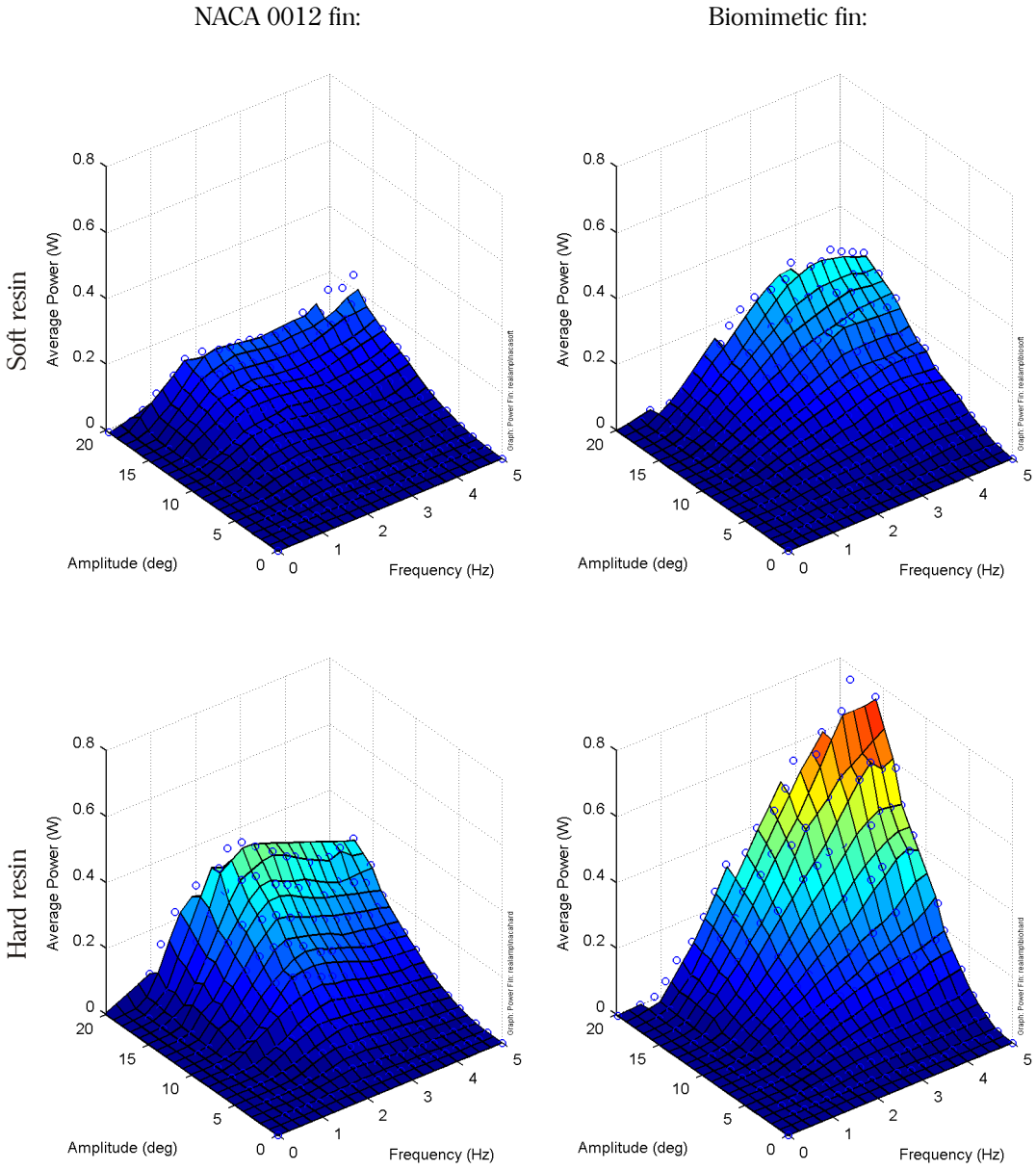

Figure 104: Power (W) surface plots for all four fins.

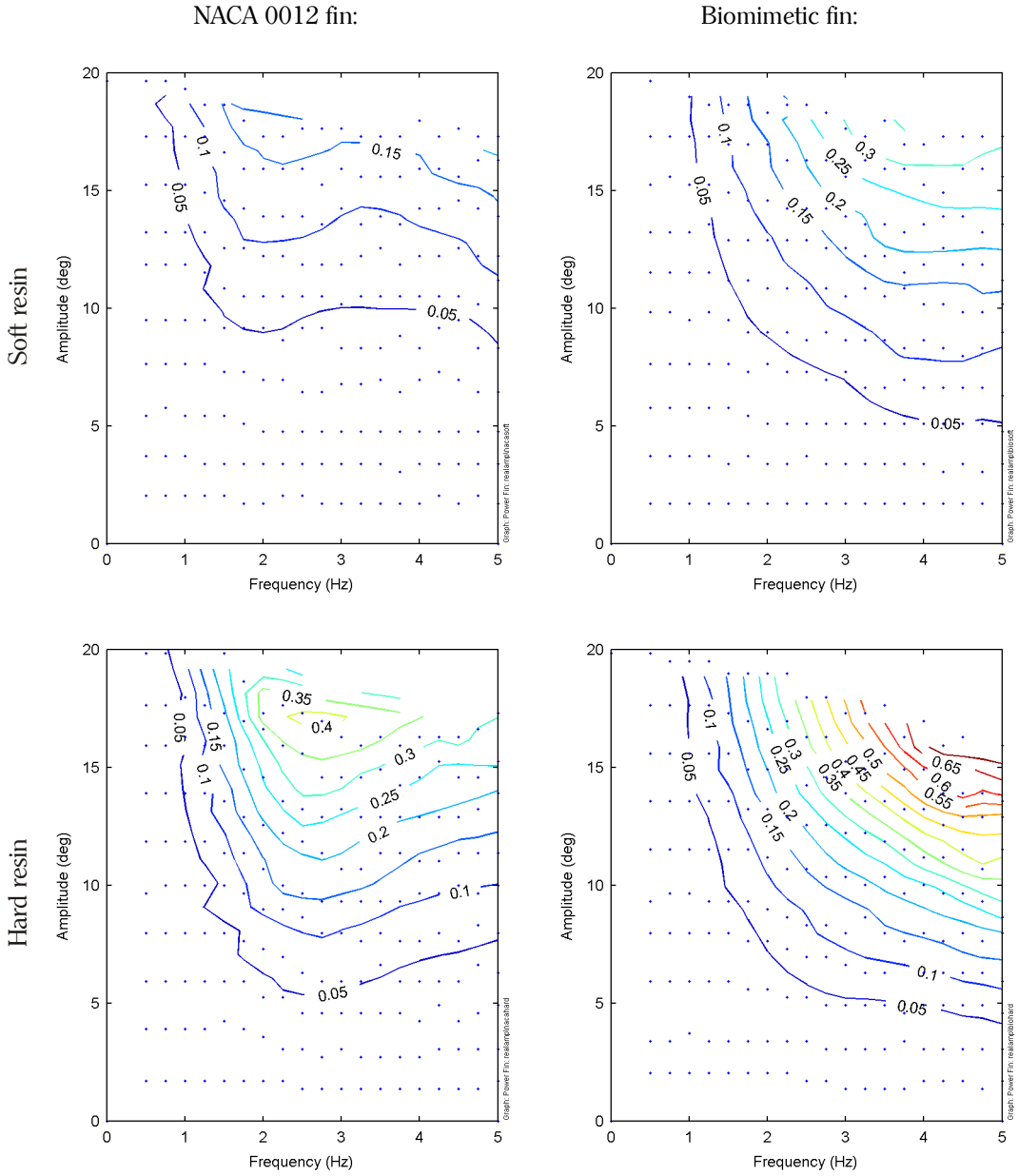

Figure 105: Power (W) contour plots for all four fins.

The hard-compound biomimetic fin operating at maximum frequency and amplitude consumed the most power, and produced the most thrust. Results for the other fins showed that the peak power consumption for each fin also corresponds with the frequency and amplitude at which it produces the greatest thrust. The resemblance between peaks and troughs on the power consumption and thrust graphs suggested a close relationship between the two.

6.3.5.2 Statistical analysis of thrust-power relationship

To help scrutinise this relationship further, Figure 106 shows a scatter plot of the mean thrust and power consumption of every test, on all of the four fins.

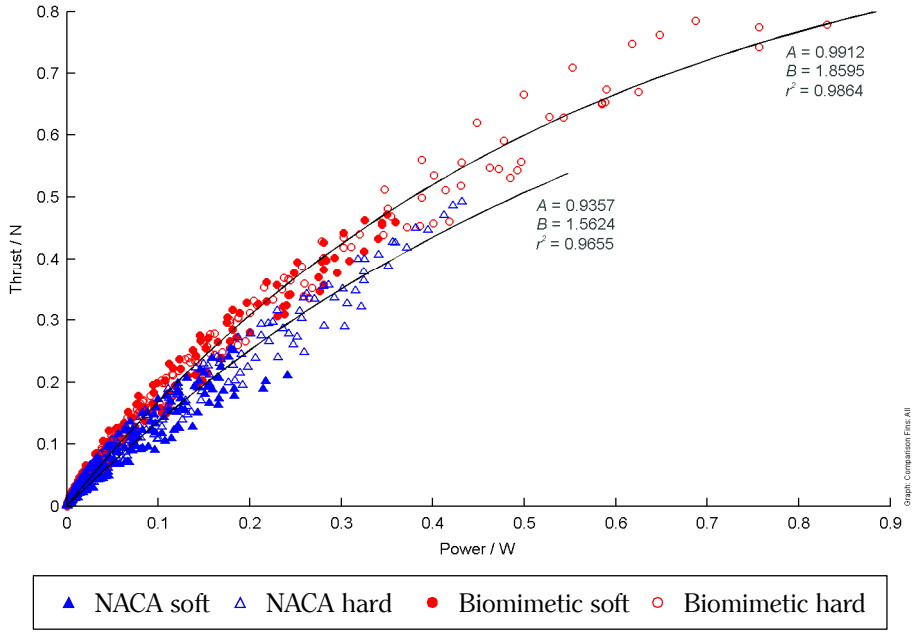

Figure 106: Thrust production against input power for all experiments.

When grouped together, it is interesting to note that the biomimetic and NACA fins follow two distinct thrust-power curves. To give a measure of the difference between the two designs, the curves were approximated by regression lines of the form shown in Eq. (52), in which A and B are the coefficients, and x and y represent the power and thrust axes respectively.

$$x = A\left(1 - e^{-By}\right) \tag{52}$$

This form of regression line was chosen as it naturally fits the shape of the data to which it is being applied. Models were fitted to the two datasets using the method of least squares, and the resulting lines are included in Figure 106. The high coefficient of determination (r^2) values indicate a good fit of the model to the data.

The separation between the two datasets was noticeable from the raw data alone, but to provide statistical confirmation, a permutation test was performed on the data. A null hypothesis was assumed, according to which the data points were scattered randomly around a common regression curve. This was the hypothesis that needed to be disproved in order to show a difference between the two datasets.

The area between the two curves, up to a power of 0.4 W, was selected as a test statistic. The 0-0.4 W range was chosen because it represented the range over which the NACA and

biomimetic fin data coincide; beyond this region, any comparison would have used extrapolated data, and therefore been less meaningful. This area was calculated for the regression lines shown above.

The data points from both sets of experiments were then randomly re-assigned into two new groups. A new regression curve was fitted to each of these groups, using the same method as with the original datasets. The test statistic was calculated and recorded for the newly re-allocated data. The process of random re-allocation was repeated 1000 times, with the help of a MATLAB program. The magnitude of the original test statistic could then be compared to those produced by the random allocations. Of specific interest was its position within the distribution of test statistics that had been generated. A p-value of less than 0.025 would have indicated statistical significance.

The results were decisive; no more extreme separations between the regression curves occurred as a result of the random re-allocations than had been observed from the original data. This indicated a p-value of less than 0.001, demonstrating the statistical significance of the separation in datasets. The null hypothesis could therefore be rejected. The regression models indicated an average advantage to the biomimetic fins of 18-26% more thrust for a given input power, in the range where the two datasets overlapped.

The randomisation test clearly shows the difference between the two fin types across the entire power range. It is also interesting to note that for both the biomimetic and NACA fin designs, the soft-compound fins followed almost identical thrust-power curves to their hard-compound counterparts, but reached around half the maximum thrust. This agrees with the findings of Hobson *et al.* described in Section 2.7.1.1 (page 40).

6.3.5.3 Further analysis of thrust-power relationship

Greater insights can be gained by looking at individual sequences of tests in more detail. The figures below show reduced datasets from all four fins, with tests grouped together by oscillation amplitude. Most of the test sequences of tests followed a similar pattern; as frequency was increased, thrust and power consumption would also increase, but only up to a point. After a certain optimal frequency, thrust would begin to reduce, and with it, power consumption would decrease also. Beyond the optimal frequency, the fins produced less thrust per unit power than they had done at lower frequencies. In order to show each dataset clearly, only test amplitudes of 8, 12, 16 and 20° are included, and the graphs are printed at different scales. For a comparison of the four fin types on the same axes, see Figure 109.

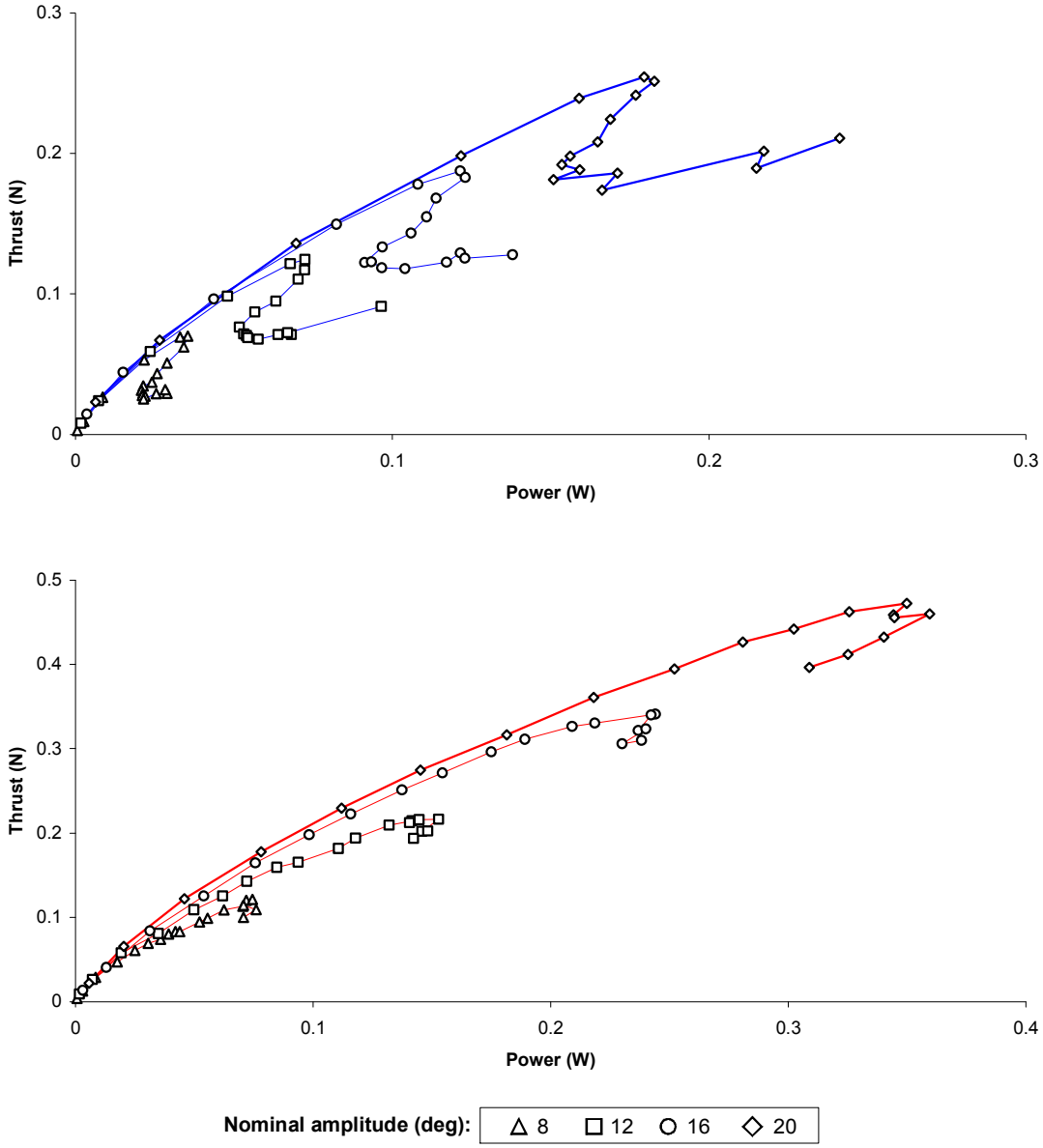

Figure 107: Thrust production against input power for the soft NACA (top) and soft biomimetic (bottom) fins, divided into amplitude groups. Frequency increases from left to right.

Figure 107 shows the results from the two fins made from the softer resin. Some interesting behaviour could be seen in the soft NACA fin; thrust and power consumption began to rise again after an initial dip. This behaviour corresponded with the fall and rise seen in its thrust generation in Figure 98, which implied the existence of a second optimal frequency beyond the range of these experiments. The shape of the graph suggests the second peak will not surpass the thrust-to-power ratio of the first optimal frequency, unless a dramatic rise in thrust production occurs.

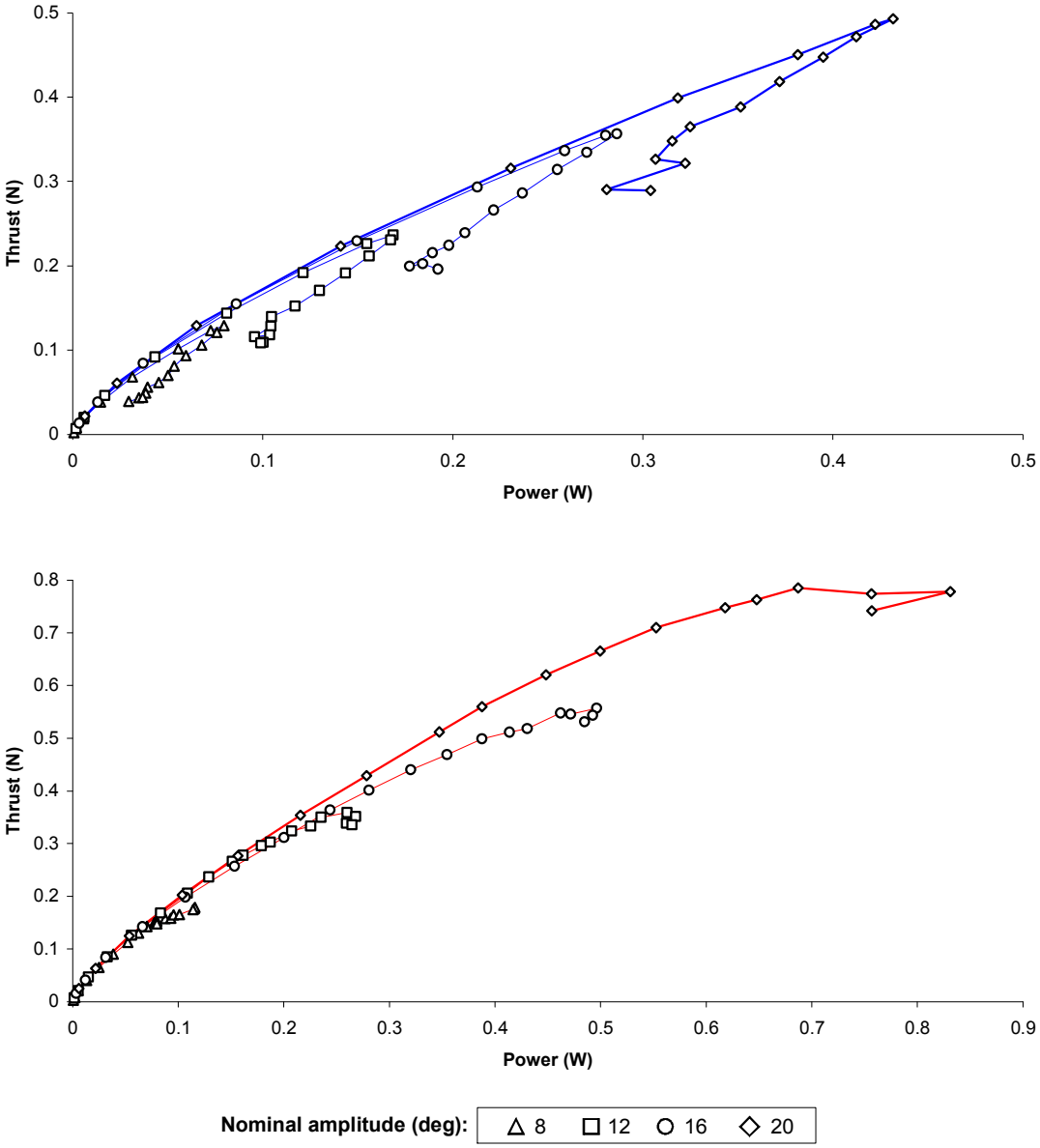

Figure 108: Thrust production against input power for the hard NACA (top) and hard biomimetic (bottom) fins, divided into amplitude groups. Frequency increases from left to right.

Figure 108 shows the results from the harder two fins. The drop-off in thrust and power consumption was less apparent in the hard biomimetic fin, which together with its thrust performance (seen in Figure 98) suggested it was well-adapted to producing thrust across the entire range of oscillation conditions tested.

An observation drawn from the four graphs in the figures above, is that the highest amplitude dataset invariably produces the best ratio of thrust to input power. Lower amplitude experiments followed a similar curve at lower frequencies, but achieved at best similar thrust for the same input power. This means that the dataset can be reduced further and still be meaningful. Figure 109 shows results from all four fin profiles on the same axes, for the experiments with

largest oscillation amplitude. Each line therefore represents the greatest thrust that could be produced by a fin, for a given input power, at any oscillation amplitude within the experimental range. As was the case in Figure 106, there was a clear difference in thrust-to-power ratio between the two fin profiles; the biomimetic design produced 18-20% more thrust per watt than the NACA fins.

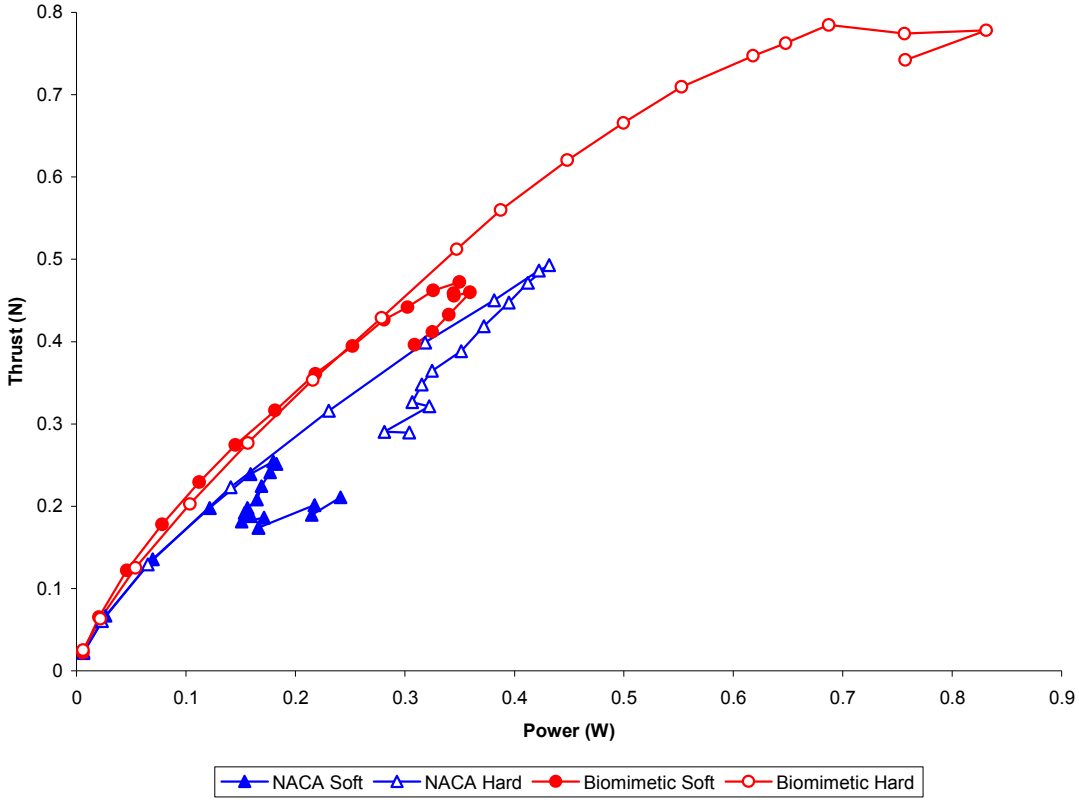

Figure 109: Optimal thrust production against input power for all four fins.

6.3.6 Optimal Frequencies

Table 10 shows the optimal oscillation frequencies of all four fins. These are the frequencies at which they produced maximum thrust, at an oscillation amplitude of 15°. The hard biomimetic fin's thrust appears to plateau towards the maximum frequency of the tests, so its optimal frequency is not possible to discern as accurately, without performing higher frequency tests.

	NACA 0012	Biomimetic
Soft	2 Hz	3.75 Hz
Hard	2.5 Hz	>5 Hz

Table 10: Optimal frequencies of fins

The optimal frequencies of each fin are shown together with their maximum thrust in Figure 110, in which dotted lines link fins of the same shape but different material stiffness. There are clearly too few data points to draw detailed conclusions, but the positions of the points at least suggest that the peak thrust is not a simple function of the fin's optimal oscillation frequency; regardless of the precise optimal frequency of the hard biomimetic fin, the two fin profiles do not lie on the same path.

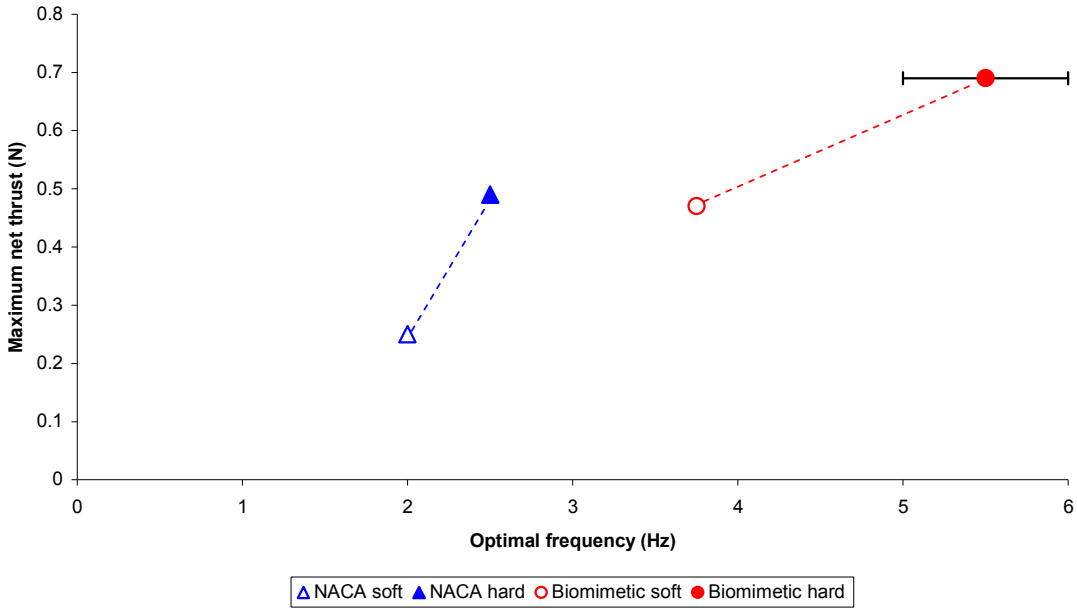

Figure 110: Maximum thrust and the frequency at which it was attained.

6.4 Discussion

6.4.1 Thrust Performance

The general behaviour observed in both versions of the biomimetic and NACA fins was similar to that of the first set of experiments. The biomimetic fins produced greater maximum thrust, and produced thrust over a wider range of frequencies and amplitudes than the NACA fins. Fins of the same stiffness profile had very similar thrust characteristics, but displayed different optimal frequencies; this finding is discussed in Section 6.4.5 (page 149).

As Figure 108 (page 145) shows, thrust produced by the hard biomimetic fin appeared to be reaching a plateau at a frequency of 5 Hz, but no peak is visible within the range of results gathered. However, the soft biomimetic fin displayed no increase in thrust beyond the oscillation frequency of 3.75 Hz. This is evidence for the biomimetic fin profile having an optimal frequency, as had been postulated after the first round of experiments.

Coincidentally, the maximum thrust readings for the hard NACA and soft biomimetic fins were almost identical. This allowed an approximate comparison of the two fin profiles, as if their stiffnesses had been tuned to generate the same thrust. Apart from the differing optimal frequencies, the biomimetic fin's thrust peaked over a slightly broader frequency band than the NACA fin. Its reduced sensitivity to oscillation frequency could be an advantage in real-world applications of flexible fin propulsion, since a biomimetic fin propulsor and its actuator would not have to be so finely tuned to produce maximum thrust. It is also consistent with the findings of the previous chapter (Section 5.4.1, page 119).

6.4.2 Force Direction

The instantaneous force plots for the four fins showed the same characteristics as those analysed in Chapter Five. The extra data gathered in this chapter for different material stiffnesses revealed similar behaviour between soft and hard fins of the same stiffness profile. The NACA fin, even when operating at its optimal frequency, did not produce thrust consistently. Its instantaneous force varied over a wide range, and the fin spent a portion of each cycle producing negative thrust. The biomimetic fin produced thrust much more consistently over each cycle. The significance of these observations is discussed in Section 5.4.2 (page 121).

6.4.3 Lateral Force

The most noticeable feature of the lateral force plots shown in Section 6.3.4 (page 138) is a difference in behaviour between the NACA and biomimetic fins. While lateral force reached a plateau in the NACA fins at approximately the same frequency as forward thrust reached a peak, lateral force generated by the biomimetic fins continued to rise as frequency was increased, and was still rising when the frequency reached its maximum.

The relationship between thrust and lateral force production was similar between the two biomimetic fins. Material stiffness had no effect; high thrust always came at the expense of increased lateral force. However, this need not be a problem in the application of fin propulsion, since lateral force could be counteracted by the inertia of the craft being propelled, or by an opposing fin, as discussed in Section 5.4.2 (page 121).

6.4.4 Power Consumption

Despite the large difference in mean thrust production for hard and soft fins of the same stiffness profile, their thrust-power curves were very similar (Section 6.3.5, page 140). This finding was of particular interest because it suggested that the relationship between power input and thrust output was defined primarily by the stiffness profile of the fin, rather than by the stiffness of the moulding material.

The chief finding reported in Chapter Five was the superior static thrust performance of a biomimetic fin over a NACA fin, for a wide range of frequencies and amplitudes. The extra results gathered in this section confirm that this was not a one-off result for a particular moulding material, but was more widely true. Not only was the thrust generated by the biomimetic fin greater over most of the oscillation conditions, but thrust-to-power ratio was consistently higher, regardless of the material used.

The data points on the thrust-power graph displayed a positive gradient, even towards the maximum power input. This suggested that if the maximum power were increased, either by increasing the amplitude or frequency of oscillation, or by using stiffer fin moulding material, thrust would increase correspondingly.

The results also show that the biomimetic fins were more efficient at converting power to thrust than the NACA fins, across the entire power range of the experiments. If a NACA fin were created that were capable of dissipating as much power as the biomimetic fin in this experiment, it would still produce less thrust than biomimetic design if it followed the same thrust-power curve as the other NACA fins.

6.4.5 Optimal Frequencies

Plotting the maximum thrust of each fin against the frequency at which it was achieved (Figure 110, page 147) yielded a small but significant insight. Although a higher optimal frequency indicated a higher maximum thrust for both of the fin profiles, the points did not fall in a way that suggested one variable was a function of the other. This shows that where a biomimetic stiffness profile brought improvement to the thrust production of a fin, it did not do so simply by altering its natural frequency by the redistribution of mass. If this was the case, a clearer relationship linking all four measurements would be expected.

This supports the theory that the improvement in thrust performance is a direct consequence of the stiffness profile itself, and not simply an incidental effect of the change on its natural frequency.

6.5 Comparison with Previous Studies

Of the papers reviewed in Chapter Two, a number concerned tests on flexible fin propulsors. Although it is difficult to draw direct comparisons between experiments carried out on different fin designs, with different oscillation and flow parameters, it was possible to extract some information from the papers, which provide a context for the findings presented in this thesis. The figures are listed in Table 11.

Study	Fin tested	Dimensions (chord x width, mm)	Aspect ratio	Max input power (W)	Max thrust (N)	Thrust-power ratio (NW^{-1})
(Kemp, *et al.*, 2003)	Pitching NACA fin, varying flexibility	152 x 152	1	17	10	1 - 2
(Heathcote, *et al.*, 2004)	Heaving flat plate, varying flexibility	90 x 300	3.3	-	-	0.8 - 4
(Prempraneerach, *et al.*, 2003)	Pitching and heaving flexible NACA	100 x 494	4.94	2.9	4.3	1 - 1.75
(Kobayashi, *et al.*, 2006)	Pitching 2-section rigid fin with flexible joint	240 x 60	0.25	-	1.6	-
This study	Pitching NACA fin, varying flexibility	120 x 120	1	0.8	0.8	0.8 - 2

Table 11: Comparison of fin studies

The comparison shows that the results were obtained under a wide variety of conditions, with power consumption and thrust production varying by an order of magnitude. However, the thrust-to-power ratios of all the experiments are comparable. The study that strays furthest form the mean in maximum thrust-to-power ratio is that of Heathcote *et al.*; even in this study, most of the experiments fell within the 1 – 2 NW^{-1} range, with the maximum readings of 4 NW^{-1} occurring in experiments using highly flexible fins at low Reynolds numbers. It is worth noting that there is no theoretical maximum thrust-power ratio, but such large values would be difficult to achieve in practical applications, as they would require large fin surfaces to move slowly in relation to the water, which would hinder manoeuvrability.

6.6 Conclusions

Chapter Five concluded that although the thrust performance of the biomimetic fin was superior to the NACA fin, it was unclear whether the improvement was caused by the stiffness profile itself, or was a side-effect, for example due to increased overall stiffness, which could be achieved by other means. The wider range of fins and improved testing methods employed in Chapter Six provided new insights into the specific role of stiffness profile in flexible fin propulsion. Consistent with the findings of Chapter Five, the thrust produced by the biomimetic fins was greater in magnitude, more consistent, and was generated over a wider range of oscillation conditions than the NACA fins. Furthermore, the new data showed that the findings of Chapter Five were not simply due to the biomimetic profile having a greater stiffness than the NACA one, but that the distribution of stiffness along the fin from leading to trailing edge itself was a cause of the improved performance. Testing of identically-shaped fins made from resins of greater stiffness helped to separate the effects that were caused by changing the overall stiffness, (and consequently the natural frequency) of a fin, from the effects of changing the stiffness *profile*.

Increasing the material stiffness led to an increase in maximum thrust, and also increased natural frequency, as would be expected of a stiffer medium. However, the stiffer fins followed very similar thrust-power curves to their softer counterparts, showing than an improvement in efficiency could not be expected to result from an increase in fin stiffness alone.

In relation to the NACA profile of the same material, the biomimetic stiffness profile resulted in increased thrust production over a wide range of frequencies. However, this cannot be taken as an indicator of superior real-world performance, since the same effect can be achieved by using a stiffer fin material. The most significant improvements resulting from the biomimetic profile were a higher thrust-to-power ratio, and the accompanying observation that thrust production was more consistent over each cycle than the NACA fin; instantaneous thrust remained positive throughout the entire oscillation under a wide range of conditions.

The other method by which stiffness profile could have indirectly affected thrust is by simply changing the natural frequency of the fin. However, the relationship between maximum thrust and the frequency at which it is achieved shows no clear correlation, which suggests there is no cause-and-effect relationship between the two. Eliminating this explanation leaves little doubt that the stiffness profile itself is the primary cause of the improvements observed in the biomimetic fin.

Chapter Seven

Summary of Conclusions and Future Work

7.1 Introduction

The experiments described in the previous chapters gave valuable insights into the role of biomimetic design in oscillating fin propulsion. They also raised new questions that will need to be addressed if future work is to continue the same themes. This chapter presents a summary of the findings documented in the previous chapters, and explores the new research opportunities that have been uncovered. It also identifies areas in the work described above that could be improved and built upon by future studies.

7.2 Summary of Conclusions

The following is a short list of findings that resulted from the experiments described in this thesis.

- Both hard and soft biomimetic fins showed a better overall response to the range of oscillation conditions than the corresponding NACA fins.
- The biomimetic fins produced more thrust per watt than the NACA fins across a wide range of oscillation conditions.
- The thrust-power curve followed by each fin was defined primarily by its stiffness profile, rather than its material stiffness.
- Increased overall stiffness and natural frequency are secondary effects of employing the biomimetic profile, but the improvement in fin performance was not attributable to them.
- Thrust produced by the biomimetic fins was more consistently positive than that produced by the NACA fins.
- The biomimetic fin allowed a seamless transition between oscillation modes up to its peak thrust output, while the NACA reduced in thrust beyond its lowest oscillation mode.

7.2.1 Support for Hypothesis

The following hypothesis was proposed at the end of Chapter Two, and guided the design of the experimental equipment, as well as the planning of all the experiments carried out subsequently. Notwithstanding the numerous other avenues of research that warranted discussion along the way, its confirmation or disproof was the central goal of the experiments described in this chapter and the previous one.

> *"Use of a biomimetic fin stiffness profile can improve the effectiveness of a flexible oscillating fin, over that of a standard NACA designated fin shape."*

The results presented in this thesis offer strong evidence that this statement is true. Chapter Five showed an advantage in thrust development of the biomimetic fin over a wide range of frequencies and amplitudes, and gave cause for further investigation into the reasons. While the results were consistent with the hypothesis being true, there was no evidence that the increased thrust and smoother instantaneous thrust were specifically due to the stiffness profile of the fin, and therefore the findings were inconclusive.

The second set of experiments, presented in Chapter Six, was designed to tackle the remaining uncertainty. The results, particularly those regarding thrust production and thrust per watt, lead to the conclusion that the real-world performance of the biomimetic fin used in these experiments was superior to that of the NACA fin, as a direct result of its modified stiffness profile. Several studies cited in this thesis (Ahlborn, *et al.*, 1997, Heathcote and Gursul, 2007, Prempraneerach, *et al.*, 2003) have concluded that a degree of flexibility is beneficial to thrust production in oscillating fin propulsion. This thesis adds to the existing body of knowledge by showing that further improvements in thrust production can be gained by optimising the distribution of flexibility along the fin. The biomimetic stiffness profile used in this thesis is not presented as an optimal solution, but as a demonstration of the value of naturally inspired design.

Further research will be necessary to determine the extent to which varying a fin's stiffness profile affects its performance, and possible directions for this research are discussed in some depth in the coming sections. However, the findings of the previous two chapters are significant in their own right, and suggest that the practice of using standard NACA aerofoil profiles by default might be improved upon, for any application in which flexible fins are employed for propulsion.

7.3 Future Work

The following sections discuss avenues for further study that arise from the studies presented in this thesis.

7.3.1 Wider Range of Oscillation Conditions

Some of the results in the previous chapters showed a tendency for thrust to increase towards the highest oscillation frequencies, suggesting a second peak beyond the first optimal frequency. However, the limitations of the test equipment (see Section 4.3.5, page 75) meant tests could not be performed at a high enough frequency to prove or disprove this supposition.

The thrust-power relationships shown, for example, in Figure 107 (page 144), suggest that no gains will be made in thrust-to-power ratio by employing higher oscillation modes, and this would be consistent with the findings of previous work (Alben, 2008), discussed in Section 2.7.1.1 (page 40). It would, however, be helpful to carry out a wider range of tests, characterising each of the fins over a wide enough frequency range to include more than one resonant frequency.

In order to achieve the higher oscillation frequencies required for these tests, the fin actuator on the test rig would have to be improved or replaced. A more powerful servomotor, capable of higher slew rates, would be the simplest way to improve the actuator, but to achieve the desired accuracy and speed, it may be necessary to look to industrial motion control equipment, or one of the other technologies explored in Section 4.3 (page 71). The test rig would have to be modified accordingly, to cope with the larger forces produced by fins oscillating at higher frequencies.

7.3.2 Visual Analysis of Fin Deflection

Many of the conclusions about fin tests in this thesis were based on the force and torque measurements obtained from the fin test rig and instrumentation described in Chapter Four. While they are a powerful tool for understanding the performance of fins, they are by no means the only one. At times in this thesis, visual observations of the fins' behaviour were cited, and were of value in forming conclusions about the performance of fins. A more robust method of recording the motion of fins would be an important area for future studies to address.

The relationship between fin tip deflection, thrust power, and efficiency would be an interesting one to study, but tip deflection is only a valid measure of fin deformation if the fin is oscillating in its lowest resonant mode. Figure 111 illustrates the difficulty of assessing fin deformation with a single measurement. A more reliable method would be to record the mode of oscillation, in terms of the number or fraction of complete waves observed at a point in time. Alternatively the amplitude of the fin's deviation at several points along its chord could be measured. Techniques such as these would require good quality high-speed footage of the

fin in motion, combined with either image processing software to perform the analysis, or scrutiny of selected frames by a human analyst.

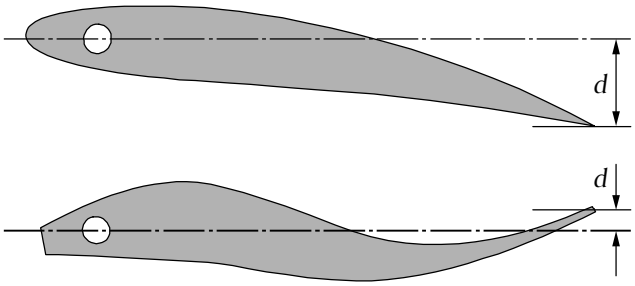

Figure 111: Measuring deformation of a flexible fin.

7.3.3 Intermediate Material Stiffnesses

The tests described in this thesis used fins made from two different resin compounds. The softer of the two compounds was the most flexible moulding resin readily available, and the fin made from the harder compound generated forces at the limit of magnitude that could be measured by the test rig. The two resins therefore spanned the entire range that would have been practical to test with the available equipment and resources. Without changes to the test equipment, the range of stiffnesses between those already tested provides room for further study, although the similarity of the graphs plotted for hard and soft resins in Chapter Six suggests there is less to be gained than from other avenues of further study. Looking beyond the materials already tested, to create harder and softer fins, including testing of a rigid fin, would require changes to be made to the test equipment, but would give interesting insights into the relationship between material stiffness and the performance of a fin. An alternative approach could be to reduce the size of the fins being tested, thus allowing a wider range of stiffnesses without overloading the rig. A good understanding of the effects of scaling on the fins would be necessary to this approach; this topic is discussed further in Section 7.3.8 (page 158).

The relationship between optimal frequency and maximum thrust is a potential area for further study, and the data gathered thus far created an interesting, but somewhat sparse graph (Figure 110, page 147). Basic conclusions were drawn from it, but extra data will be needed to determine what kind of relationship, if any, links the maximum mean thrust of a fin with the frequency at which it is achieved.

These two variables were of particular interest in this thesis because they had a bearing on the central hypothesis being tested (see Section 6.4.5, page 149). With extra data, other variables could be studied in relation to fin stiffness, such as power consumption, lateral force, and thrust consistency, shedding further light on the factors influencing fin performance.

7.3.4 Different Stiffness Profiles

Modelling the biomimetic fin on the body of a pumpkinseed sunfish was a decision taken at an early stage in the study, and yielded many interesting results. The reasons for the decision are discussed in Section 5.2.1 (page 110). There are, however, many other possible sources of stiffness data that could have served equally well. A possible direction for further study would be to compare alternative biomimetic fin designs from a variety of sources. For example, the local stiffness along the fin rays of a pumpkinseed sunfish have been measured in previous work (Lauder, *et al.*, 2006), and would provide an interesting contrast.

7.3.5 Real-World Applications

The trigger for the investigations documented in this thesis was the Bathymysis unmanned submarine, whose design is discussed in Appendix A. Its utilisation of crude flexible fins for propulsion prompted the subsequent literature study, and the experiments that followed. A satisfying extension to the work carried out so far would be to apply the insights gained experimentally to the Bathymysis, creating an improved submarine, able to generate more thrust and consume less power, through the use of optimised fins. The biomimetic fin design would be a good candidate for use on the submarine, and although the fins would need to be scaled up to produce adequate thrust, the information gained from the investigations in this thesis would be helpful in optimising its actuation methods.

Applying the fins to a submarine would enable real-world performance tests that go far beyond those possible with a single fin. A good example of the kind of novel investigations that can be carried out on biomimetic swimming robots is found in Madeleine (Long, *et al.*, 2006), the four-finned robot submarine produced by Vassar College and reviewed in Section 2.9.4 (page 50).

The Bathymysis submarine was a group project, and continued to undergo many revisions and upgrades after those discussed in Appendix A. Sadly, this meant it would have been impractical to revert it to its original, finned form. Even if a refit had been completed, its internal design and methods of operation were so different from those of the original submarine that comparison with its former self would have been fruitless. Consequently, at the time of writing, the biomimetic fins researched in this thesis have not been incorporated into the submarine. A number of projects have, however, sprung from the original work on the Bathymysis, including a number of novel propulsion technologies.

7.3.6 Flowing Water Tests

The experiments in Chapter Five and Chapter Six both gathered data from fin tests in standing water, rather than from a flow tank. While static thrust is an accepted and helpful measure of a fin or propeller's performance, data for each fin in moving water is important to gain a complete picture of their performance in relation to each other. This is therefore recommended as a priority for future research.

Bollard efficiency is a useful method of comparing one fin's performance with another, but cannot take the place of real efficiency data, derived from power flowing into and out of the fin. Since a fin in stationary water exerts force without movement, its output power will always be zero regardless of its effectiveness at generating thrust. Discussions of energy efficiency will be relevant only when measurements of thrust and forward speed can be taken simultaneously.

Any future sets of experiments using a flowing water test tank should test fins at a range of speeds, up to that at which their net thrust is zero. This encompasses the range of speeds at which a fin may be used as a propulsor in a real-world application. In practice, a propulsor would never operate under zero net thrust conditions, where the thrust and drag on the fin are equal and balance each other out, allowing it to move at constant speed. This is because there will always be an additional drag force acting on the fin: that of the body being propelled.

To gather data similar to that presented in this thesis, but at a range of flow velocities, would require many more experiments to be performed, and necessitate an expansion of the automated testing methods described in the previous chapters. The test rig software would need to be given closed-loop control of the stream velocity in a flow tank. It could then be programmed to carry out large numbers of experiments without human intervention. The analysis methods would also need to be expanded, in order to extract useful information from the experimental data.

7.3.7 Flow Visualisation Techniques

Methods of flow visualisation, such as Particle Image Velocimetry (PIV) or dye trails could give valuable insights into the performance of the fins. While analysing the force-time profile of a fin helps to reveal its interactions with the water and the reasons for its behaviour, a much fuller picture of the fin's performance can be gained from looking at the way vortices are created, and how they interact with each other, and the fin itself.

Previous work makes frequent use of PIV systems, but other methods of flow visualisation are gaining popularity. In several hydrodynamic studies at the Massachusetts Institute of Technol-

ogy used fluorescent dye to highlight and analyse the vortices in the wake of an object. Dye can be imparted to the water either by applying it as a soluble coating to the fins under test, or releasing it under slight pressure from an opening on, or close to, the fin.

Improvements in PIV software are making it easier to analyse wake patterns without the use of complex and expensive laser and imaging equipment. This is making simple flow analysis more practical for investigations that might otherwise have used more conventional methods to analyse flow characteristics. Future work building on this thesis would gain greatly from use of these recently developed technologies.

7.3.8 Fin Dimensions

All of experiments documented in this thesis were carried out on fins of the same length and height. While this was necessary to keep the variable space manageable, a good next step would be to determine, by experimentation, the effects of scaling the fins in different directions. Greater understanding in this area would aid the design of fins for real-world applications, such as the Bathymysis, which would require larger fins than those tested.

The Reynolds number at which fins operate is only one factor in the relationship, since the fins are intended to operate at a range of flow speeds, down to zero. Also, the stiffness properties of the fin will not scale in the same way as the effects on the surrounding fluid, making the interaction between the two is a complex problem. However, a good understanding of the relationships governing the scaling of flexible fins would allow fins to be tested on a much smaller scale than that at which they are intended to be used. Smaller fins would require smaller testing facilities, and would be easier to actuate over a wide range of frequencies and amplitudes.

Another area in need of further study relating to the fin's dimensions is aspect ratio. While previous work (Hobson, *et al.*, 2003) identified an aspect ratio of 1:1 as being optimal, this research was carried out at a private research establishment, and not all of the data leading to its conclusions has been made available. Further investigation is therefore warranted, to confirm the finding, and to provide data supporting it. A series of experiments could be carried out, starting with a fin of high aspect ratio, perhaps 2:1, which could then be trimmed in steps, down to a low aspect ratio, around 1:5. The re-use of the same fin in multiple tests would remove the need for several fins to be cast for each experiment.

7.3.9 Decoupling Stiffness Profile from Shape Profile

In a homogenous fin, stiffness profile is dictated by shape. The only way to truly isolate their effects from each other would be to develop a manufacturing method able to create fins in which the shape and stiffness profile are independent from each other.

One way of achieving this would be to compute a two-dimensional internal structure with a given stiffness profile, and manufacture it using an accurate method such as laser cutting. This 'skeleton' could then be encased it in a relatively soft layer of silicone rubber of any shape; even a flat sheet. An example is shown in Figure 112, in which the darker areas represent a stiffer material, and the lighter background a highly flexible silicone resin.

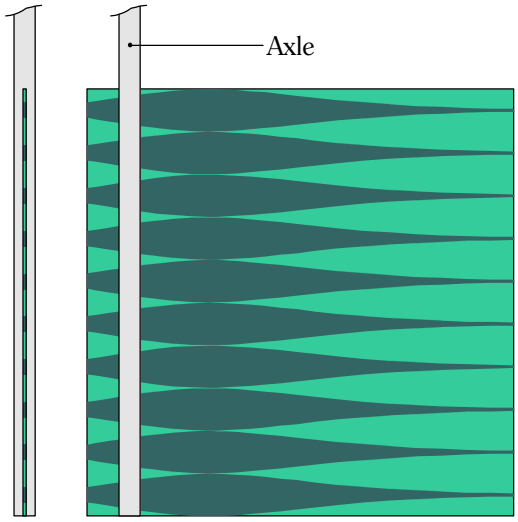

Figure 112: Example of a flat fin using a biomimetic stiffness profile.

For shapes other than a flat sheet, the stiffness profile of the soft rubber compound would have to be taken into account and offset by the stiffness profile of the internal structure.

7.3.10 Numerical Studies

An entirely different approach to understanding flexible fins is to use numerical modelling in stead of, or more realistically, as a supplement to, experiments. Numerical studies have the advantage of being able to test a far wider range of variables than would be possible in experiments, but fluid interactions are hard to model, and take a great deal of processing power, especially when dealing with three-dimensional models. Using a combination of Finite Element Analysis (FEA) to model the fin, and Computational Fluid Dynamics (CFD) to model the water surrounding it, a complete dynamic model of the functioning fin could be built, and used to explore many aspects of the fin's design and actuation that would be hard to test experimentally.

7.3.11 Unconstrained Lateral Motion

In all the experiments of Chapter Five and Chapter Six, the fins as they were constrained in all axes, so that the forces they generated could be measured. In this configuration, the fin's axle exerted a force on the fin, often several times larger than the thrust, to keep it from moving laterally; this is discussed in Section 5.4.2 (page 121). However, the fin actuator was also

capable of oscillating fins without constraining them in the lateral direction. This design feature was included as an aid to future experiments, in which the effect of lateral force being applied to the fin could be observed. The fin axle was supported at the top of the rig by a low-backlash universal joint, coupled to the servomotor. The bottom of the axle was bonded to the fin, and in the middle, it was supported by a bearing. The bearing could either be clamped in the centre of the rig, to support the axle rigidly, or released, to roll freely from one side of the rig to the other, in an arc centring on the universal joint. The set-up is shown diagrammatically in Figure 113, with the fin in two different positions. In the diagram the axle has been truncated, which emphasizes the rotation of the fin about the *x* axis; in reality the fin moves in a much flatter arc.

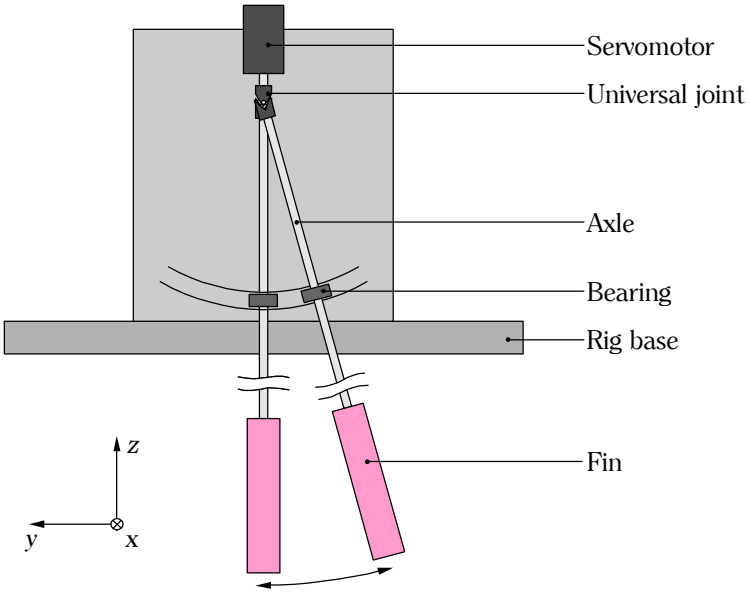

Figure 113: Front view of fin actuator mechanism.

To perform the same sets of experiments again, without applying lateral force to the fins, would be an interesting avenue of study. However, the control and measurement systems on the test rig would need improvement to make this possible. Without lateral constraint, the fin would have a tendency to wander to one side of the rig under its own net lateral force. The control system would need either to counter this actively, or to be accurate enough that the fin drifts by only a negligible amount throughout each fin test. Also, the force measurement system currently depends on the forces and torque acting on the fin at a known location. Movement of the fin from side to side would require a revision of the force equations derived in Section 4.4.2 (page 76), to account for the changing instantaneous fin location.

It is possible that with no means of reacting forces in the *y* direction, the thrust production would decrease. However, allowing the fin to follow a path in which only thrust can be

generated may facilitate greater efficiency. With extra data, the relationship between lateral force and thrust could be explored further.

7.3.12 New Rapid Prototyping Technologies

Rapid Prototyping (RP) technology is advancing at a considerable rate. Some of the fin manufacturing methods devised for the purposes of this thesis relied on technologies that have since been improved or made more cost-effective. Other techniques that were judged to be unworkable at the time of writing are becoming more viable due to new RP technologies.

Recent advances are allowing RP models to be built directly from flexible resins, removing the need for resin casting altogether. It is even possible to combine resins of different stiffness in complex structures within the same model, opening the way for complex biomimetic fin replicas to be built, with greater speed and accuracy than has previously been possible. The technology removes the need for a fin's stiffness profile to be dictated by its shape, allowing the effects of both to be studied in isolation from each other, as has been proposed in Section 7.3.9 (page 158).

7.3.13 Fin Profile Optimisation

So far, only two stiffness profiles have been tested in this investigation, and one has been found to exhibit better performance than the other. Another goal of future experiments should be to optimise the design of the fins, through a repeated cycle of testing and modification. To achieve this through physical testing alone would be prohibitively time consuming, so such a process would require numerical modelling techniques, as described in Section 7.3.10 (page 159). If an accurate method could be developed for testing fin designs numerically, genetic or neural optimisation methods could then be used to improve the designs iteratively.

7.3.14 Active Stiffness Control

Another direction in which the research may be taken is to alter the stiffness of a fin while it is in use. Stiffness could then be optimised for different oscillation conditions. A team at the University of Bath has recently begun working in collaboration with several other universities, under a project examining fish locomotion and sensing, funded by the European Union[9]. One of the goals of the collaboration is the creation of a biomimetic propulsion model with an internal structure allowing its stiffness to be varied while in use. It is hoped that this project may be able to make use of, and further some of the ideas presented in this thesis.

[9] Fish Locomotion and Sensing (FILOSE) - www.filose.eu

References

1. Ahlborn, B., Chapman, S., Stafford, R., and Harper, R., 1997. Experimental simulation of the thrust phases of fast-start swimming of fish, pp. 2301-2312.
2. Ahlborn, B., Harper, D., Blake, R., Ahlborn, D., and Cam, M., 1991. Fish without footprints. Journal of Theoretical Biology 148, 521-533
3. Alben, S., 2008. Optimal flexibility of a flapping appendage in an inviscid fluid. Journal of Fluid Mechanics 614, 355-380.
4. Alben, S., Madden, P. G., and Lauder, G. V., 2007. The mechanics of active fin-shape control in ray-finned fishes. Journal of the Royal Society Interface 4, 243-256.
5. Alben, S., and Shelley, M., 2005. Coherent locomotion as an attracting state for a free flapping body. Proceedings of the National Academy of Sciences of the United States of America 102, 11163-11166.
6. Alvarado, P. V. Y., and Youcef-Toumi, K., 2006. Design of machines with compliant bodies for biomimetic locomotion in liquid environments. Journal of Dynamic Systems Measurement and Control-Transactions of the Asme 128, 3-13.
7. Anderson, J. M., and Kerrebrock, P. A., 1999. Vorticity Control Unmanned Undersea Vehicle (VCUUV) - An Autonomous Robot Tuna. Proceedings of the Unmanned Untethered Submersible Technology Symposium 1999.
8. Anderson, J. M., Streitlien, K., Barrett, D. S., and Triantafyllou, M. S., 1998. Oscillating foils of high propulsive efficiency. Journal of Fluid Mechanics 360, 41-72.
9. Askeland, D. R., and Phulé, P. P., 1989. The science and engineering of materials. Thompson.
10. Bandyopadhyay, P. R., Low-Speed Maneuvering Hydrodynamics of Fish and Small Underwater Vehicles. Annual Meeting of the Society-for-Integrative-and-Comparative-Biology, Chicago, Illinois, 2001, pp. 102-117.
11. Bandyopadhyay, P. R., 2005. Trends in biorobotic autonomous undersea vehicles. Oceanic Engineering, IEEE Journal of 30, 109-139.
12. Bandyopadhyay, P. R., Castano, J. M., Nedderman, W. H., and Donnelly, M., J., 2000. Experimental Simulation of Fish-Inspired Unsteady Vortex Dynamics on a Rigid Cylinder. 122, 219-238.
13. Behkam, B., and Sitti, M., Modeling and Testing of a Biomimetic Flagellar Propulsion Method for Microscale Biomedical Swimming Robots. Advanced Intelligent Mechatronics. Proceedings, 2005 IEEE/ASME International Conference on, 2005, pp. 37-42.
14. Breder, C. M., 1926. The Locomotion of Fishes. Zoologica IV, 159-297.
15. Breder, C. M., 1965. Vortices and Fish Schools. Zoologica New York 50, 97-114.

16. Brindlinger, G., Fan, T., Jones, M., and Lai, M., 2006. Group Project Report. University of Bath.
17. Buchholz, J. H. J., and Smits, A. J., 2005. On the evolution of the wake structure produced by a low-aspect-ratio pitching panel. 546, 433-443.
18. Carlton, J., 1994. Marine propellers and propulsion. Butterworth-Heinemann.
19. Chen, I. M., Li, H. S., and Cathala, A., 2003. Mechatronic design and locomotion of amoebot - A metamorphic underwater vehicle. Journal of Robotic Systems 20, 307-314.
20. Collins, K. M., 2006. Bathymysis - The BURST AUV. In: DSTL, (Ed., (SAUC-E) 2006 - Journals. University of Bath, Bath.
21. Combes, S. A., and Daniel, T. L., 2003a. Flexural stiffness in insect wings I. Scaling and the influence of wing venation. Journal of Experimental Biology 206, 2979-2987.
22. Combes, S. A., and Daniel, T. L., 2003b. Flexural stiffness in insect wings II. Spatial distribution and dynamic wing bending. Journal of Experimental Biology 206, 2989-2997.
23. Dong, H., Mittal, R., and Bozkurttas, M., 2005. Wake Structure and Performance of Finite Aspect-Ratio Flapping Foils, 43rd AIAA Aerospace Sciences Meeting and Exhibit. AIAA, Reno, Nevada.
24. Dudek, G., Prahacs, C., Saunderson, S., Giguere, P., Sattar, J., and Jenkin, M., 2008. Amphibious robotic device. In: Office, U. P., (Ed., USA.
25. Epps, B. P., Alvarado, P. V. y., Youcef-Toumi, K., and Techet, A. H., 2009. Swimming performance of a biomimetic compliant fish-like robot. Experiments in Fluids 47, 927-939.
26. Farnell, D. J. J., David, T., and Barton, D. C., 2005. Numerical model of self-propulsion in a fluid. J. R. Soc. Interface 2, 79-88.
27. Fish, F. E., 1996. Transitions from drag-based to lift-based propulsion in mammalian swimming. American Zoologist 36, 628-641.
28. Gopalkrishnan, R., Triantafyllou, M. S., Triantafyllou, G. S., and Barrett, D., 1994. Active Vorticity Control in a Shear Flow Using a Flapping Foil. Journal of Fluid Mechanics 274, 1-21.
29. Guglielmini, 2004. Modelling of thrust generating foils, University of Genoa.
30. Heathcote, S., and Gursul, I., 2007. Flexible flapping airfoil propulsion at low Reynolds numbers. AIAA Journal 45, 1066-1079.
31. Heathcote, S., Martin, D., and Gursul, I., 2004. Flexible flapping airfoil propulsion at zero freestream velocity. AIAA Journal 42, 2196-2204.
32. Heathcote, S., Wang, Z., and Gursul, I., 2008. Effect of spanwise flexibility on flapping wing propulsion. Journal of Fluids and Structures 24, 183-199.

33. Hobson, B., and Kemp, M., 2002. Integration of a Hovering Module with the Morpheus AUV. IEEE Journal of Oceanic Engineering.
34. Hobson, B., Kemp, M., Le Goff, I., and Leonessa, A., Oscillating fin thrusters for multi-view classification maneuvering on MCM UUVs. Oceans 2003 MTS/IEEE: Celebrating the Past...Teaming toward the Future, 2003, pp. 2167-2169.
35. Horlock, J. H., 1978. Actuator Disk Theory: Discontinuities in Thermo Fluid Dynamics. McGraw-Hill.
36. Hover, F. S., Haugsdal, O., and Triantafyllou, M. S., 2004. Effect of angle of attack profiles in flapping foil propulsion. Journal of Fluids and Structures 19, 37-47.
37. Jacobs, E. N., Ward, K. E., and Pinkerton, R. M., 1933. The Characteristics of 78 Related Airfoil Sections from Tests in the Variable-Density Wind Tunnel. National Advisory Committee for Aeronautics.
38. Jones, E. A., Lucey, K. S., and Ellerby, D. J., 2007. Efficiency of labriform swimming in the bluegill sunfish (Lepomis macrochirus). 210, 3422-3429.
39. Kármán, T. V., and Burgess, J. M., 1935. General aerodynamic theory: perfect fluids. In: Durand, W. F., (Ed., Aerodynamic Theory, vol. II. Springer Verlag, Leipzig.
40. Kemp, M., and Hobson, B., Assessing Performance of Oscillating Foil Thrusters. Unmanned Untethered Submersible Technology Symposium 2001, Durham, NH, 2001.
41. Kemp, M., Hobson, B., and Pell, C., 2003. Energetics of the Oscillating Fin Thruster, Unmanned Untethered Submersible Technology Symposium 2003, Durham, NH.
42. Klimaytys, G., 2006. The Design of an Artificially Intelligent Control System for an Automated Underwater Vehicle. University of Bath.
43. Kobayashi, S., Nakabayashi, M., and Morikawa, H., 2006. Bioinspired Propulsion Mechanism in Fluid Using Fin with Dynamic Variable-Effective-Length Spring. Journal of Biomechanical Science and Engineering 1, 280-289.
44. Koochesfahani, M. M., 1989. Vortical Patterns in the Wake of an Oscillating Airfoil. AIAA Journal 27, 1200-1205.
45. Lai, J. C. S., and Platzer, M. F., 1999. Jet characteristics of a plunging airfoil. AIAA Journal 37, 1529-1537.
46. Lang, A. W., Motta, P., Hidalgo, P., and Westcott, M., 2008. Bristled shark skin: a microgeometry for boundary layer control? Bioinspiration & Biomimetics 3, Article No.: 046005.
47. Lauder, G., and Madden, P., 2007. Fish locomotion: kinematics and hydrodynamics of flexible foil-like fins. Experiments in Fluids 43, 641-653.
48. Lauder, G. V., 2000. Function of the Caudal Fin During Locomotion in Fishes: Kinematics, Flow Visualization, and Evolutionary Patterns. American Zoology 40, 101-122.

49. Lauder, G. V., How fishes swim: flexible fin thrusters as an EAP platform. Electroactive Polymer Actuators and Devices (EAPAD) 2007, San Diego, California, USA, 2007, pp. 652402-652408.
50. Lauder, G. V., and Drucker, E. G., 2002. Forces, Fishes, and Fluids: Hydrodynamic Mechanisms of Aquatic Locomotion. 17, 235-240.
51. Lauder, G. V., Madden, P. G. A., Mittal, R., Dong, H. B., and Bozkurttas, M., 2006. Locomotion with flexible propulsors: I. Experimental analysis of pectoral fin swimming in sunfish. Bioinspiration & Biomimetics 1, S25-S34.
52. Lentink, D., Muijres, F. T., Donker-Duyvis, F. J., and van Leeuwen, J. L., 2008. Vortex-wake interactions of a flapping foil that models animal swimming and flight. 211, 267-273.
53. Liao, J. C., Beal, D. N., Lauder, G. V., and Triantafyllou, M. S., 2003. Fish exploiting vortices decrease muscle activity. Science 302, 1566-1569.
54. Licht, S., Polidoro, V., Flores, M., Hover, F. S., and Triantafyllou, M. S., 2004. Design and projected performance of a flapping foil AUV. IEEE Journal of Oceanic Engineering 29, 786-794.
55. Lindsey, C. C., 1978. Form, function and locomotory habits in fish. In: Hoar, W. S., and Randall, D. J., (Eds.), Fish Physiology, vol. VII.
56. Liu, J., Dukes, I., Knight, R., and Hu, H., 2004. Development of fish-like swimming behaviours for an autonomous robotic fish. Control 2004, Bath, UK.
57. Long, J. H., McHenry, M. J., and Boetticher, N. C., 1994. Undulatory Swimming - How Traveling Waves Are Produced and Modulated in Sunfish (Lepomis-Gibbosus). Journal of Experimental Biology 192, 129-145.
58. Long, J. H., and Nipper, K. S., 1996. The importance of body stiffness in undulatory propulsion. American Zoologist 36, 678-694.
59. Long, J. H., Schumacher, J., Livingston, N., and Kemp, M., 2006. Four flippers or two? Tetrapodal swimming with an aquatic robot. Bioinspiration & Biomimetics 1, 20-29.
60. Lu, X. Y., and Yin, X. Z., 2005. Propulsive performance of a fish-like travelling wavy wall. Acta Mechanica 175, 197-215.
61. McHenry, M. J., Pell, C. A., and Long, J. J., Jr., 1995. Mechanical control of swimming speed: stiffness and axial wave form in undulating fish models. Journal of Experimental Biology 198, 2293-2305.
62. Nakabayashi, M., Kobayashi, R., Kobayashi, S., and Morikawa, H., 2009. Bioinspired Propulsion Mechanism Using a Fin with a Dynamic Variable-Effective-Length Spring - Evaluation of Thrust Characteristics and Flow around a Fin in a Uniform Flow. Journal of Biomechanical Science and Engineering 4, 82-93.
63. Nudds, R. L., Taylor, G. K., and Thomas, A. L. R., 2004. Tuning of Strouhal number for high propulsive efficiency accurately predicts how wingbeat frequency and stroke ampli-

tude relate and scale with size and flight speed in birds. Proceedings of the Royal Society of London Series B-Biological Sciences 271, 2071-2076.

64. Pattinson, C., 2006. High Efficiency Propulsion for Autonomous Underwater Vehicles. University of Bath.
65. Prempraneerach, P., Hover, F. S., and Triantafyllou, M. S., The effect of chordwise flexibility on the thrust and efficiency of a flapping foil. 13th International Symposium on Unmanned Untethered Submersible Technology, Durham, NH, 2003.
66. Punning, A., Anton, M., Kruusmaa, M., and Aabloo, A., A Biologically Inspired Ray-like Underwater Robot with Electroactive Polymer Pectoral Fins. IEEE Mechatronics and Robotics, Aachen, Germany, 2004, pp. 241-245.
67. Read, D. A., Hover, F. S., and Triantafyllou, M. S., 2003. Forces on oscillating foils for propulsion and maneuvering. Journal of Fluids and Structures 17, 163-183.
68. Rediniotis, O. K., Wilson, L. N., Lagoudas, D. C., and Khan, M. M., 2002. Development of a shape-memory-alloy actuated biomimetic hydrofoil. Journal of Intelligent Material Systems and Structures 13, 35-49.
69. Riggs, P., 2006. Technical Description of the Bathymysis, a Multi-purpose Biomimetic Submersible Robot, International Conference of Bionics Engineering, Changchun, China.
70. Riggs, P., 2006. Use of Oscillating Fins in Propulsion and Liquid Handling. University of Bath.
71. Roark, R. J., 1943. Roark's formulas for stress and strain. McGraw-Hill.
72. Schnipper, T., Andersen, A., and Bohr, T., 2009. Vortex wakes of a flapping foil. Journal of Fluid Mechanics 633, 411-423.
73. Sellen, R. G., 2006. The WaveDrive: A Biomimetic Undulating Fin Device. University of Bath.
74. Sfakiotakis, M., Lane, D. M., and Davies, J. B. C., 1999. Review of Fish Swimming Modes for Aquatic Locomotion. IEEE Journal of Oceanic Engineering 24, 237-252.
75. Shin, S., Bae, S. Y., Kim, I. C., and Kim, Y. J., 2009. Effects of flexibility on propulsive force acting on a heaving foil. Ocean Engineering 36, 285-294.
76. Shin, S., and Kim, H. T., 2008. Numerical simulation of fluid-structure interaction of a moving flexible foil. Journal of Mechanical Science and Technology 22, 2542-2553.
77. Terada, Y., and Yamamoto, I., 2004. An animatronic system including lifelike robotic fish. Proceedings of the IEEE 92, 1814-1820.
78. Thomson, E. A., 1997. 'Penguin boat' plies the Charles, MIT Tech Talk.
79. Triantafyllou, G. S., Triantafyllou, M. S., and Grosenbaugh, M. A., 1993. Optimal Thrust Development in Oscillating Foils with Application to Fish Propulsion. Journal of Fluids and Structures 7, 205-224.

80. Triantafyllou, M. S., Techet, A. H., and Hover, F. S., 2004. Review of Experimental Work in Biomimetic Foils. IEEE Journal of Oceanic Engineering 29, 585-594.
81. Triantafyllou, M. S., and Triantafyllou, G. S., 1995. An efficient swimming machine, Scientific American.
82. Triantafyllou, M. S., Triantafyllou, G. S., and Gopalkrishnan, R., 1991. Wake Mechanics for Thrust Generation in Oscillating Foils. Physics of Fluids 3, 2835-2837.
83. Tuncer, I. H., and Kaya, M., 2005. Optimization of flapping airfoils for maximum thrust and propulsive efficiency. AIAA Journal 43, 2329-2336.
84. Vandenberghe, N., Zhang, J., and Childress, S., 2004. Symmetry breaking leads to forward flapping flight. Journal of Fluid Mechanics 506, 147-155.
85. Wallis, C. L. B., 2006. An Investigation into Computer Vision Techniques for Underwater Object Recognition. University of Bath.
86. Wardle, C. S., Videler, J. J., Arimoto, T., Franco, J. M., and He, P., 1989. The Muscle Twitch and the Maximum Swimming Speed of Giant Bluefin Tuna, Thunnus-Thynnus L. Journal of Fish Biology 35, 129-137.
87. Waterhouse, G., 2006. Performance Enhancement of a Low Cost Underwater Vehicle Hull. University of Bath.
88. Webb, P. W., 1984. Form and Function in Fish Swimming. Scientific American 251, 72-82.
89. Weihs, D., 1973. Hydromechanics of Fish Schooling. Nature 241, 290-291.
90. Wilga, C. D., and Lauder, G. V., 2004. Hydrodynamic function of the shark's tail. Nature 430, 850.
91. Yu, J. Z., Tan, M., Wang, S., and Chen, E., 2004. Development of a biomimetic robotic fish and its control algorithm. IEEE Transactions on Systems Man and Cybernetics Part B-Cybernetics 34, 1798-1810.
92. Yu, J. Z., Wang, L., and Tan, M., 2005. A framework for biomimetic robot fish's design and its realization, Acc: Proceedings of the 2005 American Control Conference, Vols 1-7, pp. 1593-1598.
93. Yu, J. Z., Wang, S., and Tan, M., Basic motion control of a free-swimming biomimetic robot fish. 42nd IEEE Conference on Decision and Control, 2003, pp. 1268-1273.
94. Yu, J. Z., Wang, S., and Tan, M., Design of a free-swimming biomimetic robot fish. 2003 IEEE / ASME International Conference on Advanced Intelligent Mechatronics (AIM 2003), 2003, pp. 95-100.
95. Zhu, Q., and Shoele, K., 2008. Propulsion performance of a skeleton-strengthened fin. Journal of Experimental Biology 211, 2087-2100.

Appendices

Appendix A : Bathymysis Submarine Project

A.1 Introduction

Early on in the investigations described in this thesis, the opportunity arose to design and build an underwater Remotely Operated Vehicle (ROV) for use in a variety of applications within the research interests of the University of Bath (Figure 114). The specification was for a small unmanned robotic submarine, propelled by oscillating fins. It was devised to address a specific research need, but gave rise to many questions; these set the course of the subsequent experiments and studies, documented in this thesis. The submarine was named Bathymysis, derived from Bath, the city, *bathos*, Greek for depth, and *Mysid*, the water-dwelling crustacean the submarine was, in part, designed to search for.

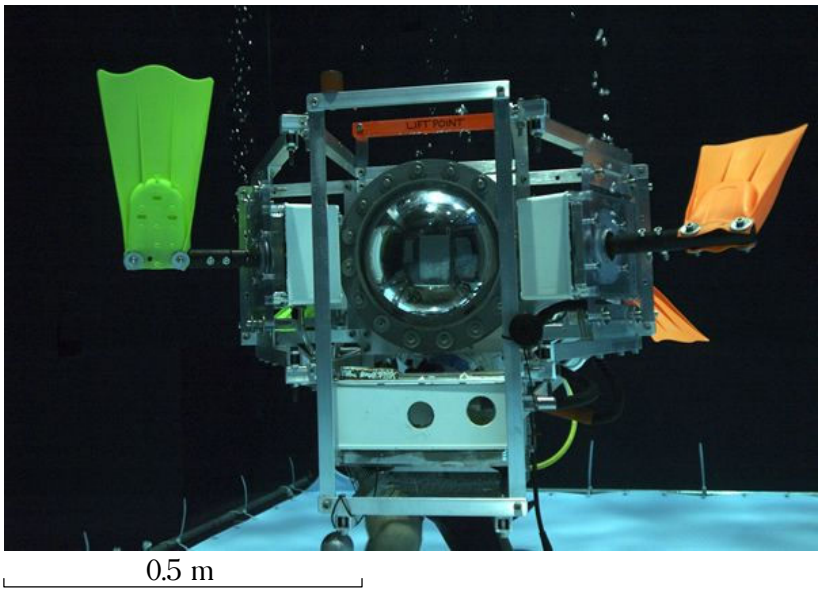

Figure 114: Bathymysis submarine.

Its uses to date have been:

- Serving as an experimental and educational tool to help students gain an interest in, and learn about underwater vehicle design.
- Playing a part in coastal ecology research, specifically by allowing biologists to search for Mysids, a food source of Grey Whales.

- Being used as an experimental platform for flexible fins, to allow assessment of fin performance in a real-world application.
- Serving as an exercise in developing a useful submarine at a low cost, through which expertise was gained to aid future submarine projects.
- Taking part, in a modified form, in the SAUC-E student autonomous submarine competition.

Bathymysis was a cooperative project; the result of the hard work of a team comprising academics, technicians and students. The individuals involved in the construction of the submarine are thanked in the acknowledgements section of this thesis. The author acted as the submarine's lead designer from its conception through to its first missions, and takes responsibility, but not credit, for all the design decisions described below. Where others took a greater role in the design of one of the submarine's systems or components, their work is documented for completeness, and they are duly referenced in the relevant sections.

A.2 Specifications

The requirements originally presented for the submarine's design were as follows. Its size and weight had to be small enough to be manageable in the field by one or two people, and able to be transported around the world without special shipping arrangements. It was intended for use in outdoor field studies, so had to be robust enough to survive the challenges this can bring, and able to be assembled and repaired using basic equipment and tools. It was to be propelled by experimental oscillating fins, to test their effectiveness in a real world application, and to make the submarine less susceptible to becoming tangled in reeds and kelp. It had to be versatile enough to support various cameras and experimental equipment, and to be capable of descending to a depth of 40 m.

The sections below break the design of Bathymysis down into categories, and explain the reasons behind the decisions that were made.

A.3 Submarine Structure

The submarine's structure comprised an external aluminium frame; a central hull, a long PVC cylinder in the centre of the frame; and a chassis inside the hull, supporting the internal components. Figure 115 is a CAD model of the submarine, with some parts removed for clarity.

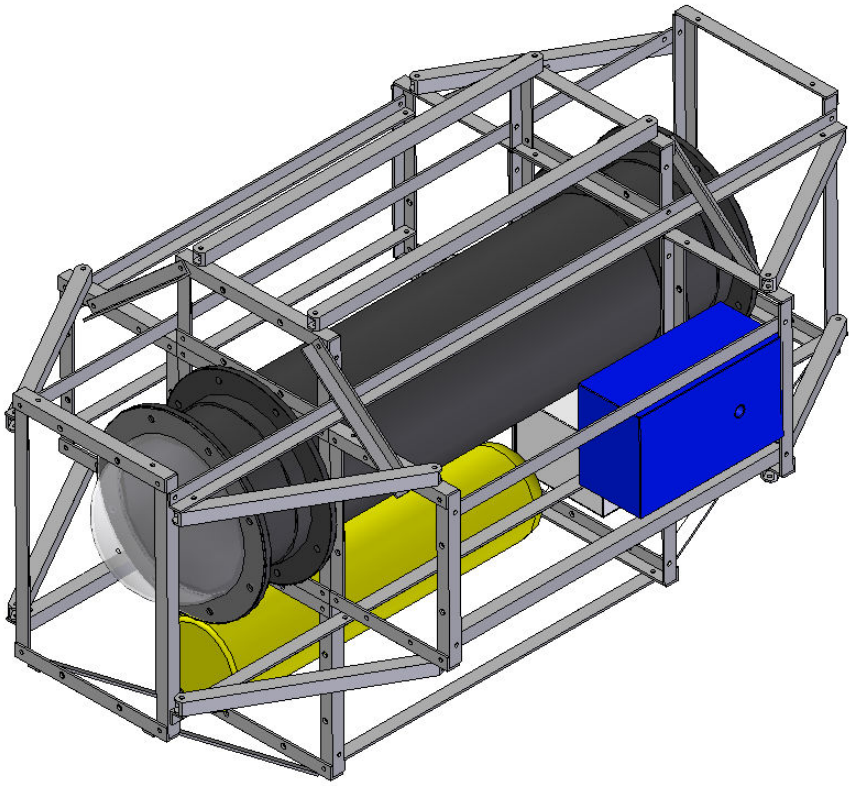

Figure 115: CAD visualisation of the Bathymysis submarine, showing the chassis and hull.

A.3.1 Hull

An important factor in keeping the total cost of the project down was the use of off-the-shelf components wherever possible, in place of bespoke manufactured parts. The submarine's hull was made of an 800 mm length of PVC ventilation pipe, 200 mm in diameter, with a wall thickness of around 3 mm. Flanges were placed along the length of the pipe to provide mounting points, and allow it to be supported in the submarine's chassis. Flanges were carefully sealed to each end of the pipe with a solvent adhesive. These provided a flat surface, to which the end covers of the hull could be attached. The pipe and flanges were sourced from Wolseley UK[10].

The hull contained the most sensitive equipment in the submarine – its computer, batteries, camera and control electronics. Its purpose was to keep the components safe and dry when the submarine was submerged, but it did not have to withstand any static pressure, because the hull was designed to operate with its internal pressure in equilibrium with its surroundings. This is explained fully in Appendix A.4.2 (page 176).

[10] www.wolseley.co.uk

A.3.2 Chassis

The submarine's chassis was designed primarily by Steve Allen, an undergraduate student at the University of Bath, and not by the author of this thesis.

Purpose

The purpose of the chassis was to support and protect the components of the submarine. It acted as a cage, preventing the more fragile parts of the submarine from coming into contact with rocks and other obstacles on the seabed. It held the fin actuator units in position and allowed them to be positioned in different configurations, as shown in Figure 124 (page 184). The frame also allowed the submarine to be picked up, carried, and hoisted from the water, and provided a stable base on which to mount extra equipment.

Construction

The frame was constructed from 19 mm L-section and box-section aluminium beams, and 19 x 3 mm aluminium bar. It was designed to be easily assembled and disassembled in the field, and comprised a small number of distinct parts, with most duplicated in several locations. This design choice ensured that any part of the frame could be repaired if it sustained damage, with only a small number of parts needing to be kept as spares.

Corrosion

An important consideration in the design of structures to be used underwater is the effect of galvanic corrosion. Galvanic corrosion occurs when dissimilar metals are immersed in an electrolyte, such as seawater, causing a voltage potential to be induced between them. If the parts are electrically connected, current flows between them. The metal with the lowest electrode potential becomes the anode, and is subject to greatly accelerated corrosion.

The use of aluminium and stainless steel in the submarine's chassis meant it was vulnerable to galvanic corrosion. The aluminium, being the more reactive metal, was the material at risk. Various measures were considered to improve the design, such as painting the frame, adding insulating sleeves and washers to isolate the stainless steel nuts and bolts, or avoiding stainless steel hardware altogether in favour of nylon fasteners. Another common way of mitigating the effects of galvanic corrosion is the addition of a sacrificial electrode, connected to the other metallic parts of the craft. The electrode is made of a more reactive metal than those used elsewhere in the construction, and its purpose is to undergo gradual decomposition in place of the more important components.

After consideration of these options, a decision was taken to leave the frame unprotected. Its purpose required it to be submerged for only a few hours at a time, unlike, for example, a boat or waterborne structure. It was decided that the effort required to protect the chassis from

corrosion would be better spent elsewhere. To reduce the frame's exposure to seawater, whenever possible it was rinsed with fresh water after each mission. Over several uses of the submarine, some small deposits of aluminium oxide could be seen around the stainless steel bolts, but the corrosion was only at the surface of the parts, and no damage to the structure occurred.

A.3.3 Front Dome and Rear Bulkhead

The hull tube was sealed with end covers, designed to allow access to the hull, to enable internal cameras to see the outside world, and to allow electrical and other connections to be made between the inside and outside of the submarine.

Front dome

The clear polycarbonate dome at the front of the submarine allowed the internal camera to see its surroundings over a wide angle. Polycarbonate is an extremely tough material, and does not shatter under sudden impact, making it ideal for this use. The dome was made by vacuum forming a flat sheet of polycarbonate, using a 200 mm piping flange as a former. This is a difficult process, as polycarbonate contains trapped moisture that tends to vaporise when the plastic is heated, forming tiny bubbles and causing it to turn opaque. Special care has to be taken when heating and preparing the plastic to avoid this. Details of this process can be found in Appendix A.

The front dome was mounted to the submarine by eight stainless steel bolts, which compressed a rubber O-ring, forming a seal between the polycarbonate dome and the flange at the front of the hull, shown in Figure 116.

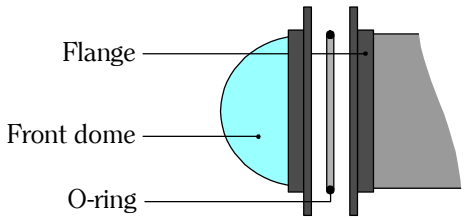

Figure 116: Attachment of front dome to the Bathymysis hull.

Rear panel

The rear panel was the only flat surface on the submarine's hull, so it was there that all of the connections to the outside world and the other parts of the submarine were mounted. The plate was initially affixed to the rear flange of the hull with eight bolts and an O-ring, using the same method as the front dome. It was made of polycarbonate sheet, 10 mm thick, and 270 mm in diameter. Holes were drilled in it to mount the various connectors required, and for the bolts to hold it in place.

Rear panel revision

The flexibility of the plastics used for the flange and rear panel meant that the rubber O-ring forming a seal between the two surfaces was not always compressed evenly. Variation in the tension of the bolts around the panel meant that the seal was not perfect, causing air to escape steadily from the submarine while submerged. Another drawback was that the rear panel was awkward to remove; its diameter was too large for it to be removed from the rear of the external chassis, so it had to be disconnected from the internal chassis before either could be extracted from the submarine.

In view of these shortcomings, the design was later revised to a 'plug' assembly, whereby the back panel was replaced by a cylindrical acrylic block, with O-rings occupying grooves in the sides (Figure 117). This redesign created a more reliable seal, because pressure was evenly distributed around the O-rings. It also allowed the back panel to be part of the internal chassis of the submarine, greatly simplifying the common task of extracting the submarine's battery, computer and electronics from the hull for maintenance.

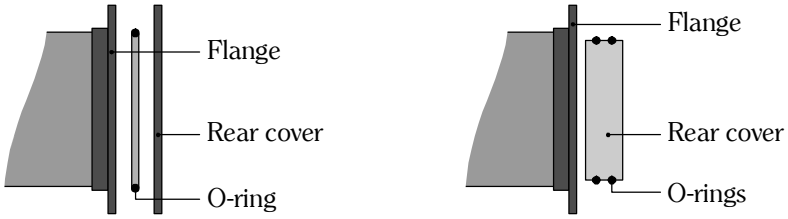

Figure 117: Rear panel assembly before (left) and after (right) revision.

The redesigned back panel was 25 mm in thickness, too thick to mount the connectors. To solve this problem, an IP68 rated waterproof container was mounted inside it, so that the enclosure's lid could be separated from the rear panel (Figure 118). The design had a number of advantages over the previous method. The wall of the enclosure inside the submarine acted as a bulkhead, meaning that in the improbable event of water leaking through any of the connectors, it would collect in the enclosure before coming into contact with any of the equipment within the hull. It also meant the arrangement of connectors on the rear panel could be changed with the purchase of a new waterproof enclosure, rather than necessitating the manufacture of an entire new rear panel.

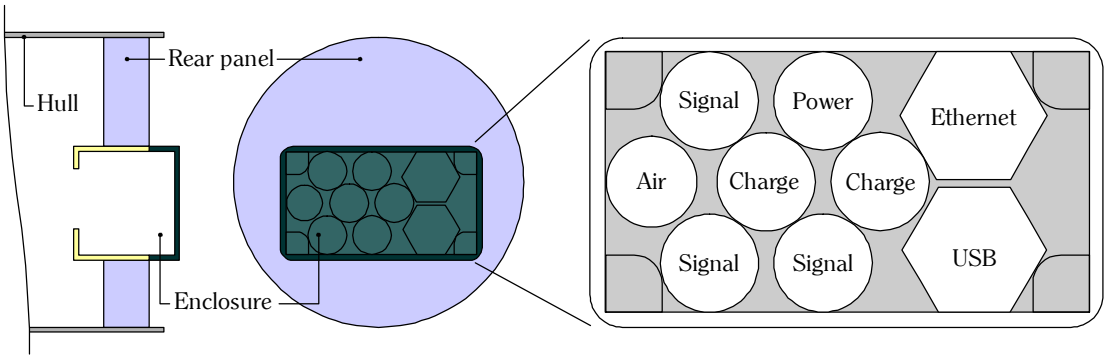

Figure 118: Layout of Bathymysis' rear panel assembly.

A.3.4 Internal Chassis

First design

All of the internal components were mounted on a frame located inside the submarine's hull. The frame could be pulled out of the hull to allow access to all of the parts. The frame was constructed from three parallel glass-fibre nylon composite rods with circular acrylic plates dividing the internal sections of the submarine. Shelves were supported between these dividers, which could be moved, along with the supporting walls, and reconfigured to allow efficient use of space. A picture of the submarines internal components is shown in Figure 119.

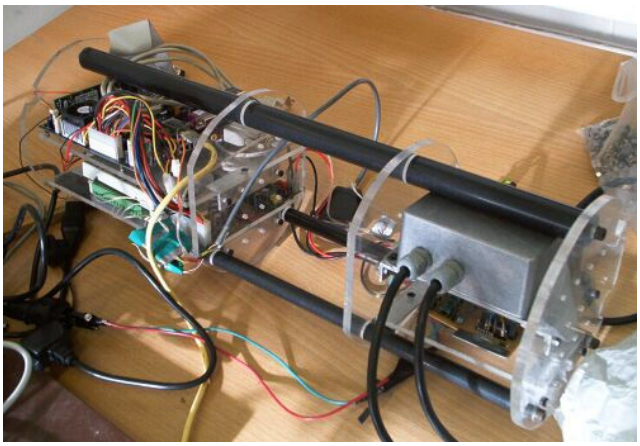

Figure 119: Bathymysis' internal structure.

The chassis served its purpose well; the only drawback to its design was that the shelves were time consuming to remove, being held in place by bolts, which were tricky to access. Frequent maintenance and modifications to the components during the design stage meant that a more convenient solution became necessary.

Updated design

This part of the design process was conducted by Keri Collins, a postgraduate student and member of the submarine team, not by the author of this thesis.

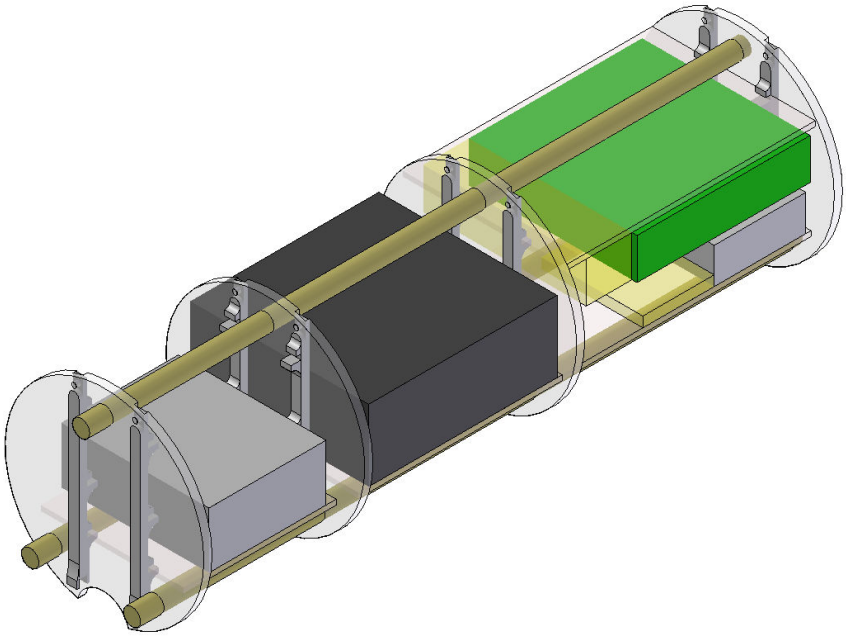

Figure 120: CAD model of the submarine's internal chassis.

When the rear panel of the submarine was redesigned, as described in Appendix A.3.3 (page 172), the opportunity was taken to modify the internal structure (Figure 120). New dividing walls were designed, to allow easier adjustment of the internal sections. The walls included replaceable rapid prototyped inserts to support the shelves, meaning the design was much more flexible in the event of changes and upgrades to the submarine's hardware. The redesign allowed the component shelves to be removed from the chassis sideways, without tools, and requiring no adjustment to the dividing walls.

Internal layout

The following configuration was selected for the internal layout of the submarine, shown in Figure 121:

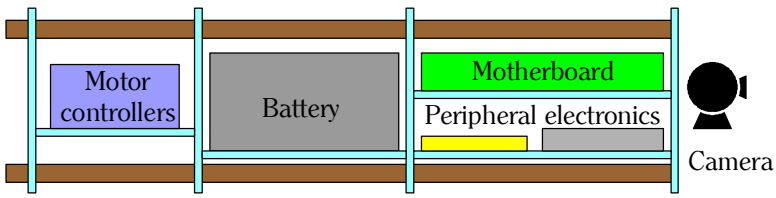

Figure 121: Internal layout of Bathymysis submarine.

The motor control circuitry was located at the rear of the submarine, so that the power cables running to the motors did not have to be routed past any of the more sensitive circuitry. The

battery was in the centre, to ensure even weight distribution and put some distance between the motor controllers and other electronics. The motherboard and control electronics were at the front of the submarine, near the camera, which pointed out of the front window.

A.4 Pneumatic System

A.4.1 Air Supply

Bathymysis was equipped with a 3 litre compressed air tank, to supply air for pressure regulation and other uses. The tank was a scuba diving reserve cylinder (known as a pony tank) capable of holding air at up to 232 bar; plenty for several dives to maximum depth and back to the surface. A second tank, made by Spare Air[11] was purchased, with a much lower capacity of 0.42 litres. This tank was useful for missions in which the submarine's mass needed to be kept to a minimum.

A.4.2 Pressure Compensation

Submarines have to be designed to survive the pressure of the lowest depths to which they are intended to dive. Some have thick, sealed hulls, strong enough to withstand the external pressure. Others have flooded or oil-filled hulls, which compress with very little change in volume, so are in no danger of imploding. A common design among deep-water AUVs is to house any parts that have to be surrounded by air in a thick, two-part glass sphere, and for all other components to be flooded with oil, to ensure incompressibility.

Bathymysis used another method, similar to a scuba diver, whereby the pressure of the air inside the submarine was increased as it descended, to cancel the effect of the external pressure on the hull. This allowed for a much thinner hull, and simplified the submarine design in many areas. It was a particular advantage for Bathymysis that the seals did not have to withstand any external pressure, as the four moving fins that propel the submarine had to be driven by rotating shafts, via seals. If these seals had to withstand the difference in pressure between the atmosphere and the maximum dive depth, they would have to have been much stronger, wasting a lot of power through friction, and requiring more power to drive the motors.

Mechanical pressure compensation

The mechanical pressure control system was based on modified scuba diving equipment. A scuba diver's air supply normally consists of a high-pressure tank, a first-stage regulator to

[11] www.spareair.com

reduce the pressure to around 10 bar, and then a second-stage regulator, to supply the diver with air at the ambient water pressure. The tank and first stage regulator were attached below the submarine, and the second stage regulator was mounted in the wall of one of its auxiliary housings. The regulator contained a flexible rubber diaphragm which, when the external pressure increased, deflected inward. The displacement caused an air valve to open, releasing extra air into the submarine. The consequent rise in internal pressure pushed the diaphragm out again, back to its normal state.

As the submarine rose and the external pressure dropped, the submarine released air via a spring-loaded dump valve, to keep the internal pressure at a safe level. The dump valve, designed for use in a scuba diving drysuit, was designed to release air when the pressure differential reached approximately 2 psi (0·14 bar).

Electronic pressure compensation

The original intention for Bathymysis was that its pressure regulation system would be entirely software-controlled, with a mechanical system remaining in place as a backup. The advantage of this kind of system is that it would be able to respond more accurately to changes in the external pressure and orientation of the submarine. For example, if the orientation of the submarine changed such that one of the fin axle seals was deeper in the water than the pressure regulator valve, the external water pressure at the seal would be higher than at the regulator, and the seal would therefore be at risk of leaking. However, if the onboard computer controlled the pressure, the system would be aware of the orientation of the submarine, and be able to raise the internal pressure of the submarine accordingly. Using this system, the submarine could operate safely even when upside-down, which would be very risky using a purely mechanical design.

Another advantage of electronic pressure control is that the computer would be able to monitor the amount of air being released into the submarine, which could serve as an early warning system for hull integrity. For example, if the hull were to spring a leak and start releasing air to the water, the computer would notice it was supplying an abnormally large volume of air to the hull, and trigger an alarm.

Initial tests on the mechanical pressure regulation system proved it to be very effective and reliable on its own. Since the submarine was weighted in such a way as to ensure it always stayed in an upright orientation, it was decided that the extra time and effort needed to add the electronic pressure regulation system was unwarranted.

A.4.3 Buoyancy control

The first option considered for controlling the submarine's buoyancy was to use an inflatable bladder. It was to be connected to the submarine's air supply via a solenoid valve, and protected against over-inflation by a spring-loaded relief valve. Another solenoid valve would allow air in the bladder to vent to the water, reducing the submarine's buoyancy. The air release system presented some problems based on the submarine's orientation. The air had to be released from a point higher than the bladder, where the water pressure is lower. This could have been achieved by running tubes to several points around the submarine, terminating in one-way valves, such that one of the valves was always higher than the bladder.

After consideration, it was decided that active buoyancy control of the submarine was not necessary at the current stage in its development. The design of its propulsion system allowed thrust to be vectored up or down, so depth control could be achieved by powered manoeuvring. For safety, the submarine was designed to be slightly buoyant, so that in the event of a drive system failure it would float to the surface. The only drawback of this method was that a small amount of downward thrust was necessary to maintain a fixed depth, which brought with it a small expenditure of energy. This was deemed a worthwhile cost for such an important fail-safe feature.

A.5 Control System

Although the submarine was primarily intended for use as a tethered ROV, it carried onboard all the equipment necessary to function with no external connections. For remote-controlled use, the only connection it needed with the surface was an armoured ethernet cable. The different elements that made up the submarine's control system are described in the sections below.

A.5.1 Power Supply

The space designed for the submarine's power source could hold several different configurations of batteries. Tests performed to date have used a single 12 v, 17 amp-hour lead acid battery, but to make more efficient use of space and increase operating time, two or three smaller lead acid batteries can be used together. Sealed deep-cycle lead acid gel batteries were selected, because of their robust simplicity and good capacity-to-cost ratio. Different battery technologies such as nickel-metal hydride or lithium-ion cells offer improved power capacity for the same volume, and these may be considered in future revisions of the submarine.

Power requirements

The power requirements of the submarine were as follows:

- Peak demand while starting up: 4.0 A
- Fins flapping (no resistance): 3.5 A
- Idle: 3.3 A

These measurements were taken while the submarine was out of the water, and therefore with very little drag acting on the fins. This explains their very low power consumption. But with a fully charged 17 Ah battery and a reasonable safety margin, an endurance of 3-4 hours could be expected, depending on the submarine's level of activity.

A.5.2 Onboard Computer

The complex movement required of the submarine's fins meant that an on-board motion control system was required. An EPIA-PD6000E Mini-ITX fanless 600 MHz low-power motherboard was chosen as the submarine's onboard computer, and combined with a 20 GB hard drive and 512 MB RAM (Figure 122).

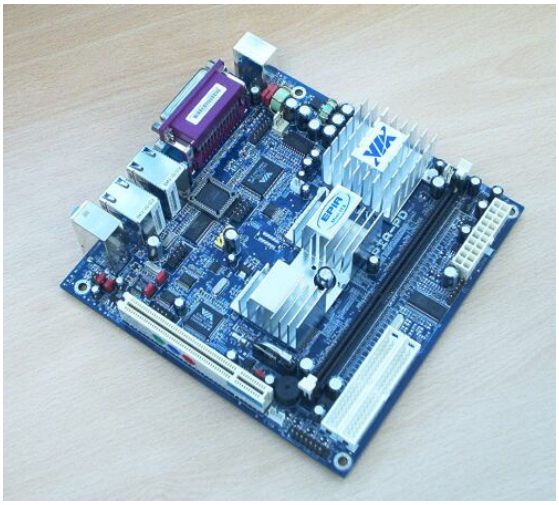

Figure 122: EPIA-PD6000E motherboard used in the Bathymysis submarine.

It had the following advantages:

- Small size (fits inside 200 mm pipe)
- Relatively low power requirements (15-25 W)
- Runs standard PC operating systems
- Several input/output ports (serial, USB)
- Low cost, readily available consumer product

The computer ran the Windows XP operating system, which proved sufficient for the submarine's requirements. It was chosen for its compatibility with hardware, and the ease with which

it could be implemented. Given the ample power of the onboard computer, its undoubted inefficiency did not prove problematic, but in future it may be realistic to switch to LINUX, or a real-time operating system that can handle the complex control systems better. A leaner OS would also allow the use of a solid-state hard disk, as opposed to the mechanical one currently in use. This would save power, and remove a potential weak point in the design by making the onboard computer more robust. Mechanical hard drives contain air, and although they are not hermitically sealed, if the air within the submarine compresses or decompresses faster than the hard drive's air pressure can equalise, the force exerted on the drive's walls may cause damage.

A.5.3 Sensors

The submarine was equipped with a variety of sensors, connected to the onboard computer via interface electronics.

Accelerometer

The accelerometer module was an ADLX-ADC, made by Procyon Engineering[12], utilising three Analog Devices[13] ADXL202 accelerometers. It was capable of measuring acceleration up to 2 g in any direction. It was used to detect the orientation of the submarine, by measuring the direction of the earth's gravitational pull. The sensor was connected to an electronic interface circuit, which converted its output to a serial data signal, which was passed to the onboard computer.

Compass

A solid-state electronic compass was used for navigation. Electronic compasses are reliable, containing no moving parts. Instead they use semiconductors exploiting the Hall effect to sense magnetic fields. A Honeywell HMC6352 sensor was selected, which could detect its orientation with respect to the earth's magnetic north, to within a few degrees. It was interfaced to the submarine's computer in the same way as the accelerometer. The accelerometer and compass could then be used together to detect the orientation of the submarine in every axis.

[12] www.procyonengineering.com

[13] www.analog.com

Camera

Bathymysis was equipped with a camera to allow it to be used for undersea survey work. A Logitech[14] QuickCam Orbit webcam was chosen, for its ability to interface simply and directly with the computer, and for its pan and tilt function. The camera was placed in the front dome of the submarine, where it had a wide field of vision. The onboard computer received the images from the camera, and sent them to the surface via the Ethernet link. The software also enabled remote panning and tilting of the camera.

Pressure sensing

The submarine was equipped with two electronic pressure sensors, interfaced to the computer via an analogue to digital converter. It was necessary to take readings of the pressure both outside (i.e. depth) and inside the submarine. This could have been achieved by a number of different sensor configurations. The design explained below was chosen because it only required one of the sensors to be exposed to the submarine's external environment, and it provided good accuracy in detecting the difference between internal and external pressure – the reading most critical to the submarine's safety. It also proved to be a cost-effective way of monitoring the pressures.

Absolute pressure gauge

A Honeywell[15] SenSym ASDX series signal conditioned pressure transducer measured the internal pressure of the submarine, in relation to an internal reference vacuum. It was capable of measuring pressures of up to 10 bar, which corresponds to a depth of approximately 100 m. It did not need to come into contact with water, meaning it was much less expensive than comparable 'wet' pressure sensors.

Differential pressure gauge

A Honeywell 143PC05D signal conditioned precision pressure transducer was used to measure a positive or negative difference in pressure between its two ports, up to ±5 psi (0.34 bar, equivalent to 3.5 metres in water). One of these ports was compatible with wet air (although not direct contact with seawater), and the other was not. Therefore the wet air compatible port was connected to the outside of the submarine via a thin, air-filled spiral-wound tube (Figure 123).

[14] www.logitech.com

[15] www.honeywell.com

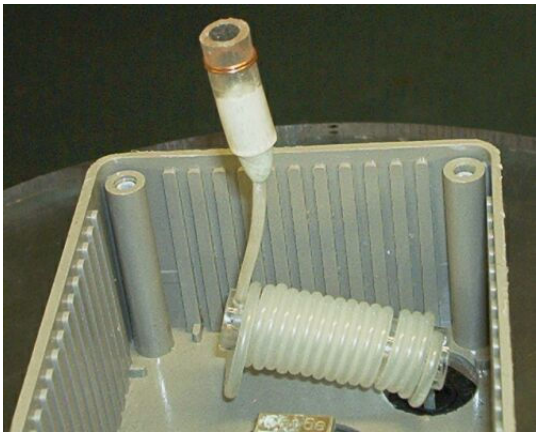

Figure 123: Spiral pressure measurement tube on Bathymysis.

As the pressure differential between the outside and inside of the submarine increased, the air in the tube was compressed, transmitting the external pressure to the port of the pressure sensor, while the seawater being measured was kept some distance from the fragile sensor. The tube was thin enough that whatever its orientation, water was unable to flow along the tube to the sensor, being held back by surface tension.

It was important that the pressure inside the submarine was kept slightly higher than the external pressure (see Appendix A.4.2, page 176, for details) so the sensors needed to give an accurate reading of the difference in pressure. If an absolute pressure gauge had been used to measure both internal and external pressure, they would both have had to operate over the wide range of pressures that the submarine will experience. The difference between the two readings (which is critical to the submarine's safety) would have been a tiny fraction of their total range, which could lead to errors. Using a narrow range differential sensor in combination with an absolute sensor for internal pressure gave better accuracy in the differential measurement, and still allowed external pressure to be calculated:

$$P_E = P_I + \Delta P \tag{53}$$

Where P_E is the calculated external pressure, P_I is the reading from the internal pressure, and ΔP is the reading from the differential pressure sensor.

Sensor interface circuit

The sensor interface circuit was designed and built by Jeff Brewster, an instrumentation engineer at the University of Bath. Its role was to allow communication between the submarine's sensors and the PC motherboard. It incorporated a Microchip[16] PIC16F877 microcon-

[16] www.microchip.com

troller, programmed using MELabs PICBASIC Compiler[17], which received simple serial commands via an RS-232 interface, read the appropriate sensor, and sent the data back to the PC.

It allowed the submarine's computer to monitor the voltage of the batteries, the current being consumed by the submarine, the accelerometer readings, the compass heading, and the internal and external pressure.

Other sensors

These sensors were not implemented on Bathymysis in its first design iteration, but have been investigated, and are likely to be added at some stage in its future development.

The internal compartments of the submarine could be fitted with leak detection loops: parallel, uninsulated wires, between which a small current could flow if water was present. These were to be connected to the onboard computer via the sensor interface circuit, and would mean the submarine could be programmed to abort its mission and surface immediately if water was detected inside any of its compartments. This was a highly unlikely circumstance, due to the positive internal pressure of the submarine (Appendix A.4.2, page 176).

The frame may in future be fitted with sensors to detect physical contact with rocks and other obstacles. This may aid navigation though obstacles outside the onboard camera's field of vision.

The simplest implementation of sonar on the submarine would be the addition of a depth sounder, pointing down to the ocean floor. Another forward-pointing sounder could be added to provide advance warning of obstacles as the submarine moves forward. More advanced sonar systems such as the CruzPro[18] PcFF80 PC Fishfinder could be added, which is able to detect multiple reflections of the same sonic 'ping' in order to build up a map of reflective objects in its beam. The use of a standard PC as the onboard computer, and the processing power that it brings means there are many more options that can be considered if sonar is found useful.

Another useful function of the submarine would be to record the conditions in the water as it caries out studies. Properties such as salinity, temperature and visibility will be easy to measure, and will provide valuable extra data for the user.

[17] www.picbasic.co.uk

[18] www.cruzpro.com

As one of the uses of Bathymysis is to carry out ecological field surveys, it may eventually be fitted with specific tools to help it carry out its tasks, for example, to collect live samples of Mysids from study areas for analysis.

A.6 External Compartments

External compartments outside the main hull housed some of the submarine's components. The waterproof compartments were connected to each other via flexible hoses, to allow air to flow between them, equalising the air pressure in different sections of the submarine. Some of the hoses acted as cable conduits, allowing transmission of electrical power and signals between the compartments.

A.6.1 Buoyancy and Pressure System

Two compartments underneath the hull of the submarine housed the buoyancy and pressure control equipment. The equipment was less sensitive to the ingress of water than the contents of the main hull; this is why it was placed at the lowest point of the submarine. For water to enter the submarine, a simultaneous failure of both hull integrity, and the pressure regulation system would be required. Either of these failures occurring on its own would have been detected rapidly, and caused a mission to be aborted safely. The arrangement of the submarine compartments ensured that the main hull would be the last area to flood under such circumstances.

A.6.2 Fin Control Boxes

The fin control mechanisms were housed in boxes on the sides of the submarine, and could be affixed to the chassis in different configurations, as shown in Figure 124. Their internal design is described in Appendix A.7.

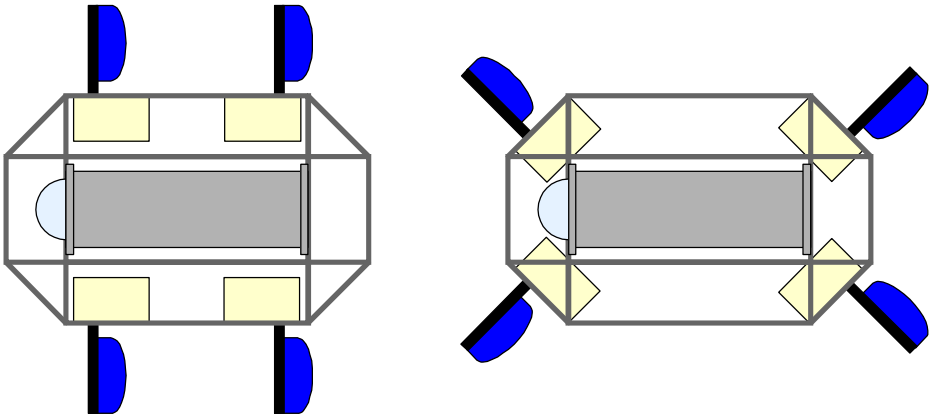

Figure 124: Bathymysis fin configurations.

A.6.3 Interconnections

The submarine was designed to maintain a positive internal air pressure at all times (a design decision explained in Section A.4.2, page 176). One of the benefits of this choice was that the connectors did not have to be specified to withstand the pressures to which the submarine was required to descend. The IP68[19] international standard indicates protection against long periods of immersion in water at depths of greater than 1 m; no upper depth limit is specified. Although IP68 parts would rarely be designed for operation at the depths of more than a few metres, as long as any air inside the submarine was pressurised to approximately the same level as the environment, the pressure differential across the connectors would be inside their specified limits, and ingress of water would not be possible.

The ability to use relatively inexpensive IP68 connectors instead of more robust wet-connect parts commonly found on commercial submarines reduced the cost of the submarine considerably, but some precautions had to be taken during assembly to ensure the reliability of this method of connection. Special care was taken to ensure that any pockets of air inside the connectors had a path to the air inside the submarine. This way, no unpressurised air cavities would exist inside the connector, which could fill with water at depth.

[19] International standard IEC 60529

A.7 Drive System

A.7.1 Fin Actuators

Each of the four fins was actuated by a mechanism housed in a waterproof box, and connected to the hull of the submarine via a flexible tube (Figure 125).

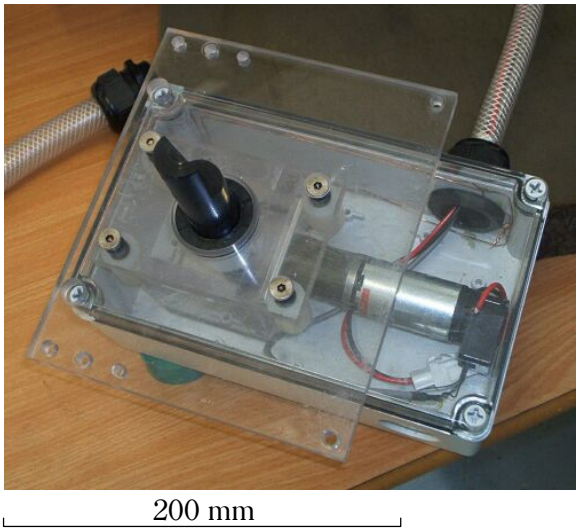

Figure 125: Bathymysis fin actuator assembly.

Each box contained a 15 W Maxon[20] A-max 32 brushed servomotor, with a Maxon GP 32 K 35:1 ratio planetary gearbox and HEDS 5540 digital position encoder. The motors were each mounted on a polycarbonate chassis, which contained a pair of bevel gears to change the axis of rotation perpendicular to the motor, and reduce its speed by a further 50%. The fin axle protruded from the mounting plate of the chassis, passed through a seal in the outer case, and connected to the fin via a standardised mounting bracket, designed to allow a variety of fins to be connected to the motor and changed easily. A CAD model of the gear assembly is shown in Figure 126:

[20] www.maxonmotor.co.uk

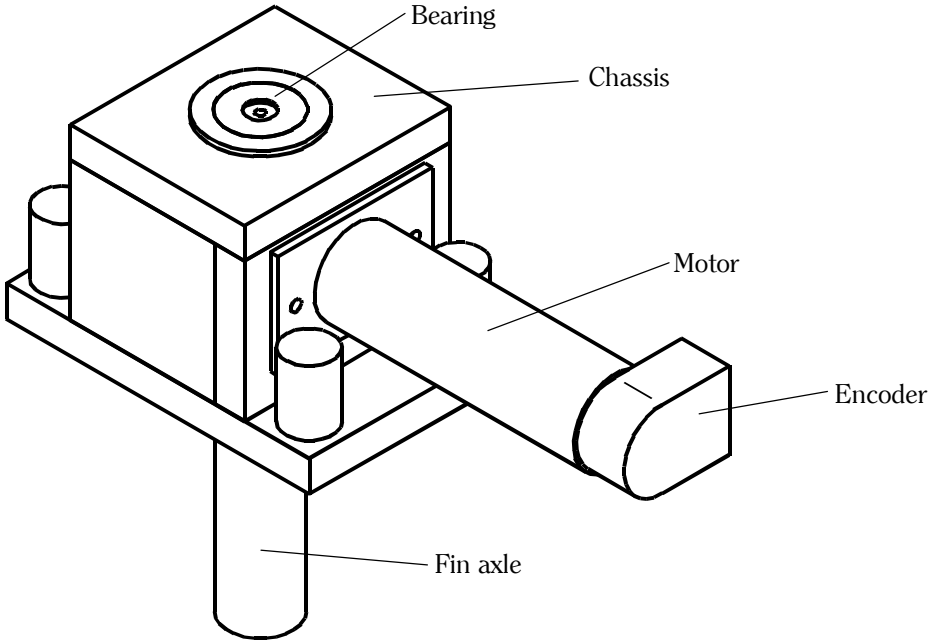

Figure 126: Fin actuator mechanism from the Bathymysis submarine.

A.7.2 Fins

The modular design of the submarine meant that different fin designs could be tested. The first set of fins produced were simple pieces of polypropylene sheet. They were capable of propelling the submarine, and served it well during testing. However, it was apparent that they were too flexible, and that the submarine's motors were capable of delivering more mechanical power to the fins than they could efficiently convert to thrust.

A search was carried out for inexpensive and readily available materials with which to make more powerful fins. Two pairs of children's swimming flippers were selected, and modified to form a set of fins capable of delivering enough thrust to manoeuvre the submarine. Despite their amateurish appearance, the flippers performed well. Their dimensions were greater than the sheet fins, and they were stiffer, although still compliant enough for some flex to be induced by the pitching of the axles. The comparative performance of the two sets of fins is discussed in Section A.8 (page 190).

A.7.3 Motor Control System

Hardware

The submarine's onboard computer controlled the motors, via interface electronics. Each motor's encoder was connected to a single DAQChina[21] Industrial Automation

[21] www.daqchina.net

normDAQ-5003 4-channel quadrature encoder counter (Figure 127), which kept track of the motor's position and passed it on to the computer via an RS-232 interface.

Figure 127: normDAQ-5003 quadrature encoder counter module (USB version).

The computer controlled the speed of the motors via a separate interface circuit, again controlled by an RS-232 interface. The circuit converted commands from the computer into direction and Pulse Width Modulated (PWM) signals with a duty cycle from 0 to 100%. These logic-level signals were passed on to a pair of Procyon Engineering[22] MotorDriver V1.0 H-bridge driver boards (Figure 128) capable of supplying up to 3A to two motors each.

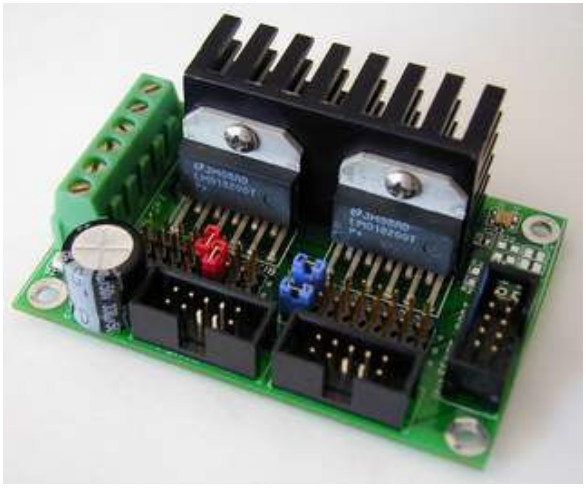

Figure 128: Procyon Engineering MotorDriver v1.0.

[22] www.procyonengineering.com

Figure 129 shows a schematic of the motor control system as a whole.

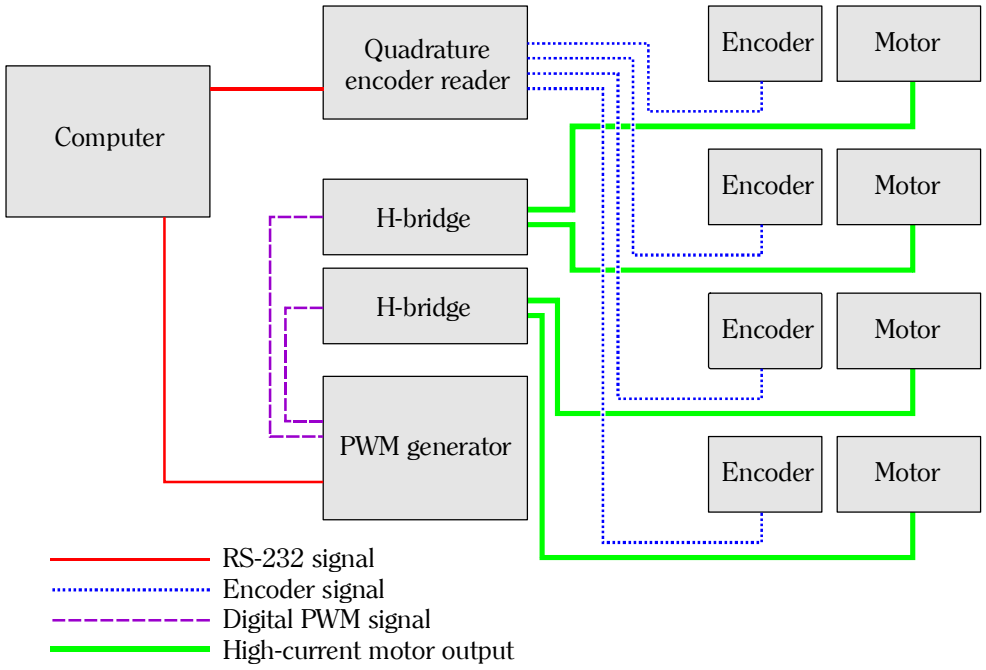

Figure 129: Motor control schematic for the Bathymysis submarine.

Software

The onboard computer ran a program that continually received information from the encoder counter module, and used it to calculate the orientation of each fin. The program received commands to tell it where the fins should be pointing. It then applied power to each motor at a predetermined duty cycle until it reaches the desired position, at which point it cut the power and waited for the next command. The duty cycle determined the speed at which the fins moved, and as this was nearly linear for each half-cycle of the wave, the overall waveform was approximately triangular.

A problem was encountered while designing the fin control software; the system relied on low-latency communications between the PC and motor control electronics. Occasionally there would be a pause in the data stream coming from the encoder reader, which meant the software no longer knew the position of the fin. Pauses in communication would last half a second or less, but this was long enough to cause a disturbance in the movement of the fin. A workaround was developed in which the software would extrapolate position data from previous two readings in the event of a pause in the data input, and this improved the fins' behaviour considerably, making the deviations in position barely noticeable. However the root cause of the problem was in the PC's drivers, which did not prioritise serial communications over other multitasking obligations. The way serial communications are handled are inherent to the operating system (Windows XP), so to fix the problem altogether, a new, real-time operating system would need to be selected. Alternatively, the control system could be moved

out of software entirely with the addition of dedicated motion control hardware for each motor.

Future phases of the submarine's development will see a more advanced control system, capable not only of moving each fin to a fixed position, but of following a path, in order to generate a range of different fin oscillation waveforms. The first steps towards accomplishing this goal have already been taken, and are described in Appendix A.9 (page 192).

A.8 Performance Experiments

A.8.1 Methods

During the development of the submarine, its straight line speed was tested as an indicator of its overall performance. The submarine's software allowed the power output to the motors to be controlled, and this setting, from 0-100% of full power, proved to be the simplest method of controlling the submarine's speed. At this stage in its development, the oscillation amplitude could be controlled, but not the frequency. Reducing the power whilst keeping the fin amplitude constant meant that oscillation frequency reduced as a consequence. All the tests on the graph below were performed at a fixed amplitude of 40° peak-to-peak. The speed was measured by timing the submarine over a fixed course of 0.75 m, which although short, was timed accurately enough to yield useful speed data.

A.8.2 Results

Figure 130 shows the steady-state straight line speed of the submarine over a series of tests using the polypropylene flippers as fins. The performance of the polypropylene sheet fins is also indicated on the graph, although unfortunately only one data point exists for the sheet fins at this amplitude. It is, however, enough to show a significant difference in performance between the two designs, highlighting the importance of fin selection in the submarine's design.

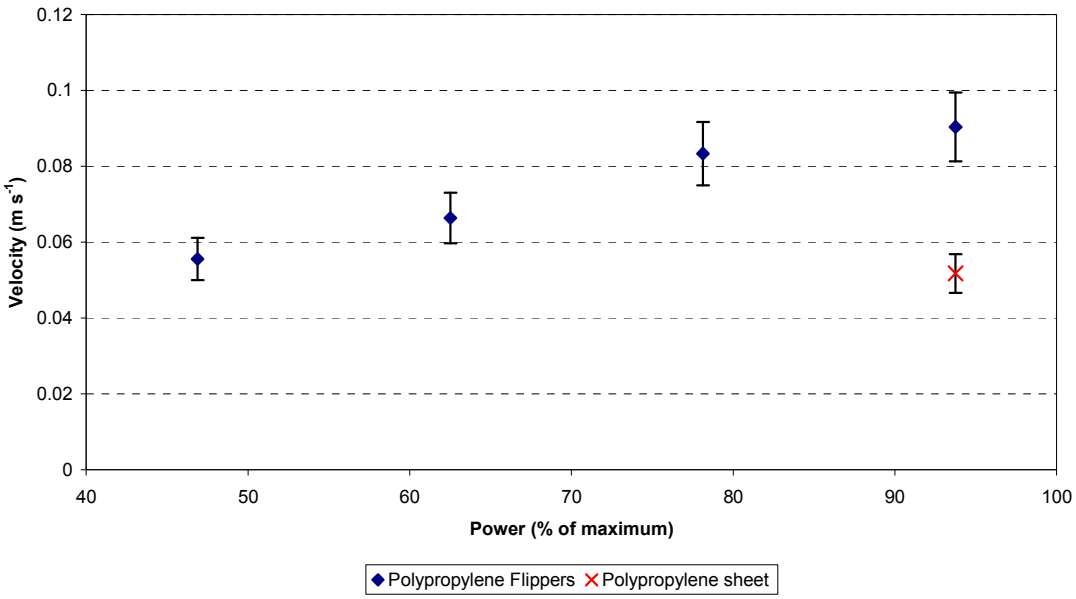

Figure 130: Submarine speed against fin power, 40° oscillation amplitude.

A.9 Applications

A.9.1 Costal Ecosystems Research Foundation

The submarine has also been used by the Costal Ecosystems Research Foundation (CERF) in British Colombia, Canada. Among many research interests, CERF studies Grey Whale *(Eschrichtius robustus)* populations, whose migratory path takes them up the pacific coast every summer, and was specifically interested in shrimp-like creatures of the Mysidacea group (Figure 131), on which the whales feed.

Figure 131: Mysid shrimp (Photo: Linden Gledhill).

A.9.2 SAUC-E Autonomous Submarine Competition

Bathymysis was an entrant in the 2006 'Student Autonomous Underwater Challenge - Europe'. SAUC-E is a competition in which autonomous submarines from academic institutions across Europe compete against each other to complete a list of tasks, without any external control, relying solely on sensor readings and programming. The tasks in 2006 were as follows:

- Submerge and pass through a validation gate (Figure 132)
- Make contact with a mid-water marker buoy
- Identify a target on the ground and drop a marker as close to its centre as possible
- Surface in a predefined recovery zone

The submarine was equipped with extra hardware and software by a team of students to allow it to complete the competition tasks. The control system was redesigned using LabVIEW (see Appendix F) to manage the navigation and mission control (Klimaytys, 2006). Image recognition algorithms were developed and tested to allow the submarine to discern the targets from visual input (Wallis, 2006).

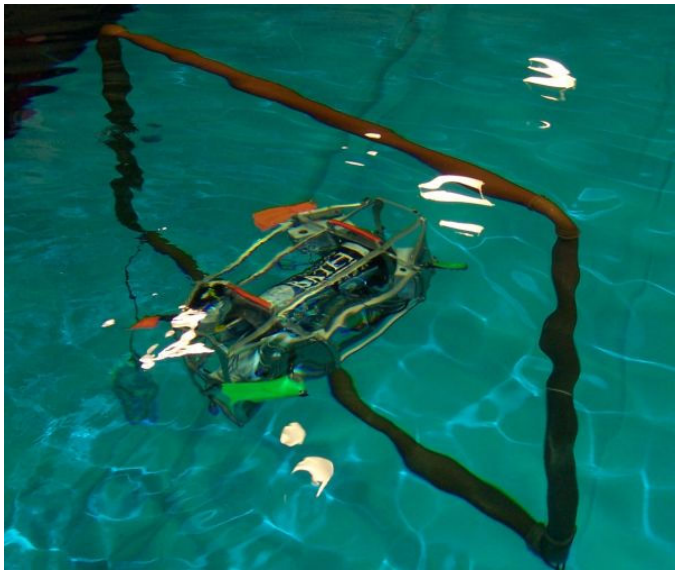

Figure 132: The Bathymysis submarine taking part in the SAUC-E competition, 2006.

Further details on the design and abilities of the submarine in its autonomous configuration are beyond the scope of this thesis but can be found in related works (Collins, 2006, Riggs, 2006).

A.9.3 Subsequent Work

An alternative, and more conventional propulsion system was developed for the submarine, using propellers instead of fins (Pattinson, 2006). The modular design of the rest of the submarine made it relatively simple to retrofit and incorporate this with the existing work.

Preliminary work was carried out on another biomimetic propulsion system, using an undulating, gymnotiform motion (see Section 2.3.1, page 28) (Sellen, 2006).

Further work was carried out on the 4-finned biomimetic propulsion system with which the submarine was developed (Brindlinger, *et al.*, 2006). Its control system was overhauled, by adding a custom-built motion control circuit to each fin motor, to free up the main computer for other tasks. Each fin was capable of receiving a target waveform from the submarine computer, and following it using PID control.

Another aspect of the continuing research on the submarine was an analysis of its hydrodynamic performance using computational fluid dynamics (CFD) tools (Waterhouse, 2006). Figure 133 shows examples of some of the results gathered, for straight-line drag. The left-hand diagram shows the pressure distribution around the hull and frame, highlighting the effect on hydrodynamic performance of the many forward-facing flat surfaces. The right-hand diagram shows the velocity distribution in the water surrounding the submarine.

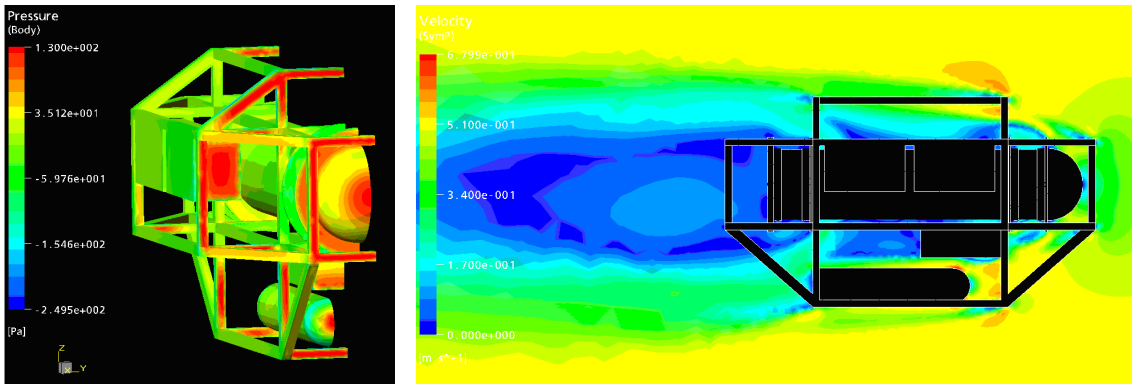

Figure 133: CFD results showing pressure distribution (left) and flow velocity (right) (Waterhouse, 2006).

The work made recommendations of improvements to the submarine's design that would reduce drag, but there are many design considerations aside from drag that any potential design changes must be weighed against.

A.10 Conclusions

The Bathymysis submarine has proved useful in a variety of areas. The Coastal Ecosystems Research Foundation (CERF) made use of the submarine in a field study in British Colombia in 2006, and has continued to use submersible ROVs designed at the University of Bath to carry out research tasks in British Colombia in subsequent years.

The Bath University Racing Submarine team (BURST) won one of the runner-up awards in the first annual 'Student Autonomous Underwater Challenge - Europe' (SAUC-E) competition of 2006, and the submarine won praise for many of its design features. Its basic design and modular structure were employed in several other autonomous submersible vehicles, and descendants of Bathymysis have gone on to enjoy success in several subsequent SAUC-E competitions.

The tests performed on the Bathymysis were somewhat crude and far from exhaustive, but they clearly showed the need for further investigation of flexible fin propulsion. The fins used in the tests were not optimised for their application, but the large difference in the performance of the two different sets showed the potential performance benefits of using appropriately designed fins. It was decided that an appropriate next step would be to undertake a thorough literature survey, in an effort to identify areas with scope for further research, within the field of flexible fin design.

Appendix B : Calculations

B.1 Nondimensional Plunge Velocity Conversion

Jet Characteristics of a Plunging Airfoil (Lai and Platzer, 1999) uses nondimensional plunge (heave) velocity as a parameter. It is the ratio between the maximum foil plunge velocity, and the velocity of the flow, and is defined as:

$$kh = \frac{2\pi f a_p}{U_0} \tag{54}$$

Where f is the plunge frequency, a_p is the plunge amplitude, and U_0 is the free stream velocity. Since double the plunge amplitude ($2a_p$) is interchangeable with the wake width, the nondimensional plunge velocity is the same as the Strouhal number multiplied by π. Therefore the figures quoted from the paper in Section 2.6.2 (page 38) have been converted to conventional Strouhal numbers, for easier comparison with the findings of other papers.

Appendix C : Supplemental Methods

C.1 Shore Hardness Testing

The Shore hardness scale is an indentation hardness test frequently used to define the properties of polymers. It characterises a material's resistance to deformation by a hard indenter of a predetermined shape. This is measured by observing the depth to which the indenter sinks into a material under a given load.

Shore hardness ratings consist of a letter and a number. The letter represents the type of test carried out, and the number is a measurement of hardness from 0 to 100; the higher the number, the harder the material. The Shore hardness test is empirical, and not directly related to any other properties of the material. While useful for comparing similar materials, in this thesis it was rejected in favour of the Young's modulus, which relates more directly to the measured behaviour of the fins.

C.2 Procedure for Vacuum Forming a Polycarbonate Dome

Figure 134 shows the polycarbonate dome used for the front of the Bathymysis submarine's hull.

Figure 134: Polycarbonate dome from the front of Bathymysis.

1. Cut 2 mm or thicker polycarbonate sheet to about 19" square. A smaller size than this may allow it to pull free from the vacuum former clamp and let air in.
2. Polycarbonate absorbs water from the air around it, which, when heated, expands, causing tiny bubbles, and turning the sheet opaque. If possible, dry the 2 mm polycarbonate sheet at 120°C for at least 3 hours. Thicker sheet requires more drying time (see Table 12).

Guage (mm)	Drying Time (hours)
1	1
1.5	1.5
2	3
3	6
4	10
5	16
6	23
8	32

Table 12: Polycarbonate drying times (Source: www.bayplastics.co.uk).

3. Place a 200 mm PVC flange, as used in the construction of the submarine on top of the circular MDF mounting, and place it on the supports, at a height of at least 100mm.
4. Set the middle 2 heaters on the Formtech 450 vacuum former to just under 5, and the outer one to just over 5 (the plastic here needs to be very soft here, and bubbling doesn't matter).
5. Wait for heaters to reach full temperature.
6. Clamp plastic onto the vacuum former securely, and position the heater over it.
7. Watch the plastic carefully. Initially, asymmetrical thermal expansion will cause it to bend upwards towards the heaters, then as it starts to soften it will sag down again. Tap it gently to see how soft it has become, but avoid touching the area that will form the window. This stage is critical. Overcooking the plastic may cause it to bubble and turn opaque. Not heating it enough will not allow it to form properly.
8. When the sheet is ready to form, pull the vacuum former's lever firmly to push the mould up through the soft plastic. Pulling it too fast will pull the plastic out of the clamp, and too slow will allow the plastic to cool down before it can be formed. As soon as the lever is locked in place, switch on the vacuum pump. Ambient pressure should now push the polycarbonate down into the mould. Be careful not to let it bottom out on the base of the forming machine. Be warned the former keeps extracting air for a fraction of a second after you release the switch. When the plastic has cooled and hardened, blow air in to help release it from the mould.

Appendix D : Fin Fabrication Techniques

In order to test different shapes and sizes of fin, it was necessary to build apparatus to fabricate the fins in an accurate and repeatable way. Several methods were considered for this process. Section 3.2 (page 57) covered the selection and testing of an appropriate resin from which to mould the fins. This appendix describes the alternative fabrication methods that were considered, and the testing and development carried out in search of the most appropriate one, based on such factors as accuracy, repeatability, and cost.

D.1 Resin Casting

Resin casting is a common way of reproducing irregular shapes very accurately. A positive mould is created, and immersed in resin to create an intermediate negative mould, from which further positive copies are made. The process is illustrated in Figure 135.

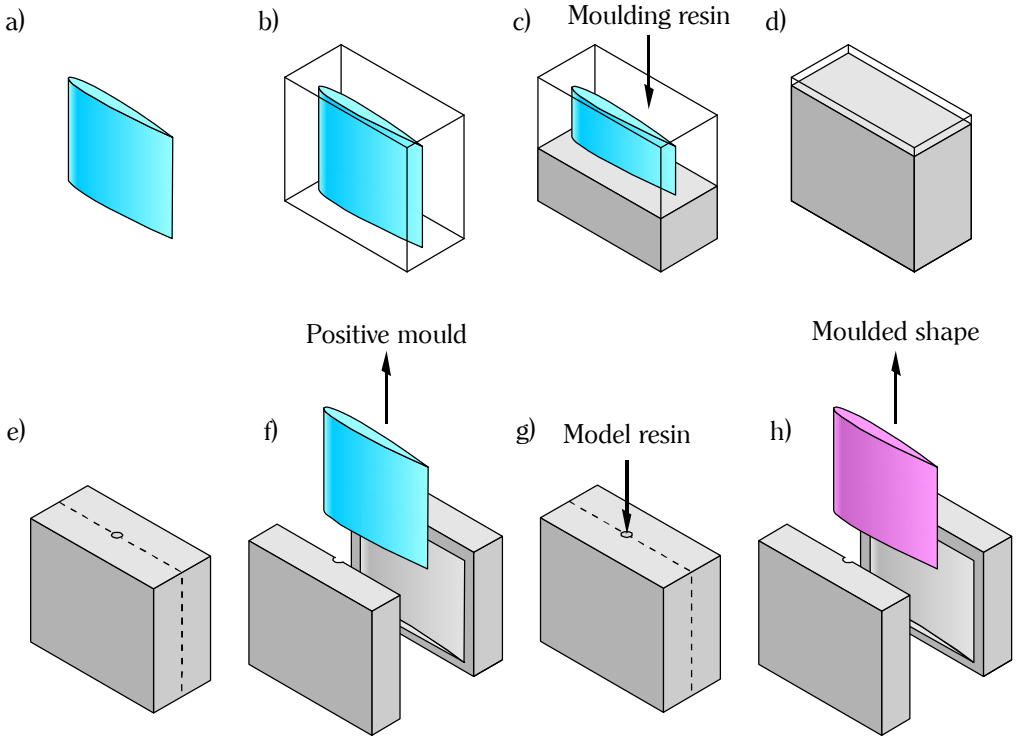

Figure 135: The resin casting process.

Table 13 shows the advantages and disadvantages of such a method.

⊕	**Advantages**
	• Extremely accurate reproduction of arbitrary source shapes.
⊖	**Disadvantages**
	• Process requires a positive mould for each fin shape required. • Costly in both time and resin

Table 13: Advantages and disadvantages of a deformable fin mould.

The positive mould could be created using a variety of techniques, chosen to achieve the best results, or could even be a real fin taken from an aquatic animal. However, since the ability to produce precise replicas of biological forms was not required in this investigation, the resin casting method was rejected in favour of less costly alternatives.

D.2 Deformable Half-Fin Mould

The following method employed a reusable, deformable mould, which allowed fins to be produced in a variety of shapes, at minimal cost.

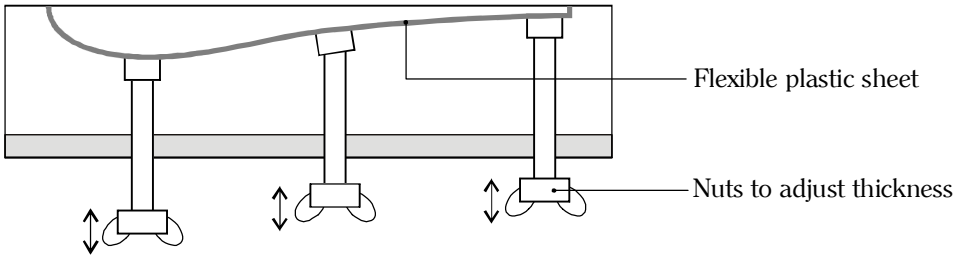

Figure 136: Fin moulding apparatus.

Figure 136 illustrates the process. A flexible plastic sheet formed the contoured part of the fin mould, and was held between two rigid aluminium plates. The mould was of fixed width and length, but the shape of the plastic sheet could be controlled by moving the supports up and down beneath it. After the profile of the fin had been defined by moving the supports to the correct positions, the edges were sealed using Copydex[23], a latex-based adhesive. Then, resin was poured into the mould and allowed to set, forming a half-fin shape, as shown in Figure 137 a) below. The resulting shape was then cut in two and folded over on itself, and the two halves glued together. Silicone is a difficult material to glue, but after some experiments, silicone bathroom sealant was found to bond the two halves securely, while still allowing flexibility.

[23] Copydex, Henkel, Winsford, Cheshire, CW7 3QY

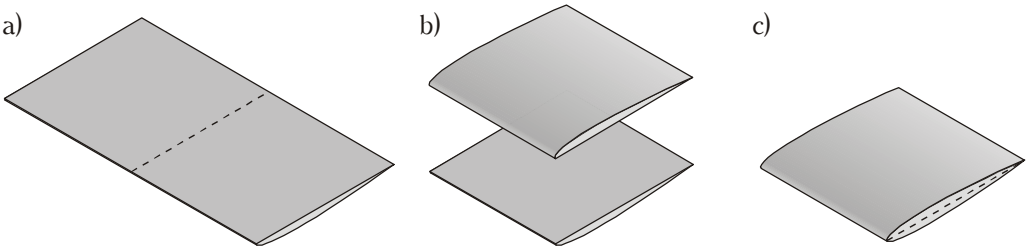

Figure 137: Fin moulding procedure.

The method's advantages and disadvantages are shown in Table 14.

⊕	**Advantages**
	• Uniform fins can be produced with a range of cross-sectional profiles. • The cost per fin produced is very low.
⊖	**Disadvantages**
	• The initial creation of the mould is more complex. • Axle cannot be moulded into the fin. • The width and length of the fin are not variable. • Difficult to achieve accurate fin thickness by varying resin volume alone. • Layer of glue and 2-part design affect stiffness of fin. • Impossible to achieve thin, feathered trailing edge.

Table 14: Advantages and disadvantages of a deformable fin mould.

The fin mould was used for some early experiments. Its inaccuracy and numerous other disadvantages meant it was quickly superseded by more reliable, repeatable methods.

D.3 Use of Rapid Prototyping Equipment

Rapid prototyping (RP) machines provide a way to create 3-dimensional shapes quickly and easily from computer models. A Stratasys Dimension BST[24] rapid prototyping machine was used to create the models used in this thesis. More information about rapid prototyping and the equipment used can be found in Appendix E.1 Incorporating the RP machine in the process of fin fabrication allowed very fine variation of fin sizes and shapes.

[24] www.stratasys.com. See Appendix F.

To produce CAD models of aerofoil shapes, aerofoil design software[25] was used to create a set of points describing a standard NACA profile, and these points were imported into the CAD system[26].

D.3.1 Positive RP mould

Rapid prototyping is a suitable method for producing a positive mould for the resin casting technique described in Appendix D.1 (page 198), but it was not pursued, for the reasons of cost and complexity described in that section.

D.3.2 Negative RP mould

A parametric CAD model was designed to produce a double-sided vertical fin mould from a set of points defining the fin perimeter, in a standard NACA 0012 aerofoil shape (Figure 138). The resulting model was built using the rapid prototyping machine.

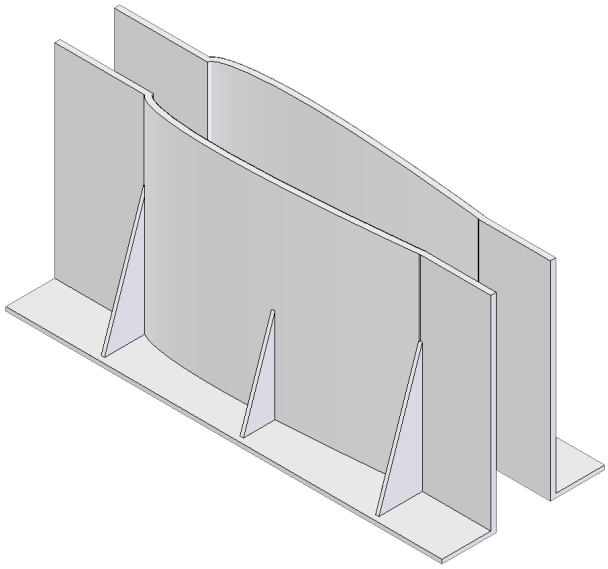

Figure 138: CAD model of the configurable fin mould.

The seam around the mould proved slightly leaky, but could be sealed using latex adhesive. The test fin produced as a proof of concept was approximately half the intended scale, and the result was promising, but producing large models on the RP machine also has drawbacks. The advantages and disadvantages are described in Table 15.

[25] 'naca45'. See Appendix F.

[26] UGS Solid Edge. See Appendix F.

⊕	**Advantages**
	• Fins are not restricted to being rectangular; they can produced in a wide variety of shapes. • The dimensional tolerance and surface finish of the fin are very accurate.
⊖	**Disadvantages**
	• Each mould uses a substantial volume of costly RP material. • Building tall, thin models can present problems for RP machines, yet building the model on its side would make poor use of the machine's resolution.

Table 15: Advantages and disadvantages of a negative RP mould.

D.3.3 RP Former

A need to economise on the amount of RP material necessary per mould inspired the following design. Instead of the whole mould being made of RP parts, RP was only used for the ends of the mould, and these supported a flexible sheet, which acted as a moulding surface for the fin. The design is shown in Figure 139. The RP mould formers were clamped opposite each other, against an L-section aluminium bracket. The small protrusions on the bottom and sides of the formers helped to locate them against the inside surfaces of the bracket. A bar passing through the clamping holes in the mould formers was used to clamp them securely in place (the clamping rod is visible in Figure 141).

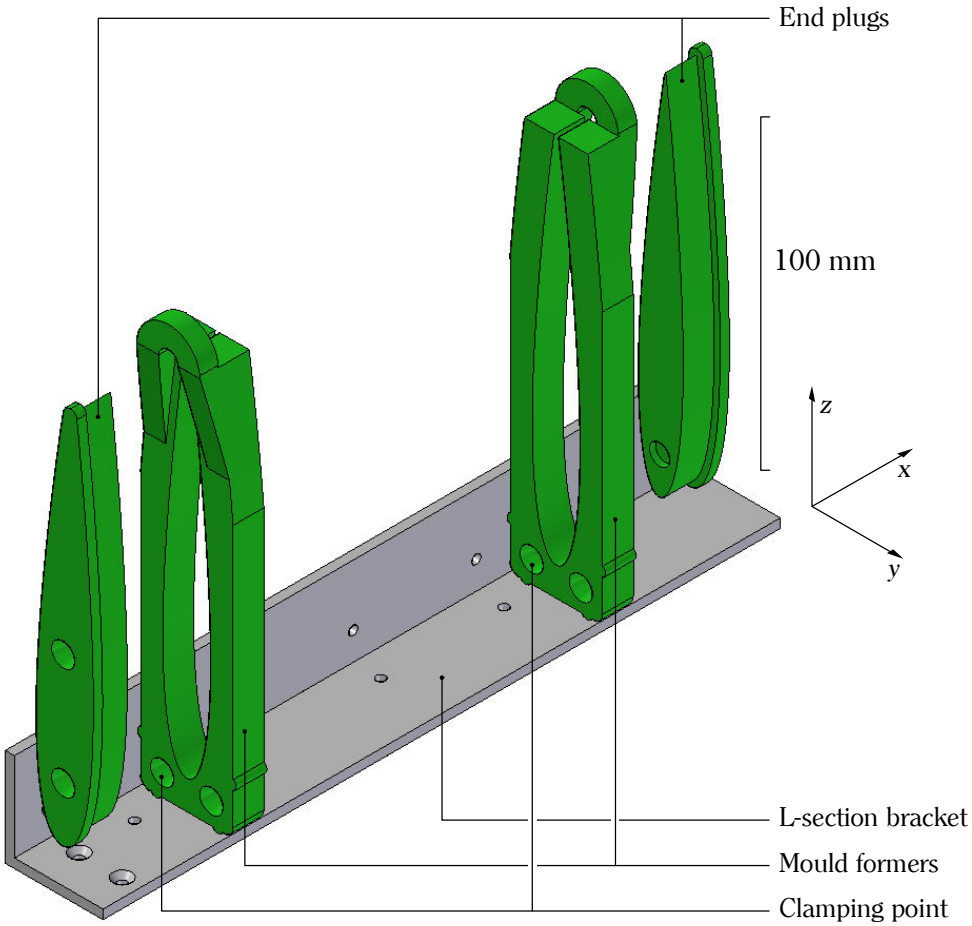

Figure 139: CAD model of parts for RP fin mould.

A rectangle of thin, flexible polypropylene was inserted into the aerofoil-shaped cavities in the mould formers, after being curled into approximately the right shape. The cavity was then sealed with the end plugs shown in Figure 139. This formed the plastic sheet into the precise shape defined in the original CAD designs. The axle was then inserted through a hole in one of the end plugs, and the mould rotated so that the axle pointed up. The seam was then clamped shut with bulldog clips (also visible in Figure 141), which formed the trailing edge of the fin, and then the mould was filled with resin through a hole in the upper mould plug. Figure 140 shows a cross-section of the mould on its side, through the fin axle, in the *x*-*y* plane according to the axes shown in Figure 139.

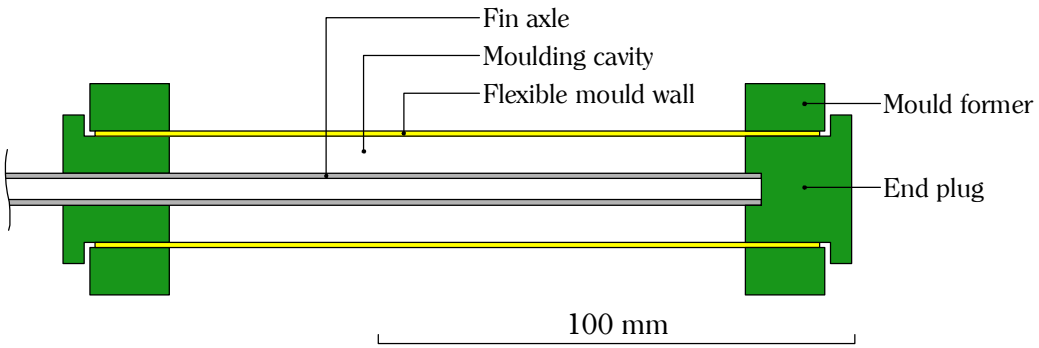

Figure 140: Cross-section through the fin mould at the axle, in the x-y plane.

Figure 141 shows the fin mould ready for use. In the photograph, the mould wall is transparent, and being supported by several vertical struts, added to provide extra stiffness. A funnel has been added to the upper end cap, so that resin can be poured in easily, inside a vacuum chamber.

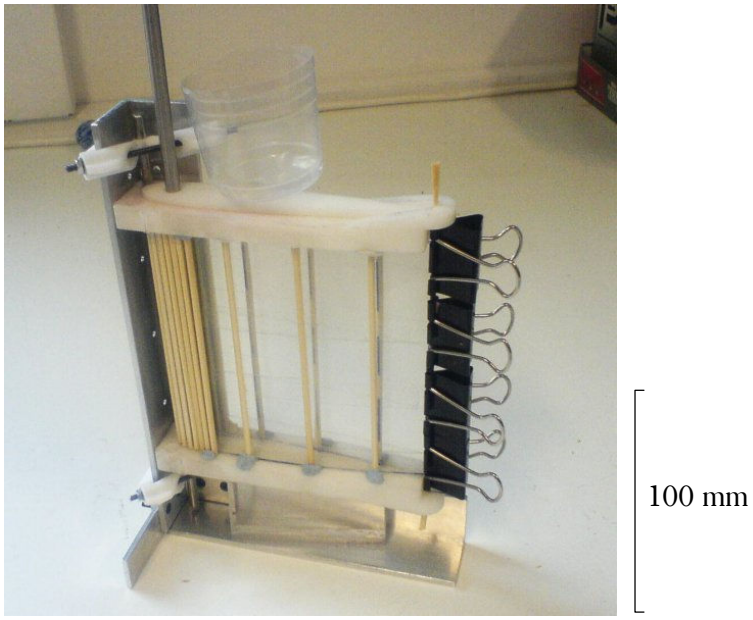

Figure 141: Flexible fin mould ready for use.

The design suffered from a number of problems, each of which had one or more potential solutions. They are listed in Table 16:

Problem and cause	Solution
Resin leaked from the bottom of the mould before it had finished curing, resulting in air entering the mould from the top, and the fin being shorter than intended.	The gaps around the base could be painted with latex adhesive, which dries to produce an airtight seal. The seal is insoluble in water and most resins, but can be easily peeled away when curing is complete.
The fin's section was not constant; its profile was wider in the middle than at the top, giving it a visible bulge, and significantly affecting its stiffness properties. Pressure on the mould walls from the weight of the resin was causing them to bend outward, and the vertical supports intended to prevent this were coming unstuck and failing to keep the walls straight.	Better attachment of the axial supports to the mould wall would help the situation, as would spars around the fin profile in the perpendicular direction. A thicker choice of plastic sheet for the outer wall would reduce deformation, but would also make the low-radius curve of the fin's leading edge hard to reproduce.
The trailing edge of the fin was uneven; 'crinkling' of the mould wall near the bulldog clips caused distortion of the moulded fin.	Thicker walls would improve the trailing edge, with the same disadvantaged described above.
The final shape of the fin depended on the volume of resin poured into the mould. The viscosity of the liquid resin made this difficult to control this accurately.	Improvements to the mould's stiffness helped its ability to hold its shape when overfilled, but the solution was never completely satisfactory.

Table 16: Problems with RP fin mould design and their solutions.

D.3.4 Redesigned RP former mould

An improved design was created, again using RP components as a former, supporting a flexible sheet. This time, spars were added to ensure the mould could not bulge, as had happened in the first design.

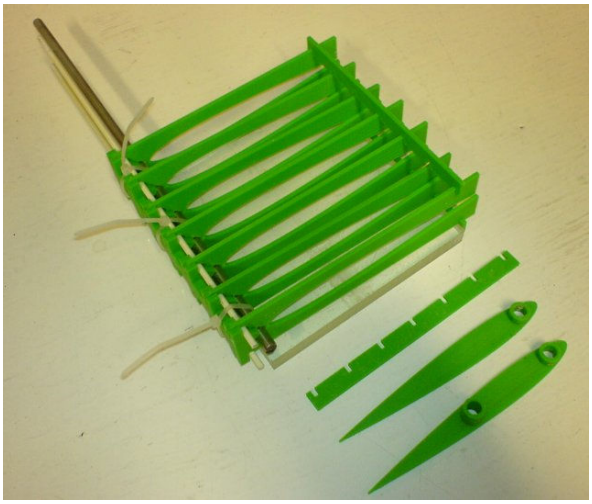

Figure 142: Improved fin mould components.

The new design (Figure 142) significantly improved the shape of the fins, reducing the distortion considerably. The spars kept the fin very close to its intended shape, but smaller, separate bulges were still visible between them. A variety of different materials were used to form the skin of the mould, but none completely overcame the problem. Materials that were stiff enough to reduce the bulging tended to be too stiff to follow the sharp profile at the leading edge of the fin.

D.4 CNC Machined Mould

Machining a mould from a block of plastic, as shown in Figure 143, was considered as an alternative to resin casting. Acrylic was an appropriate choice of mould material as it is stiff, inexpensive and easy to machine.

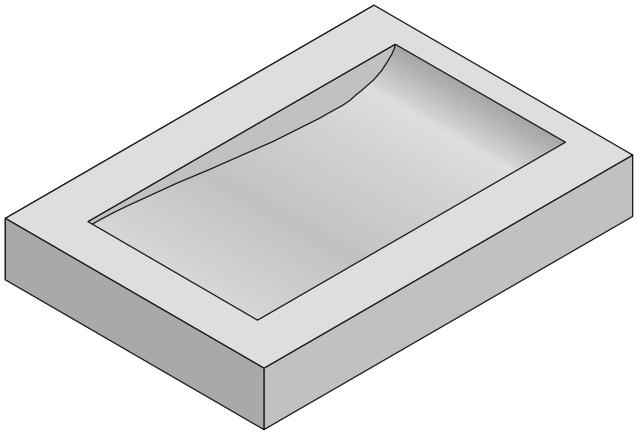

Figure 143: CNC machined mould.

The combination of smooth contours and sharp corners needed for a rectangular fin model mean its shape is not conducive to CNC machining alone. However, the method has been

used in similar studies (Kemp, *et al.*, 2003), and proved effective. Its advantages and disadvantages are shown in Table 17.

⊕	**Advantages**
	• Fins can be produced in any shape that can be cut by a CNC machine. • Resulting fins reproduce CAD data very accurately.
⊖	**Disadvantages**
	• A new mould is required for each different fin shape. • The shape of a fin mould is difficult to produce using a CNC mill.

Table 17: Advantages and disadvantages of a deformable fin mould.

Appendix E : Equipment

E.1 Rapid Prototyping

Rapid-prototyped models used in this thesis were built using a Stratasys Dimension BST Rapid Prototyping machine (Figure 144).

Figure 144: Stratasys Dimension BST Rapid Prototyping machine.

It employs the Fused Deposition Modelling (FDM) method, in which a filament of ABS plastic is deposited on the model, building up layers one at a time.

E.2 CNC Machining

A Deckel Maho DMU 50 Universal Milling Machine (Figure 145) was used to create the moulds for the silicone rubber fins.

Figure 145: Deckel Maho DMU 50 Universal Milling Machine.

E.3 Servomotor

The specifications of the Hitec RCD HS-5645MG servomotor used to actuate the fin are as follows:

CONTROL SYSTEM	:+PULSE WIDTH CONTROL 1500usec NEUTRAL	
OPERATING VOLTAGE RANGE	:4.8V TO 6.0V	
OPERATING TEMPERATURE RANGE	:-20 TO +60°C	
TEST VOLTAGE	:AT 4.8V	:AT 6.0V
OPERATING SPEED	:0.23sec/60° AT NO LOAD	:0.18sec/60° AT NO LOAD
STALL TORQUE	:10.3kg.cm(143.03oz.in)	:12.1kg.cm(168.03oz.in)
OPERATING ANGLE	:45°/ONE SIDE PULSE TRAVELING 400usec	
DIRECTION	:CLOCK WISE/PULSE TRAVELING 1500 TO 1900usec	
IDLE CURRENT	:3mA	:3mA
RUNNING CURRENT	:350mA	:450mA
DEAD BAND WIDTH	:1usec	
CONNECTOR WIRE LENGTH	:300mm(11.81in)	
DIMENSIONS	:40.6x19.8x37.8mm(1.59x0.77x1.48in)	
WEIGHT	:60g(2.11oz)	

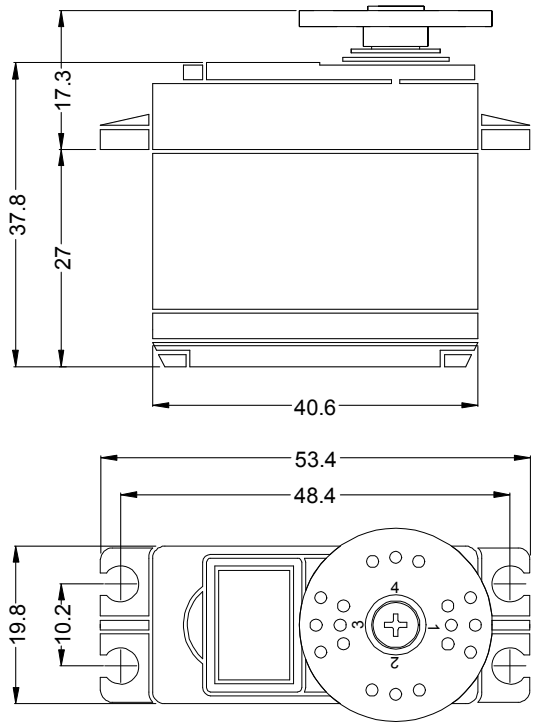

Figure 146: Hitec RCD HS-5645MG servomotor specifications.

Further information can be found at the manufacturer's website, www.hitecrcd.com.

E.4 Servo Controller

The specifications of the SSC03A Pololu Micro Serial Servo Controller are shown in Table 18, and the board itself is shown in Figure 147.

PCB size	23 x 23 mm
Number of servo ports	8
Pulse width range	0.25 - 2.75 ms
Resolution	0.5 µs (12-bit)
Supply voltage	5 - 16 v
I/O voltage	0 - 5 v
Baud rate	1200 - 38400 (auto detect)
Current consumption	5 mA (average)

Table 18: Pololu Micro Serial Servo Controller specifications.

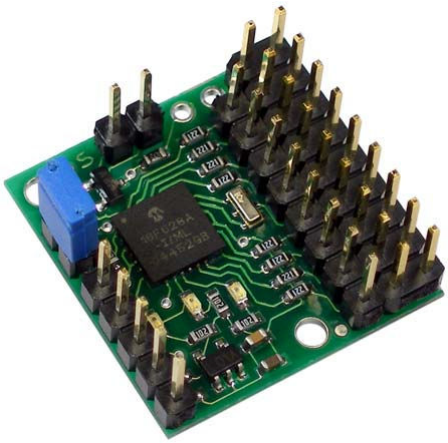

Figure 147: Pololu Micro Serial Servo Controller.

Further information can be found at the manufacturer's website, www.pololu.com.

E.5 Force Sensors

The specifications of the FSS1500-NSB force sensors are shown in Table 19.

Characteristics		Min.	Typ.	Max.	Unit
Operating force		0		1500	g
Zero pressure offset		-15		+15	mV
Span		150	180	210	
Temperature effects (0 - 50°C)	Offset		±0.5		
	Span		-2200		ppm/°C
Temperature effects on bridge impedance			+2200		
Linearity (BSL)			±0.7	±1.5	% span
Mechanical hysteresis			±0.5		
Repeatability at 300g			±1.5		mV
Input impedance		4.0	5.0	6.0	kΩ
Output impedance		4.0	5.0	6.0	
ESD (direct contact, terminals and plunger)		8			kV
MCTF (main cycles to failure at 50°C)			20		million cycles

Table 19: FSS1500-NSB specifications.

Further information can be found at the supplier's website, www.sensortechnics.com.

Appendix F : Software Packages

Several software packages were used in the research described in this thesis. They are summarised below.

F.1 Programming Languages

F.1.1 LabVIEW

LabVIEW is a graphical programming language useful for its simplicity and compatibility with many items of test equipment. Its strength is in creating quick programs to get data from hardware without a great deal of prior knowledge. It is well supported with many extensions and functions. Information on LabVIEW, its applications, and features, can be found on the National Instruments website: www.ni.com/labview.

F.1.2 PureBasic

PureBasic is a low-level programming language based on the rules and syntax of the original BASIC languages of the 80s, but far exceeding them in versatility. It is a compiled language, and can be used to write entire applications in Windows, LINUX, and Mac OS. It is far more streamlined and efficient than contemporaries such as Visual Basic, and it is useful for creating complex programs, and getting the best performance from hardware. It was used for the control of the test rig and data acquisition equipment in this work, as well as for image analysis experiments. Further details and specifications can be found on the PureBasic website: www.purebasic.com.

F.1.3 MATLAB

MATLAB is high-level numerical and graphical computing language. It was used extensively in this work for the interpretation, analysis, and visualisation of data. Further information is available at: www.mathworks.co.uk.

F.2 Computer Aided Design Software

F.2.1 UGS Solid Edge

UGS Solid Edge was used extensively for the design, drafting of the components of the fin test rig, and for modelling the fin designs. A particularly valuable feature is its ability to handle parametric designs. These are models where features depend on a set of parameters, such as

an aerofoil profile, and if these underlying parameters are changed, the model can update to reflect those changes. Further information on Solid Edge can be found at: www.ugs.com.

F.2.2 Catalyst

The Stratasys Rapid Prototyping machine (used to generate many of the components used in the experimental equipment) is operated by the Catalyst software (Figure 148). It takes the models created in Solid Edge and calculates the extrusion paths necessary to build them.

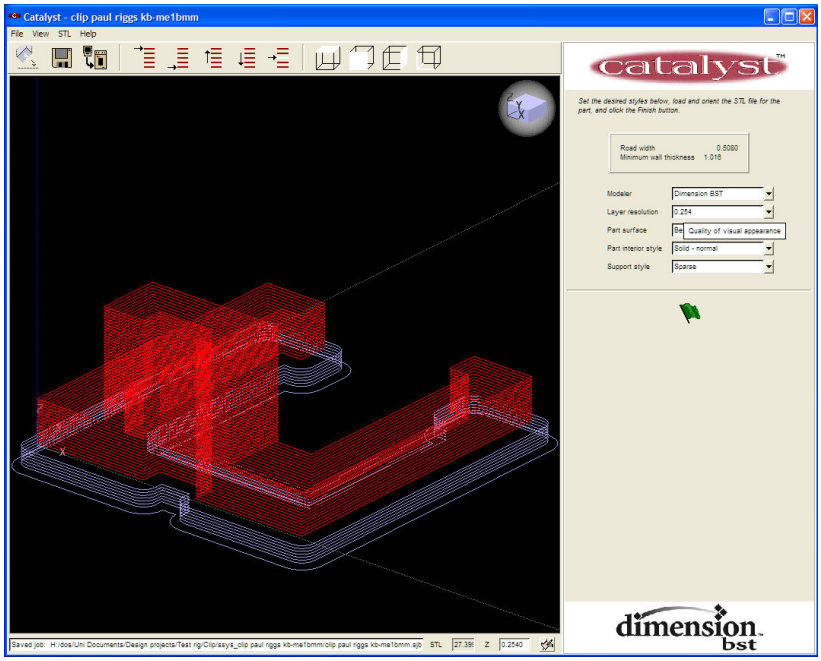

Figure 148: Catalyst rapid prototyping software.

F.2.3 Aerofoil shape generation

CAD models of aerofoils were produced using an academic computer program from the University of Sydney, known simply as 'naca45.exe'. A picture of the software in use is shown in Figure 149.

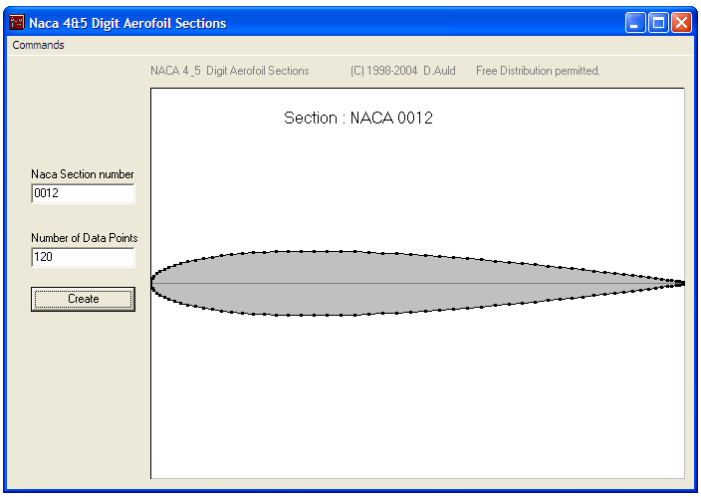

Figure 149: NACA Aerofoil generation program.

Appendix G : Programs

The test rig control and data acquisition software contained over 3000 lines of PureBasic code. The most fundamental procedures in the code are presented below, as they help to shed more light on the experimental process. The code in its entirety can be found on the supplemental data CD included with this thesis. Likewise, numerous MATLAB routines were used to process the data. These programs are also included.

G.1 Experiment Setup

Procedure for setting up a sequence of experiments to be executed by the test rig control software:

Variable	Description
`LoAmp, HiAmp, AmpStep`	Variables defining the range and step size of amplitudes to be used in the experiment set
`LowFreq, HiFreq, FreqStep`	Variables defining the range and step size of frequencies to be used in the experiment set

```
LoAmp.f = 2     :  HiAmp.f = 20  :  AmpStep.f = 2
LoFreq.f = 0.5   : HiFreq.f = 5   : FreqStep.f = 0.25

Waveform = #Sine
WaveCenter.f = 0.5
RampCycles.f = 3
Oscillations.f = 15
PauseBetween.f = 110
ZeroTime.f = 10
SaveFileName.s = "nacasoft"

TimeTotal = 0

Amplitude.f = LoAmp
Repeat
  Frequency.f = LoFreq
  Repeat

    AddElement(CommandList())
    CommandList()\Command = #CommandPause
    CommandList()\Wait = PauseBetween
    CommandList()\TimeSoFar = TimeTotal
    TimeTotal + (PauseBetween * 1000)

    AddElement(CommandList())
    CommandList()\Command = #CommandZero
    CommandList()\Wait = ZeroTime
    CommandList()\TimeSoFar = TimeTotal
    TimeTotal + (ZeroTime * 1000)

    AddElement(CommandList())
    CommandList()\Command = #CommandTest
    CommandList()\SaveFileName = SaveFileName
    CommandList()\Frequency = Frequency
    CommandList()\Amplitude = Amplitude
    CommandList()\Oscillations = Oscillations
    CommandList()\Waveform = Waveform
    CommandList()\WaveCenter = WaveCenter
    CommandList()\RampCycles = RampCycles
    CommandList()\TimeSoFar = TimeTotal
    TimeTotal + ((Oscillations * 1000) / Frequency)

    Frequency + FreqStep
  Until Frequency > HiFreq
  Amplitude + AmpStep
Until Amplitude > HiAmp
```

G.2 Wave Generation

Procedure for calculating fin position as a function of time:

Variable	Description
PhaseFraction	Value between 0 and 1 representing the phase angle / 2π
Cycle	Number of cycles completed by the fin
WaveCenter	The asymmetry value, between 0 and 1
RampCycles	Number of cycles in which amplitude is to increase from 0 to its final value
Cycle	Number of cycles completed by the fin

```
Procedure.f CalcAngle(PhaseFraction.f, Cycle.f)

  Shared WaveCenter.f, RampCycles.f

  ; Adjust phase fraction consistent with asymmetry value
  If PhaseFraction < WaveCenter / 2
    AdjustedPhaseFraction.f = PhaseFraction / (WaveCenter / 2) * 0.25
  ElseIf PhaseFraction > 1 - (WaveCenter / 2)
    AdjustedPhaseFraction.f = (PhaseFraction - (1 - (WaveCenter / 2))) / (WaveCenter
/ 2) * 0.25 + 0.75
  Else
    AdjustedPhaseFraction.f = ((PhaseFraction - (WaveCenter / 2)) / (1 - WaveCenter)
* 0.5) + 0.25
  EndIf

  Select ServoWaveform
    Case #Sine
      Position.f = ServoAmplitude * Sin(AdjustedPhaseFraction * 2 * #PI)

    Case #Triangle
      If AdjustedPhaseFraction < 0.25
        Position.f = ServoAmplitude * (AdjustedPhaseFraction * 4)
      ElseIf AdjustedPhaseFraction < 0.75
        Position.f = ServoAmplitude * ((AdjustedPhaseFraction - 0.5) * -4)
      Else
        Position.f = ServoAmplitude * ((AdjustedPhaseFraction - 1) * 4)
      EndIf

    Case #Square
      If AdjustedPhaseFraction < 0.25
        Position.f = ServoAmplitude
      ElseIf AdjustedPhaseFraction < 0.75
        Position.f = -ServoAmplitude
      Else
        Position.f = ServoAmplitude
      EndIf

  EndSelect

  ; Ramp amplitude if required
  If Cycle < RampCycles
    RampAmplitude.f = Cycle / RampCycles
  Else
    RampAmplitude = 1
  EndIf

  ProcedureReturn Position * RampAmplitude

EndProcedure
```

G.3 Data Conversion

Procedure for calculating forces and torques from raw sensor data:

Variable	Description
`F0, F1, F2`	Forces at sensors
`Faz, Fbz, Fby`	Forces at sensor locations in direction of axes
`Tx, Ty, Tz`	Torques acting on rig about axes
`Fx, Fy`	Forces acting on fin, derived from torques
`FinDirection`	Direction of centre of oscillation in relation to *y* axis

```
For Channel = 0 To nChannels - 1 ; Channel numbers start from 0
  ; Retrieve raw reading from memory location
  RawReading(Channel) = PeekW(MemHandle + (BufferPosition * 2) + ((Channel) * 2))
  ; Clean up data and add global offset
  RawReading(Channel) = RawReading(Channel) & 65535 + GlobalOffset
  ; Apply scalar and offset to convert raw reading to force
  Reading(Channel) = (RawReading(Channel) - ROffset(Channel)) * RScalar(Channel)
Next

; Primary measurements:
F0.f = Reading(0)
F1.f = Reading(1)
F2.f = Reading(2)
RealAngle.f = Reading(3) - Angle0

; Derive component forces:
Faz.f = F0
Fbz.f = (F1 + F2) / Sqr(2)
Fby.f = (F1 - F2) / Sqr(2)

; Calculate torques about pivot
Tx.f = ((Fbz - Faz) * YSensor) - Tx0
Ty.f = ((Faz + Fbz) * XSensor) - Ty0 ; Need rig dimensions
Tz.f = (Fby * XSensor) - Tz0

; Calculate forces at fin
Fx.f = Ty / ZFin
Fy.f = Tx / ZFin

; Calculate thrust, lateral, torque
Thrust.f = Fx * Cos(FinDirection) - Fy * Sin(FinDirection)
Lateral.f = Fx * Sin(FinDirection) + Fy * Cos(FinDirection)
Torque.f = -Tz - (Fy * XFin)

; Work out target position of fin
Phase = Int(CurrentDataPointTime) % ServoPeriodms
PhaseFraction.f = Phase / ServoPeriodms
ServoCycles.f = Int(CurrentDataPointTime) / ServoPeriodms
ServoTargetAngle.f = CalcAngle(PhaseFraction, ServoCycles)
```

G.4 Post-Experiment Analysis

Table 20 lists the MATLAB programs that were developed to assist in analysing the data from the test equipment. They can be found in the supplementary data CD that accompanies this thesis.

Program	Description
`v2_analyse_save`	Analyse data from a set of tests and save summary to a file
`v2_comparegraph`	Compare data from two experiment sets
`v2_forcetrace`	Produce a force trace plot from a single test data file
`v2_globalset`	Define global variables
`v2_plotgraph3d`	Plot 3D surface graphs from data summary files
`v2_readfile`	Read data from a CSV file
`v2_savegraph2d`	Format, resize, and save 2D graph to a file
`v2_savegraph3d`	Format, resize, and save 3D graph to a file

Table 20: Command list parameters

Appendix H : Data

H.1 Example Data File

The following is an extract from the start of a data file produced by the test rig software. Several thousand of these files over the course of this investigation, between them containing many millions of data samples.

```
Date,15:37:21, 08/10/2008
FileVersion,5
SampleRate,1000
Tx0,0.376911
Ty0,3.577199
Tz0,0.001241
Angle0,3.435227
XSensor,0.220700
YSensor,0.068000
XFin,0.077000
ZFin,-0.265000
FinDirection,4.712389
Waveform,0.000000
WaveCenter,0.500000
RampCycles,3.000000
Experiment,Y
FinCycles,15.000000
Frequency,3.750000
Amplitude,2.000000

Time,Channel0,Channel1,Channel2,Channel3,F0,F1,F2,Angle,Tx,Ty,Tz,Phase,TargetAngle,Th
rust,Lateral,Torque
0.000000,744,911,888,499,5.328091,7.709827,7.690469,0.632570,0.001275,0.002057,0.0017
80,0.000000,0.000000,-0.004813,0.007764,-0.001410
1.000000,744,911,888,501,5.328091,7.709827,7.690469,-
0.045397,0.001275,0.002057,0.001780,0.003745,0.000059,-0.004813,0.007764,-0.001410
2.000000,744,909,888,501,5.328091,7.689528,7.690469,-0.045397,0.000299,-0.001111,-
0.001387,0.007491,0.000235,-0.001130,-0.004191,0.001474
3.000000,744,911,888,501,5.328091,7.709827,7.690469,-
0.045397,0.001275,0.002057,0.001780,0.011236,0.000528,-0.004813,0.007764,-0.001410
4.000000,744,909,888,501,5.328091,7.689528,7.690469,-0.045397,0.000299,-0.001111,-
0.001387,0.014981,0.000939,-0.001130,-0.004191,0.001474
...
```

H.2 Example Log File

The following is an extract from a log file for a series of experiments on the hard compound biomimetic fin.

```
Filename,biohard

FileNumber,Frequency,Amplitude,Cycle,TxAvg,TyAvg,TzAvg,TxRMS,TyRMS,TzRMS,OK
1,0.500000,2.000000,0,0.000065,0.000017,-0.000083,0.002222,0.003156,0.002090,OK
1,0.500000,2.000000,1,-0.000122,0.000712,0.000030,0.005483,0.008336,0.003493,OK
1,0.500000,2.000000,2,-0.000407,0.001531,-0.000223,0.005125,0.011794,0.003654,OK
1,0.500000,2.000000,3,-0.000347,0.000891,-0.000703,0.004831,0.015270,0.004080,OK
1,0.500000,2.000000,4,-0.000329,0.001871,-0.000035,0.008623,0.016050,0.004606,OK
1,0.500000,2.000000,5,-0.000317,0.001851,-0.000452,0.005316,0.014430,0.004496,OK
1,0.500000,2.000000,6,-0.000291,0.001215,-0.000522,0.005918,0.014885,0.004248,OK
1,0.500000,2.000000,7,-0.000386,0.001826,-0.000230,0.007145,0.015661,0.004832,OK
1,0.500000,2.000000,8,-0.000347,0.001896,-0.000463,0.004768,0.013834,0.004126,OK
1,0.500000,2.000000,9,-0.000361,0.001478,-0.000192,0.006502,0.017419,0.004472,OK
1,0.500000,2.000000,10,-0.000394,0.002147,0.000086,0.009896,0.016161,0.004968,OK
1,0.500000,2.000000,11,-0.000282,0.002303,-0.000411,0.005096,0.014585,0.003871,OK
1,0.500000,2.000000,12,-0.000240,0.001353,-0.000521,0.004337,0.015804,0.004177,OK
...
```